Transferts du cadmium et du zinc par phase fluide et vapeur dans les processus hydrothermaux et volcaniques: étude expérimentale, modélisation physico-chimique et applications géologiques

Elena Bazarkina

▶ To cite this version:

Elena Bazarkina. Transferts du cadmium et du zinc par phase fluide et vapeur dans les processus hydrothermaux et volcaniques: étude expérimentale, modélisation physico-chimique et applications géologiques. Géochimie. Université Paul Sabatier - Toulouse III, 2009. Français. NNT : . tel-00457869

HAL Id: tel-00457869

https://theses.hal.science/tel-00457869

Submitted on 18 Feb 2010

THÈSE

En vue de l'obtention du

DOCTORAT DE L'UNIVERSITÉ DE TOULOUSE

Délivré par *l'Université Toulouse III - Paul Sabatier*
Discipline ou spécialité : *Géochimie*

Présentée et soutenue par *Elena BAZARKINA*
Le *15 décembre 2009*

Titre : *Transferts du cadmium et du zinc par phase fluide et vapeur dans les processus hydrothermaux et volcaniques: étude expérimentale, modélisation physico-chimique et applications géologiques*

JURY

Didier Beziat - Professeur à l'Université Paul-Sabatier, Toulouse France
Pascal Philippot - Professeur à l'Université Denis Diderot, Paris France
Igor Khodakovsky - Professeur à l'Université de Dubna, Russie
Andrew Berry - Senior Lecturer, Imperial College London, London UK
Jacques Schott - Directeur de Recherche au CNRS, LMTG Toulouse France
Andrew Bychkov - Professeur à l'Université d'Etat de Moscou, Russie
Gleb Pokrovski - Chargé de Recherche au CNRS, LMTG Toulouse France
Alexander Zotov - Directeur de Recherche à l'IGEM RAS, Moscou Russie

Ecole doctorale : *Sciences de l'Univers, de l'Environnement et de l'Espace*
Unité de recherche : *Laboratoire des Méchanismes et Transferts en Geologie (LMTG)*
Directeur(s) de Thèse : *Gleb Pokrovski, Alexander Zotov*
Rapporteurs : *Pascal Philippot, Igor Khodakovsky*

To my father Fedor Bazarkin

Acknowledgements

Résumé étendu

Cette étude a pour but de quantifier le rôle de la phase fluide et vapeur sur le comportement du zinc et du cadmium dans les processus hydrothermaux et volcaniques, en combinant mesures expérimentales en laboratoire (solubilité, potentiométrie, coefficients de partage) et spectroscopie d'absorption de rayons X (XAS) in situ avec modélisations physico-chimiques et analyses des fluides naturels.

L'identité, la structure et la stabilité des complexes que forme en solution aqueuse le cadmium avec le chlorure (Cl), le plus important continuant des fluides géologiques, ont été déterminées, dans une large gamme de température ($20 \leq T \leq 500°C$), pression ($1 \leq P \leq 2000$ bar) et concentration de ligand ($0 \leq m_{Cl} \leq 18$ mole/kg H$_2$O), par essais de solubilité et potentiométrie, combinés à des mesures in situ par spectroscopie XAS. Nos résultats mettent en évidence la formation de complexes de stoechiométrie $CdCl_m(H_2O)_n^{2-m}$ ayant des géométries octaédriques ou tétraédriques selon T et m_{Cl}. Ces changements structuraux reflètent l'évolution des propriétés du solvant (constante diélectrique, densité, liaisons hydrogène) et de l'affinité chimique métal-ligand avec la température et l'activité du ligand. Elles sont similaires à ceux subis par d'autres métaux de transition comme Zn, Fe, Co, Ni. L'évolution de la géométrie des complexes Cd-Cl$_n$ en fonction du nombre de ligand (n) est en bon accord avec nos mesures potentiométriques indépendantes du volume standard molaire de ces espèces chlorurées. L'information structurale fournie par la spectroscopie d'absorption X peut donc être utilisée pour mieux contraindre les propriétés thermodynamiques d'espèces aqueuses obtenues par les méthodes de solubilité ou potentiométrie. Les paramètres thermodynamiques (G, H, S, Cp, V et coefficients du modèle HKF) générées pour ces complexes dans une large gamme de T et P démontrent que le chlorure est largement responsable du transport de Cd par les fluides hydrothermaux et que les autres ligands naturels comme les hydroxydes et les sulfures jouent un rôle mineur dans le transfert de ce métal.

Ces résultats, couplés avec une révision critique des données de la littérature sur la spéciation aqueuse du zinc, indiquent que les complexes chlorurés de Cd sont beaucoup plus stables que leurs analogues de Zn. Ceci est en accord avec des mesures de coefficients de partage liquide-vapeur pour les deux métaux que nous avons conduites dans le système H$_2$O-NaCl et qui montrent un plus fort fractionnement de Cd en faveur de la phase liquide riche en sel. Dans un système minéral-vapeur, en l'absence de liquide, nos mesures de solubilité de ZnO et CdO dans la phase vapeur H$_2$O-NaCl-HCl indiquent un enrichissement de la vapeur en Cd versus Zn. L'ensemble de ces résultats a été traité dans le cadre d'un modèle de densité qui est le paramètre macroscopique de la phase fluide/vapeur le mieux connu dans une très large gamme de T-P-composition.

Ces mesures peuvent rendre compte de l'enrichissement en Cd dans les condensats de fumeroles du volcan Kudryavy analysées lors de travaux de terrain durant cette thèse et ceux d'autres volcans actifs reportés dans la littérature. Au cours de ce travail de terrain, nous avons mis au point une nouvelle méthode de prélèvement des condensats de fumerolles de haute température. Ces échantillons ont été traités et analysés par diverses techniques analytiques (ICP-MS, ICP-AES, chromatographie ionique) afin de mettre en œuvre un procédé analytique dépourvu d'artéfacts de prélèvement et de traitement d'échantillons de gaz et fumeroles volcaniques (e.g. précipitation, perte, dégazage, interférences analytiques) et de générer un petit ensemble cohérent de

concentrations de Cd, Zn, de principaux ligands et d'autres métaux majeurs et traces dans les condensats du volcan Kudryavy.

L'ensemble des données expérimentales et analytiques obtenues permet de mieux interpréter le comportement du cadmium et du zinc dans les milieux de haute *T-P* et de proposer un nouveau traceur géochimique des processus hydrothermaux basé sur le rapport Cd/Zn. Ainsi, un fluide hydrothermal ou une vapeur volcanique en équilibre avec une phase minérale-porteuse de Cd et Zn (e.g. sphalérite cadmifère) aura tendance à s'enrichir en Cd vis-à-vis de Zn lorsque la teneur en chlore dans la phase fluide (ou vapeur) augmente. La pression aurait également un effet important sur le rapport Zn/Cd. Par exemple, une sphalerite, précipitée à partir d'un fluide salin porteur de Cd et Zn, serait enrichie en Cd d'autant plus que la pression est forte. Ceci peut servir d'un traceur de pression lors de la formation de gisements de zinc et d'autres métaux. En revanche, dans un système liquide-vapeur, lors de l'ascension et l'ébullition d'un fluide métallifère, la phase vapeur sera appauvrie en Cd par rapport de la saumure coexistante. Ceci permettrait de tracer les phénomènes d'ébullition et de séparation de phase que subissent la majorité des fluides hydrothermaux.

Les résultats de ce travail contribuent au développement des modèles thermodynamiques et structuraux des fluides des hautes températures et pressions ; ils permettent de mieux comprendre le comportement d'autres métaux d'intérêt économique associés à Cd et Zn comme Cu, Pb, Au. Ils peuvent avoir des implications pour l'extraction des minerais et les procédées de dépollution de mines de métaux de base, ainsi que pour l'interprétation des fractionnements isotopiques de Zn et Cd dans les processus hydrothermaux et volcaniques sur notre planète.

Mots clés: cadmium, zinc, fluide hydrothermal, complexes avec chlorure, constants de stabilité, propriétés thermodynamiques spectroscopie XAS, solubilité, potentiomètrie, ratio Cd/Zn,.

Расширенное резюме

Цель диссертации – исследование кадмия и цинка в гидротермальных/вулканических обстановках с использованием экспериментальных методов (растворимость, потенциометрия, распределеeие жидкость-пар), in situ спектроскоскопии поглощения рентгеновских лучей, и физико-химическим моделирования природных флюидов.

Стехиометрия, структура и стабильность форм нахождения кадмия в водных растворах были измерены в широком диапозоне температур ($20 \leq T \leq 500°C$), давлений ($1 \leq P \leq 2000$ bar) и концентраций хлора ($0 \leq m\text{Cl} \leq 18$ моль/кг H$_2$O) с использованием методов растворимости, потенциометрии и спектроскории поглощения рентгеновских лучей (XAS). Полученные данные демонстрируют образование хлоридных комплексов $CdCl_m(H_2O)_n^{2-m}$ с октаэдрической и тетраэдрической структурой в зависимости от температуры и солености. Термодинамические параметры поолученные для этих частиц указывают на то, что они являются доминирующими формами нахождения кадмия в гидротермальных флюидах, в то время как гидроксидные комплексы и комплексы содержащие серу не играют существенной роли в переносе кадмия в типичных гидротермальных и вулканических условиях.

Наши результаты по кадмию и критический обзор литературных данных по водным частицам цинка показывают, что комплексообразование с хлором гораздо сильнее у кадмия, чем у цинка. Это подтверждают: 1) наши экспериментальные данные по распределению жидкость-пар в системе H$_2$O-NaCl, в которой кадмий обогащает жидкую фазу рассола сильнее чем цинк, и 2) наши данные по растворимости CdO and ZnO в малоплотной паровой фазе в системе H$_2$O-NaCl-HCl, согласно которым в паровой фазе с увеличением концентрации хлора растворимость CdO растет на несколько порядков сильнее, чем растворимость ZnO. Эти эксперименты в хорошем согласии с обогащением Cd газов вулкана Кудрявый, конденсаты которых были отобраны и проанализированы в рамках настоящей работы, а также с литературными данными. Комплекс экспериментальных, аналитических и термодинамических данных был получен в настоящей работе для интерпретации поведения кадмия и цинка в природных гидротермальных флюидах. Показано, что Zn/Cd отношение может быть индикатором эволюции и состава рудообразующего флюида. Эти новые данные необходимы для понимания механизмов транспорта и отложения цинка, кадмия и ассоциированных с ними экономически важных металлов (Cu, Pb, Au).

Ключевые слова: кадмий, цинк, гидротермальные флюиды, хлоридные комплексы, константы устойчивости, термодинамические свойства, спектроскопия поглощения рентгеновских лучей XAS, растворимость, потенциометрия, Cd/Zn отношение.

Extended abstract

The goal of this work is to quantify the role of the vapor and fluid phases in the behavior of zinc and cadmium in hydrothermal/volcanic environments, using a combination of laboratory experiments in model systems (solubility, potentiometry, partitioning) and in situ X-ray absorption spectroscopy (XAS) measurements with physical-chemical modeling and analyses of natural fluids.

The identity, structure and stability of aqueous complexes formed by cadmium with chloride, which is the major constituent of geological fluids, were determined in a wide range of temperature ($20 \leq T \leq 500°C$), pressure ($1 \leq P \leq 2000$ bar) and ligand concentration ($0 \leq m_{Cl} \leq 18$ m/kg H_2O) using solubility and potentiometry experiments combined with XAS spectroscopy. Our results show the formation of Cd-Cl complexes with stoichiometries $CdCl_m(H_2O)_n^{2-m}$ and octahedral or tetrahedral geometries depending on T et m_{Cl}. The thermodynamic parameters generated for these species imply that chloride is largely responsible for the Cd transport by hydrothermal fluids, and that other natural ligands like hydroxide and sulfur play a minor role in the Cd transfers at elevated temperatures.

These results, coupled with a critical revision of the literature data on Zn aqueous speciation and solubility, indicate that aqueous and gaseous Cd chloride complexes are far more stable than their Zn analogs. This is in agreement with i) our vapor-liquid partition coefficients measurements for both metals in the system H_2O-NaCl, which reveal a stronger fractionation of Cd in favor of the brine, and with ii) our CdO and ZnO solubility measurements in H_2O-NaCl-HCl vapors, which show Cd versus Zn enrichment in the vapor phase. These experiments are in agreement with the Cd enrichments in fumaroles of the Kudryavy volcano sampled and analyzed during this thesis work, and data on condensates and sublimates from other volcanoes reported in the literature.

The ensemble of experimental, analytical and thermodynamic data obtained in this work permits to better interpret the Cd and Zn behavior in high T-P environments, and to propose a new geochemical tracer of hydrothermal fluid evolution and composition based on the Zn/Cd ratios in the fluid and minerals formed therefrom. The results of this study contribute to the development of thermodynamic and structural models of high T-P fluids and allow better constraints on the behavior of other metals of economic interest associated with Cd and Zn like Cu, Pb, Au.

Key words: cadmium, zinc, hydrothermal fluids, chloride complexes, stability constants; thermodynamic properties, X-ray absorption spectroscopy XAS, solubility, potentiometry, Cd/Zn ratio

x

CONTENTS

Bazarkina, E.F., Zotov, A.V., Akinfiev, N.N.,"Potentiomentric study of cadmium chloride complexes from 1 to 1000 bar at 25°C" submitted to *Geology of Ore deposits* in August 2009

Chapter IV. STRUCTURE AND STABILITY OF CADMIUM CHLORIDE COMPLEXES IN HYDROTHERMAL FLUIDS

Bazarkina E.F., Pokrovski G.S., Zotov A.V., Hazemann, J.-L., "Structure and stability of cadmium chloride complexes in hydrothermal fluids" submitted to *Chemical Geology* in October 2009

Chapter V. MODELING OF Cd/Zn RATIOS IN HYDROTHERMAL FLUIDS AND VAPORS AND COMPARISON WITH NATURAL OBSERVATIONS

Chapter VI. CONCLUSIONS AND PERSPECTIVES

References

ANNEX :

Pokrovski G.S., Tagirov B.R., Schott J., Bazarkina E.F., Hazemann J.L., Proux O "An in situ X-ray absorption spectroscopy study of gold-chloride complexing in hydrothermal fluids", *Chemical Geology* 259 (2009), pp. 17-29

List of abbreviations

AAS	Atomic absorption spectroscopy
CCWT	Continuous Cauchy wavelet transform
EXAFS	Extended X-ray absorption fine structure
FT	Fourier transform
HKF	Helgeson-Kirkham-Flowers equation of state (Helgeson et al., 1981)
HPLC	High performance liquid chromatography
ICP-AES	Inductively coupled plasma atomic emission spectrometry
ICP-MS	Inductively coupled plasma mass spectrometry
LCF	Linear combination fit
m	Molality units (number of moles of component per kg of water)
M	Molarity units (number of moles of components per liter of solvent)
NMR	Nuclear magnetic resonance
ppm, ppb, ppt	Weight units: part-per-million, part-per-billion, part-per-trillion
PCA	Principal component analysis
P_{sat}	Pressure of saturated vapor
SEM	Scanning electron microscopy
XAS	X-ray absorption spectroscopy
XAFS	X-ray absorption fine structure
XANES	X-ray absorption near edge structure
XRD	X-ray diffraction
wt%	Weight percents units: part-per-hundred

List of Figures

names.

List of Tables

Tables from the article submitted to *Chemical Geology,* chapter IV

Chapter I. INTRODUCTION

I-1. Geochemistry of cadmium and zinc

Chemistry, mineralogy, and economic significance

Cadmium and zinc make up a column of the periodic table (together with mercury, Fig. I-1), thus their physical and chemical properties are very similar one to another. These elements are typical metals possessing two valence electrons. Their position in the periodic classification immediately follows the transition series, and in keeping with the usual periodic trends, they have comparatively high electronegativity values for metallic elements and form bonds with nonmetals of significant covalent character. The covalent properties are increased on going down the column from zinc to mercury.

Legend:
- ■ hydrogen
- ■ alkali metals
- ■ alkali earth metals
- ■ transition metals
- ■ poor metals
- ■ nonmetals
- ■ noble gases
- ■ rare earth elements

1 H	2											13	14	15	16	17	2 He
3 Li	4 Be											5 B	6 C	7 N	8 O	9 F	10 Ne
11 Na	12 Mg											13 Al	14 Si	15 P	16 S	17 Cl	18 Ar
19 K	20 Ca	21 Sc	22 Ti	23 V	24 Cr	25 Mn	26 Fe	27 Co	28 Ni	29 Cu	30 Zn	31 Ga	32 Ge	33 As	34 Se	35 Br	36 Kr
37 Rb	38 Sr	39 Y	40 Zr	41 Nb	42 Mo	43 Tc	44 Ru	45 Rh	46 Pd	47 Ag	48 Cd	49 In	50 Sn	51 Sb	52 Te	53 I	54 Xe
55 Cs	56 Ba	57 La	72 Hf	73 Ta	74 W	75 Re	76 Os	77 Ir	78 Pt	79 Au	80 Hg	81 Tl	82 Pb	83 Bi	84 Po	85 At	86 Rn
87 Fr	88 Ra	89 Ac	104 Rf	105 Db	106 Sg	107 Bh	108 Hs	109 Mt	110 Ds	111 Rg							

58 Ce	59 Pr	60 Nd	61 Pm	62 Sm	63 Eu	64 Gd	65 Tb	66 Dy	67 Ho	68 Er	69 Tm	70 Yb	71 Lu
90 Th	91 Pa	92 U	93 Np	94 Pu	95 Am	96 Cm	97 Bk	98 Cf	99 Es	99 Fm	101 Md	102 No	103 Lr

Figure I-1. *Periodic table of the elements. Studied elements, Zn and Cd, are marked in grey.*

Zinc, a common metal widely found in Nature, is released into the environment through mining and industrial operations, and though the natural weathering of ores. Zinc forms many own minerals. The most common are sphalerite α-ZnS, wurtzite β-ZnS, zincite ZnO, smithsonite $ZnCO_3$, zincosite $ZnSO_4$, willemite Zn_2SiO_4. Sphalerite is the most important industrial mineral of Zn. Cadmium resembles zinc in its chemistry in many respects. As a result, obtaining zinc free from a cadmium impurity is difficult (Bailey et al., 2002). Cadmium usually follows its "big brother", zinc, but occurs in nature only as a minor component (the 67th in order of abundance in the Earth's crust). The own minerals of cadmium are very rare. The most known of them, greenockite β-CdS, monteponite CdO, otavite $CdCO_3$, cadmoselite CdSe and hawleyite α-CdS, originate mainly from Cd-bearing zinc ores and their weathering products. Occurrences of very rare Cd-Zn-In sulfudes were

described in high-temperature fumarolic mineralization at the Kudryavy volcano, Kuril Islands, Russia (Kovalenker et al., 1993).

Zinc has been used by humans since Roman times. The industrial revolution of the 19th century resulted in a large increase of the Zn (and consequently, Cd) world production (Fig. I-2). Nowadays zinc stands fourth among all metals in world production – being exceeded only by iron, aluminum, and copper (Tolcin, 2009). Despite the constant increase of production, Zn prices do not show systematic increase at least over the five last years (Fig. I-3a), mainly due to the constant improvement in extraction and mining technologies. About 3/4 of zinc used is consumed as metal, mainly as a coating to protect iron and steel from corrosion (galvanized metal), as alloying metal to make bronze and brass, as zinc-based die casting alloy, and as rolled zinc. The remaining 1/4 is consumed as zinc compounds mainly by the rubber, chemical, paint, and agricultural industries (Tolcin, 2009). The growing concern over cadmium toxicity (see below) has lead to significant restrictions, especially in the European Union, of the use of cadmium in most of its applications (Tolcin, 2008). As a result, the production of Cd has stabilized since 1990's (Fig. I-2b), and the prices on average did not change over the last 5 years despite several short-term fluctuations (e.g., Fig. I-3b). However, cadmium is unavoidable byproduct from mining, smelting, and refining of zinc-bearing sulfide ores and can be useful for numerous industrial applications. Cadmium has such unique properties as excellent resistance to corrosion, particularly in alkaline and seawater environments, low melting temperature and rapid electrical exchange activity, both high electrical and thermal conductivity. According to the International Cadmium Association (2003), Cd industrial use is shared as follows: 79% – NiCd batteries, 11% – pigments, 7% – coatings, 2% – stabilizers for plastics, and 1% – other minor uses. NiCd batteries have a high number of charge-discharge cycles, high rate of energy discharge, and a wide operating temperature that is very important for industrial applications and aircraft electrical systems. The main advantage of NiCd batteries in comparison with other batteries is their stability in harsh weather environments. However, for such applications as laptops or cellular phones, NiCd batteries are nowadays completely replaced by Li-ion batteries which have greater energy density (power-to-weight ratio). One of the uses of cadmium attracting the growing interest is solar cells. Cadmium telluride (CdTe) thin-film solar cells are an alternative to traditional crystalline silicon solar cells and are practical for commercial rooftop applications and large scale, ground-mounted utility systems (Tolcin, 2008). Another small but important application is the use of cadmium sulfide crystals in radiation detection devices and photo-sensitive elements. It should be mentioned that cadmium wasting or storage might be more dangerous for humans than accurate and rational using with recycling.

Biogeochemistry and environmental aspects

Larger differences between cadmium and zinc are in their biochemistry. Whereas zinc is essential to life, cadmium is highly toxic. Zinc is an important constituent of enzymes; the daily requirement for an adult is 15–20 mg of Zn (WHO, 2006). Thus, it is essential for humans and animals and comparatively nontoxic, with drinking water limits of 3 ppm (WHO, 2006). The biochemical role of cadmium for different life organisms is still poorly known. For humans cadmium is classified as extremely toxic. The drinking water limit of Cd is as low as 3 ppb, which is 2-5 times lower than those for mercury, arsenic, lead and uranium and 1000 times lower than that for zinc (WHO, 2006). The reason for the high cadmium toxicity may in part lie in its similarity to zinc: for example, it can

substitute for Zn in enzymes, but because of the stronger Cd bonding and stereo-chemical differences, the function of such Cd-bearing enzyme is perturbed. The most notable widespread example of cadmium poisoning occurred in 1940's along the lower Jinzu river in central Japan, where approximately 200 people developed a disease called "itai-itai" after eating rice grown in paddies watered from the river, which was contaminated with cadmium released from lead and zinc mine wastes (Nogawa and Kido, 1996). The tragic incident of cadmium poisoning in Japan was associated with the fact that high toxic effects of cadmium have been unknown for a long time and consequently, its concentrations in the Zn mine wastes have not been controlled.
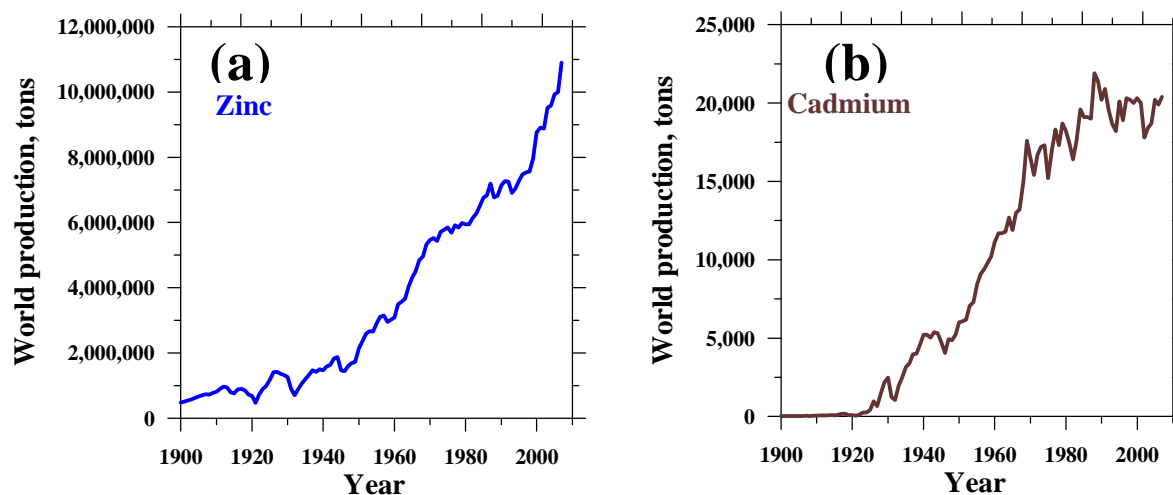
Figure I-2. *World production of zinc (a) and cadmium (b) during 1900-2007 according to U.S. Geological Survey (2008a, b).*

Figure I-3. *Prices for Zn (a) and Cd (b) in US dollars in 2004-2009 according to www.metalprices.com. LB = pounds (1LB = ~ 0.45 kg); LME = London Metal Exchange; FOB Warehouse USA= selling price includes all costs plus transportation to final warehouse in USA.*

In the 20th century significant amount of both Zn and Cd were mined and deposited in the biosphere (Nriagy, 1988, 1990; Callender, 2003). In many instances, the inputs of these metals from anthropogenic sources exceed the contributions from natural sources (weathering, volcanic eruptions, forest fires) by several times (Adriano, 1986). Mining releases metals to the fluvial environment as tailings and to the atmosphere as metal-enriched dust whereas smelting releases metals to the

atmosphere as a result of high-temperature refining processes (Callender, 2003). As it was shown by Callender (2003), both Zn and Cd transport to the lakes via water (fluvial) is many times greater than that by air (atmospheric). In the case of Zn, fluvial inputs to the ocean are also dominant (Callender, 2003). However, natural atmospheric emissions of Cd (volcanoes) are most likely the cause of substantial atmospheric Cd fluxes to the marine environment (Nriagu, 1990; Callender, 2003).

Abundance of zinc and cadmium in Nature

Cadmium is far less abundant in Nature than zinc. Zinc is the 23rd most abundant element in the Earth's crust whereas cadmium is only . As it was mentioned before, most cadmium occurs as an isomorphic substitution for zinc in Zn-bearing minerals. The chemical similarity of Cd and Zn explains correlations between Zn and Cd concentrations occurring in Nature. Thus, different magmatic rocks are characterized by stable Cd/Zn weight ratios $\sim 1 \times 10^{-3}$ very close to average value of Cd/Zn in the Earth's continental crust (Table I-1). It is interesting to note that primitive chondrites are characterized by average Cd/Zn ratio of 2.3×10^{-3} (Table I-1, Wombacher et al., 2008) which is close to the Cd/Zn crustal ratio (Rudnick and Gao, 2003). Variations in Cd/Zn ratio for different types of chondrites are expected to be caused by secondary processes (Wombacher et al., 2008). In the Earth's crust, the elevated Cd/Zn ratios are observed for sedimentary and metamorphic rocks, ocean water, hydrothermal ores and volcanic gases (Table I-1). For example, some sedimentary rocks like shales are characterized by elevated Cd/Zn ratios in comparison with the average continental crust with values up to 14×10^{-3} (Table I-1, Heinrichs et al., 1980). Both cadmium and zinc have nutrient-like profiles in seawater with depleted values in warm surface water and the most enriched concentrations in deep waters (Lynch-Strieglitz, 2003). In the case of zinc, the nutrient-like profile can be easily explained by the fact that it is a necessary nutrient for phytoplankton and diatoms. In the case of cadmium, the factors controlling its concentrations in seawater are still poorly understood (Elderfield and Rickaby, 2000; Lynch-Stieglitz, 2003; Lacan et al., 2006).

The highest Cd/Zn ratios (up to 2000×10^{-3}) are observed for hydrothermal/volcanic settings (Table I-1). In hydrothermal ores and volcanic minerals both Zn and Cd are concentrated mainly in sphalerite (ZnS). The Cd/Zn ratio in sphalerites is controlled by the Cd content. Although the typical Cd contents in hydrothermal ZnS are 0.1-0.5 wt% that corresponds to a Cd/Zn ratio $\sim (2-10) \times 10^{-3}$, up to 13.5 wt % Cd were described in some skarn sphalerites (Cook et al., 2009) that corresponds to a Cd/Zn ratio of $\sim 150 \times 10^{-3}$, which is 2 orders of magnitude higher than average crystal value. CdS-ZnS solid solutions recently described in fumaroles of the Kudryavy volcano (Chaplygin et al., 2007) demonstrate that the Cd/Zn ratio ranges from 17×10^{-3} to $25,000 \times 10^{-3}$. Cd/Zn ratios measured in the volcanic gases are also anomalously high (Table I-1). It should be noted that host rocks of volcanoes usually have compositions close to andesite-basalts. Thus, the volcanic gases are up to ~ 3 orders of magnitude more rich in Cd than the host andesites, andesite-basalts or basalts.

It is interesting to note that the Cd/Zn ratio was proposed for distinguishing between different genetic deposit types (e.g., Qian, 1987; Decrée et al., 2008) or for tracking changes in fluid-rock interactions for some ore deposits (e.g., Gottesmann and Kampe, 2007). For example, in the Zn-Pb Tumurtijn–Ovoo deposit, Mongolia, the Cd/Zn ratio in ores was found to be sensitive to the type of ore , ranging from $(1.7\pm0.3) \times 10^{-3}$ in metamorphic ores to $(3.5\pm0.3) \times 10^{-3}$ in spatially associated hydrothermal-metasomatic ores (Gottesmann and Kampe, 2007). Such variations might reflect, at least partly, the major chemical difference between cadmium and zinc which is the tendency of cadmium to

form more covalent bonding than zinc, and thus more stable complexes in the fluid phase. Knowledge of Zn and Cd speciation in the fluid phase at hydrothermal conditions is thus required may help to use the Cd/Zn ratios as potential indicators of the origin and composition of ore-bearing fluids as well as post-precipitation processes.

Table I-1. Abundance of zinc and cadmium in Nature.

	Cd, ppm	Zn, ppm	Cd/Zn$\times 10^{-3}$	Reference
Upper Continental Crust	0.090	67	1.3	Rudnick and Gao, 2003
Bulk Continental Crust	0.080	72	1.1	Rudnick and Gao, 2003
Primitive chondrites (CI)	0.275	120	2.3	Wombacher et al., 2008
Magmatic rocks				
Granites	0.087	52	1.7	Wedepohl, 1972 ; Heinrichs et al., 1980
Andesites	0.058	74	0.8	Wedepohl, 1972 ; Heinrichs et al., 1980
Basaltes	0.10	114	0.9	Wedepohl, 1972 ; Heinrichs et al., 1980
Sedimentary and metamorphic rocks				
Sandstones	0.071	45	1.6	Heinrichs et al., 1980
Calcareous rocks	0.068	15	4.5	Heinrichs et al., 1980
Deep see clays	0.40	170	2.3	Callender, 2003
Shales	0.30-1.4	95-100	3-14	Heinrichs et al., 1980; Callender, 2003
Ocean (total)	0.00005	0.002	25	Callender, 2003
Ore sphalerites (ZnS)				
Epithermal deposits	2,594-9,582	50,000*	5-20	Cook et al., 2009
Skarn deposits	2,262-73,800	50,000*	5-150	Cook et al., 2009
Strata-bound deposits	1,011-6,938	50,000*	2-14	Cook et al., 2009
Volcanic gases				
Kudryavy volcano, Kuril Islands (T=535-940°C)	0.09-0.88	0.25-13.5	50-880	Taran et al., 1995
Augustine volcano, Alaska (T=390-870°C)	0.004-0.43	0.24-38	4-58	Symonds et al., 1990
Mount St.Helens, Pacific Northwest USA (T=710°C)	0.041	0.019	2092	Symonds and Reed, 1993
Colima volcano, Mexico (T=740-830°C)	0.045-0.740	5.0-8.1	9-91	Taran et al., 2001

* Average Zn concentration in sphalerite (ZnS).

Ore-deposits geology of Zn and Cd

All cadmium in the world is produced from Zn-bearing minerals and consequently mainly from Zn ores, and to a lesser degree from Zn-bearing Pb and Cu ores. Worldwide, 95% of the zinc is mined from sulfidic ore deposits, in which sphalerite (ZnS) is present together with Cu, Pb, Fe sulfides. All these Zn-bearing deposits have been formed from a range of ore-forming processes in a variety of geologic and tectonic environments over at least the last two billion years of the Earth's history. The deposits display a broad range of relationships to host rocks, such as stratiform, strata-bound, and discordant ores. The sulfides may be present as open-space fill and replacement of sediments or sedimentary rocks, filling porosity created by displaced pore fluids in sediments, or precipitated directly on the sea floor. Consequently, there is no united single scheme for Zn deposits providing rigorous classification criteria. Nevertheless, three major types can be distinguished:

- Mississsippi Valley-type (MVT) with such examples as Lead Belt and Viburnum trend in USA (e.g., Sangster, 1990; Leach et al., 1995) and a group of Irish type deposits (e.g., Lisheen deposit, Hitzman et al., 2002);
- Sedimentary exhalative (SEDEX) deposits with such examples as Red Dog in Alaska USA (e.g., Moore et al., 1986), Sullivan deposit in Canada (e.g., Lydon et al., 2000), Gorevsk deposits in Russia (e.g., Smirnov, 1977), and a group of Broken Hill type deposits in Australia (e.g., Parr and Plimer, 1993);
- Volcanogenic massive sulfide (VMS) with typical examples of Bell Allard and Norita in Canada; Scuddles in Australia, Los Frailes in Spain, and deposits in Southerth Urals in Russia (e.g., Galley et al., 2007).

Despite this rough classification, there is a continuum between the characteristics of SEDEX and VMS deposits on the one hand, and SEDEX and MVT deposits on the other hand. It can be demonstrated by the general model of its formation (Fig. I-4). The distinction between the three classes of deposits is based on the typical physical, chemical and geological attributes of member deposits and their respective geological environments. MVT deposits are located in carbonate platform settings, typically in relatively undeformed orogenic foreland rocks, commonly in foreland thrust belts, and rarely in rift zones (Leach and Sangster, 1993; Paradis et al., 2007). The platform carbonate sequences commonly overlie deformed and metamorphosed continental crustal rocks, and have some hydrologic connection to sedimentary basins affected by orogenic events (Paradis et al., 2007). MVT deposits usually occur in platform carbonates at shallow depths on flanks of sedimentary basins. The MVT deposits/districts are localized by geological features that permit upward migration of fluids, such as faults and basement highs. Other structures such as barrier reef complexes, breccias, paleokarsts, depositional margins near carbonate/shale edges, and facies tracts could also be important in trapping mineralized fluids (Paradis et al., 2007). SEDEX deposits occur in intra-cratonic and epicratonic sedimentary basins, the tectonic settings are variable and include intra-cratonic rifts driven by mantle plumes, reactivated rifted margins, and far-field backarc rifting (Nelson et al., 2002; Goodfellow and Lydon, 2007). All SEDEX deposits formed during periods of tectonism, typically manifested by fault reactivation, intrabasin clastic sedimentation, and in many cases magmatism manifested by volcanism and/or sill emplacement. Most deposits occur in reduced marine basins that formed during the sag phase of basin history, adjacent to deeply penetrating, commonly strike-slip

faults. These structures cut the regional carbonate or shale seal and tap metal-bearing fluids from hydrothermal reservoirs in syn-rift highly permeable clastic sedimentary rocks (Nelson et al., 2002; Goodfellow and Lydon, 2007). The most common feature among all types of VMS deposits is that they are formed in extensional settings, including both oceanic seafloor spreading and arc environments. Modern seafloor VMS deposits are recognized in both oceanic spreading ridge and arc environments (Galley et al., 2007), but deposits that are still preserved in the geological record formed mainly in oceanic and continental nascent-arc, rifted arc and back-arc settings (Allen et al., 2002; Galley et al., 2007). This is because during subduction-driven tectonic activity much of the ancient ocean-floor is subducted, leaving only a few ophiolite suites as remnants of obducted ocean-floor (Galley et al., 2007). To summarize, both SEDEX and MVT deposits occur within or in the platforms with a thick sedimentary basin and are thought to result from the migration of basinal saline fluids at T typically between 70 and 200°C (Fig. 1-4b), whereas VMS deposits occur in submarine volcanic-sedimentary belts, and are formed from convective hydrothermal fluids driven by, and/or magmatic fluids from, a sub-volcanic intrusion with $T > 350$°C. Both SEDEX and VMS deposits are formed by hydrothermal systems that vented fluids onto the sea floor, so that the age difference between the ores and the immediate host rocks is always small. In contrast, MVT deposits formed in the subsurface, and so the age difference between ores and host rocks can be much larger than for SEDEX deposits (Leach et al., 2001).

(a)   **(b)**
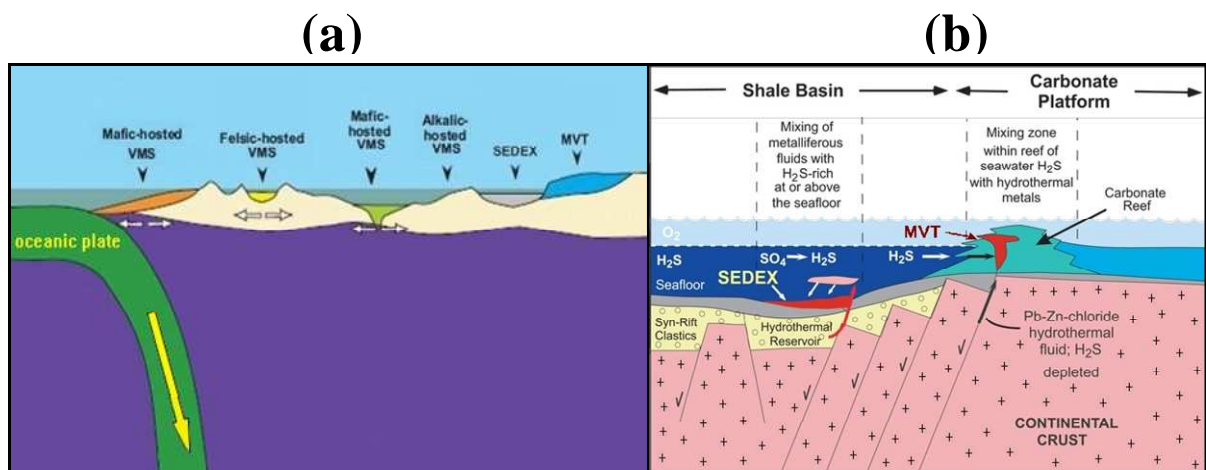
Figure I-4. *(a) General model for the formation of sedimentary exhalative (SEDEX), volcanogenic massive sulfide (VMS) and Mississippi Valley-type (MVT) deposits in the zone of ocean plate subduction and back-arc rifting. Modified from Nelson et al. (2002). (b) Detailed model for the formation of SEDEX and MVT deposits. This model indicates that both SEDEX and MVT deposits formed by the mixing of metalliferous fluids with ambient anoxic waters at the seafloor (i.e. SEDEX deposits) and within permeable carbonate rocks (i.e. MVT deposits). Modified from Goodfellow (2007).*

The composition, temperature and metal concentrations of the hydrothermal fluids that operated in these geological settings can be studied by deep drilling and submersible sampling in the case of modern hydrothermal systems or by analyses of individual inclusions in ore and gangue minerals in the case of ancient hydrothermal systems. A large data set available from both deep drilling/submersible samples and fluid inclusions for hydrothermal fluids responsible for Zn ores

formations was recently summarized by Yardley (2005) and is presented in Fig. I-5. The Zn concentrations vary from 0.05 up to 10^5 ppm as a function of temperature (Fig I-5a) and Cl content (Fig. I-5b). Data for cadmium are very scarce. Metz and Trefry (2000) reported Cd concentrations in the modern hydrothermal fluids from 10 to 100 ppb at T = 200-350°C and Cl contents from 20,000 to 45,000 ppm. To interpret rigorously the cadmium and zinc transport and fractionation by aqueous fluids at high temperatures and pressures, we need to know the identity and properties (structure, thermodynamic stability) of the dominant aqueous species responsible for their transport.

(a)   **(b)**
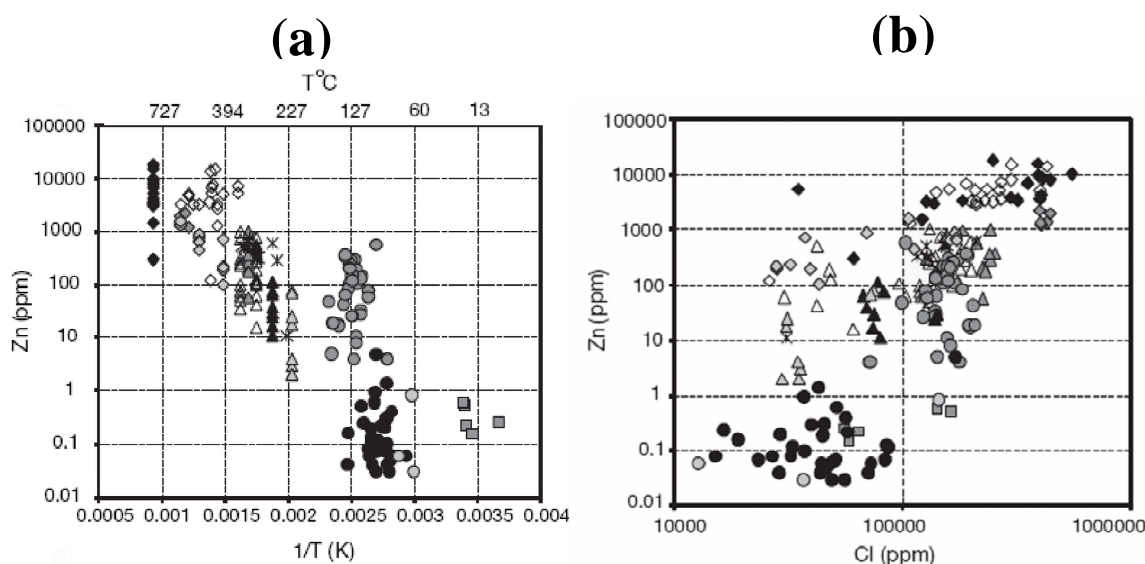
Figure I-5. *Concentrations of Zn in hydrothermal ore-forming fluids as a function of temperature (a) and salinity (b). Summarized data from deep drilling samples and fluid inclusions (Yardley, 2005).*

I-2. Cadmium and zinc aqueous species in hydrothermal fluids

Major ligands for Cd and Zn in hydrothermal fluids

The major natural ligands capable of transporting Cd under hydrothermal conditions are OH^-/H_2O, Cl^-, and HS^-/H_2S. The thermodynamic properties of cations Zn^{2+} and Cd^{2+} are very well known and recommended values of standard thermodynamic functions can be found in CODATA (1989). In aqueous solution the Zn^{2+} and Cd^{2+} cations undergo hydrolysis with formation of $Zn(OH)_n^{2-n}$ and $Cd(OH)_n^{2-n}$ hydroxide complexes, where $1 \leq n \leq 4$. The stability constants of Zn and Cd hydroxide species at ambient T-P are well known from extensive experimental studies, and compilations of the thermodynamic properties of these complexes were reported (Baes and Mesmer, 1976; Wagman et al., 1982; Martell and Smith, 1998; Zhang and Muhammed, 2001). Based on these data and theoretical correlations with other metal hydroxide complexes, Shock et al. (1997) reported HKF parameters of $Zn(OH)_n^{2-n}$ and $Cd(OH)_n^{2-n}$ allowing calculations at elevated T-P (SUPCRT, http://geopig.asu.edu/index.html/). However, for zinc the predicted temperature dependence was shown to be too strong by recent experiments up to 300°C (Bénézeth et al., 2002), which indicate that

these complexes may be much weakern at high *T-P* than predicted by Shock et al. (1997). It is thus expected that the currently available predictions for cadmium hydroxide complexes stabilities given by Shock et al. (1997) might suffer from the same flaw at elevated temperatures. To resolve the discrepancies about the role of hydroxide complexes in Cd and Zn transport by high-temperature fluids, additional experiments are required, particularly at temperatures above 300°C, which will be a part of this work.

A recent review of the available low-temperature experimental studies of Zn and Cd aqueous complexes with sulfide can be found in Rickard and Luther (2006). Despite the generally stronger chemical affinities of both metals for the "softer" sulfide ligand than for "borderline" chloride (e.g., Pearson, 1963), sulfides complexes are unlikely to be important for these metals in acidic high-temperature hydrothermal solutions. The stabilities of Zn-S/HS complexes were shown to exhibit very weak temperature dependence, whereas the domain of predominance of Zn-Cl complexes expands rapidly with increasing temperature (Rickard and Luther, 2006; Tagirov et al., 2007). Despite the higher chemical affinity of Cd to the sulfide ligand compared to Zn, and the lack of experimental data for Cd-S complexes at temperatures above ambient, the Cd-S/HS complexes are also expected to be minor in comparison to CdCl species. This conclusion is dictated by the generally low sulfur concentrations in most natural hydrothermal fluids, typically less than 0.1 wt% (Barnes, 1979), whereas chloride is by far more abundant ligand in hydrothermal fluids, with concentrations attaining 10-30 wt% (Barnes, 1979). Moreover, in acidic and near-neutral solutions typical of Cd/Zn ore deposit formation, the concentration of charged HS^- ligands is low compared to the neutral H_2S^0 which has a much weaker complexing capacity. Analyses of natural hydrothermal fluids (see above, Fig. I-4) indicate positive correlations between Zn and Cl concentrations, thus implying that chloride complexes are likely to be dominant for Zn and other base metals (e.g., Yardley, 2005). Thus, it can be assumed that chloride complexes play a main role in the both cadmium and zinc transport in hydrothermal settings. We discuss the available data on structures and stabilities of Cd-Cl and Zn-Cl complexes below.

Molecular structures of Cd and Zn complexes in aqueous solution

The structures of cadmium and zinc aqueous species in chloride solutions were studied using X-ray diffraction (XRD), Nuclear Magnetic Resonance (NMR), Raman, Infrared, and X-ray absorption spectroscopies (XAS) (e.g., Irish et al., 1963; Waters et al., 1973; Drakenberg et al., 1978; Fontana et al., 1978; Shuvell and Dunham, 1978; Ackerman et al., 1979; Caminiti et al., 1980; Buback, 1983; Paschina et al, 1983; Anderson et al., 1995; Mosselmans et al., 1996; Mayanovic et al., 1999; Bassett et al. 2000; Seward and Driesner, 2004; Liu et al. 2007) and computational theoretical methods (e.g., 1992; Butterworth et al., 1992; Rudolph and Pye, 1998). Most of these studies agree about *a)* octahedral structures of the ions Cd^{2+} and Zn^{2+} which are coordinated by 6 water molecules in the nearest atomic sphere of the metal; *b)* tetrahedral structures of $CdCl_4^{2-}$ and $ZnCl_4^{2-}$; *c)* the presence of water molecules in the first coordination shell of intermediate chloride species $CdCl_nH_2O_m^{2-n}$ and $ZnCl_nH_2O_m^{2-n}$; *d)* the decrease of the average number of water molecules with increasing *T* and Cl concentration in such species; and *e)* the coordination change from octahedral to tetrahedral with increasing Cl concentration in solution for both zinc and cadmium chloride complexes. However, these even rather accurate and detailed spectroscopic measurements at ambient conditions are still difficult to interpret in terms of formation of a mixture of Zn and Cd chloride species in solution, and

to determine the exact 'moment' for the octahedral-to-tetrahedral transition as a function of ligation number. For example for zinc, this transition is likely to occur at the formation of the second chloride complex $ZnCl_2^0$ (Buback, 1983; Mayanovic et al., 1999; Bassett et al., 2000; Liu et al., 2007). For cadmium the coordination change was proposed at the formation of the second $CdCl_2^0(aq)$ or third $CdCl_3^-$ complex, depending on the solvent (Ahrland, 1979). It should be noted, that the formation of low-coordination tetrahedral species with both increasing m_{Cl} and T, demonstrated for other base metals (e.g., Fe, Zn, Co, Ni), is expected to significantly increase ore-metal solubility (e.g., Crerar et al., 1985; Susak and Crerar, 1985).

The structure of cadmium and zinc aqueous species at temperatures above ambient remain very poorly known. Few scarce structural data were reported for Cd-Cl complexes using XAS, but they explored very limited T and m_{Cl} ranges ($m_{Cl} \leq 1m$, $T \leq 250°C$, Mosselmans et al., 1996; Seward and Driesner, 2004). These data do not allow derivation of the identity and stability of the dominant Cd-Cl complexes. For zinc, more spectroscopic studies at elevated T are available. The major Zn-Cl complexes identified by Raman and X-ray absorption spectroscopy at T above 300°C are $ZnCl_2(H_2O)_2^0$ and $ZnCl_4^{2-}$ (Buback, 1983; Mayanovic et al., 1999; Bassett et al., 2000; Liu et al., 2007). However, these data are debatable because they do not cover systematically the sufficient range of m_{Cl} and T to reveal unambiguously structures and stoichiometries of the different possible Zn chloride species. The major limitations of the spectroscopic methods are: *a)* the difficulty to detect the presence of oxygen atoms (i.e., water or hydroxide ligands) in the first coordination shell of the metal in its chloride complexes; *b)* the difficulty to interpret the XAS spectra in case of a mixture of species in solution; and *c)* the lack of confrontation of the structural spectroscopic data with thermodynamic information about the complex stabilities. The latter limitation is probably the most important one and a rigorous confrontation between structural and thermodynamic data has not been done so far for Zn and Cd, to the best of our knowledge. Unfortunately, the existing thermodynamic data for chloride complexes of both elements at elevated T-P appear to be surprisingly contradictory, prohibiting their comparison with the few structural results discussed above. In the two following sections, we will present the state of the art about the stabilities and stoichiometries of the major aqueous Cd and Zn chloride complexes reported in the literature.

Thermodynamic properties of cadmium chloride complexes

Numerous experimental studies were performed **at $T \leq 50$ - $100°C$** to determine the stability constants of stepwise formation for chloride complexes $CdCl_n^{2-n}$, where n ranges between 1 and 4 (because the water activity is close to one in most studies of aqueous solutions, structural H_2O molecules present in these complexes are omitted for clarity). These studies have been conducted using potentiometry (e.g., Vanderzee and Dawson, 1953; Reilly and Stokes, 1970; Gutz and Neves, 1985; Tomaš et al., 2001), calorimetry (e.q., Gerding, 1966; Provost and Wulf, 1970), polarography (e.q., Eriksson, 1953), solubility (e.q., King, 1949), ebulliometry (e.q., Oliveira, 1979), and ultrasonic absorption measurements (Valleau and Turner, 1964). The majority of databases and review compilations show a decent agreement as for the stability constants values for the first three cadmium chloride complexes at 25°C and 1 bar (Table I-2, Latimer, 1952; Glushko, 1972; Wagman et al., 1982; Sverjensky et al., 1997; Archer, 1998; Pivovarov, 2005). The only exceptions are a) the NBS data of Wagman et al. (1982) that are likely to contain errors as it was demonstrated by a more recent review of these data by Archer (1998), and b) an old report of the $CdCl^+$ formation constant recommended by

Latimer (1952). Data on the $CdCl_4^{2-}$ stability constant, however, are scarcer than those for the lower Cl number species. Nevertheless, the two existing reviews of Sverjensky et al. (1997) and Pivovarov (2005) report comparable values (within < 0.3 log unit, Table I-2). The distribution of cadmium species in a H_2O-NaCl-HCl solution at pH ~2 as a function of total m_{Cl} at 25°C and 1 bar calculated according to Sverjensky et al. (1997) is presented in Fig.I-6a.

Table I-2. Stability constants of cadmium chloride complexes at 25°C and 1 bar from the literature.

| Source | $\log_{10} \beta^0_n \quad (Cd^{2+} + nCl^- = CdCl_n^{2-n})$ | | | |
	$CdCl^+$	$CdCl_2^0$	$CdCl_3^-$	$CdCl_4^{2-}$
Latimer, 1952	1.35	2.17	2.00	-
TKV Database (Glushko et al., 1972)	1.96	2.58	1.97	-
SUPCRT (Sverjensky et al., 1997; http://geopig.asu.edu/index.html/)	1.97*	2.59*	2.40*	1.47*
Critical Database (Martell and Smith, 1998)	1.98±0.03	2.60±0.10	2.40±0.10	-
NBS 1982 (Wagman et al., 1982)	2.71	3.35	2.72	-
Critical review of NBS data (Archer, 1998)	1.97	2.63	2.00	-
Pivovarov, 2005**	2.00±0.02	2.70±0.05	2.40±0.10	1.20±0.20

"-" = not available.
*Taken from Turner et al. (1981).
**Calculated from data of Eriksson (1953).

(a) **(b)**
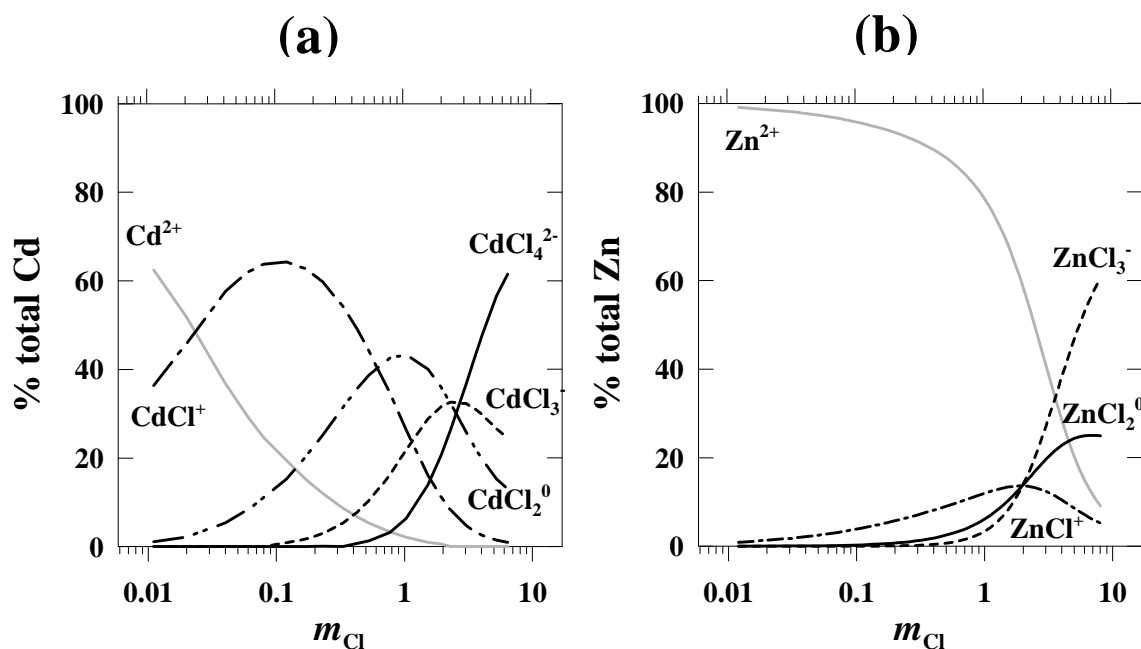
Figure I-6. *Distribution of Cd (a) and Zn (b) species in a NaCl-HCl aqueous solution at 25°C and 1 bar as a function of m_{Cl} calculated using the HKF-model parameters from the SUPCRT database (Sverjensky et al., 1997; http://geopig.asu.edu/index.html/).*

In contrast, the available data from different experimental and theoretical studies **at temperatures above ambient** are surprisingly inconsistent and display large variations in the temperature dependence of the stability constants for all Cd-Cl species. This can be seen in Table I-3, where we compared the reported values of the standard partial entropy $S^0_{298.15}$ for each chloride complex, derived from the log K_i *vs T* dependence between 20 and 100°C in different studies. It can be seen in this Table that differences in the $S^0_{298.15}$ values for a same complex attain almost 40 cal · mol^{-1}·K^{-1} (e.g., for CdCl$_3^-$ between Latimer, 1952 and Sverjensky et al., 1997). Such a difference in $S^0_{298.15}$ corresponds to a difference of more than 2.5 orders of magnitude of the CdCl$_3^-$ stability constant when extrapolating these data to 150°C. The situation is even worse at higher temperatures, typical of Zn and Cd ore formation (~200-400°C). For example, only one experimental work at *T* up to 250°C is available for the first chloride complex CdCl$^+$ (Palmer et al., 2000) , to the best of our knowledge.

Table I-3. Standard molal entropy $S^0_{298.15}$ for cadmium chloride complexes from the literature.

Source	$S^0_{298.15}$, cal · mol^{-1}·K^{-1}			
	CdCl$^+$	CdCl$_2^0$(aq)	CdCl$_3^-$(aq)	CdCl$_4^{2-}$
Latimer, 1952	5.6	17.0	50.7	-
Provost and Wulff, 1970	8.0	23.0	48.0	-
TKV Database (Glushko et al., 1972)	7.4	25.0	39.3	-
SUPCRT (Sverjensky et al., 1997 ; http://geopig.asu.edu/index.html/)	0.8	10.3	10.9	0.2
NBS 1982 (Wagman et al., 1982)	10.4	29.1	48.5	-
Critical review of NBS data (Archer, 1998)	7.1	25.7	45.1	-

"-" = not available.

This brief analysis of the available data shows that although the stability constants of all cadmium chloride complexes at ambient conditions are accurately constrained by numerous experimental measurements, large disagreements exist as to the temperature dependence of the formation constants. The discrepant entropy (and enthalpy) values for most Cd-Cl complexes do not allow reliable extrapolations above 100-150°C. The SUPCRT thermodynamic database (http://geopig.asu.edu/index.html/) widely used by geologists in modeling hydrothermal fluids contains a complete set of the HKF equation-of-state parameters for the four Cd-Cl species derived from the ambient *T-P* data and using empirical correlations amongst thermodynamic values of different metal complexes (Sverjensky et al., 1997). However, as we showed above, these data are in clear disagreement with other sources (Table I-3) and thus cannot be used with confidence at elevated *T-P*. Thus, there is an urgent need for systematic experimental data of the identities and stabilities of Cd-Cl species in high-temperature solutions.

Thermodynamic properties of zinc chloride complexes

Zinc complexing with chloride in aqueous solution in a wide T range has attracted far more considerable attention than that of his "little brother" cadmium. As a result, numerous experimental and modeling studies are available on the stability of zinc chloride complexes $ZnCl_n^{2-n}$, where n ranges from 1 to 4. The available formation constants for these zinc chloride complexes **at 25°C and 1 bar** are given in Table I-4. Despite the large volume of available experimental and theoretical studies listed in this Table, the stabilities of all Zn-Cl complexes exhibit surprisingly larger variations amongst different data sources than their Cd analogues (Table I-2), attaining more than one log unit (in terms of $\log_{10} \beta^0_n$). This is due to the fact that Zn-Cl complex stabilities are 1-2 orders of magnitude lower that their Cd counterparts (e.g., Fig. I-6). This renders it more difficult accurate direct measurement of Zn-Cl interactions at ambient conditions, so that most stability constants reported in Table I-4 are based on extrapolations from high-temperature conditions where the stability of Zn-Cl species is higher. For $ZnCl^+$ and $ZnCl_2^0$(aq) most reported data are in decent agreement, within 0.2-0.4 log units, except the old NBS report (Wagman et al., 1982) and the revision of Pivovarov (2005) who used few selected sources of data. Their values of stability constants derived by the original authors (Ruaya and Seward, 1986; Bourcier and Barnes, 1987; Plyasunov and Ivanov, 1991) from three high-temperature solubility studies are in excellent agreement within 0.1 log unit. The data for Zn-Cl species from the most popular amongst geologists database SUPCRT (http://geopig.asu.edu/index.html/), based on a critical revision by Sverjensky et al. (1997) of selected solubility studies (e.g., Ruaya and Seward, 1986) are slightly different from the original values cited above (by ~ 0.2-0.4 log units) likely because of different extrapolation procedures used. For the higher ligand number complexes, $ZnCl_3^-$ and $ZnCl_4^{2-}$, the agreement is worse, and differences between the SUPCRT database and the solubility studies cited above attain more than one order of magnitude in terms of overall stability constant (β^0_n). Note also that these discrepancies further increase for the 'last' $ZnCl_4^{2-}$ species, for which the limited amount of available data does not allow derivation of the consistent value.

Table I-4. Stability constants of zinc chloride complexes at 25°C and 1 bar from the literature.

Source	$\log_{10} \beta^0_n$ ($Zn^{2+} + nCl^- = ZnCl_n^{2-n}$)			
	$ZnCl^+$	$ZnCl_2^0$(aq)	$ZnCl_3^-$	$ZnCl_4^{2-}$
TKV Database (Glushko et al., 1972)	0.38	0.60	-	-
Turner et al., 1981	0.49	0.62	0.51	0.20
SUPCRT (Sverjensky et al., 1997; http://geopig.asu.edu/index.html/)	0.20	0.25	-0.02	-
Critical Database (Martell and Smith, 1998)	0.40±0.10	0.60	-	-
NBS 1982 (Wagman et al., 1982)	-0.53	-1.04	-0.008	-1.09
Ruaya and Seward, 1986	0.42	0.62	0.34	0.19
Bourcier and Barnes, 1987	0.43	0.61	0.53	0.20
Plyasunov and Ivanov, 1990	0.49	0.62	0.10	-1.00
Pivovarov, 2005*	-0.30±0.10	0.00±0.20	-0.40±0.30	-1.50±0.50

"-" = not available.

*Recalculated from experimental data of Ferri and Salvatore (1988) and Sillén and Liljeqvist (1944).

In contrast with Cd, the stability of Zn-Cl complexes **at hydrothermal temperatures (typically to 350°C)** has been a subject of several solubility studies summarized in Table I-5. The comparison of these data shows that while the data for the uncharged $ZnCl_2^0$(aq) complex are very consistent over a wide T range (with a single exception of Plyasuvov and Ivanov, 1991), the situation for the other complexes is less good, with differences attaining 4 orders of magnitude **(!)** at $T > 300°C$ for $ZnCl^+$ and $ZnCl_4^{2-}$. The distribution of Zn-Cl complexes in a 0.1m and 2m NaCl solutions at 350°C/P_{sat} according to different original solubility studies are illustrated in Fig. I-7. The values suggested by Ruaya and Seward (1986), Bourcier and Barnes (1987) and Wesolowski et al. (1998) imply that $ZnCl^+$ and $ZnCl_2^0$(aq) are the dominant species at chloride concentrations typical of most Zn-bearing ore-forming fluids (0.1-2.0m NaCl). This conclusion is also supported by the solubility data of Cygan et al. (1994) at supercritical temperatures (300-600°C). In contrast, the stability constant values of Plyasunov and Ivanov (1991) suggest that $ZnCl_4^{2-}$ is by far the major species at $m_{Cl} > 1m$. It should be emphasized that the identity (~ number of Cl ligands) of the dominant Zn species exerts a major control of Zn-bearing mineral solubilities as a function of pH and chloride concentration. The discrepancies apparent in Fig. I-7 imply that in most saline hydrothermal fluids, the solubility dependence of Zn sulfides and silicates as a function of acidity and chlorinity will be different if modeled using different data sources (e.g., Ruaya and Seward, 1986 versus Plyasunov and Ivanov, 1991).

Table I-5. Stability constants of zinc chloride complexes at elevated temperatures from available solubility studies and the SUPCRT database.

	$\log_{10} \beta^0_n$ ($Zn^{2+} + nCl^- = ZnCl_n^{2-n}$)			
	$\log_{10} \beta^0_1$	$\log_{10} \beta^0_2$	$\log_{10} \beta^0_3$	$\log_{10} \beta^0_4$
$T = 200°C$, $P = 15.5$ bar (P_{sat})				
SUPCRT (Sverjensky et al., 1997; http://geopig.asu.edu/index.html/)	4.0	4.1	3.2	-
Ruaya and Seward, 1986	4.01±0.02	3.98±0.04	3.0±0.1	4.2±0.1
Bourcier and Barnes, 1987	3.1±0.3	4.3±0.2	5.2±0.2	4.4±0.1
Plyasunov and Ivanov, 1991	2.2	4.9	3.0	4.3
Wesolowski et al., 1998	2.5±0.1	4.2±0.1	-	-
$T = 350°C$, $P = 165.2$ bar (P_{sat})				
SUPCRT (Sverjensky et al., 1997; http://geopig.asu.edu/index.html/)	7.7	9.4	8.8	-
Ruaya and Seward, 1986	8.0±0.1	9.5±0.1	-	-
Bourcier and Barnes, 1987	7.0	9.3	9.3	7.7
Plyasunov and Ivanov, 1991	5.3	11.2	9.7	11.4

"-" = not available.

350°C, P_{sat}

(a)

0.1 mCl

ZnCl$_2^0$

ZnCl$^+$

Ruaya and Seward, 1986

(b)

2 mCl

ZnCl$_2^0$

ZnCl$_3^-$

ZnCl$^+$

Ruaya and Seward, 1986

(c)

0.1 mCl

ZnCl$_4^{2-}$

ZnCl$_3^-$

ZnCl$_2^0$

Plyasunov and Ivanov, 1991

(d)

2 mCl

ZnCl$_4^{2-}$

ZnCl$_2^0$

Plyasunov and Ivanov, 1991
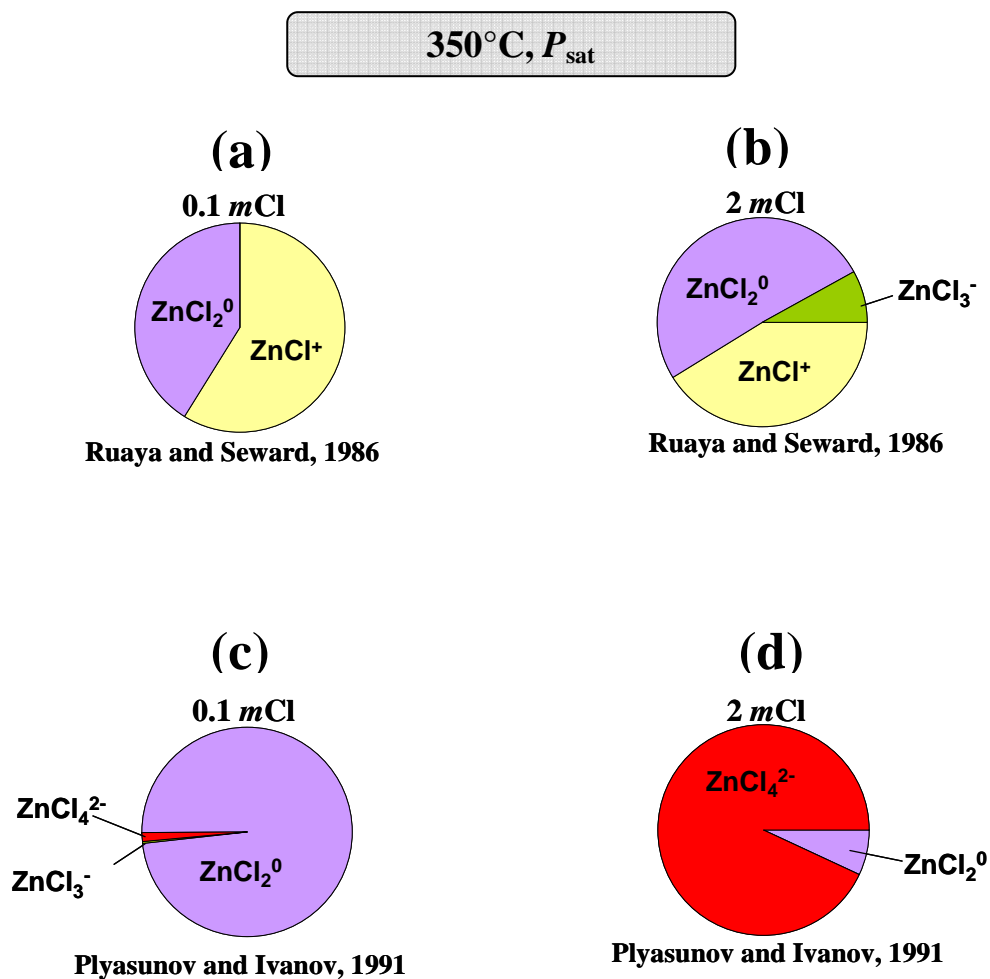
Figure I-7. *Distribution of Zn chloride complexes in 0.1m Cl (a, c) and 2m Cl (b, d) aqueous solutions at 350°C and P_{sat}, calculated from data of Ruaya and Seward, 1986 (a, b) and Plyasunov and Ivanov, 1991 (c, d), using the stability constants reported in Table I-5.*

This short critical revision demonstrates that it would be difficult to resolve the existing discrepancies of the sole basis of the existing solubility studies. It is clear that more experimental data, particularly combining complementary approaches (e.g., solubility, in situ spectroscopy, potentiometry) are required to enable a self consistent set of stability constants for this important base metal. The present study is a modest attempt to acquire such new necessary data for both Zn and Cd using different experimental methods and to better understand their transport and precipitation by high-temperature geological fluids responsible for the formation of the majority of these metals resources on our planet.

I-3. Aims of the present study

The growing need for Zn and Cd mineral resources, better understanding of ore formation processes, and improving ore treatment and extraction technologies in environmentally responsible manner require knowledge of cadmium and zinc behavior in geological fluids in a wide range of physical-chemical conditions (e.g., temperature, pressure, density, fluid composition) and scales (from atomic to geological). This study is aimed at quantifying the identity, stability and structure of cadmium and zinc aqueous complexes responsible for the transport and precipitation of these metals in hydrothermal fluids and vapors, and applying these data to model Cd and Zn transport and Cd/Zn ratios in hydrothermal/volcanic environments.

The main objectives of the present study are thus the following:

- To determine the identity, stability and structure of aqueous cadmium chloride complexes in the wide temperature and pressure range of hydrothermal fluids;
- To investigate the behavior of cadmium and zinc in hydrothermal brine and vapor phases formed during boiling and immiscibility phenomena of ore-bearing fluids;
- To quantify physical-chemical factors controlling the Cd/Zn ratios in hydrothermal and volcanic fluids and minerals;
- To confront the obtained new experimental and thermodynamic data with geological information on Cd and Zn distribution and contents in natural hydrothermal-volcanic environments.

I-4. Manuscript organization

The present manuscript is composed of an Introduction (the present Chapter I) and the following five chapters describing the methodology, different experimental, analytical or modeling parts of this study, together with a brief discussion of the perspectives of this work. The content of each of the five following chapters is resumed below:

- **Chapter II: METHODS.** This part of manuscript presents the experimental, analytical, and thermodynamic approaches employed or developed in this work. The advantages and complementarities of each method are discussed.

- **Chapter III: POTENTIOMETRIC STUDY OF CADMIUM CHLORIDE COMLEXES FROM 1 TO 1000 BAR AT 25°C.** This chapter presents an article submitted to Russian journal *Geology of Ore Deposits* in August 2009 (Bazarkina et al., 2009a) and will be published in both Russian and English. In this paper, the effect of pressure on the stability of cadmium chloride complexes at ambient temperature was measured, for the first time, using in situ potentiometric methods. The partial molal volumes for the four cadmium chloride complexes derived from these data were used in the framework of the revised HKF equation

of state to provide improved pressure-dependent HKF parameters for each Cd-Cl species, thus allowing calculations of their thermodynamic properties at pressures up to 5000 bar.

- **Chapter IV: STRUCTURE AND STABILITY OF CADMIUM CHLORIDE COMPLEXES IN HYDROTHERMAL FLUIDS.** This chapter presents an article submitted to *Chemical Geology* in October 2009 (Bazarkina et al., 2009b). In this work, in situ X-ray absorption spectroscopy was combined with solubility measurements to investigate systematically the stoichiometry, structure and stability of cadmium chloride aqueous complexes in high *T-P* saline hydrothermal fluids to 450°C and 600 bar. These new data were compared with the available structural and thermodynamic information on major Zn-Cl complexes, and a new potential geochemical tracer of the fluid composition using the Zn/Cd ratio has been proposed.

- **CHAPTER V: Cd/Zn RATIO IN LOW-DENSITY HYDROTHERMAL VAPORS, BOILING WATER-SALT HYDROTHERMAL SYSTEMS AND VOLCANIC GASES: COMPARISON OF EXPERIMENTS IN MODEL SYSTEMS WITH GEOLOGICAL OBSERVATIONS.** This part of the manuscript describes the results of measurements of Cd and Zn solubility in low-density fluids and vapor-liquid partitioning coefficients in the system $H_2O+NaCl\pm HCl$ pertinent to natural boiling hydrothermal fluids. These data, combined with thermodynamic calculations of CdS and ZnS solubilities, where compared with natural analyses of Zn, Cd, associated metals and main volatile ligands S and Cl in high *T-P* fumaroles of the Kudryavy volcano, sampled and analyzed during this study. The potential use of the Cd/Zn ratio in the fluid and mineral phases for tracing the fluid evolution and composition is discussed.

- **Chapter VI: CONCLUTIONS AND PERSPECTIVES.** This last chapter gives a summary of the results obtained above and discusses near-future research perspectives opened up by the present PhD work.

- **ANNEX.** This annex presents a published article not directly related to the thesis results. "An in situ X-ray absorption spectroscopy study of gold-chloride complexing in hydrothermal fluids" published in 2009 in *Chemical Geology* 259, pp. 17-29, by Pokrovski G.S., Tagirov B.R., Schott J., Bazarkina E.F., Hazemann J.L., Proux O.

Chapter II. METHODS

Studies of the chemical speciation of metals in geological fluids require a range of complementary experimental, analytical and theoretical approaches applicable to the extremely wide temperature, pressure and concentration range of crustal fluids. In this work, we combined laboratory experiments (potentiometry, solubility, partitioning coefficients measurements, and in situ X-ray absorption spectroscopy XAS), modern analytical methods of analyses of natural and synthetic aqueous solutions, field sampling of high-temperature natural fluids, and thermodynamic modeling to assess the identity, structure and stoichiometries of Cd- and Zn-bearing complexes responsible for Cd and Zn transport in natural settings. The present chapter briefly describes the methods employed in this work.

II-1. Potentiometry

Potentiometry is a selective electrochemical method for studies of element speciation in aqueous solutions. This method is based on the determination of the difference in electric potentials between an indicator and a reference electrodes. This difference is a function of the thermodynamic activity of components in the chemical reaction involving production or consummation of electrons which is described by the Nernst equation:

$$\Delta E = E_{ind} - E_{ref} = E^0 + \frac{R \cdot T}{n \cdot F} \cdot \ln(a_i) + E_j = E^0 + 2.3026 \cdot \frac{R \cdot T}{n \cdot F} \cdot \log(a_i) + E_j \qquad \text{(II-1)}$$

where ΔE = measured difference in potentials between the indicator electrode (E_{ind}) and reference electrode (E_{ref}); E^0 = standard potential of used indicator electrode relative to reference electrode; R = universal gas constant (8.31439 J·mol^{-1}·K^{-1}); T = temperature in Kelvin; n = number of electrons participating in chemical reaction; F = Faraday constant (96,493.1 C·mol^{-1}); a_i = activity of the measured component; E_j = liquid-junction potential.

In this study, the potentiometric method was used to investigate Cd-Cl complexes stability by measuring the Cd^{2+} activity in aqueous solution at 25°C as a function of total chloride concentration and pressure. Two types of potentiometric measurements at 25°C were performed: *1)* as a function of KCl concentration at 1 bar in aqueous solutions with constant Cd(NO$_3$)$_2$ concentration; and *2)* as a function of pressure (1-1000 bar) in Cd(NO$_3$)$_2$ - KCl solutions. Measurements at 1 bar were performed to *i)* verify the efficiency and performance of the Cd-selective electrode, and *ii)* refine the CdCl$_4^{2-}$ stability constant that was reported with a large discrepancy in previous studies (see chapter I-2 above). Measurements at elevated pressures were performed to obtain the individual volumetric properties of CdCl$^+$, CdCl$_2^0$(aq), CdCl$_3^-$, and CdCl$_4^{2-}$ aqueous species, for which only theoretical predictions are currently available (Sverjensky et al., 1997; http://geopig.asu.edu/index.html/).

A Cd-selective electrode with a solid CdS-Ag$_2$S membrane (®"Niko-analit", Russia) was modified for measurements at elevated pressures (1-1000 bar) by adapting a rubber tube filled with oil

for pressure compensation (Fig. II-1). The membrane of this electrode is selective to Cd^{2+} free ions due to the electrochemical reaction of solid CdS in the membrane with the free Cd^{2+} ion in solution:

$$Cd^{2+} + Ag_2S(s) + 2\bar{e} = CdS(s) + 2Ag(s) \qquad (II-2)$$
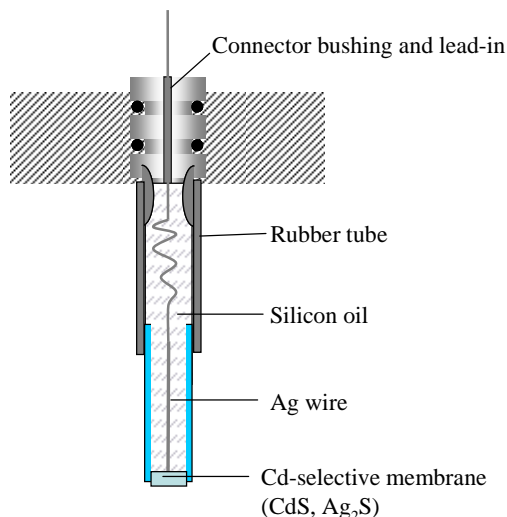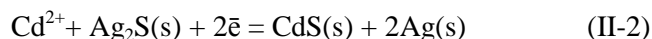
Figure II-1. *Scheme of the Cd-selective solid-contact electrode used for experiments at 1-1000 bar and 25°C.*

At ambient pressure, a classical Ag/AgCl reference electrode with liquid junction (3m KCl) was used. At elevated pressures, a specially designed reference electrode described elsewhere (Fig II-2a, Zotov et al., 2006) was employed. The special construction of this electrode enables pressure compensation and allows stable flow of the reference solution into the experimental solution even at elevated pressures, so that the value of E_j is constant. The liquid junction is thus may be considered to be constant over the estimated concentration and pressure range and thus appears as a single adjustable parameter of the calibration curve ($E^0 + E_j$; eq. II-1). The potentiometric cell used for measurements at ambient and elevated pressures is thus the following:

Cu, Ag, Ag_2S-CdS | $Cd(NO_3)_2 \pm$ KCl solution || KCl (3m) | AgCl, Ag,Cu

The electrodes were fixed in the cover of a Ti-alloy autoclave (internal volume ~500 cm^3) presented in Fig. II-2b. The temperature was controlled with a K-type thermocouple. The pressure was maintained with a hydraulic hand-driven pump and measured using a sapphire tenso-resistive pressure transducer (to 1500 bar) and a standard pressure gauge (to 1600 bar), both externally calibrated using a precision piston pressure gauge. The uncertainties of pressure measurements and fluctuations during the experiment do not exceed ±10 bar. Calibration was performed at 25°C with $Cd(NO_3)_2$ solutions. The calibration curves at 1 and 1000 bar are presented in Figure II-3. For two-valent ions the theoretical Nernst slope at 25°C is -29.58 mV/pCd. The used in this study Cd-selective electrode demonstrates slopes very close to this theoretical value in the concentration range 10^{-1}-$10^{-5}m$ $Cd(NO_3)_2$. However, as

it was shown by Baumann (1971) and Rozhkova et al. (2009) ion-selective electrodes of this type can be used down to 10^{-8}-$10^{-9}m$ of the ion concentration in solution where complexes of the measured element dominate over its ions and if the total concentration of the measured element $\geq 10^{-3}$-$10^{-4}m$.
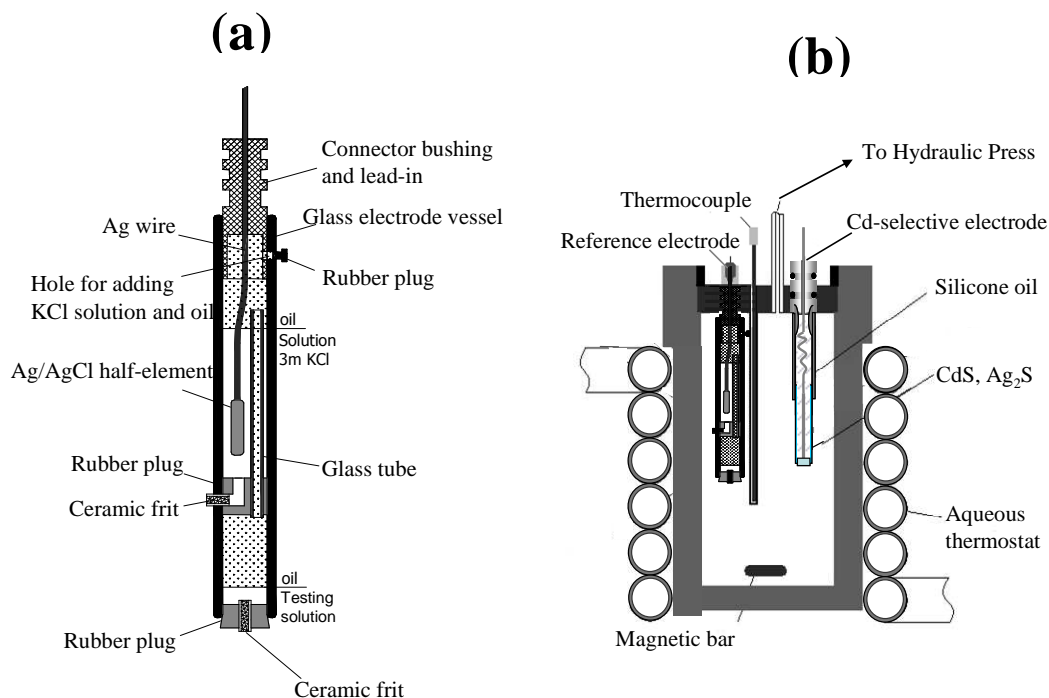
Figure II-2. *(a) Scheme of the reference electrode used for experiments at high pressure (Zotov et al., 2006); (b) Scheme of the experimental setup used for high-pressure measurements.*
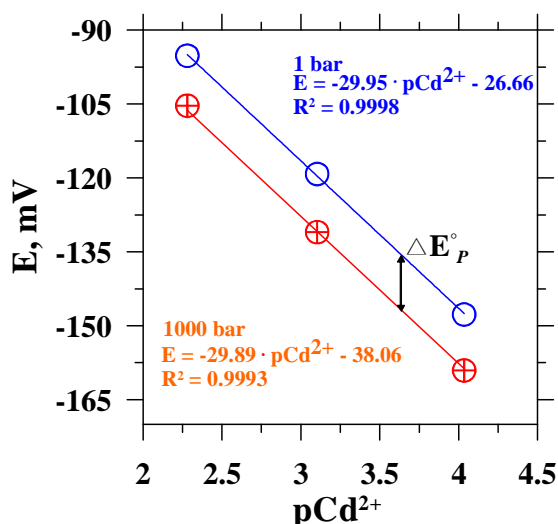
Figure II-3. *Calibration curves of the Cd-selective electrode at 25°C and pressures 1 and 1000 bar. $\Delta E°_P$ denotes the pressure-dependent change in the standard potential (see equation II-I). R^2 represents the squared correlation coefficient.*

II-2. Solubility

Solubility is the most common method used to determine the metal speciation in aqueous solutions at high T-P. This method is based on measurement of the total dissolved concentration of the given chemical element in a solution equilibrated with a stable element-bearing solid phase (commonly oxide, sulfide, or poorly soluble salt). The dissolved concentration depends on both the solution composition (e.g., ligand concentration, pH, redox potential) at given temperature and pressure (T-P) and the identity and stability of the element aqueous species. The solubility approach is particularly efficient to study the metal speciation at elevated T-P because of the following reasons: *i)* true thermodynamic equilibrium between the solution and the solid phase (the primary requisite for the interpretation) is more easily attained at elevated T-P than at ambient conditions, so that a number of artifacts common to low-T measurements such as slow kinetics, metastable equilibria, bad solid crystallinity, are eliminated at elevated T-P; *ii)* potentiometric and spectroscopic measurements are usually more delicate to apply at hydrothermal conditions, particularly at supercritical T-P; *iii)* because of the availability of many efficient analytical techniques for measurements of total dissolved concentrations (see section II-6 below), multi-element experiments in systems closely matching natural hydrothermal fluids may be performed.

Different complementary techniques were used in this work for solubility measurements of zincite (ZnO, cubic), monteponite (CdO, cubic) and greenockite (CdS, hexagonal) at 350-400°C, 165-600 bar and 0-5m of total Cl concentration. The chemical reactions controlling ZnO, CdO and CdS solubility in Cl-bearing fluids are the following:

$$ZnO(s) + nCl^- + 2H^+ = ZnCl_n^{2-n} + H_2O \qquad \text{(II-3)}$$
$$CdO(s) + nCl^- + 2H^+ = CdCl_n^{2-n} + H_2O \qquad \text{(II-4)}$$
$$CdS(s) + nCl^- + 2H^+ = CdCl_n^{2-n} + H_2S^0 \qquad \text{(II-5)}$$
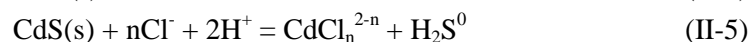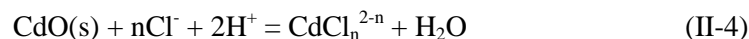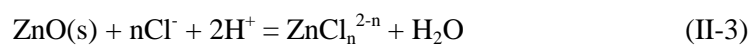
where n = 1, 2, 3, 4. Varying total chloride concentration (NaCl) and fluid acidity (HCl) in equilibrium with these solids, together with measuring total Zn and Cd concentrations and taking into account independent structural information, we have derived for Cd the identities and stabilities of the dominant chloride complexes at elevated T-P. Although data for Zn we obtained were not sufficient to estimate the stabilities of Zn chloride complexes in the same T-P range, they allowed useful qualitative estimations of Zn-Cl species structures and stoichiometries in comparison with literature data.

II-2-1. Hydrothermal pretreatment of CdO and ZnO solids

The important condition of a reliable solubility measurement is the stability and good crystallinity of the solid phase used. The majority of commercial metal oxide and sulfide compounds are known to contain amorphous impurities, fine particles and surface defects that may lead to 'artificial' increase in dissolved metal concentrations in comparison to the well-crystalline material. The presence of such particles and defects may also result in irreproducible 'solubility' values and/or irregular kinetic patterns precluding unambiguous determination of the steady-state concentrations. Consequently, the commercial powders of zincite (ZnO, cubic) and monteponite (CdO, cubic) were treated before experiments. First, the initial powders were washed several times with deionized water

to remove ultrafine particles. After that, the washed slurry was treated in water at 350°C and saturated vapor pressure (P_{sat}) for a month in a titanium autoclave quenched at the end of the run; the solid was then recovered and dried at 100°C for 24h. Scanning electron microscopy (SEM) performed on the initial (Fig. II-4 a,b) and final (Fig. II-4 c,d) products showed that such treatment was extremely beneficial, resulting in significant crystallinity improvement and elimination of surface defects and ultrafine particles for both CdO and ZnO. During the reactor quench, the formation of $Cd(OH)_2$ solid could not be avoided completely, however, and the resulting solid contained about 10% of hydroxide phase as detected by X-ray diffraction. These hydrothermally treated solids were used for solubility measurements in pure water and Cl-bearing solutions using Coretest and batch reactor techniques described below.
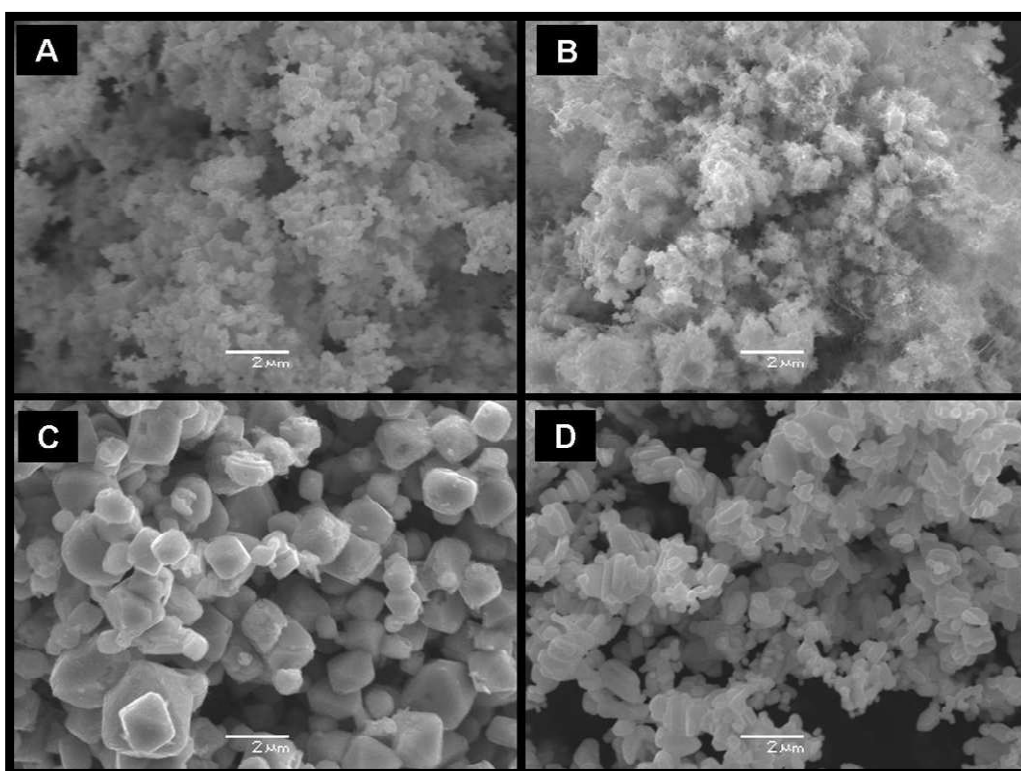
Figure II-4. *SEM images of solids before the hydrothermal treatment: CdO (A) and ZnO (B); and after the hydrothermal treatment: CdO (C) and ZnO (D).*

II-2-2. CdO and ZnO solubility in pure water and low-saline solutions at 350-400°C and 220-400 bar

For measurements of hydrothermally treated zincite (ZnO, cubic) and monteponite (CdO, cubic) solubility in pure H_2O and low-saline and low-dense NaCl-HCl aqueous solutions containing up to 0.02m NaCl and up to 0.03m HCl at 350-400°C and 400-220 bar we used a flexible-cell reactor (Coretest®) allowing multiple samples of the fluid phase at given *T-P* conditions (Fig. II-5). The experimental setup was similar to that described elsewhere (Pokrovski et al., 2008). Briefly, the reactor consists of a titanium flexible reaction cell (150 cm^3) inside a large-volume (800 cm^3) stainless-steel pressure autoclave with water as a pressure medium. This construction is placed into a rocking furnace, which is temperature controlled within ±1°C. A gas-driven high-pressure pump allows delivery of water into the vessel to maintain *P* during sampling, and a back-pressure regulator served to release water from the vessel during heating or addition of solution into the reaction cell.

During the experiment, small amounts of fluid phase (~2 g) were periodically extracted from the flexible cell via titanium tubing and two high *T–P* valves and trapped into a titanium ampoule. The rapid fluid transfer into the ampoule (< 1 s) under experimental *T-P* allows avoiding solute losses induced by metal precipitation and volatile degassing during sampling at elevated *T* (Pokrovski et al., 2008). During the run, the fluid composition in the cell (*m*NaCl and *m*HCl) can be modified by injecting a given quantity of a new solution using a calibrated manual pump.
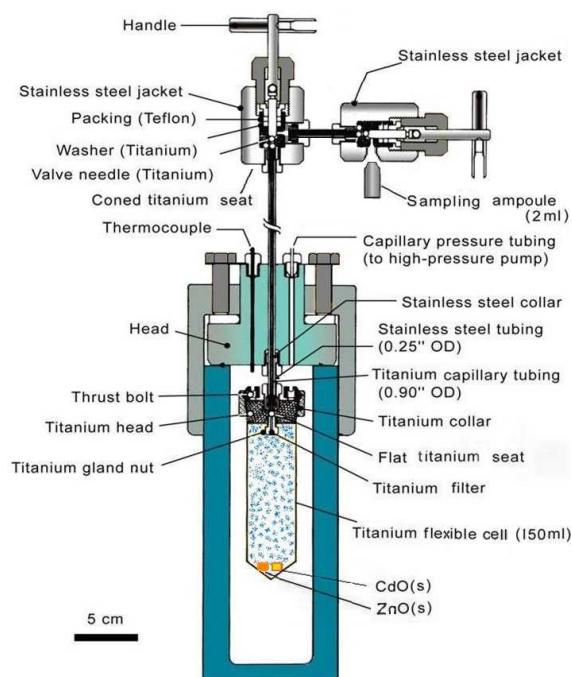
Figure II-5. *Scheme of the flexible-cell reactor Coretest with high T-P sampling used in solubility experiments at 350-400°C and 200-600bar in pure water and low-saline solutions.*

The major advantage of this flexible cell is the possibility of accurate and reversible pressure changes during experiment. The other important advantage is low detection limits for the measured dissolved concentrations. The smaller reaction volume in comparison to a constant-volume titanium reactor (e.q., Fig II-8 below) limits, however, the amount of sampled fluid. The other disadvantage is that this technique cannot be applied for measurements on highly soluble solids at elevated T or concentrated salt solutions because sampling with capillary may fail owing to solute precipitation upon the fluid extraction at high T-P to ambient conditions.

Our measurements on Zn in low-density chloride-bearing vapors complement those performed by many authors in high-dense saline liquids (Ruaya and Seward, 1986; Burcier and Barnes, 1987; Plyasunov and Ivanov, 1991; Cygan at al., 1994; Wesolowski et al., 1998). For Cd, however, the solubility data at elevated T are very limited (see chapter I-2) in both low- and high-density chloride solutions. Therefore, in addition to the data in low-density fluids, we performed solubility measurements of CdO and CdS at 400°C and 600 bar in concentrated H_2O-NaCl-HCl solutions using batch-reactor quenching technique, which is described below.

II-2-3. CdO and CdS solubility in saline solutions at 400°C and 600 bar

Batch autoclaves (Fig. II-6) made of Ti-alloy were used for monteponite (CdO) and greenockite (CdS) solubility measurements in NaCl-HCl-H_2O solutions containing 0-5.23m NaCl and 0-0.13m HCl at 400°C and 600 bar. Details about this technique may be found elsewhere (Pokrovski et al., 2006). Briefly, the solid phase is put in a titanium holder, which is fixed in the upper part of the autoclave so that it does not contact the solution at ambient T-P. The reactors are placed vertically in a temperature-controlled (±1°C) furnace. Experimental P in our runs was calculated from the degree of filling of the autoclave using the PVTX properties of the H_2O-NaCl system at 400°C and 600 bar (Anderko and Pitzer, 1993; Bakker, 2003) and assuming that low concentrations of HCl ($m_{HCl} \leq$ 0.13m) and dissolved Cd ($m_{Cd} \leq 0.15m$) do not significantly modify these properties. The maximum error of P estimations does not exceed ±50 bar. At the end of the run, the reactor was quenched in cold water to rapidly separate the solid from the solution.

The dissolved Cd contents were determined by AAS in quenched solutions and by weight loss of the solid phase. These two independent approaches for solubility determination allow accurate assessment the possible errors of solubility measurements. However, the eventual solid re-crystallization and metal adsorption on the reactor walls result in elevated detection limits in comparison to high-T sapling technique (see section II-2-2 above). These limits were estimated to be ~0.002m Cd from experiments in pure water and deluted NaCl solutions. Consequently, the batch-reactor method was found to be successful only for concentrated NaCl solutions (> 0.8m NaCl), in which CdO and CdS solubilities are above 0.004m Cd. Our measurements of CdO and CdS solubility provide new data about Cd speciation at such high-T-P conditions. These solubility measurements were combined with XAS spectroscopy data for Cd (see below). For better understanding both Cd and Zn behavior during the evolution of hydrothermal fluids, solubility data were complemented by measurements of Cd and Zn distribution coefficients between the coexisting liquid and vapor phases in the H_2O-NaCl-HCl system.

Obturator

Basket for solid
phase (CdO or CdS)

Fluid phase

~ *4 cm*
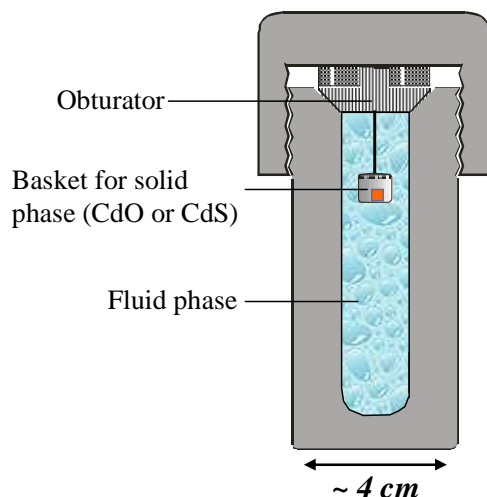
Figure II-6. *Scheme of the batch quench-based autoclave used in solubility experiments at 400°C and 600 bar.*

II-3. Vapor-liquid partitioning

Vapor-liquid partitioning experiments provide the unique information on the individual behavior of metals in the co-existing liquid and vapor phases, which cannot be derived from solubility measurements in a single vapor or liquid phase. In this study, we investigated vapor-liquid partitioning of cadmium and zinc in the H_2O-NaCl-HCl system at 400°C and 450°C. We assumed that small amounts of HCl ($< 0.1m$) do not change the vapor-liquid equilibrium curve of H_2O-NaCl system which is well known and was described in details elsewhere (Fig. II-7, Bischoff, 1991). The critical points are 2.2 wt% NaCl and 281 bar at $T = 400$°C and in 8.8 wt% NaCl and 423 bar at $T = 450$°C. Our experiments on Cd and Zn distribution between the co-existing vapor and liquid phases were performed using titanium-alloy rocking autoclave externally heated at controlled temperature (±2°C) and pressure (±2 bar). A NaCl-HCl aqueous solution with small amounts of $CdCl_2$ and $ZnCl_2$ chlorides was introduced under an argon flux into the autoclave. Samples of the vapor and liquid phases were periodically taken through titanium capillary tubes fixed at both ends of the reactor and analyzed for Cd, Zn, Na and Cl. The large autoclave volume (~500 cm^3) allows multiple separated sampling of the coexisting liquid and vapor phases (Fig. II-8).
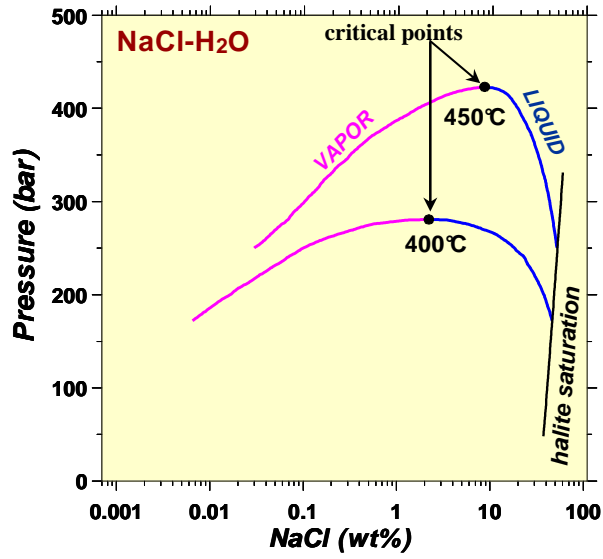
Figure II-7. *Vapor-liquid equilibrium curves at 400°C and 450°C in the H$_2$O-NaCl system according to Bischoff (1991).*
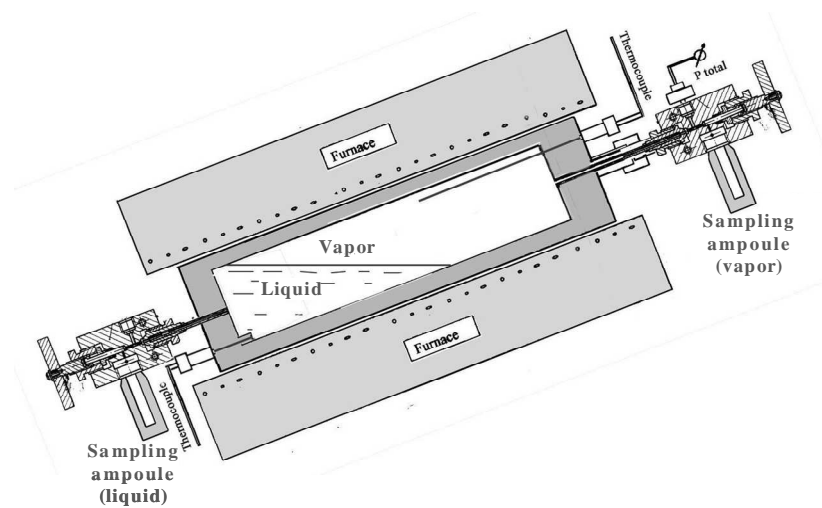
Figure II-8. *Scheme of the rocking Ti autoclave used in vapor-liquid partitioning experiments at 400°C and 450°C.*

Two types of sampling were applied: slow sampling by drops of condensate with a sampling rate of 0.03-0.1 cm^3/s and rapid sampling into titanium ampoule (1 cm^3) with a sampling rate $\geq$ 1 cm^3/s. The agreement between both methods is good for all liquid samples, but is worse for vapor samples. The majority of rapid vapor samples to the ampoule have shown the presence of Cd-bearing solid phases and, consequently, too high Cd concentrations (10-100 times higher in comparison with slow sampling by drops). The temperature and pressure decrease during the rapid sampling is likely to contaminate the low-concentrate and low-density vapor by precipitating some Cd oxides/hydroxides in the sampling capillary and ampoule. It should be noted that the vapor sampling in this autoclave is different from that in the Coretest reactor. In the latter, the total volume of autoclave is ~2 times bigger attenuates the pressure drop during the sample transfer to the ampoule. Moreover, the system of double valves (Fig. II-5) and back-pressure regulator further minimizes the pressure change during sampling which is less than 1% in contrast to the present autoclave where pressure drops may attain 10% of the total P value. Thus, in the partitioning autoclave, the slow sampling drop by drop of the vapor condensate, was considered to be more correct. Only few rapid samples at the highest pressure near the critical point have shown an agreement with the corresponding slow samples, and thus were included in the data analysis (vapor density near critical point is high and pressure decrease during sampling is thus weaker in comparison with samplings at low pressures far from critical point).

Solubility and partitioning methods described above are very efficient for characterizing the bulk Cd and Zn transport by the fluid/vapor phase. However, the interpretation of such solubility and partitioning data in terms of individual stoichiometry and thermodynamic properties of aqueous species is often ambiguous. To assess these properties, we combined these methods with in situ spectroscopy described below.

II-4. X-ray absorption spectroscopy

The X-ray absorption spectroscopy (XAS) is a powerful element-specific technique which provides in-situ information on the identity, stoichiometry, and geometric and electronic structure of molecular species. The other name of this technique widely used in literature is X-ray fine structure (XAFS) spectroscopy. The acronym XAS (or XAFS) covers both X-ray absorption near edge structure (XANES) and extended X-ray absorption fine structure (EXAFS) spectroscopies. Though the two have the same physical origin, this distinction is convenient for the interpretation. XANES is strongly sensitive to formal oxidation state and coordination chemistry (e.g., octahedral vs tetrahedral coordination) of the absorbing atom, while the EXAFS is used to determine the distances, coordination numbers, and species of the neighbors around the absorbing atom. In this study XAS was combined with solubility measurements to derive the identity, the stability and the structure of aqueous chloride complexes of cadmium in a wide T-P and Cl concentration range. All XAS measurements were performed on BM-30B beamline at the European Synchrotron Radiation Facility (ESRF, Grenoble, France).

The principles and terminology used in XAS are based on the interactions of X-rays with matter. X-ray absorption spectra are obtained by tuning the photon energy in a range where bound electrons can be excited (0.1-100 keV photon energy, Fig. II-9). The energy is proportional to frequency and inversely proportional to wavelength:

$$E = \frac{\hbar \cdot c}{l} = \hbar \cdot f \qquad\qquad \text{(II-6)}$$

where $\hbar$ = Planck's constant ($\sim 4.14 \times 10^{-18}$ keV/Hz); c = speed of light ($\sim 3 \times 10^8$ m/s); l = wavelength; f = the frequency.
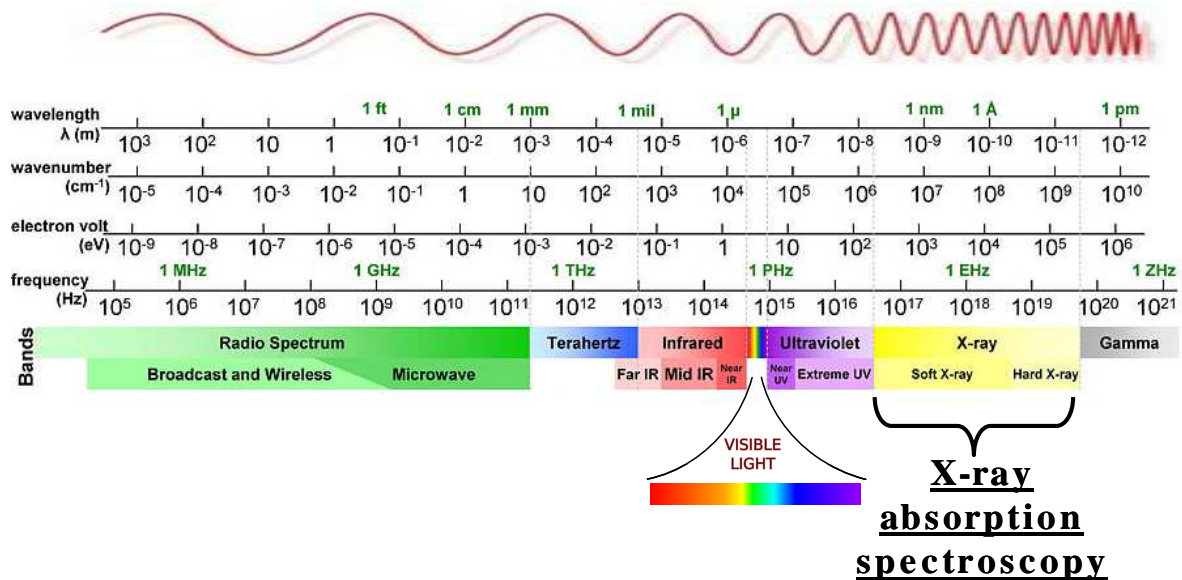
Figure II-9. *Spectrum of photon energy in wavelength, frequency and energy with common names.*

The schematic illustration of X-ray interactions with an atom is presented in Fig. II-10. X-ray absorption occurs when an atom acquires all the energy of an X-ray, which is used to excite electrons into higher energy electron orbitals that are unoccupied or into the continuum where the electron is no longer associated with the atom (Fig. II-10). The empty electron orbital is called a hole and the excitation of core electrons creates core holes. A relaxation process occurs with the release of energy as electron transitions from a higher-energy electron orbital to fill the core hole. Following an absorption event, the atom is said to be in an excited state, with one of the core electron levels left empty (a so-called core hole), and a photo-electron. The excited state will eventually decay typically within a few femtoseconds (10^{-15} s) of the absorption event. There are two main mechanisms for the decay of the excited atomic state following an x-ray absorption event. The first one is the X-ray fluorescence (Fig. II-10b), in which a higher energy electron core-level electron fills the deeper core hole, ejecting an X-ray of well-defined energy. The fluorescence energies emitted in this way are characteristic of the atom, and can be used to identify the atoms in a system, and to quantify their concentrations. The second process for de-excitation of the core hole is the Auger effect, in which an electron drops from a higher electron level and a second electron is emitted into the continuum and possibly even out of the sample (Fig. II-10c). In the hard X-ray regime (> 2 keV), X-ray fluorescence

is more likely to occur, but for lower energy Auger processes dominate (Fig. II-9). Due to photoelectrical effect, in which an X-ray is absorbed by a core-level with binding energy, a photo-electron with wave-number k is created and propagates away from the atom to the continium (Fig. II-10). This photo-electron can scatter from the electrons of this neighboring atom, and the scattered photo-electron can return to the absorbing atom (Fig. II-11) and it will alter the absorption coefficient (see below). This is the physical description and the origin of the XAS method.

(a)   **(b)**   **(c)**
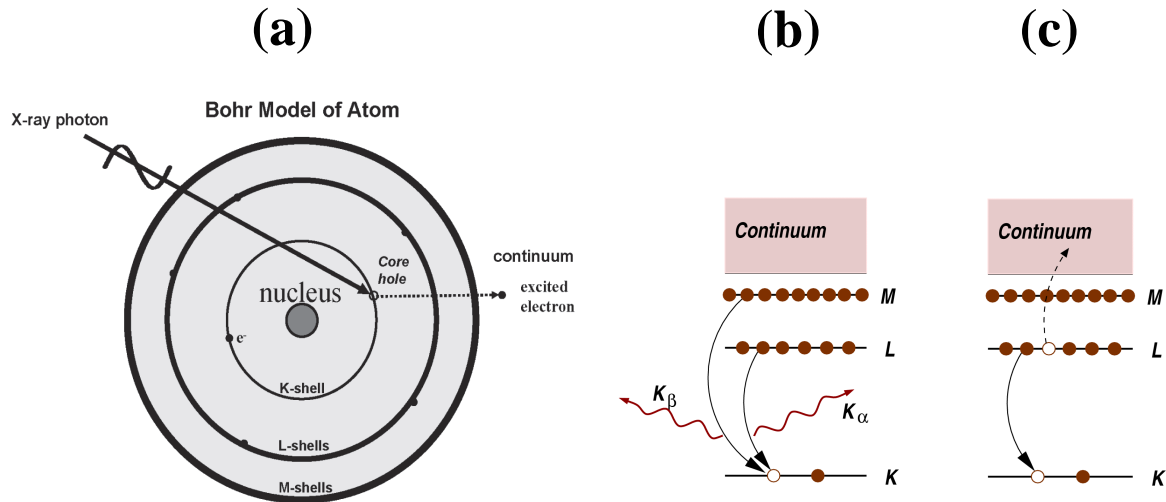
Figure II-10. *Interactions of X-ray with an atom (a); decay of the excited state: X-ray fluorescence (b) and the Auger effect (c). Taken from Newville (2004).*
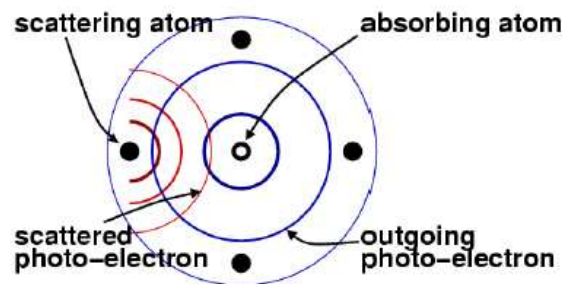
Figure II-11. *Interactions of photoelectron with neighboring scattering atoms used in X-ray absorption spectroscopy.*

The number of photons transmitted (I_t) through a sample is given by the intensity of X-rays impinging on the sample (I_0) decreased exponentially by the thickness of the sample (x) and the

absorption coefficient of the sample (μ). The absorption coeffiecient (μ) is the probability that X-ray will be absorbed according to the Beer's law:

$$I_t = I_0 e^{-\mu x} \qquad\qquad \text{(II-7)}$$

XAS can be measured either in transmission, $\mu x = \ln(I_0/I_t)$, or fluorescence, $\mu x = I_f/I_0$, geometries (Fig. II-12). An XAS measurement is simply a measure of the energy dependence of μ at and above the binding energy of a known core level of a known atomic species. Since every atom has core-level electrons with well-defined binding energies, we can select the element to probe by tuning the X-ray energy to an appropriate absorption edge. These absorption edge energies are well-known (usually to within a tenth of percent), and tabulated. The edge energies vary with atomic number approximately as Z^2, so both K and L levels can be used in the hard x-ray regime, which allows most elements to be probed by XAS with X-ray energies between 5 and 35 keV. Since the XAS is a small part of the total absorption, a fairy precise and accurate measurement of $\mu(E)$ is required, and errors in the measurement of $\mu(E)$ can degrade or even destroy the XAS. The principle characteristics of the incident X-ray beam are the energy resolution, the reproducibility, and stability in time. For transmission measurements the beam should be well-aligned on the sample is homogenous. For concentrated samples (wt % level) XAS should be measured in transmission. For lower concentration samples (down to the ppm level), the fluorescence is the preferred technique.
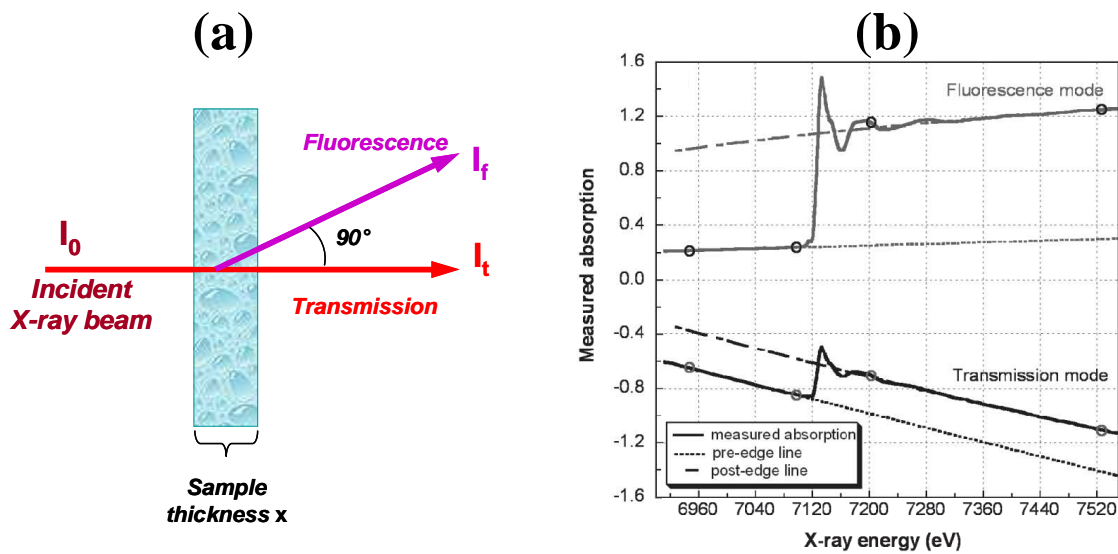
Figure II-12. *X-ray absorption and fluorescence. (a) The scheme of measuring. An incident beam of monochromatic X-rays of intensity I_0 passes through a sample of thickness x. Transmitted beam has intensity I_t, fluorescent beam has intensity I_f. (b) Typical fluorescence and transmission spectra.*

XANES spectrum

The X-ray absorption near edge structure (XANES) is the part of the absorption spectrum near an absorption edge, ranging from approximately −50 to +200 eV relative to the edge energy (Fig. II-13a). The binding geometry and the oxidation state of the atom directly affect the XANES part of the absorption spectrum. This absorption edge has the properties that it is linear and smooth below the absorption edge, increases sharply at the edge (like a step), and then oscillates above the edge. The main "step-like" feature of the absorption edge is due to the excitation of the photoelectron into the continuum (Fig. II-10). The absorption edge for some elements includes "decorations" in the region of the step. These "decorations" may be isolated peak(s), shoulder(s), or a strong peak at the top of the step, called a "white" line. These features are caused by differences in the density of unoccupied electron orbitals that can be occupied by the excited photoelectron, and are a function of the cluster geometry and absorber redox state. The edge energy for an element in a higher oxidation state is usually shifted by up to several electronvolts to a higher energy, thus providing a direct fingerprint of redox state.

In case of a single dominant redox state like for Zn(II) and Cd(II) in the majority of their terrestrial samples, the shape of the main edge reflects the coordination number and symmetry of the nearest atomic shell around these metals, so that changes of the dominant species between octahedral-like and tetrahedral-like may be quantified (see Chapter IV below for details). Because of the lack of "simple" quantitative physical models of the XANES phenomenon as compared to EXAFS (see below), the interpretation of XANES requires spectra of reference compounds with well-known structures. Such compounds are lacking for most aqueous systems. An alternative approach that has made an enormous progress in the last 5-10 years, owing to the increasing computer power, is *ab-initio* quantum-chemical modeling of XANES spectra. In this study, we used the FDMNES computer code (Joly, 2001) to model XANES spectra of Cd-H_2O-Cl complexes in aqueous solution (see chapter IV). This approach was successful in a number of recent studies of the metal speciation in high *T-P* aqueous solutions and provided valuable constraints on the metallic species geometry and electronic configurations which are difficult to obtain *a priori* (e.g., Testemale et al., 2004, 2009; Brugger et al., 2007; Pokrovski et al., 2009).
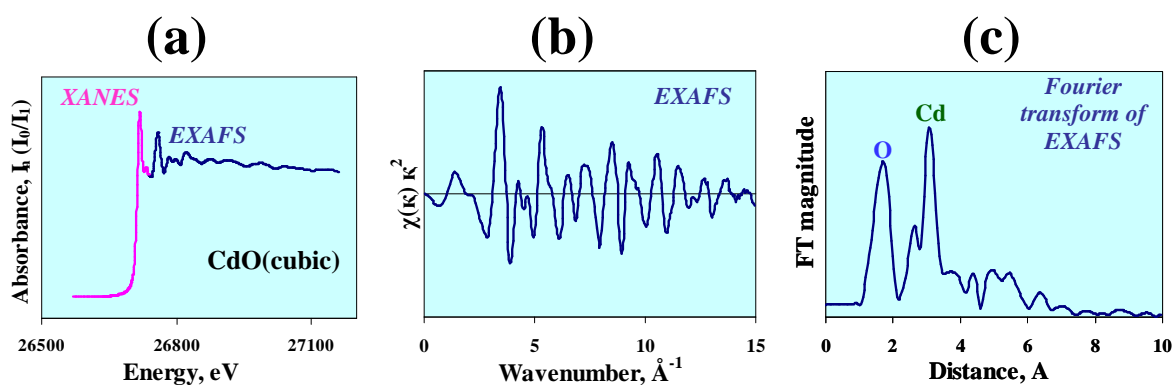
Figure II-13. *Normalized XAS spectrum of solid CdO(cub.) (a); its extracted EXAFS spectrum (b); and its Fourier transformed EXAFS spectrum (c).*

EXAFS spectrum

The extended X-ray absorption fine structure part of the spectrum (EXAFS) is the oscillatory part of the absorption coefficient above the absorption edge to approximately 1000 eV or higher (e.g., Fig. II-13b). The EXAFS spectrum contains information on the identities and numbers of atoms in coordination with the absorber atom, their interatomic distances, and the degree of local molecular bonding structural and thermal disorder. The EXAFS oscillations result from the interference between the outgoing and scattered electronic waves which are shifted in phase. As a result, such EXAFS oscillations only occur for elements with neighboring atoms. In the absence of coordinated atoms the EXAFS signal is absent.

Each atom at the same radial distance from the absorber contributes to the same component of the EXAFS signal. This group of atoms is called a shell. The number of atoms in the shell is called the coordination number. All photoelectron scattering configurations that start at the absorber atom, go to one or more neighboring atoms, and then return to the absorber atom contribute to the EXAFS signal. These configurations are called scattering paths. The primary quantity of EXAFS is then $\chi(k)$, the oscillations as a function of photo-electron wave number k, which is a sum of the contributions from all scattering paths of the photoelectron:

$$\chi(k) = \sum_i \chi_i(k) \qquad\qquad \text{(II-8)}$$

where:

$$\chi_i(k) = \frac{(N_i S_0^2) \cdot F_{eff_i}(k)}{k R_i^2} \cdot \sin\left[2kR_i + \varphi_i(k)\right] \cdot e^{-2\sigma_i^2 k^2} \cdot e^{\frac{-2R_i}{\lambda(k)}} \qquad\qquad \text{(II-9)}$$

The terms $F_{eff_i}(k)$, $\varphi_i(k)$, and $\lambda(k)$ are the effective scattering amplitude of the photoelectron, the phase shift of the photoelectron, and the mean free path of the photoelectron, respectively and are calculated *ab-initio* using for example the FEFF6 *ab-initio* code (Zabinski et al., 1995). The wave number of the photo-electron, k, is defined as

$$k^2 = \frac{2m_e \cdot (E - E_0 + \Delta E_0)}{\hbar} \qquad\qquad \text{(II-10)}$$

where m_e is the electron mass, $\hbar$ is the Plank's constant, E_0 is absorption edge energy, and ΔE_i relates to a change in the photoelectron energy. This value is used to align the energy scale of the theoretical spectrum to match the measured spectrum. S_0^2 is the passive electron reduction factor which has a value usually between 0.7 and 1.0 and can be estimated from measurements of reference compounds with a well-known structure. Values of N_i, R_i, and σ^2 represent the structural parameters of the atomic environment around the absorber atom. N_i represents the number of absorber neighbors for each scattering atom within a particular shell. R_i is an average distance in Å between each scatterer and the absorber. Because all of the coordinating atoms in a shell are not fixed at positions of exactly a distance R_i from the central absorber atom, σ^2 accounts for the disorder in the interatomic distances. σ^2 is the mean-square displacement of the bond length between the

absorber atom and the coordination atoms in a shell. This term has contributions from static (structural heterogeneity) disorder as well as dynamic disorder (thermal). The EXAFS process occurs on the femto-second (10^{-15}s) time scale, while thermal vibrations occur on a much longer time scale of 10^{-10} to 10^{-12}s. Thus, the atoms are essentially "frozen" at one position during the excitation process, and the EXAFS spectrum measures the distribution of the distances between the absorber atom and each of the coordinating atoms within a shell in terms of a σ^2 value. The static disorder component of σ^2 is due to differences in the position of the minima themselves. Thus, for example, if two interatomic distances are separated by only 0.010Å, with one atom at 2.00Å and another atom at 2.10Å, the contributing EXAFS signal could be modeled with one scattering path at 2.05Å with a mean disorder of 0.05 Å such that there is an additional σ^2 term due to the static disorder of 0.0025Å^2. The dynamic (thermal) disorder caused by the vibrations of atoms in the shell. This dinamic disorder is well known for crystals, the increasing temperature results in increasing thermal disorder. All XAS analysis in this study was performed with the Athena and Artemis packages (Ravel and Newville, 2005) based on the IFEFFIT program (Newville et al., 2001).

Hydrothermal spectroscopic cell and spectra acquisition

In our study XANES and EXAFS spectra were collected from aqueous Cd solutions in both transmission and fluorescence modes at the Cd K-edge (~26.7 keV) over the energy range 26.5-27.6 keV on BM30B-FAME bending-magnet beamline (Proux et al., 2005) at the European Synchrotron Radiation Facility (ESRF, Grenoble, France) (Fig. II-14). The storage ring was operated at 6 GeV with a ~200 mA current. The beam energy was selected using a Si (220) double-crystal monochromator with sagittal focusing. The energy was constantly calibrated using a cadmium metal foil; its K-edge energy was set at 26,711 eV as the maximum of the first derivative of the main-edge spectrum. The beam size was 1000 µm horizontal × 300 µm vertical. X-ray photon flux on the sample was about 10^{12} photons/s. Silicon diodes collecting scattered radiation from a Kapton foil were employed for measuring the intensities of the incident (I_0) and transmitted (I_1 and I_2) X-ray beams while fluorescence spectra were collected in the 90° geometry using a Canberra solid-state 30-element germanium detector (energy resolution = 300eV, shaping time = 125ns). Total acquisition time for each XAS scan was ~30min.

(a)　　　　　　　　**(b)**
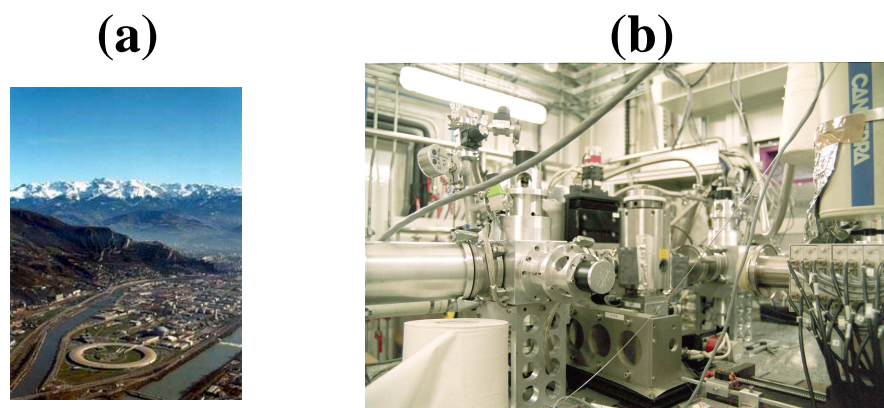
Figure II-14. *(a) Photo of the European Synchrotron Radiation Facility in Grenoble in France; (b) Photo of the full experimental setup with a hydrothermal cell on the beamline BM30B-FAME.*

XAS experiments were carried out using a high T-P cell developed at the Institut Néel (Grenoble) and recently described in detail elsewhere (Testemale et al., 2005; Pokrovski et al., 2005, 2009a,b). The apparatus consists of an internal cell inserted in a high-P stainless-steel reactor which has a water-cooling jacket and three beryllium windows for X-ray beam passage (Fig. II-15a). The autoclave is pressurized by helium gas with low absorption constant for X-rays. Pressure in the sample space is always balanced with that of He gas through the pistons. The cell design permits operation up to ~2000 bar and ~500°C (depending of the amplitude of the fluid expansion and the thickness of Be windows). The temperature in the sample space is maintained within ±1°C with Mo heating resistances (Fig. II-15b) and Pt–Pt/Rh thermocouples connected to a Eurotherm® temperature controller. The optical path through the vertically oriented cell remains constant owing to the low temperature expansion coefficient of glassy carbon. Temperature gradients through the sample space do not exceed 10°C at an experimental T of 450°C.

The internal cell consists of a vertically oriented sapphire or glassy-carbon tube polished inside, and two sapphire coaxial rods equipped with Viton O-ring seals and inserted into the tube from each end (Fig. 15b). The rods delimit the sample space, in which experimental solid and solution are placed, and can move in the tube in response to pressure changes like a piston in a syringe. The volume of the sample space is about 0.1 to 0.2 cm^3 which corresponds to a height of 3 to 6 mm, depending on T-P conditions. The Viton O-rings are situated outside the heating zone (at < 100°C when the sample-space temperature is 400°C) to avoid their thermal degradation. This results in a relatively small 'dead-volume' space between the rods and glassy-carbon tube (< 20-30% of the total cell volume) that produces minimal solute diffusion and solid precipitation below or above the hot sample space. Additional details about the cell properties and operation limits are given in Pokrovski et al. (2006, 2009a, b).
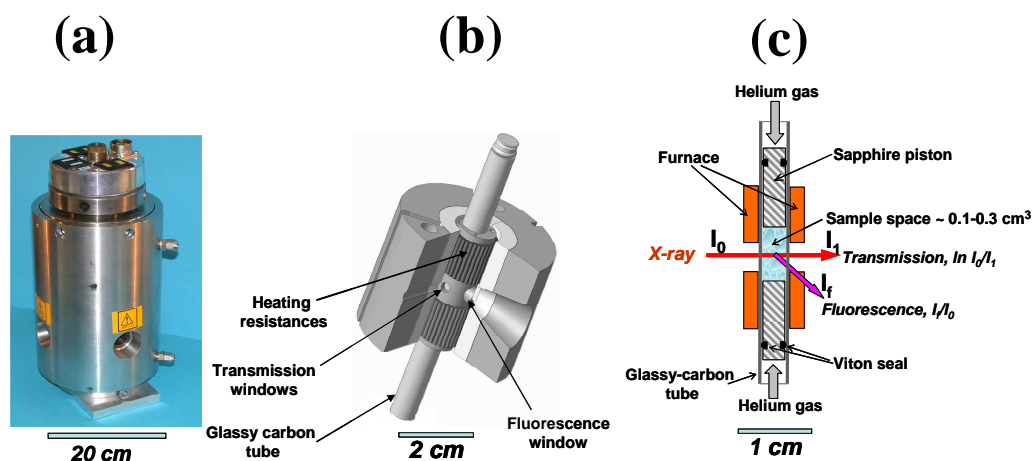
Figure II-15. *X-ray cell used for XAS measurements: (a) stainless steel high-P reactor with Be windows; (b) furnace with Be windows; (c) internal glassy-carbon cell.*

II-5. *Sampling and analyses of natural high–temperature fumaroles gases (Kudryavy volcano, Kuril Islands, Russia)*

The experimental approaches described above allow studies of metal speciation, solubility and partitioning in relatively simple model systems at carefully controlled laboratory conditions. In order to be applicable for solving geological problems, the results obtained using such approaches require confrontation with data on natural hydrothermal-volcanic fluids which are far more complex than any laboratory system. Active volcanoes and modern hydrothermal systems on Earth provide an excellent opportunity for such confrontations. Such types of natural fluids may be studied in situ. In September 2006 we performed a field work at the Kudryavy volcano which is a good example of modern hydrothermal-volcanic systems. Its geological setting, techniques used for the sampling of volcanic gases, and the subsequent preparation and treatment of samples before analyses are described below.

Geological setting

Kudryavy volcano (991 m elevation) is located in the northern part of Iturup, Kuril Islands, Russia (Fig. I-16a). The chain of subduction-zone volcanoes of the Kuril Arc goes along the boundary of the Pacific plate, which is converging with northeastern Eurasia at a velocity of 8–9 m per century (Yudovskaya et al., 2008). The part of the oceanic crust subducting beneath the Kurile Arc is the oldest in the Pacific plate (about 120 Ma, Yudovskaya et al., 2008). Beneath the southern segment of the arc the crustal thickness is about 15 km and the slab depth is approximately 120–150 km (Yudovskaya et al., 2008). There are eight active and numerous extinct volcanoes on Iturup Island. The Kudryavy volcano of basalt-andesite composition together with volcanoes Medvezhy, Sredny and Men'shoi Brat, represents a volcanic ridge in the Medvezhya caldera in the northern part of the island. An epoch of caldera formation finished with a giant dacite extrusion in its central part (Ermakov and Steinberg, 1999). The younger basalt-andesitic volcanoes developed along a linear fault and deformed the edifice of the dacite volcano. The Kudryavy cone was superimposed on the slope of this older volcano. High-temperature vents are confined to fractures and faults related to an andesitic extrusive stock exposed in the center of the eastern crater. Although the western crater appears to be the center of the youngest basaltic lava flows, only low-temperature fumarolic vents are active there. The active fumarole degassing is closer in age to the younger andesite-basaltic melts (Yudovskaya et al., 2008). The chemical and isotopic compositions of fumarole's gases at Kudryavy volcano are typical of arc volcanism (Taran et al., 1995).
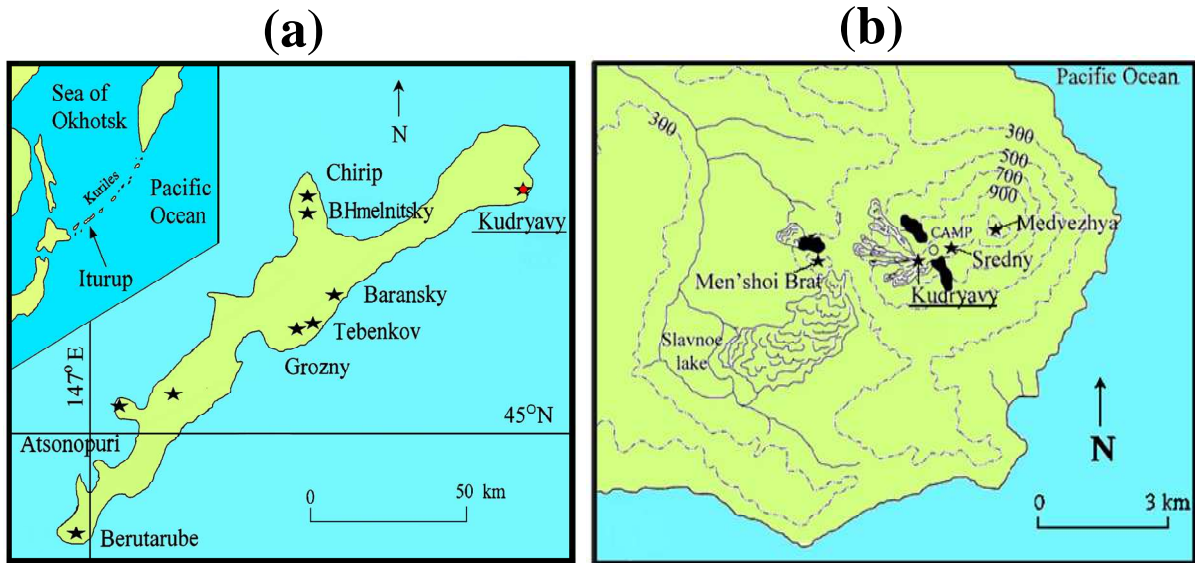
Figure II-16. *(a) Location map of the Kudryavy volcano on Iturup Island, Kuril Arc;*
(b) Sketch map of the north-eastern part of Iturup Island.

Since the last magmatic eruption in 1883, the volcanic activity at Kudryavy volcano is limited to abundant fumarolic emissions (Fig. II-17) with rare phreatic explosions, the last of which occurred in 1999. The total emission rate of volcanic gases on Kudryavy volcano was estimated as 30,000 tons per day (Botcharnikov et al., 1998). Three low-temperature (<200°C) fumarole's fields are located in the western part of the crater zone. Four high-temperature (>200°C) fumarole's fields occupy the largest area (Fig. II-17b) in the northeastern part of the elongate summit formed by merged craters (maximum temperature of gases in brackets, °C): "Main" (870), "Dome" (730), "Molybdenum" (650) and "Rhenium" (600). The temperatures of these foumaroles vary within 20°C annually (Korzhinsky et al., 2002). The highest temperature of 940°C was measured in the crater in 1992 (Korzhinsky et al., 2002). The "Rhenium" field contains very rare in nature minerals such as rheniite ReS_2, cadmoinite $CdIn_2S_4$ and kudriavite $(Cd, Pb)Bi_2S_4$. The literature on the composition of the volcanic gas and sublimates is extensive (Taran et al., 1995; Korzhinsky et al., 1996; Fischer et al., 1998a, b; Shmulovich and Churakov, 1998; Tkachenko et al., 1999; Wahrenberger et al., 2002; Botcharnikov et al., 2003; Chaplygin at al., 1997; Yudovskaya et al., 2008).

(a)   **(b)**
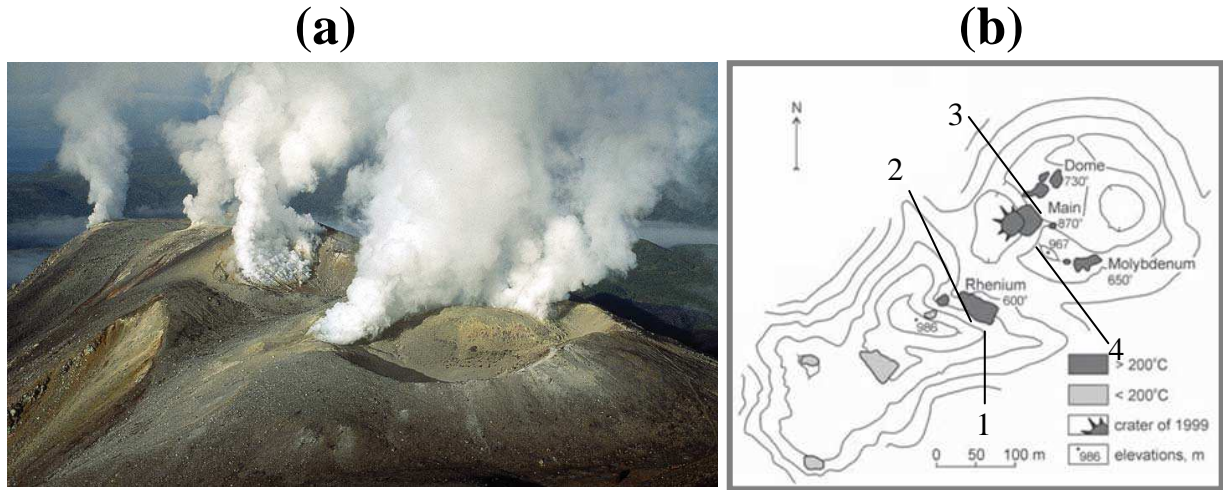
Figure II-17. *(a) Photo of the top of the Kudryavy volcano from the Sredny volcano. Situated on the right-hand side is the northeast crater enclosing the highest-temperature "Main" and "Dome" fumarole's fields, together with the "Molybdenum" field on the southern rim. The "Rhenium" field is on the steep inner wall of the destroyed crater. The low-temperature sites are on the far side of the top (Chaplygin et al., 2007) (b) Map of the fumarole's fields on top of the Kudryavy volcano with indicated sample points.*

Our samples of volcanic condensates were collected in September 2006 in high-temperature fumarole's fields: 4 samples from "Rhenium", 2 samples from "Dome", and 1 sample from "Main" field (Table II-1). These samples were complemented by major gas components analyses in 5 samples from "Main", "Dome", "Rhenium" and "Molybdenum" fumarole's fields.

Table II-1. Samples of volanic condensates from Kudryavy volcano (Kuril Islands, Russia).

Sampling Point	Date	Fumarole's field	T_{tube}, °C	Sample description
1	26/09/06	Rhenium	550-350	2 simultaneous samples without and with 3M $NH_4(OH)$ matrix
2	27/09/06	Rhenium	550-350	2 simultaneous samples without and with 3M $NH_4(OH)$ matrix
3	27/09/06	Dome	700-465	2 simultaneous samples without and with 3M $NH_4(OH)$ matrix
4	30/09/06	Main	820-620	1 sample with 3M $NH_4(OH)$ matrix

T_{tube} = temperature gradient in the main sampling tube (measured at the tube ends).

Sampling technique

The classical techniques commonly used for volcanic gases sampling are presented in Fig. II-18. In both techniques, gases are sampled from the vents using ~1m-long and ~1cm-internal diameter quartz tube. One end of this main tube is inserted into the gas vent and the other end is connected via a

silicone rubber tube to a sample vessel. The silicon rubber tube is ~50 cm-long for sampling from the vents with $T \geq 500°C$. "Giggenbach bottle" (Fig. II-18a) is an evacuated flask (~250-300 cm^3 volume) containing an alkaline matrix (~50 cm^3 of ~3-5M KOH, NaOH or Cd(CH$_3$COO)$_2$ aqueous solution). This flask is equipped with a Teflon stopcock that opens the access to the flask. Due to evacuation, volcanic gas enters to the flask through this special entry (Fig. II-18a). The presence of the uncondensable gases (e.q., CO$_2$, SO$_2$, H$_2$S, H$_2$, N$_2$, O$_2$, Ar) limits however the total sample amount that can be collected into the "Giggenbach bottle" (usually less than 20 mg in a flask of 300 cm^3 for vents with $T \geq 500°C$). The main advantage of this technique is that these uncondensable gases can be measured which is impossible for other techniques, and both H$_2$S and SO$_2$ concentrations can be calculated following the method described by Giggenbach and Goguel (1989). In this study the "Giggenbach bottles" with Cd acetate matrix were used to collect 5 samples from "Main", "Dome", "Rhenium" and "Molybdenum" fumarole's fields. Another classical method is sampling of volcanic gas condensates using a quartz condenser cooled by water circulation (Fig. II-18b). The amount of the sample is not limited that is very important for trace metals analyses, but the temperature gradient, however, is rather large and cannot be avoided. It should be noted that both classical techniques cannot be performed directly from the main quartz tube. Moreover, the both techniques require the use of a rather long (~50 cm) silicon rubber tube, usually the same for all samples. Thus, possible losses and cross-contamination of metals during sampling cannot be excluded.
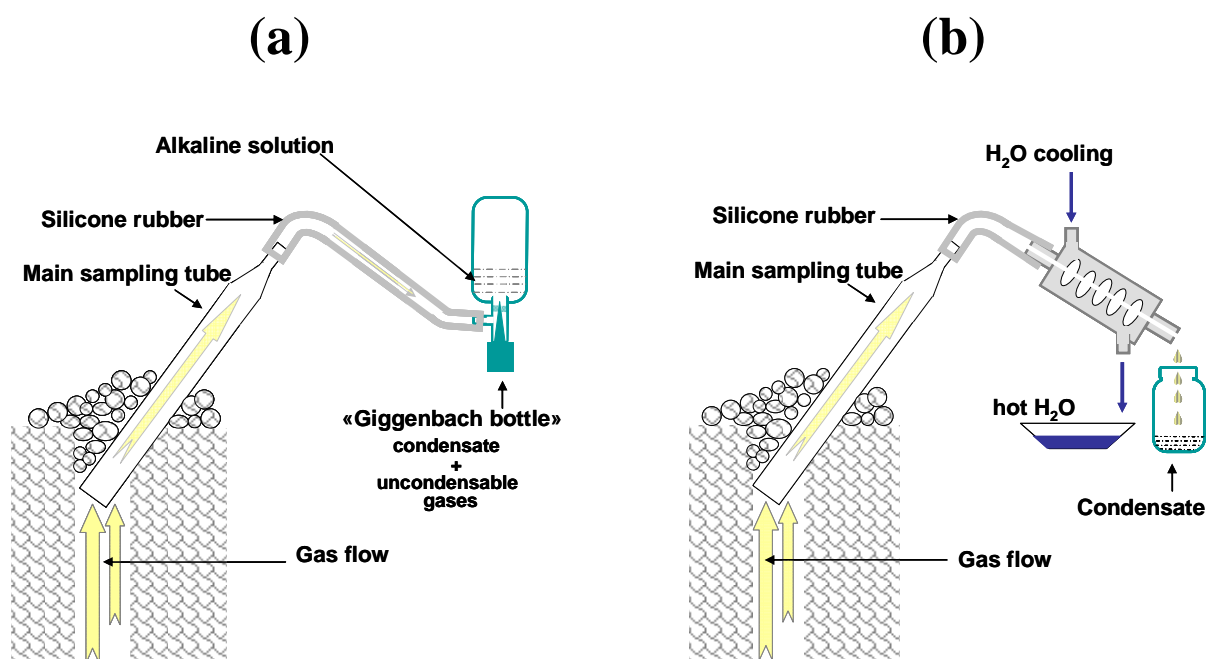
Figure II-18. *Classical techniques for volcanic gases sampling: (a) "Giggenbach bottle"; (b) condensates sampling with water cooling.*

In this study, an alternative technique of condensate sampling was developed. Our technique is based on cooling of the volcanic gas by air in the second quartz tube (Fig. II-19). The main sampling tube used in this technique is ~1m-long and 2.5cm-internal diameter. Such rather big

diameter helps to increase the volcanic gas flow passing though it and thus, minimize the temperature gradients. The second quartz tube is 15cm-long, 0.5cm-internal diameter and of an angle-like shape (~75°) that allows hanging it up directly on the main tube as it shown in Fig II-19. One end of this second tube is in the part where the flow is the hottest and the most rapid, the other end is inside the vessel for condensate collecting (Fig II-19). Each second tube was used only for one sample. After sampling, all second tubes were named, closed with inert Teflon film, transported to the laboratory and analyzed.
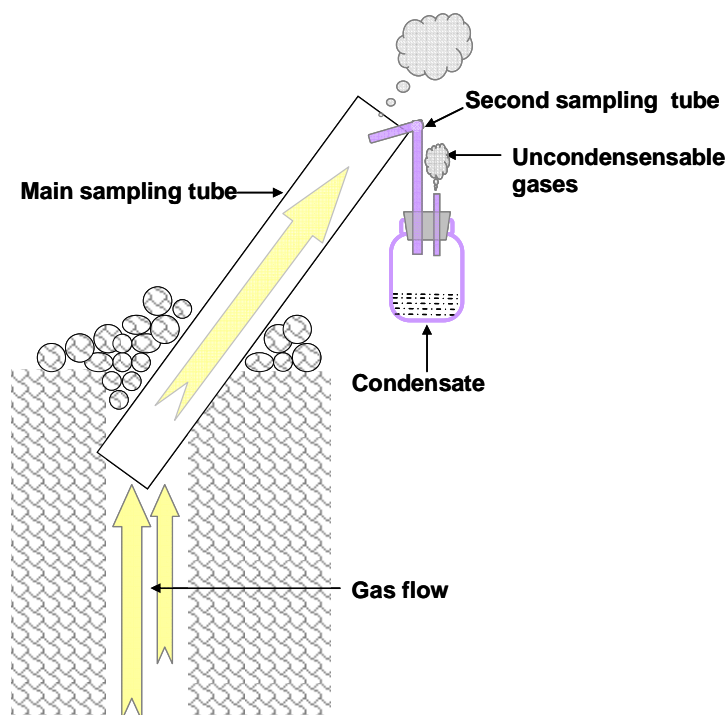
Figure II-19. *Sampling technique used in this study. For each sample, analyses of volcanic condensates were complemented by analyses of precipitates in the sampling quartz tube.*

This technique can be used only for sampling of aqueous condensates, all uncondensable and high volatile components being lost during such sampling (Fig. II-19). The exit of quartz tube for uncondensable gases is very small (internal diameter is 2 mm) and the temperature of condensates in the vessel do not exceed ~50°C. Thus, any loss of metals through this tube seems to be unlikely. Two types of condensate samples were collected at the same time: into an empty vessel and into a vessel with alkaline solution of 3M NH$_4$OH (see Table II-1 above). Samples without ammonia contained the precipitated sulfur, while samples with ammonia were transparent. The comparison of different treatments of these two types of condensates was performed to estimate the possible loss of metals during the samples treatment (see below). Thus, the main advantages of our sampling design are the following: *a)* possibility of sampling at high temperatures; *b)* possibility to collect simultaneous samples of gas condensates; *c)* comparison of sampling with and without ammonia; *d)* all losses of trace metals during high-temperature gas sampling can be estimated for each sample by analyzing

precipitats in the corresponding second tube. The details about sampling treatment and analyses are given below.

Sample treatment and analyses

Samples with and without ammonia matrix were treated differently. Matrix-free samples were transferred into a clean 60 cm^3 Teflon baker (Savilex) and slowly evaporated at 40-45°C on an electrical hotplate in a clean room. The dry residue was dissolved in the same closed baker at 80-90°C for few hours in the presence of 2-4 g of aqua regia prepared from bi-distilled 70% HNO_3 and 30% HCl (1:2). The bakers were then opened and the aqua regia was slowly evaporated at 60-70°C until the solution mass was reduced to 0.3-0.5 g. The latter was then diluted to 20-30 g with 1.5% HNO_3-0.5% HCl and reserved for metals and total sulfur analyses by ICP-MS and ICP-AES.

Samples with ammonia matrix were treated as follows. The presence of ammonia results in the formation of soluble polysulfides efficiently stabilizing all sulfur and most metals in solution. The condensate with NH_4OH matrix was divided into two weighed parts and treated by two different methods. The first part, dedicated to metals analyses, was treated in the same way as samples without ammonia (see above). The second part was transferred into a clean polypropylene baker and reacted with 2-3 cm^3 of an aqueous hydrogen peroxide solution (~2 cm^3 of ultrapure 30 wt% H_2O_2 in water) at room temperature for a day. This results in the oxidation of all sulfur forms to sulfate. The solution was then divided into two weighed parts. One part was diluted with water for sulfate, chloride and fluoride analyses by HPLC, the other part was diluted with 1.5 % HNO_3-0.5 % HCl for metal and total sulfur determination by ICP-MS and ICP-AES.

The sampling tubes were broken, placed in a clean 200 cm^3 Teflon baker (Savilex) and treated with aqua regia similarly to the condensate matrix-free samples. After vaporization down to 0.3-0.5 g, the solutions were diluted with the same acid matrix similarly to the condensate samples (HNO_3-HCl) and analyzed by ICP-MS and ICP-AES. The analyses of samples from "Giggenbach bottles" were performed by V. Shapar and I. Timofeeva at the Institute of Volcanology and Seismology (IVIS DVO RAS, Petropavlovsk-Kamchatsky, Russia) following the method described by Giggenbach and Goguel (1989).

II-6. Analytical methods

Various complementary analytical techniques were used to analyze element concentrations in aqueous experimental and natural samples: Atomic Absorption Spectroscopy (AAS), Inductively Coupled Plasma Mass Spectrometry (ICP-MS), Inductively Coupled Plasma Atomic Emission Spectrometry (ICP-AES), and High Performance Liquid Chromatography (HPLC). In this chapter we present briefly the foundations and complementarities of these methods for analyses of our laboratory and natural solutions. Solid samples were analyzed routinely by X-ray diffraction (XRD) and Scanning Electron Microscopy (SEM); these techniques will not be presented here.

Atomic Absorption Spectroscopy (AAS)

Atomic Absorption Spectroscopy is a common analytical method for determination of elements concentration in solution. This technique can be used to analyze over 70 different elements.

The principles of AAS method are based on the Beer-Lambert law of light absorption (similar to that of X-ray). Briefly, the valence electrons of the atoms can be promoted to higher orbitals for a short amount of time by absorbing a set quantity of energy (i.e. light of a given wavelength). This amount of energy (or wavelength) is specific to a particular electron transition in a particular element, and in general, each wavelength corresponds to only one element. In order to analyze a sample for its atomic constituents, it has to be atomized. Then the sample should be illuminated by light. The light transmitted is finally measured by a detector. The detected signal is proportional to the concentration of the element in the sample. There are two main methods to atomize the sample: the flame and graphite furnace. The temperature required to atomize the sample is 2,000-3,000°C. Thus, an aqueous sample can be mixed with a stream of gas-based fuel (acetylene), aerosoled and burned (in flame) or it can be heated in the close resistant furnace (graphite furnace). The measured light intensity is compared to measured intensities of standards with known concentrations, and then is computed to the concentration by interpolation along the calibration line. The main advantages of AAS analytical method are low cost, good signal stability, and good reproducibility. The disadvantages are *a)* each measurement is for a single element, and *b)* rather high detection limit (10-100 ppb for many elements in the flame mode). In this study, Cd and Zn analyses using AAS were performed with the following acquisition parameters: flame = air/acetylene, air flow = 7000 cm^3/min, acetylene flow = 2500 cm^3/min, absorption wavelength = 228.8 nm for Cd and 213.9 nm for Zn, integration time = 3 replicates × 3s, Cd hollow cathode intensity = 8 mA, Zn hollow cathode intensity = 10 mA. The standard solutions were prepared from Aldrich standard aqueous solutions of 1000±5 ppm. The matrix for all standards and samples was 1 wt% HNO_3 – 1 wt% HCl. The analyzed concentration range is 20 ppb – 8 ppm both for Cd and Zn, the reproducibility is ±5-10%. The detection limits were estimated to be 2 ppb and 10 ppb for Cd and Zn, respectively.

Inductively Coupled Plasma Mass Spectrometry (ICP-MS)

Mass spectrometry is a technique for separating ions by their mass-to-charge (m/z) ratios. The detection is based on the fact that mass of each element (isotope) is unique. This analytical method can be divided into two broad applications: multi-element analysis of solutions, and determination of the isotopic composition. ICP-MS (Inductively Coupled Plasma Mass Spectrometry) is a type of mass spectrometry that is highly sensitive and capable of simultaneous analysis of a range of metals at above the part per trillion level (ppt). ICP (Inductively Coupled Plasma) - this is a high-temperature plasma (ionized argon) sustained with a radio-frequency electric current, which acts to produce ions. The ICP torch consists of 3 concentric quartz glass tubes and a coil of the radio-frequency generator surrounding the torch. Argon gas is typically used to create the plasma. It is ionized in the intense magnetic field created by the radio-frequency generator. A stable, high-temperature plasma of about 5,000-10,000°C is generated as the result of the collisions between the neutral and ionized argon atoms. Solvent evaporates prior to reaching the actual plasma and atomization of the elements present in the sample solution occurs in the extremely high temperature of the plasma. MS (Mass Spectrometry) assures the ions extraction from the plasma through a series of cones into a mass spectrometer, usually a quadrupole. The ions are separated on the basis of their mass-to-charge ratio by a magnetic field and a detector receives an ion signal proportional to the concentration. The concentration of a sample can be determined through calibration with elemental standards. The advantages of ICP-MS are multi-element analyses and very low detection limits (ppt). The main

disadvantages are *a)* the high sensitivity to the matrix, *b)* poor signal stability in time, and *c)* interferences between measured elements, argon and matrix. In this study, ICP-MS was used for multi-element (including Cd and Zn) analyses of volcanic condensates and Cd and Zn analyses in low-concentrated experimental solutions. The analyzed concentration range is 0.1-1000 ppb, the reproducibility is ±20%. The matrix for all samples is 1.5 wt% HNO_3 - 0.5 wt% HCl. The aliquot 5 ppb of indium (In) was added into all samples to control the signal changes with time, and to serve as internal standard.

Inductively Coupled Plasma Atomic Emission Spectrometry (ICP-AES)

Inductively coupled plasma atomic emission spectroscopy (ICP-AES), also referred to as inductively coupled plasma optical emission spectroscopy (ICP-OES), is an analytical technique complementary to AAS and ICP-MS. It is a type of emission spectroscopy that uses the inductively coupled plasma to produce excited atoms and ions that emit electromagnetic radiation which can then be detected. The intensity of this emission is proportional to the concentration of the element. The ICP-AES is composed of two parts: the plasma (ICP) and the optical spectrometer. Due to the high temperature of ICP (to 10,000°C), thermal excitation of valence electrons to higher allowed energy states takes place. When relaxation to the ground state occurs the energy difference between the excited state and the ground state is emitted as a quantized photon. The photon wavelengths emitted are commonly in the visible-to-ultra-violet portion of the electromagnetic spectrum (see Fig. II-9, section II-4 above). By separating the various emission wavelengths with a monochromator, qualitative information is gathered. The intensity of each line is compared to previous measured intensities of known concentrations of the element and its concentration is then computed by extrapolation along the calibration line. The advantages of this technique are *a)* multi-element analyses, *b)* good signal stability, *c)* linearity of signal in a wide range of analyzed concentrations, and *d)* good reproducibility. In this study, ICP-AES was used to analyze volcanic condensates for As, B, Ca, Cd, Cu, Fe, K, Mg, Na, Pb, S, and Zn. The analyzed concentration range is 0.01 – 500 ppm, the reproducibility for all analyzed elements is ±2-5%. The main disadvantage is rather high detection limits for most elements (on the order of ppb). The matrix-matched ($HCl-HNO_3-NaCl-NaHSO_4$) multi-element standard solutions was prepared from Aldrich standard solutions 1000±5 ppm of each element.

High-performance liquid chromatography (HPLC)

High-performance liquid chromatography (HPLC), also referred as high-pressure liquid chromatography, is a form of column chromatography used frequently to separate, identify, and quantify aqueous compounds. HPLC utilizes a column that holds chromatographic packing material (stationary phase), a pump that moves the mobile phases through the column, and a detector that measures the retention times of the molecules. Retention time varies depending on the interactions between the stationary phase, the analyzed molecules, and the used solvent. Thus, the HPLC analysis contains following paths: sample injection to the solvent flow, ions separation on the ion-exchange resin, anions detection by conductivity measurement, anions identification by a characteristic time of passage, quantification by the calibration.

In this study, all HPLC analyses were performed with a Dionex ICS 2000. This apparatus consists of an automatic sampler, a pump for solvent circulation with regulated debit, a detection cell

CDM-3, P/N 50 776 measuring continuously the conductivity and the temperature of the mobile phase, a suppressor (SRS) neutralizing the conductivity of analyzing species, a separation column AS18 and a storage column AG9-SC, and a computer code for data treatment (peaks intensity as a function of retention time in the column). The solvent used is 0.003M KOH aqueous solution with a rate of 1 cm^3/min. The anions analyzed (corresponding retention time are given in brackets) are choride Cl$^-$ (4.3 min), sulfate SO$_4^{2-}$ (5.6 min), fluoride F$^-$ (3.3 min). The analyzed concentration range is 0.1 – 200 ppm, the reproducibility for all analyzed elements is ±2-5%.

II-7. Thermodynamic calculations

Calculations of mineral solubilities and aqueous species distribution and stabilities were performed using the HCh software package and OptimA program (Shvarov and Bastrakov, 1999; Shvarov, 2008) based on the minimization of the total Gibbs free energy of the system. The HKF parameters of species were retrieved using the UT-HEL program (Shvarov, 2008). The thermodynamic properties of the main fluid constituents H$_2$O, H$^+$, OH$^-$, Na$^+$, K$^+$, NO$_3^-$ and Cl$^-$ were adopted from the SUPCRT92 database (Johnson et al., 1992); those for Cd^{2+}, Zn^{2+} and NaOH^0 from Shock et al. (1997), those for NaCl^0 from Sverjensky et al. (1997); and those for HCl^0 and H$_2$S^0/HS$^-$ were taken from Tagirov et al. (1997) and Akinfiev et al. (2008), respectively. The thermodynamic properties of monteponite (CdO, cubic) were taken from Naumov et al. (1974) and Wagman et al. (1982), those of zincite (ZnO, cubic) and greenockite (CdS, hexagonal) from Robie and Hemingway (1995).

The activities of all aqueous species are defined as:

$$a_i = m_i \cdot \gamma_i \qquad \text{(II-11)}$$

where m_i = species molality (mol/ kg H$_2$O); γ_i = species activity coefficient. The activity coefficients of neutral species are assumed to be one. The activity coefficients of charged species were calculated using the extended Debye-Hückel equation:

$$\log \gamma_i = \frac{-A \cdot z_i^2 \sqrt{I}}{1 + B \cdot \mathring{a}_i \sqrt{I}} + b \cdot I \qquad \text{(II-12)}$$

where A and B refer to the Debye-Hückel electrostatic parameters and were taken from Helgeson and Kirkham (1974); I is the effective molal ionic strength ($I = 0.5 \cdot \Sigma \ z_i^2 \cdot m_i$); z_i and $\mathring{a}_i$ represent the ionic charge and the distance of the closest approach for i-th species, respectively; b is the extended term parameter for KCl or NaCl dominated solutions which is a function of T and P (Oelkers and Helgeson, 1990).

Chapter III. POTENTIOMETRIC STUDY OF CADMIUM CHLORIDE COMLEXES FROM 1 TO 1000 BAR AT 25°C

This chapter presents an article submitted to the Russian journal *Geology of Ore Deposits* in August 2009 (Bazarkina E.F., Zotov A.V., Akinfiev N.N. "Potentiometric study of cadmium chloride complexes from 1 to 1000 bar at 25°C"). If accepted, the full text of this article will be published in 2010 in both Russian and English languages. Here we present an extended abstract in English and the full text in Russian of this article. All tables and figures are given in English in the end of the full article text.

Extended abstract

The present study is devoted to the determination of the standard thermodynamic properties of aqueous chloride complexes of cadmium at 25°C as a function of pressure (1-1000 bar) using a potentiometric method. Cd-Cl complexes are the main aqueous species responsible for the transport of this metal in a wide *T-P* range. The aims of this study were the following: 1) to measure the stability constant of the $CdCl_4^{2-}$ complex at 25°C and 1 bar, which is poorly known at present (see chapter I); 2) to measure the pressure dependence on the stability constants of all cadmium chloride complexes; 3) to derive from these data the individual standard molal partial volumes and corresponding HKF parameters for these complexes; 4) to estimate the effect of pressure on Cd contents in hydrothermal sphalerites (ZnS). Measurements were performed using the potentiometric method described in detail in Chapter II-1. Briefly, an isothermal potentiometric cell with liquid junction and equipped with a solid-contact Cd-selective electrode with a CdS-AgS membrane was used for measurements of the Cd^{2+} free ion activity in aqueous solutions with a constant $Cd(NO_3)_2$ concentration ($0.01m$) and variable KCl concentrations ($0 – 2m$ Cl) at 25°C and pressures from 1 to 1000 bars. The potentiometric data were treated using the HCh software package (Shvarov, 2008), which includes special modules for optimization of the Gibbs free energies/stability constants (OptimA program) and for derivation of HKF-model parameters (UT-HEL program).

At pressure of 1 bar and 25°C, our measurements show that with increasing Cl concentration from 0 to $2m$ the activity of Cd^{2+} decreases by ~3 orders of magnitude due to the stepwise formation of cadmium chloride complexes. In the terms of pCd (pCd=-lg a_{Cd2+}) it corresponds to the increase by ~3 orders of magnitude (Tab. 1, Fig. 2a). At Cl concentrations below $1m$ our experimental results confirm the values of stepwise stability constants for $CdCl^+$, $CdCl_2^0$(aq) and $CdCl_3^-$ given by Archer (1998) from a revision of available literature data. For Cl concentrations above $1m$ the differences between our data and the predictions of Archer (1998) exceed the estimated experimental uncertainties. This clearly demonstrates the presence of a forth complex, likely $CdCl_4^{2-}$ in these concentrated solutions. The logarithm of its stepwise equilibrium constant ($logK_4$), according to the reaction $CdCl_3^- + Cl^- = CdCl_4^{2-}$, was found to be -0.88±0.25 using the optimization logarithm of OptimA program (Shvarov, 2008). There are very fragmentary experimental data for this complex

stability in the literature. Our value is 2 orders of magnitude higher than the experimental determination of Reilly and Stokes ($\log K_4 = -3.37$, Reilly and Stokes, 1970), but is in good agreement with a value recently recommended in the theoretical review of Sverjensky et al. (1997), $\log K_4 = -0.93$ (Tab. 2).

Our measurements **at elevated pressures** show that in aqueous solutions with 0.025-1.4m Cl, the pressure increase from 1 to 1000 bar results in a Cd^{2+} activity increases up to 0.16 log units. The largest pressure effect corresponding to an increase of 0.16±0.02 log unit of Cd^{2+} activity was measured in the 1.4m Cl solution (Tab. 3). Our data allow derivation, for the first time, of the stability constants for cadmium chloride complexes at 1000 bar. The stepwise stability constants for $CdCl^+$, $CdCl_3^-$ and $CdCl_4^{2-}$ are found to have weak dependence with pressure, less than 0.05 log units of K_i in the pressure range 1-1000 bar, whereas the stepwise stability constant of $CdCl_2^0(aq)$ decreases by 0.33 log units at 1000 bar in comparison to the ambient pressure. Thus, the following values of stepwise stability constants at 25°C and 1000 bar are obtained in this study (in log units): 2.00±0.03, 0.31±0.10, -0.67±0.15, -0.86±0.25 for $CdCl^+$, $CdCl_2^0(aq)$, $CdCl_3^-$ and $CdCl_4^{2-}$, respectively.

To calculate the individual standard partial molal volumes V_i^0 of cadmium chloride complexes, from the generated stability constants at 1 and 1000 bar, we used several theoretical models. These models are based on a linear correlation between the non-solvation (non-electrostatic) contribution $\Delta_n V^0$ to the standard partial molal volume V^0 and the ligation number n in the complex (Hovey, 1988). These correlations are functions of species geometry, so that coordination changes with increasing the number of Cl ligand in the complex should be taken into account (e.g., Swaddle and Mak, 1983). The structure and geometry of aqueous Cd species stem from spectroscopic measurements. As show our XAS work (Chapter IV, Bazarkina et al., 2009b) and previous studies (e.g., Bol et al., 1970; Ohtaki et al., 1974; Caminiti et al., 1980; Rudolph and Pye, 1998), the structure of Cd^{2+} is octahedral as imposed by the presence of 6 water molecules in the inner atomic shell of the ion, whereas low-ligand number cadmium chloride complexes ($CdCl^+$ and probably $CdCl_2^0(aq)$) are octahedral and high-ligand chloride complexes ($CdCl_3^-$, $CdCl_4^{2-}$ and, probably, $CdCl_2^0(aq)$) are tetrahedral, according to our own work (Bazarkina et al., 2009b) and previous spectroscopic data. The octahedral or tetrahedral coordination in these species are completed by the presence of water molecules in the first coordination shell of the metal. Thus, following these structural data, several correlation models were tested: 1) a linear correlation between $\Delta_n V^0$ and ligands number n for *all* Cd chloride complexes including Cd^{2+} assuming the same coordination for all complexes (e.g., for acetate complexes, Zotov et al., 2006); 2) a linear correlation for the octahedral Cd^{2+}, $CdCl^+$, and $CdCl_2^0(aq)$, which corresponds to the coordination change to tetrahedral at the formation of the $CdCl_3^-$ complex (e.g., Drakenberg et al, 1978; Arhland, 1979); 3) a linear correlation for the tetrahedral $CdCl_2^0(aq)$, $CdCl_3^-$ and $CdCl_4^{2-}$, which corresponds to the coordination change between octahedral (Cd^{2+} and $CdCl^+$) and tetrahedral upon the formation of $CdCl_2^0(aq)$ (e.g., Paschina et al., 1983; Anderson and Irish, 1988; Bazarkina et al., 2009b). It was found that only the model 3 with a linear correlation for $CdCl_2^0(aq)$, $CdCl_3^-$ and $CdCl_4^{2-}$ allows description of our measurements at $P > 1$ bar within experimental uncertainties (see Fig. 3). This findings are thus in agreement with our structural results from XAFS spectroscopy (Chapter IV, Bazarkina et al., 2009b) indicating that the three Cd-Cl complexes above are tetrahedral in a wide T-P range. According to this model, the partial molal volumes of $CdCl^+$, $CdCl_2^0(aq)$, $CdCl_3^-$ and $CdCl_4^{2-}$ were found to be 2.2±3.0, 42.2±5.0, 63.5±10.0 and 81.3±15.0 cm^3/mol, respectively (Tab. 4). These values are different by 3 to 20 cm^3/mol from those

predicted by Sverjensky et al. (1997). Our new values allow refinement of the P-dependent HKF parameters (a_1, a_2, a_3, a_4) for Cd-Cl species using the revised HKF-model correlations (Tab. 4). The corresponding non-solvation $\Delta_n V^0$ and solvation $\Delta_s V^0$ contributions to the standard partial molal volume V^0 calculated for all Cd-Cl species are given in Tab. 5. The linear correlation between non-solvation input to the molal volume and ligand number is presented in Fig. 5.

These parameters allow far more reliable predictions of Cd-Cl species stabilities and Cd-bearing minerals solubilities at pressures to 5000 bar (i.e., the 'official' pressure limit of the HKF model). The pressure dependence of Cd-Cl complexes calculated with HKF-parameters obtained in this study (Tab. 4) is given in Fig. 4. Our new data for Cd-chloride complexes together with the available thermodynamic properties of Zn-chloride complexes (Sverjensky et al., 1997) permit to estimate, for the first time, the effect of pressure on the Cd content in sphalerite from hydrothermal settings. Our equilibrium calculations indicate that the pressure increase will result in an increase of Cd content in sphalerite in equilibrium with a Cd- and Zn-bearing hydrothermal fluid (Fig. 6). It should be mentioned, however, that more accurate modeling of Cd/Zn ratios and Cd contents in hydrothermal minerals will require more reliable pressure-dependence data for Zn-Cl complexes. Thus, work is currently in progress to refine the only existing theoretical values of partial molal volumes of zinc chloride complexes (Sverjensky et al., 1997) using the experimental and theoretical approaches for cadmium chloride complexes developed in our work.

УДК 553.2:550.4

ПОТЕНЦИОМЕТРИЧЕСКОЕ ИССЛЕДОВАНИЕ УСТОЙЧИВОСТИ ХЛОРИДНЫХ КОМПЛЕКСОВ КАДМИЯ В ЗАВИСИМОСТИ ОТ ДАВЛЕНИЯ (1-1000 БАР) ПРИ 25°C

© 2010 г.   Е.Ф. Базаркина, А.В. Зотов, Н.Н. Акинфиев

Институт геологии рудных месторождений, петрографии, минералогии и геохимии РАН

119017, Москва, Ж-17, Старомонетный пер., 35

Проведены потенциометрические измерения в изотермической цепи с жидкостным соединением с использованием кадмиевого ионно-селективного твердоконтактного измерительного электрода в системе $Cd(NO_3)_2$-KCl-H_2O при 25°C и 1-1000 бар. При давлении 1 бар определена константа равновесия реакции ступенчатого комплексообразования четвертого хлоридного комплекса кадмия $CdCl_4^{2-}$ ($\lg K^0_4$ = -0.88±0.25). Впервые для всех хлоридных комплексов кадмия экспериментально установлены зависимости констант их устойчивости от давления: при увеличении давления от 1 до 1000 бар устойчивость констант образования первого, третьего и четвертого комплексов меняется меньше, чем на 0.05 логарифмической единицы, константа второго комплекса – на 0.33 логарифмической единицы. На основании этих данных были определены значения парциальных мольных объемов четырех хлоридных комплексов кадмия при стандартных условиях: $V^0(CdCl^+)$ = 2.20±3, $V^0(CdCl_{2\ (р-р)})$ = 42.21±5, $V^0(CdCl_3^-)$ = 63.47±10, $V^0(CdCl_4^{2-})$ = 81.35±15 см³·моль⁻¹. Линейная зависимость несольватационных вкладов мольных объемов от числа лигандов нарушается между первым и вторым комплексом. Такое поведение мольных объемов связано со сменой координации от октаэдрической у Cd^{2+} и $CdCl^+$ на тетраэдрическую у $CdCl_{2\ (р-р)}$, $CdCl_3^-$ и $CdCl_4^{2-}$. С использованием корреляционных зависимостей (Shock and Helgeson, 1988) получены HKF-параметры для расчета объемных свойств комплексов кадмия в широком диапазоне температур и давлений. Получены оценки влияния давления на концентрацию кадмия в сфалерите, находящемся в равновесии с H_2O-$NaCl$ гидротермальным флюидом. С ростом давления содержание Cd в сфалерите увеличивается.

_____

Адрес для переписки: А.В. Зотов. E-mail: *azotov@igem.ru*

ВВЕДЕНИЕ

Хлоридные комплексы являются одной из важнейших форм нахождения металлов в природных водах и гидротермальных флюидах (Barnes, 1979). Их устойчивость сильно зависит от температуры (Ruaya and Seward, 1986; Bourcier and Barnes, 1987; Рыженко, Брызгалин, 1987) и, как предполагается, в меньшей степени от давления (Sverjensky et al., 1997). Однако, в работе Дж. Хемли с соавторами (Hemley et al., 1992), экспериментально исследовавших сложную многокомпонентную сульфидно-хлоридную систему в присутствии твердофазных минеральных буферов, было отмечено существенное влияние давления на перенос рудных компонентов и их отложение. Экспериментальные исследования влияния давления на устойчивость хлоридных комплексов проведены только для небольшой группы металлов (Na, K, Li, Rb, Cs, Fe, Mg) и отсутствуют для большинства рудных компонентов. Цель работы – экспериментально проверить теоретические оценки влияния давления (Sverjensky et al., 1997) на примере хлоридных комплексов кадмия.

Кадмий – редкий, рассеянный в природных системах металл подгруппы цинка. Кадмий и цинк, обладая очень близкими химическими свойствами, в большинстве геологических обстановок мигрируют и рассеиваются вместе (Goldschmidt, 1958; Соловов и др., 1990; Иванов, 1997). Однако, различными исследователями было отмечено, что отношение Cd/Zn в гидротермальных рудах варьирует для разных генетических типов руд (напр., Макеев, 1985; Gottesmann and Kampe, 2007). Были предложены геотермометры с использованием Cd-содержащих сфалеритов (Макеев, 1985, Таусон и Чернышев, 1977). Д. Гричуком на основании анализа Cd/Zn отношения в природных объектах было предложено использовать Cd/Zn отношения для определения вклада магматического флюида при образовании гидротермальных месторождений (Гричук, 2005).

Устойчивости хлоридных комплексов кадмия при атмосферном давлении посвящено большое количество экспериментальных исследований, обобщенных в ряде сводных работ: в базах термодинамических данных ТКВ (Глушко, 1972), Critical 1998 (Martell and Smith, 1998) и Slop07, являющийся дополненной версией SupCrt 92 (Johnson et al., 1992; Shock et al., 1997; Sverjensky et al. 1997 и др.), а также в критическом анализе данных NBS, проведенном Д. Арчером (Archer, 1998). Константы устойчивости первых трех комплексов ($CdCl^+$, $CdCl_2$ (р-р) и $CdCl_3^-$) при 25°С и 1 бар находятся в хорошем согласии, тогда как значение термодинамической константы устойчивости четвертого хлоридного комплекса $CdCl_4^{2-}$ дано только в Slop07 по данным Д. Сверженского (Sverjensky et al., 1997), причем оно сильно отличается (на 2 порядка) от результатов П. Рейли и Р. Стокса (Reilly and Stokes, 1970).

По спектрометрическим данным в ряду Cd^{2+} – $CdCl_4^{2-}$ происходит смена координации водных частиц - от октаэдрического иона Cd^{2+} к тетраэдрическому комплексу $CdCl_4^{2-}$ (Caminiti et al., 1980; Mosselmans et al., 1996; Seward and Driesner, 2004; Bazarkina et al., 2009). Переход от октаэдрической к тетраэдрической структуре согласно разным авторам осуществляется либо на втором, либо на третьем комплексе (Ahrland, 1979; Paschina et al, 1983). Интересно сопоставить структурные представления по спектрометрическим данным со значениями мольных объемов на основании потенциометрических измерений.

Таким образом, в настоящем исследовании были поставлены следующие задачи: 1) опробировать потенциометрическую ячейку с твердоконтактным Cd-селективным электродом и определить константу устойчивости четвертого хлоридного комплекса кадмия при

стандартных условиях; 2) экспериментально определить зависимость устойчивости хлоридных комплексов кадмия от давления и получить мольные объемы комплексов, связав их со структурными особенностями; 3) оценить влияние давления на содержание Cd в сфалеритах, находящихся в равновесии с гидротермальным Cl-содержащим флюидом.

МАТЕРИАЛЫ И МЕТОДИКА ЭКСПЕРИМЕНТА

Материалы

Экспериментальные растворы и растворы солевых мостиков приготовлены в моляльной шкале растворением твердых фаз $Cd(NO_3)_2 \times 4H_2O$ и KCl марки х.ч. в дистиллированной воде.

Методика измерений при атмосферном давлении

Использована потенциометрическая ячейка с переносом:

Cu, Ag, Ag$_2$S-CdS	Измеряемый раствор	KCl (3m)	AgCl, Ag, Cu	, (I)
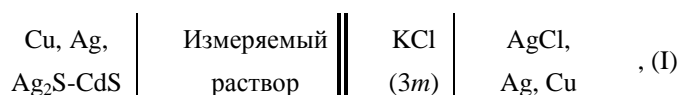
где в качестве измерительного электрода применялся твердоконтактный Cd-селективный электрод с сульфидной мембраной Ag_2S-CdS (ООО «Нико аналит»), а в качестве электрода сравнения − хлорсеребряный электрод, соединенный с измеряемым раствором через солевой мостик 3m KCl. Ячейка калибровалась в растворах $Cd(NO_3)_2$. Получена линейная зависимость электродвижущей силы (ЭДС) от логарифма активности иона кадмия, взятого с отрицательным знаком (-lg a(Cd^{2+}) = pCd) в интервале 10^{-1}-$10^{-5}m$ $Cd(NO_3)_2$ с наклоном S = -29.95 мВ/(ед. pCd) и R$_{коррел.}$ = 0.9998. Полученный наклон калибровочной прямой близок к нернстовскому для двухвалентных катионов (-29.58 мВ/(ед. pCd)).

Для изучения хлоридных комплексов кадмия при атмосферном давлении измерения ЭДС проводились в растворах с постоянной концетрацией $Cd(NO_3)_2$ (0.01m) и переменной концентрацией KCl (0-2m). Для этого в исходный раствор 0.01m $Cd(NO_3)_2$ добавляли измеренные по объему количества раствора, содержащего 0.01m $Cd(NO_3)_2$ и 0.1 или 3.0m KCl, измеряя сдвиг ЭДС. Для пересчета на моляльности использовали плотность растворов KCl (Lide, 2004), пренебрегая присутствием 0.01m $Cd(NO_3)_2$.

В ходе измерений было отмечено «отравление» Cd-селективного сульфидного электрода в концентрированных хлоридных растворах (≥ 1-1.5m KCl), из-за чего показания в этих растворах были нестабильны во времени. «Отравление» вызванно, по-видимому, образованием вторичных фаз на поверхности Cd-селективной мембраны. Поэтому время каждого измерения с сульфидным электродом сокращали, определяя достижение равновесия стабильностью измеряемого значения ЭДС в пределах ±0.2 мВ. Затем электрод промывали дистилированной водой. Работоспособность электрода проверяли по воспроизводимости калибровки. Если наклон калибровки изменялся более чем на 2.0 мВ/(ед. pCd) или калибровка сдвигалась более, чем на 2.0 мВ по E^0, поверхность мембраны очищалась шлифовальной бумагой и проводилась новая калибровка. ЭДС измеряли pH-метром-иономером «Эксперт-001» с точностью ±0.1 мВ. Однако в хлоридных растворах из-за «отравления» Cd-селективной мембраны точность измерений ухудшалась с увеличением концентрации KCl и достигала ±2-3

мВ при концентрациях KCl более 1m. Это было учтено в дальнейших измерениях при повышенных давлениях. При всех измерениях температура 25°C поддерживалась с точностью ±0.5ºC.

Методика измерений при повышенных давлениях

Измерения производили в потенциометрической ячейке (I) используя лабораторную технику и методику, описанные ранее (Зотов и др., 2006). Для работы при повышенных давлениях Cd-селективный электрод был разгружен по давлению посредством резиновой трубки, залитой силиконовым маслом. В качестве электрода сравнения использовали хлорсеребряный электрод специальной конструкции с масляным заполнением, обеспечивающий работу солевого мостика при высоких давлениях (Зотов и др., 2006). Калибровка при повышенных давлениях позволила измерить обратимый сдвиг стандартного потенциала ячейки $\Delta E^0{}_P = E^0{}_P - E^0{}_{P=1}$. При 1000 бар $\Delta E^0{}_P$ составляет 11.4±0.3 мВ, при этом сохраняется наклон, близкий к теоретическому (фиг. 1).

При повышенных давлениях измерения ЭДС проводили в трех растворах с постоянной концентрацией $Cd(NO_3)_2$ 0.01m и концентрацией KCl 0.025, 0.53 и 1.41m. Для повышения точности измерений при повышенных давлениях: 1) использовали не абсолютные значения измеренных ЭДС, а разность между ЭДС при давлении P и 1 бар, тем самым уменьшалась погрешность, связанная с диффузионным потенциалом; и 2) измерения каждого раствора в зависимости от давления (1 − 1000 и 1000 − 1 бар) повторяли 3-4 раза, тем самым уменьшая возможную ошибку из-за «отравления» Cd электрода в хлоридных растворах. Точность измерений при повышенных давлениях составляет ±0.5-0.8 мВ.

Методика расчетов

При анализе полученных экспериментальных данных принимали возможность образования четырех хлоридных комплексов кадмия $CdCl_n^{2-n}$, где $n = 1 − 4$. Реакции ступенчатого комплексообразования и их термодинамические константы равновесия выражены как:

$$Cd^{2+} + Cl^- = CdCl^+ \qquad\qquad (1)$$

$$K^0{}_1 = \frac{[CdCl^+]}{[Cd^{2+}]\cdot[Cl^-]} \cdot \frac{\gamma_{CdCl^+}}{\gamma_{Cd^{2+}} \cdot \gamma_{Cl^-}} \ ,$$

$$CdCl^+ + Cl^- = CdCl_{2\,(p\text{-}p)} \qquad\qquad (2)$$

$$K^0{}_2 = \frac{[CdCl_{2\,(p\text{-}p)}]}{[CdCl^+]\cdot[Cl^-]} \cdot \frac{\gamma_{CdCl_{2(p\text{-}p)}}}{\gamma_{CdCl^+} \cdot \gamma_{Cl^-}} \ ,$$

$$CdCl_{2\,(p\text{-}p)} + Cl^- = CdCl_3^- \qquad\qquad (3)$$

$$K^0_3 = \frac{[CdCl_3^-]}{[CdCl_{2(p-p)}]\cdot[Cl^-]}\cdot\frac{\gamma_{CdCl_3^-}}{\gamma_{CdCl_{2(p-p)}}\cdot\gamma_{Cl^-}} \ ,$$

$$CdCl_3^- + Cl^- = CdCl_4^{2-} \qquad\qquad\qquad (4)$$

$$K^0_4 = \frac{[CdCl_4^{2-}]}{[CdCl_3^-]\cdot[Cl^-]}\cdot\frac{\gamma_{CdCl_4^{2-}}}{\gamma_{CdCl_3^-}\cdot\gamma_{Cl^-}} \ ,$$

где в прямых скобках даны концентрации в моляльной шкале, а γ - коэффициенты активности. Коэффициенты активности заряженных частиц рассчитывали по уравнению Дебая-Хюккеля в третьем приближении:

$$\lg\gamma_i = \frac{-A\cdot Z_i^2\sqrt{I}}{1+B\cdot \mathring{a}_i\sqrt{I}} + b_{KCl}\cdot I \ , \qquad\qquad (5)$$

где A и B – коэффициенты Дебая-Хюккеля для чистого растворителя (Helgeson et al., 1981); I – ионная сила раствора; Z_i – заряд; параметр $\mathring{a}$ принят равным для всех заряженных частиц 4.5Å; b_{KCl} –эмпирический коэффициент «близкодействующих взаимодействий» для KCl (Oelkers and Helgeson, 1990). Коэффициенты активности нейтральных частиц приняты равными 1.

Экспериментальные данные представлены в единицах pCd:

$$pCd = -\lg a(Cd^{2+}) = -\lg[Cd^{2+}] - \lg\gamma_{Cd}^{2+}, \qquad\qquad (6)$$

где $a(Cd^{2+})$, $[Cd^{2+}]$ и $\gamma_{Cd}2+$.– активность свободного иона Cd^{2+}, его концентрация в моляльной шкале и его коэффициент активности, рассчитанный по уравнению (5).

В опытах при атмосферном давлении pCd определяли как:

$$pCd = pCd_{исх} + \Delta pCd = pCd_{исх} + (E - E_{исх})/S \ , \qquad\qquad (7)$$

где $pCd_{исх}$ – рассчитанное значение pCd для исходного $0.01m$ раствора $Cd(NO_3)_2$; E – измеренная ЭДС в растворе $Cd(NO_3)_2$-KCl, $E_{исх}$ – ЭДС в исходном растворе $0.01m$ $Cd(NO_3)_2$; S – нернстовский наклон калибровочной прямой (-29.58 мВ/ед. pCd).

В опытах при повышенном давлении pCd_P определяли как:

$$pCd_P = pCd_{1бар} + \Delta pCd_P = pCd_{1бар} + (\Delta E_P - \Delta E^0_P)/S \ , \qquad\qquad (8)$$

где $pCd_{1бар}$ – рассчитанное значение pCd в растворах $Cd(NO_3)_2$-KCl при давлении 1 бар с использованием констант реакций (1) − (4), принятых в настоящей работе; ΔE_P – измеренная разность ЭДС при давлении P и при давлении 1 бар; ΔE^0_P – разность стандартного потенциала ячейки при давлении P и 1 бар, определенная по сдвигу калибровки; S – нернстовский наклон калибровочной прямой (-29.58 мВ/ед. pCd).

Для расчета термодинамических равновесний применяли программный пакет HCh (Shvarov and Bastrakov, 1999; Шваров, 2008), включающий программу UT-HEL для расчета НКФ параметров состояния водных компонентов (Tanger and Helgeson, 1988) и программу

OptimA для описания экспериментальных данных путем оптимизации свободной энергии водных частиц.

НKF-параметры базовых водных частиц H^+, OH^-, K^+, NO_3^-, $KOH^0_{(p-p)}$, $KCl^0_{(p-p)}$, $HCl^0_{(p-p)}$ и Cd^{2+} взяты из базы термодинамических данных Slop07 (Johnson et al., 1992; Shock et al., 1997; Sverjensky et al., 1997). Стандартные свободные энергии образования ($\Delta_f G^0_{298.15}$) и стандартные энтропии ($S^0_{298.15}$) для $CdCl^+$, $CdCl_2^0{}_{(p-p)}$ и $CdCl_3^-$ были приняты на основании критического термодинамического анализа Д. Арчера (Archer, 1998). Величина и погрешность значения $\Delta_f G^0_{298.15}$ для $CdCl_4^{2-}$ расчитаны с помощью программы OptimA по измерениям в $Cd(NO_3)_2$-KCl растворах при давлении 1 бар при доверительной вероятности 0.95 и с учетом констант образования $CdCl^+$, $CdCl_2^0{}_{(p-p)}$ и $CdCl_3^-$, принятых по Д. Арчеру (Archer, 1998). Статистический вес экспериментальных точек принят равным обратной величине квадрата погрешности экспериментального определения pCd, рассчитанного из уравнения (8).

Использование полученных значений сдвига величин pCd в диапазоне давлений 1 – 1000 бар по (8) позволило оценить параметры уравнения НKF a_1 - a_4 парциальных мольных объемов комплексов. Для этого сначала по экспериментальным данным при 1000 бар с помощью программы OptimA были расчитаны значения $\Delta G^0_{298.15,\ 1000\ бар}$ четырех хлоридных комплексов кадмия. Затем, используя очередное приближение для мольного объема комплекса при стандартных условиях с использованием программы UT-HEL (Шваров, 2008) оптимизировали параметр a_1 этого комплекса и рассчитывали соответствующий этому новому значению новую величину $V^0_{298.15}$. По найденному таким образом значению $V^0_{298.15}$, используя корреляции НKF-модели (Shock and Helgeson, 1988), определяли новые параметры a_1 - a_4. Процедуру оптимизации параметра a_1 повторяли до тех пор, пока на очередной итерации изменение мольного объема комплекса не превышало 0.05 см^3·моль$^{-1}$.

Возвращаясь к оптимизации $\Delta G^0_{298.15,\ 1000\ бар}$, следует отметить, что из-за трудностей оптимизации при большом числе параметров (4 свободные энергии Гиббса) и небольшом количестве экспериментальных точек (3 раствора) было введено дополнительное ограничение – линейная зависимость несольватационных вкладов в мольные объемы ($\Delta_n V^0_{298.15}$) от числа лигандов (n) (Hovey, 1988). При этом было использовано несколько моделей: линейность для всех частиц (ион Cd^{2+} и четыре хлоридных комплекса кадмия), только для 2-4 комплексов и т.д. Мольный объем иона Cd^{2+} ($n = 0$) известен (Shock et al., 1997) и пересмотру не подвергался. Расчет по моделям проводился методом итераций таким образом, чтобы с одной стороны, значения $\Delta G^0_{298.15,\ 1000\ бар}$ четырех хлоридных комплексов кадмия наилучшим образом описывали экспериментальные данные при давлении 1000 бар, а с другой стороны, чтобы соответствующие значения $\Delta_n V^0_{298.15}$ несольватационных вкладов отвечали выбранной линейной зависимости от числа лигандов.

Несольватационный вклад в мольный объем расчитывали по формуле:

$$\Delta_n V^0_{298.15} = V^0_{298.15} - \Delta_s V^0_{298.15} , \hspace{3cm} (9)$$

где $V^0_{298.15}$ – стандартный мольный объем комплекса; $\Delta_s V^0_{298.15}$ - сольватационный вклад в мольный объем, рассчитанный как $\Delta_s V^0_{298.15} = -\omega Q$, где ω- коэффициент Борна, а Q – функция Борна для мольного объема ($Q = 2.4685 \cdot 10^5$, Tanger and Helgeson, 1988).

Для оценки значения стандартной энтропии $CdCl_4^{2-}$ была использована эмпирическая линейная корреляция несольватационного вклада в энтропию от числа лигандов. Несольватационный вклад в энтропию расчитывали по формуле:

$$\Delta_n S^0_{298.15} = S^0_{298.15} - \Delta_s S^0_{298.15} \qquad , \qquad\qquad (10)$$

где $S^0_{298.15}$ – стандартная энтропия, $\Delta_s S^0_{298.15}$ - сольватационный вклад в энтропию, расчитанный как $\Delta_s S^0_{298.15} = \omega \cdot Y$, где ω- коэффициент Борна, а Y – функция Борна для энтропии ($Y = -5.81 \cdot 10^5$, Tanger and Helgeson, 1988).

Значения ω для хлоридных комплексов были определены с помощью программы UT-HEL (Шваров, 2008) по корреляции ω с энтропией (Shock et al., 1989). Значения теплоемкости и параметры c_1, c_2 были взяты по литературным данным (Sverjensky et al., 1997). Эти параметры не связаны с давлением, роли которого посвящено настоящее исследование, однако они нуждаются в ревизии в связи с пересмотром значений стандартных свободных энергий и энтропий хлоридных комплексов кадмия (Archer, 1998; Bazarkina et al. 2009b).

РЕЗУЛЬТАТЫ ИЗМЕРЕНИЙ ПРИ ДАВЛЕНИИ 1 БАР

Результаты экспериментальных измерений при атмосферном давлении приведены в табл. 1. Увеличение концентрации KCl до $2m$ приводит к уменьшению активности свободного иона Cd^{2+} на 3 порядка вследствие образования хлоридных комплексов кадмия. При концентрациях хлора $>1.8m$ измеренные значения pCd выходят за нижний предел чувствительности измерительного электрода ($10^{-5}m$ Cd^{2+}). Однако, в работах Е. Бауман (Baumann, 1971) и Д. Рожковой с соавторами (Рожкова и др., 2009) было показано, что в присутствии комплексообразователя ионоселективные электроды работают обратимо до очень низких концентраций измеряемого иона (до 10^{-8} – $10^{-9}m$), если общая концентрация этого элемента в растворе достаточно высока (10^{-3} – $10^{-4}m$).

Экспериментальные результаты (pCd) хорошо описываются с использованием констант устойчивости первых трех хлоридных комплексов кадмия, принятых по Д. Арчеру (Archer, 1998). При более высоких концентрациях KCl необходимо учитывать четвертый хлоридный копмлекс. Результаты оптимизации $\Delta_f G^0_{298.15}$ четвертого хлоридного комплекса кадмия показаны на фиг. 2 и представлены в виде константы устойчивости в табл. 2 в сравнении с литературными данными. Полученная константа устойчивости $CdCl_4^{2-}$ составляет -0.88±0.25 логарифмической единицы, что на ~2 порядка выше константы предложенной П. Рейли и Р. Стоксом (Reilly and Stokes, 1970) и в пределах погрешности совпадает с величиной, предложенной Д. Сверженским (Sverjensky et al., 1997). При максимальной концентрации KCl ($2m$) комплекс $CdCl_4^{2-}$ составляет 20% от общей концентрации растворенного кадмия.

Полученные результаты показывают возможность использования Cd-селективного электрода с сульфидной мембраной $CdS-Ag_2S$ в хлоридных растворах, однако возможность применения такой потенциометрической ячейки ограничивается небольшой продолжительностью (1-2 часа) и сравнительно невысокой концентрацией хлоридов ($\leq 2m$), причем при концентрациях $>1m$ время нахождения Cd-селективного электрода в растворе рекомендуется сокращать до минимального (см. Методику измерений при давлении 1 бар).

Указанные ограничения, связанны с «отравлением» поверхности мембраны Cd-селективного сульфидного электрода.

РЕЗУЛЬТАТЫ ИЗМЕРЕНИЙ ПРИ ПОВЫШЕННЫХ ДАВЛЕНИЯХ 1-1000 БАР

Результаты измерений при давлениях 1-1000 бар в трех растворах $Cd(NO_3)_2$ содержащих 0.025, 0.53 и 1.41m KCl, приведены в табл. 3. Изменения pCd при увеличении давления отражают зависимость констант устойчивости хлоридных комплексов кадмия от давления. Максимальное изменение pCd по сравнению с атмосферным давлением (ΔpCd_P = -0.16±0.03) было получено для раствора 1.41m KCl при давлении 1000 бар. Изменение pCd в первом растворе (0.025m KCl) находится в пределах погрешности измерений и принято равным нулю при всех давлениях (до 1000 бар). Для двух других растворов зависимости ΔE_P и ΔpCd_P от давления близки к линейным. Для оптимизации свободных энергий Гиббса хлоридных комплексов кадмия были использованы значения ΔpCd_P, отвечающие максимальным изменениям при давлении 1000 бар.

Из-за трудностей оптимизации при большом числе оптимизируемых параметров ($\Delta G^0_{298.15, 1000\ бар}$ четырех комплексов) и малом количестве экспериментальных точек (ΔpCd_P при 1000 бар для трех растворов) было введено дополнительное ограничение – линейность зависимости несольватационных вкладов в мольные объемы иона и хлоридных комплексов кадмия от числа лигандов. При этом рассматривали 3 модели: 1) линейность для всех хлоридных комплексов с ионом Cd^{2+}, что соответствует предположению об одинаковой (октаэдрической) координации всех водных частиц кадмия; 2) линейность для иона и первых двух комплексов, что соответствует смене координации (на тетраэдрическую) при образовании третьего хлоридного комплекса; 3) линейность для второго, третьего и четвертого комплексов что соответствует смене координации (на тетраэдрическую) при образовании второго хлоридного комплекса. Сравнение результатов расчета, соответствующих этим моделям, с экспериментальными данными и расчетом по данным Slop 07 (Shock et al., 1997; Sverjensky et al., 1997) представлены на фиг. 3. Наилучшим образом экспериментальные данные описываются с помощью модели 3 (фиг. 2б и 3). Описания по другим моделям не укладываются в пределы экспериментальной ошибки.

Зависимость констант ступенчатого комплексообразования от давления представлена на фиг. 4. Наши данные подтверждают предсказанную теоретически слабую зависимость устойчивости хлоридных комплексов кадмия от давления (Sverjensky et al., 1997). Для первого, третьего и четвертого комплекса при при 25°C с увеличением давления от 1 до 1000 бар значения их констант устойчивости меняются меньше, чем на 0.05 логарифмической единицы. Для второго хлоридного комплекса кадмия влияние давления значительно сильнее: с увеличением давления от 1 до 1000 бар значение его константы устойчивости уменьшается на 0.33 логарифмической единицы, при увеличении давления до 2000 бар – на 0.58 логарифмической единицы.

Найденные значения мольных объемов и HKF параметров приведены в табл. 4. Линейная зависимость несольватационной составляющей мольного объема хлоридных комплексов кадмия ($\Delta_n V°$, табл. 5) от числа лигандов (n) нарушается между n равным 1 и 2 (фиг. 5). Скачок в значении несольватационного вклада отвечает смене координации при

переходе от CdCl$^+$ к CdCl$_2$ $_{(р-р)}$. Подобное скачкообразное изменение мольных объемов при смене координации было описано для ионов (Swaddle and Mak, 1983). Наши данные по мольным объемам комплексов подтверждают переход от октаэдрической к тетраэдрической структуре на втором хлоридном комплексе кадмия, как было предположено по спектрометрическим измерениям (Bazarkina et al., 2010).

ОЦЕНКА ВЛИЯНИЯ ДАВЛЕНИЯ НА СОДЕРЖАНИЕ Cd В СФАЛЕРИТЕ

Известны попытки рассматривать величину Cd/Zn в сфалерите как генетический индикатор рудоотложения (Jonasson and Sangsyer, 1978; Xuexin, 1984; Gottesmann and Kampe, 2007). Отмечалось, что более низкие содержания Cd характерны для сфалеритов из руд в вулканогенно-осадочных породах, тогда как относительно высокие концентрации Cd наблюдаются в сфалеритах из более глубинных магматических месторождений. В связи с этим мы попытались оценить роль давления при вхождении Cd в сфалериты, находящиеся в равновесии с гидротермальным флюидом.

При расчете использованы следующие термодинамические данные: для хлоридных комплексов кадмия – из табл. 4, для хлоридных комплексов цинка – согласно рекомендации Д.Сверженского (Sverjensky et al., 1997), для твердых фаз (ZnS и CdS) – из сводки Р. Роби и Б. Хемингуэя (Robie and Hemingway, 1995). Поскольку барические свойства хлоридных комплексов цинка не обоснованы экспериментально, а даны лишь на основании корреляционных соотношений (Sverjensky et al., 1997), приведенные ниже расчеты следует рассматривать как первые ориентировочные оценки.

Равновесие между ZnS и CdS описывается реакцией:

$$ZnS_{\text{тв. р-р}} + CdCl_j^{2-j} = CdS_{\text{тв. р-р}} + ZnCl_i^{2-i} + (i-j)Cl^- , \qquad (11)$$
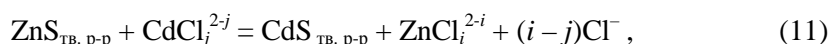
где ZnS$_{\text{тв. р-р}}$ и CdS$_{\text{тв. р-р}}$ - компоненты твердого раствора Cd-сфалерита, а CdCl$_j^{2-j}$ и ZnCl$_i^{2-i}$ – превалирующая форма Cd и Zn в гидротермальном флюиде при заданной концентрации NaCl. Выражение для термодинамической константы равновесия реакции (11) в предположении идеальности твердого раствора имеет вид:

$$\lg K_{11}^0 = \lg\left(\frac{x}{1-x} \cdot \frac{a_{ZnClj}}{a_{CdCli}} \cdot a_{Cl}^{i-j} \right) , \qquad (12)$$

где x – мольная доля CdS в сфалерите, a_{ZnClj} и a_{CdCli} – активности превалирующих форм Zn и Cd во флюиде, а a_{Cl} – активность иона Cl$^-$ в гидротермальном растворе. Таким образом, при заданном соотношении активностей Zn и Cd и фиксированной активности Cl$^-$ в растворе мольная доля CdS в сфалерите определяется как:

$$\lg x = \lg K_{11}^0 - \lg\left(K_{11}^0 + \frac{a_{ZnCl_j}}{a_{CdCl_i}} \cdot a_{Cl}^{i-j} \right) . \qquad (13)$$

Проведенные нами оценочные расчеты показали, что в гидротермальных растворах в диапазоне температур T = 150-300°C и концентраций m_{NaCl} = 0.1-1m превалирующими формами Zn и Cd являются соответственно ZnCl$^+$ (i = 1) и CdCl$_3^-$ (j = 3). Расчет константы равновесия реакции (11) в этом случае свидетельствует о заметной роли давления на состав твердого

раствора, причем влияние давления противоположно влиянию температуры. Принимая весовое отношение Cd/Zn=0.04 (характерное значение для вулканических газов (Taran et al., 1995)) в растворе постоянным, при концентрации NaCl 0.5m получим, что при 300°C равновесное содержание CdS в сфалерите возрастает на порядок с ростом давления от 85 до 2000 бар (фиг. 6а). Увеличение температуры при постоянном давлении (1000 бар), напротив, понижает мольную долю CdS в сфалерите, равновесном с хлоридным флюидом (0.5m NaCl) с тем же Cd/Zn отношением (0.04) (фиг. 6б). Важно отметить, что концентрация NaCl, контролируя превалирующие формы хлоридных комплексов Cd и Zn, сильно влияет на величину равновесной мольной доли CdS в сфалерите, но общая закономерность – возрастание равновесного содержания CdS с давлением – сохраняется.

Очевидно, что равновесное содержание Cd в сфалерите сильно зависит и от соотношения Cd/Zn во флюиде. Наши оценки проказывают, что при одинаковом изначальном отношении Cd/Zn во флюиде и близких температурах, гидротермальные сфалериты при более высоких давлениях будут содержать более высокую мольную долю Cd. Таким образом, давление может быть одним из важных факторов, влияющих на распределение кадмия в гидротермальных сфалеритах (Jonasson and Sangster, 1978; Xuexin, 1984; Gottesmann and Kampe, 2007).

ЗАКЛЮЧЕНИЕ

Если рассматривать металлы второй группы периодической системы, то проведенная работа является первой попыткой экспериментально исследовать барические свойств полного набора хлоридных комплексов (n=1-4) Потенциометрическим методом была изучена устойчивость всех четырех комплексов кадмия в зависимости от давления и определены их парциальные мольные объемы. Установлено соответствие измеренных мольных объемов комплексов с их структурой, определенной спектрометрическими методами, - со сменой от октаэдрической к тетраэдрической координации в ряду $Cd^{2+} - CdCl_4^{2-}$.

Константы устойчивости хлоридных комплексов кадмия относительно слабо зависят от давления. В целом, наши экспериментальные данные подтвердили теоретические предсказания Д. Сверженского (Sverjensky et al., 1997). По-видимому, данные Д. Сверженского могут быть успешно использованы для оценочных термодинамических расчетов по влиянию давления.

Приближенные расчеты равновесного распределения кадмия между гидротермальным флюидом и сфалеритом, несмотря на ряд сделанных допущений, показали, что давление может влиять на содержание Cd в сфалерите. Однако, для более точных расчетов, необходимо прежде всего уточнить мольные объемы хлоридных комплексов цинка.

БЛАГОДАРНОСТИ

СПИСОК ЛИТЕРАТУРЫ

Глушко В.П. и др. Термические константы веществ. М.: Изд-во ВИНИТИ, 1972. Выпуск VI. Часть 1. (http://www.chem.msu/sgi-bin/tkv.pl).

Гричук Д.В. Отношение Cd/Zn как индикатор вклада магматических флюидов в питание гидротермальных систем // Докл. VII Междунар. конф. «Новые Идеи в Науках о Земле». М.: Изд-во КДУ, 2005. Т. 2. С. 83.

Зотов А.В., Королева Л.А., Осадчий Е.Г. Потенциометрическое изучение стабильности ацетатных комплексов европия в зависимости от давления (1 – 1000 бар) при 25°C // Геохимия. 2006. № 4. С. 384-394.

Иванов В.В. Экологическая геохимия элементов. Книга 5 «Редкие d-элементы». М.: Экология, 1997.

Макеев А.Б. Изоморфизм кадмия и марганца в сфалерите. Л.: Наука, 1985.

Рожкова Д.В., Зотов А.В., Базаркина Е.Ф. Нижний предел сохранения линейной зависимости E-pX ионоселективных электродов в присутствии комплексообразователя (на примере фторидселективного электрода) // Докл. IX Междунар. конф. «Новые Идеи в Науках о Земле». М.: Изд-во РГГРУ, 2009. Т. 3. С. 286.

Рыженко Б.Н., Брызгалин О.В. Электролитическая диссоциация кислот в условиях гидротермального процесса // Геохимия. 1987. № 1. С. 137-142.

Соловов А.П., Архипов А.Я., Бугров В.А. и др. Справочник по геохимическим поискам полезных ископаемых. М: Недра, 1990.

Таусон В.Л., Чернышев Л.В. Исследование фазовых отношений и структурных особенностей смешанных кристаллов в системе ZnS-CdS // Геохимия. 1977. № 9. С. 1299-1311.

Шваров Ю.С. HCh: Новые возможности термодинамического моделирования геохимических систем, предоставляемые Windows // Геохимия. 2008. № 8. С. 834-839.

Archer D. Thermodynamic properties of import to environmental processes and remediation. I. Previous thermodynamic property values for cadmium and some of its compounds // J. Phys. Chem. Ref. Data. 1988. V. 27. P. 915-946.

Arhland S. Complex Formation in protic and aprotic media // Pure Appl. Chem. 1979. V. 51. P. 2019-2039.

Bazarkina E.F., Pokrovsky G.S., Zotov A.V. Structure and stability of cadmium chloride complexes in hydrothermal fluids // Chemical Geol. 2010 (в печати).

Barnes H.L. Solubilities of ore minerals // Geochemistry of hydrothermal ore deposits. New York: Wiley, 1979. 2nd edition. P. 404-459.

Baumann E.W. Sensitivity of the fluoride-selective electrode below micromolar range // Analyt. Chim. Acta. 1971. V. 54. P. 89-197.

Bourcier W. L., Barnes H. L. Ore solution chemistry-VII. Stabilities of chloride and bisulfide complexes of zinc to 350°C // Econ. Geol. 1987. V. 82. P. 1839–1863.

Caminiti R., Licheri G., Paschina G. et al. X-ray diffraction and structural properties of aqueous solutions of divalent metal-chlorides // Z. Naturforsch. 1980. V. 35a. P. 1361-1367.

Goldschmidt V.M. Geochemistry. London: Oxford University Press, Amen House: 1958.

Gottesmann W., Kampe A. Zn/Cd ratios in calsilicate-hosted sphalerite ores at Tumurtijn-ovoo, Mongolia // Chemie der Erde (=Chem. Erde – Geochem). 2007. V. 67. P. 323 – 328.

Hovey. J. K. Thermodynamics of aqueous solutions: Ph. D. dissertation. Edmonton, Canada, Univ. Albertta: 1988.

Helgeson H.C., Kirkham D.H., Flowers G.C. Theoretical prediction of the thermodynamic behaviour of aqueous electrolytes at high pressures and temperatures: IV. Calculation of activity coefficients, osmotic coefficients, and apparent molal and standard and relative partial molal properties to 600°C and 5 kbar. Amer. J. Sci. 1981. V. 281. P. 1249-1561.

Hemley J.J., Cygan G.L., Fein J.B. et al. Hydrothermal ore-forming processes in the light of studies in rock-buffered systems // Econ. Geol. 1992. V. 87. P. 1-43.

Johnson J.W., Oelkers E.H., Helgeson H.C. SUPCRT92: a software package for calculating the standard molal thermodynamic properties of minerals, gases, aqueous species, and reactions from 1 to 5000 bar and 0 to 1000°C // Comput. Geosci. 1992. V. 18. P. 899-947.

Jonasson I.R., Sangster D.F. Zn:Cd ratios for sphalerites separated from some Canadian sulphide ore samples. Paper Geol. Surv. Can. 1978.V. 78-1B. P. 195-201.

Lide D.R. (ed.) Handbook of geochemistry and physics. Boca Raton: CRS Press, 2004. 84th edition.

Martell E., Smith R.M. Critically selected stability constants of metal complexes, NIST standard reference database 46, Version 5.0. Gaithersburg: NIST. 1998. MD 20899.

Mosselmans J.F.W., Schofield P.F., Charnock J.M. et al. X-ray absorption studies of metal complexes in aqueous solution at elevated temperatures // Chem. Geol. 1996. V. 127. P. 339-350.

Oelkers E.H., Helgeson H.C. Triple-ion anions and polynuclear complexing in supercritical electrolyte solutions // Geochim. et Cosmochim. Acta. 1990. V. 54. P. 727-738.

Paschina G., Piccaluga G., Pinna G., Magini M. Chloro-complexes formation in $ZnCl_2$-$CdCl_2$ aqueous solutions : An x-ray diffraction study. J. Chem. Phys. 1983. V. 78. P. 5745-5749.

Reilly P.J., Stokes R.H. The activity coefficients of cadmium chloride in water and sodium chloride solutions at 25°C // Aust. J. Chem. 1970. V. 23. P. 1397-1405.

Robie R.A., Hemingway B.S. Thermodynamic properties of minerals and related substances at 298.15 and 1 bar (105 pascals) pressure and at high temperatures // U. S. Geol. Surv. Bull. 2131. 1995.

Ruaya, J. R., Seward, T. M. The stability of chloro-zinc (II) complexes in hydrothermal solutions up to 350°C // Geochim. et Cosmochim. Acta. 1986. V. 50. P. 651–662.

Seward T.M., Driesner T. Hydrothermal solution structure: experiments and computer simulations // Aqueous systems at elevated temperatures and pressures: physical chemistry in water, steam and hydrothermal solutions. London: Elsevies Ltd., 2004. P. 149-182.

Sharps J.A., Brown Jr. G.E., Stebbins J.F. Kinetics and mechanism of ligand exchange of Au(III), Zn(II), and Cd(II) chlorides in aqueous solutions: an NMR study from 28-98°C // Geochim. et Cosmochim. Acta. 1993. V. 57. P. 721-731.

Shock E.T., Helgeson H.C. Calculation of the thermodynamic and transport properties of aqueous species at high pressures and temperatures: correlation algorithms for ionic species and equation of state prediction to 5 kb and 1000°C // Geochim. et Cosmochim. Acta. 1988. V. 52. P. 2009-2036.

Shock E.L., Helgeson H.C., Sverjensky D.A. Calculation of the thermodynamic and transport properties of aqueous species at high pressures and temperatures: standard partial molal properties of inorganic neutral species // Geochim. et Cosmochim. Acta. 1989. V. 53. P. 2157-2183.

Shock E.L., Sassani D.C., Willis M., Sverjensky D.A. Inorganic species in geologic fluids: Correlations among standard molal thermodynamic properties of aqueous ions and hydroxide complexes // Geochim. et Cosmochim. Acta. 1997. V. 61. P. 907-950.

Shvarov Yu. S., Bastrakov E.N. HCh: a software package for geochemical equilibrium modelling. User's Guide. Canberra: Australian Geological Survey Organization, 1999. Record 199/25.

Sverjensky D.A., Shock E.L. Helgeson H.C. Prediction of the thermodynamic properties of aqueous metal complexes to 1000°C and 5 kb // Geochim. et Cosmochim. Acta. 1997. V. 61. P. 1359-1412.

Swaddle T.W., Mak M.S. The partial molar volumes of aqueous metal cations: their prediction and relation to volumes of activation for water exchange // Canad. J. Chem. 1983. V. 61. P. 473-480.

Taran Y.A., Hedenquist J.F., Korzhinsky M.A. et al. Geochemistry of magmatic gases from Kudryavy volcano, Iturup, Kuril islands // Geochim. et Cosmochim. Acta. 1995. V. 59. P. 1749–1761.

Tanger J.C., Helgeson H.C. Calculation of the thermodynamic and transport properties of aqueous species at high pressures and temperatures: revised equation of state for the standard partial properties of ions and electrolytes // Amer. J. Sci. 1988. V. 288. P. 19-98.

Vanderzee C.E., Dawson H.J. The stability constants of cadmium chloride complexes: variation with temperature and ionic strength // J. Amer. Chem. Soc. 1953. V. 75. P. 5659-5663.

Von Damm K.L. Seafloor hydrothermal activity: black smoker chemistry and chimneys. Annu. Rev. Earth Planet. Sci. 1990. V. 18. P. 173-204.

Xuexin, S. Minor elements and ore genesis of the Fankou lead-zinc deposits, China. Mineral. Deposita. 1984. V. 19. P. 95-104.

Table 1. Potentiometric measurements in $Cd(NO_3)_2$-KCl solutions as a function of KCl concentration at 25°C and 1 bar (Run 1).

mCd(NO$_3$)$_2$	mKCl	$E - E_{init}$, мВ	ΔpCd	pCd = pCd$_{init.}$ + ΔpCd
0.0100	0	0	0	2.281*
0.0100	0.0032	-1.4	0.03	2.31
0.0100	0.011	-5.1	0.15	2.43
0.0100	0.025	-10.7	0.34	2.62
0.0100	0.040	-14.7	0.47	2.75
0.0100	0.099	-25.1	0.82	3.10
0.0100	0.21	-35.8	1.18	3.46
0.0100	0.36	-45.0	1.48	3.77
0.0100	0.54	-52.7	1.74	4.02
0.0100	0.70	-57.7	1.90	4.18
0.0100	0.85	-62.0	2.03	4.31
0.0100	1.04	-64.7	2.11	4.39
0.0100	1.30	-70.5	2.30	4.58
0.0100	1.50	-77.4	2.47	4.75
0.0100	1.66	-81.4	2.61	4.89
0.0100	1.80	-84.6	2.73	5.01
0.0100	1.92	-86.8	2.83	5.11
0.0100	2.02	-88.6	2.94	5.22
Uncertainty		±0.9-3.0**	±0.03-0.10**	±0.03-0.10**

* pCd$_{init.}$ − calculated using Slop07 database (Johnson *et al*., 1992; Shock *et al*., 1997; Sverjensky *et al*., 1997) ;

** Uncertainty increases with increasing mKCl (see in the main text for details).

Table 2. Stepwise stability constants of cadmium chloride complexes at 25°C and 1 bar.

lg K^0_1	lg K^0_2	lg K^0_3	lg K^0_4	Reference
2.00	0.70	-0.59	-	Vanderzee, Dawson, 1953
1.93	0.43	-0.28	-3.37	Reilly, Stokes, 1970
1.96	0.62	-0.62	-	TKV Database (Glushko et al., 1972)
1.97	0.62	-0.18	-0.93	Slop07 (Sverjensky *et al.*, 1997)
1.98±0.03	0.62±0.10	-0.20±0.15	-	Critical Database (Martell, Smith, 1998)
1.97	0.64	-0.63	-	Archer, 1998 (NBS critical review)
1.97*	**0.64***	**-0.63***	**-0.88±0.25****	**This study**

* Taken from Archer (1998);
** The value of lg K^0_4 was obtained by Gibbs free energy optimization of $CdCl_4^{2-}$ complex from the experimental data derived in this study (Table 1) and assuming the values of stability constants K^0_1, K^0_2, K^0_3 from Archer (1998). Calculations were performed using the OptimA program (Shvarov, 2008).

Table 3. Potentiometric measurements in $Cd(NO_3)_2$-KCl solutions at 25°C as a function of pressure (1 – 1000 bar).

P, бар	ΔE^0_P, мВ	ΔE_P, мВ	$\Delta E_P - \Delta E^0_P$, мВ	ΔpCd_P	pCd_P
Run 2: 0.01m Cd(NO$_3$)$_2$ - 0.025m KCl					
1	0	0	0.0	0.0	2.613*
200	-2.3	-2.3	0.0	0.0**	2.613
500	-5.7	-5.3	0.4	0.0**	2.613
700	-8.0	-8.1	-0.1	0.0**	2.613
900	-10.3	-10.0	-0.3	0.0**	2.613
1000	-	-	-	0.0**	2.613
Uncertainty	±0.3	±0.5	±0.8	±0.027	±0.027
Run 3: 0.01m Cd(NO$_3$)$_2$ - 0.53m KCl					
1	0	0.0	0.0	0.0	4.077*
200	-2.3	-1.7	0.6	-0.020	4.058
500	-5.7	-4.3	1.4	-0.047	4.031
700	-8.0	-6.0	2.0	-0.067	4.011
900	-10.3	-7.7	2.6	-0.087	3.991
1000	-11.4	-8.6	2.8	-0.095	3.983
Uncertainty	±0.3	±0.2	±0.5	±0.017	±0.033
Run 4: 0.01m Cd(NO$_3$)$_2$ - 1.41m KCl					
1	0	0	0.0	0.0	4.948*
200	-2.3	-1.4	0.9	-0.032	4.916
500	-5.7	-3.6	2.3	-0.078	4.870
700	-8.0	-4.9	3.2	-0.110	4.838
900	-10.3	-6.1	4.2	-0.141	4.807
1000	-11.4	-6.8	4.6	-0.156	4.792
Uncertainty	±0.3	±0.2	±0.5	±0.017	±0.033

* Calculated with stability constants derived in this study (Tab. 2).

Table 4. HKF parameters of cadmium chloride complexes.

HKF parameter	$CdCl^+$	$CdCl_{2\ p-p}$	$CdCl_3^-$	$CdCl_4^{2-}$
$\Delta_f G^0_{298.15}$, cal $\cdot$ mol^{-1}	-52629[1]	-84883[1]	-115399[1]	**-145583**
$S^0_{298.15}$, cal $\cdot$ mol$^{-1}\cdot$K^{-1}	7.06[1]	25.72[1]	45.15[1]	50.61[2]
$C^0p_{298.15}$, cal $\cdot$ mol$^{-1}\cdot$K^{-1}	11.1[3]	116.0[3]	97.8[3]	42.5[3]
$V^0_{298.15}$, cm$^3\cdot$ mol^{-1}	**2.20**	**42.21**	**63.47**	**81.35**
$a_1\times10$, cal $\cdot$mol$^{-1}\cdot$bar^{-1}	**2.2303**	**7.5221**	**10.8045**	**13.8329**
$a_2\times10^{-2}$, cal $\cdot$ mol^{-1}	**-2.3357**	**10.5852**	**18.5994**	**25.9938**
a_3, cal $\cdot$K$\cdot$ mol$^{-1}\cdot$bar^{-1}	**6.6681**	**1.5895**	**-1.5605**	**-4.4669**
$a_4\times10^{-4}$, cal $\cdot$K$\cdot$ mol^{-1}	**-2.6824**	**-3.2166**	**-3.5479**	**-3.8536**
c_1, cal $\cdot$mol$^{-1}\cdot$K^{-1}	16.6729[3]	73.7011[3]	72.0276[3]	53.6809[3]
$c_2\times10^{-4}$, cal $\cdot$K$\cdot$ mol^{-1}	-0.7693[3]	20.5956[3]	16.8832[3]	5.6267[3]
$\omega\times10^{-5}$, cal $\cdot$mol^{-1}	0.4372[4]	-0.0495[4]	0.9378[4]	2.4766[4]

In bold − HKF parameters obtained from experimental data derived in this study; the others – the revised literature data and HKF model correlations.

[1] Taken from Archer (1998);

[2] Calculated from linear correlation between non-electrostatic contribution of entropy $\Delta_n S°_{298.15}$ ($\Delta_n S^0_{298.15} = S^0_{298.15} - \Delta_s S^0_{298.15}$) and ligands number ($n$) for $n = 0$ to 3 (Cd^{2+}, $CdCl^+$, $CdCl_2(aq)$), and extrapolated to $n = 4$ ($CdCl_4^{2-}$);

[3] Calculated using experimental data of Bazarkina et al. (2009);

[4] Calculated using the correlation of ω with $S^0_{298.15}$ (Shock and Helgeson, 1988).

Table 5. Standard partial molal volumes $V^0_{298.15}$ for cadmium ion and chloride complexes with corresponding solvation and nonsolvation contributions

Species	Born parameter	Molal volume, cm³/mol		
	$\omega \times 10^{-5}$, cal·mol^{-1}	$V^0_{298.15}$	$\Delta_s V^0_{298.15}$ [2]	$\Delta_n V^0_{298.15}$ [3]
Cd^{2+}	1.2528[1]	-16.00 [4]	-3.09	-12.91
$CdCl^+$	0.5394[1]	2.20±3.00	-1.08	3.27±3.00
$CdCl_{2\ (p-p)}$	-0.038[1]	42.21±5.00	0.12	42.09±5.00
$CdCl_3^-$	1.4662[1]	63.47±10.00	-2.31	65.78±10.00
$CdCl_4^{2-}$	3.206[1]	81.35±15.00	-6.11	87.46±15.00

[1] Calculated using the correlation of ω· with $S^0_{298.15}$ (Shock and Helgeson, 1988);

[2] Solvation contribution to the molal volume calculated as $\Delta_s V^0_{298.15} = \omega\ Q = -\omega \times 2.4685 \times 10^5$ (Tanger and Helgeson, 1988);

[3] Nonsolvation contribution to the molal volume $\Delta_n V^0_{298.15} = V^0_{298.15} - \Delta_s V^0_{298.15}$ (Tanger and Helgeson, 1988);

[3] Taken from Shock et al. (1997).
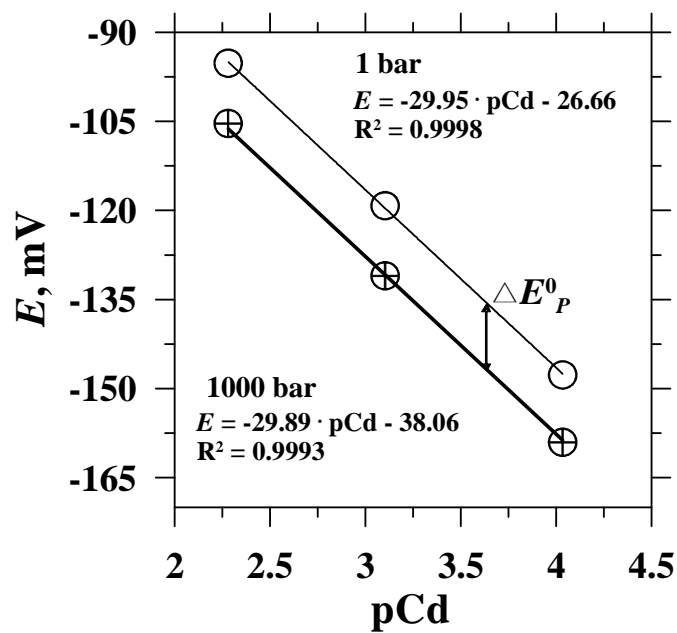
Fig. 1. Calibration curves of the Cd-selective electrode at 25°C and pressures 1 and 1000 bar. ΔE^0_P denotes the pressure-dependent change in the standard potential ($\Delta E^0_P = E^0_P - E^0_{P=1}$), at 1000 bar ΔE^0_P is -11.4±0.3 mV. R^2 represents the squared correlation coefficient.

(a) **(b)**
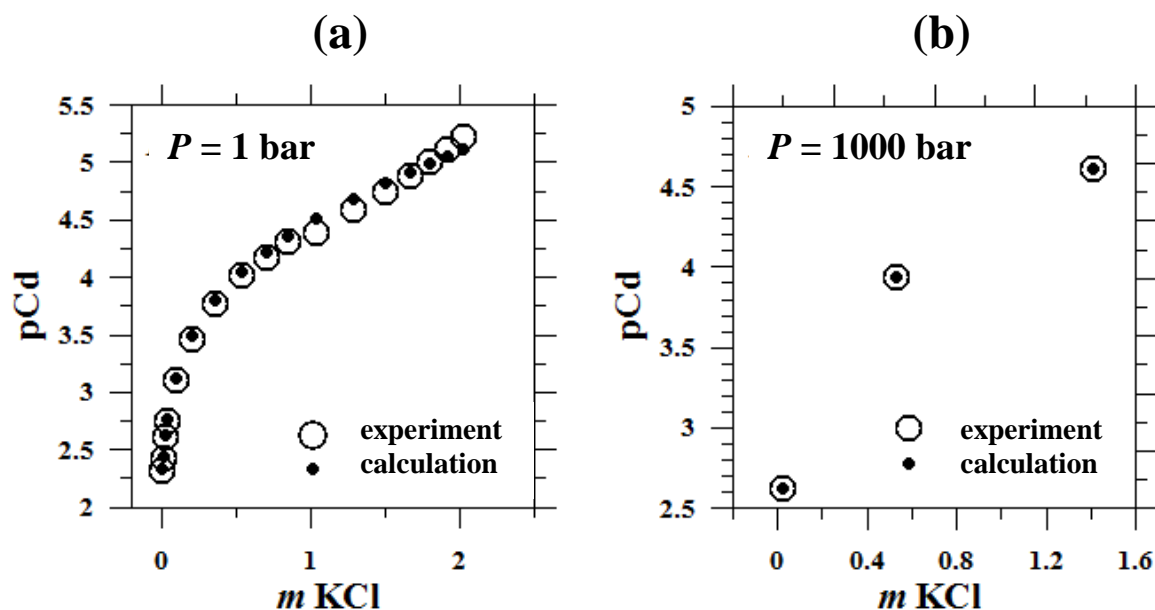
Fig. 2. pCd as a function of KCl concentration at 1 bar (a) and 1000 bar (b). The empty circles represent the experimental data and the filled circles represent the pCd calculated in the OptimA program (Shvarov, 2008). At 1 bar, the Gibbs free energy of $CdCl_4^{2-}$ was optimized using the experimental data derived in this study (Tab. 1) and the Gibbs free energy of $CdCl_1^{+}$, $CdCl_2^{0}$, $CdCl_3^{-}$, and $CdCl_4^{2-}$ taken from Archer (1998). At 1000 bar, free Gibbs energy of four cadmium chloride complexes were optimized using the experimental data derived in this study (Tab. 3) and theoretical models of linear correlation between nonsolvation contribution to the molal volume and ligands number. At 1000 bar only the best optimization result (model 3) is given. The comparison of different models with experimental data is presented in Fig. 3.
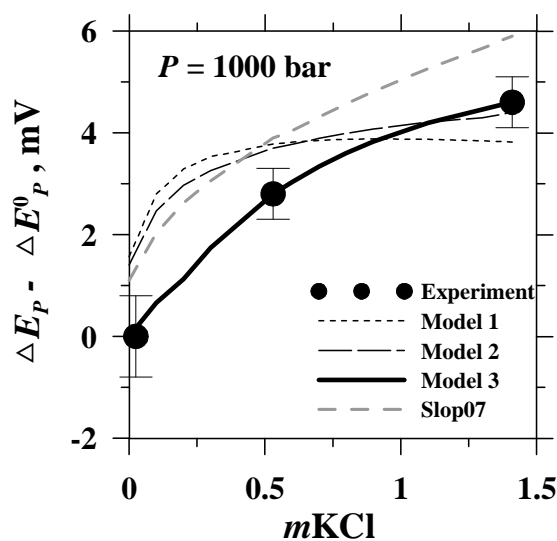
Fig. 3. The effect of pressure on the E (e.m.f.) as a function of m_{KCl}. The filled circles represent the experimental data (Tab. 3), the black solid and two dashed curves represent the calculation performed with optimization results and using the theoretical models (1, 2, 3), and the gray dashed curve represents calculation performed with Slop07 database (Shock et al., 1997; Sverjensky et al., 1997). The theoretical models are based on the linear correlation between ligands number and nonsolvation input to the molal volume for the species with the same coordination. Thus, model 1 corresponds to the same aqueous coordination for cadmium ion and all four chloride complexes, model 2 corresponds to the coordination change between $CdCl_3^-$ and $CdCl_4^{2-}$, model 3 – between $CdCl^+$ and $CdCl^0_2(aq)$.
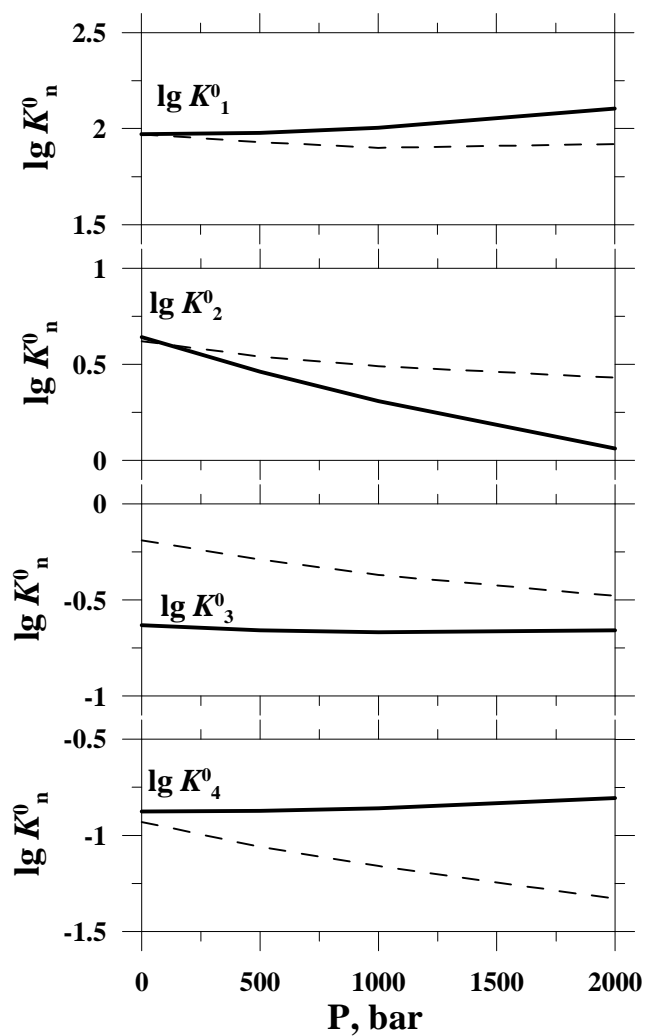
Fig. 4. Cadmium chloride complexes stability as a function of pressure at 25°C. Solid lines represent the calculation with thermodynamic properties of cadmium chloride complexes derived in this study (Tab. 4), and dashed lines − with thermodynamic properties taken from Slop07 database (Sverjensky et al., 1997).
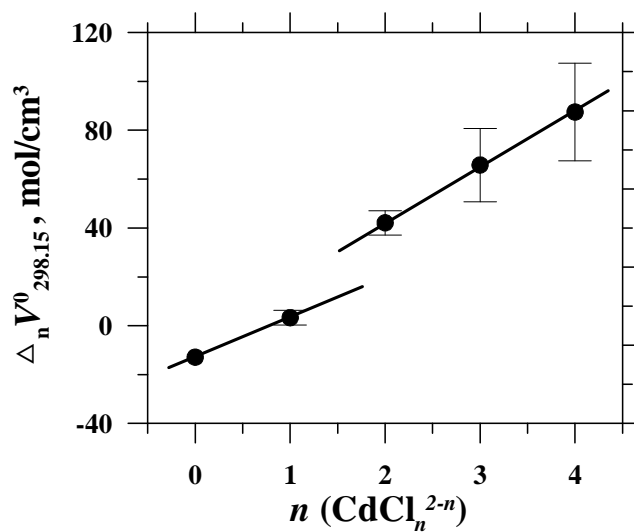
Fig. 5. Nonsolvation contribution to the standard partial molal volume of $CdCl_n^{2-n}$ species as a function of ligands number. Coordination change takes place between octahedral species with $n = 0 - 1$ (Cd^{2+} and $CdCl^-$) and tetrahedral species with $n = 2 - 4$ ($CdCl_2^0{}_{(aq)}$, $CdCl_3^-$, $CdCl_4^{2-}$).
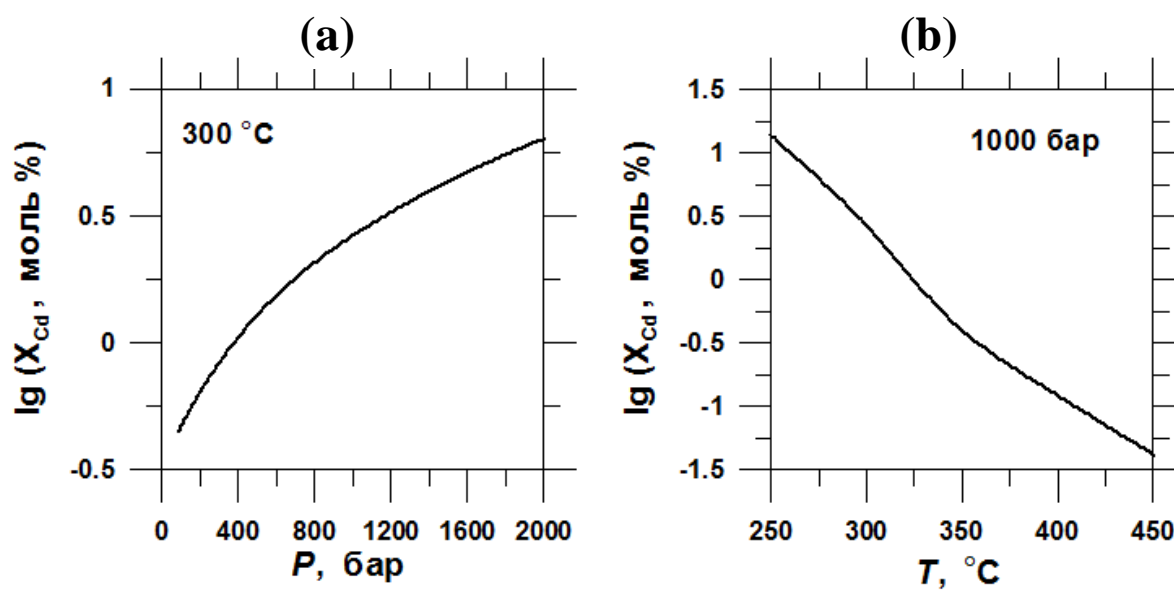
Fig. 6. Cadmium content in sphalerite in equilibrium with hydrothermal fluid containing 1m NaCl: (a) as a function of pressure at 300°C, and (b) as a function of temperature at 1000 bar. The Cd/Zn weight ratio in fluid is 0.001.

Chapter IV. STRUCTURE AND STABILITY OF CADMIUM CHLORIDE COMPLEXES IN HYDROTHERMAL FLUIDS

This chapter presents an article submitted to *Chemical Geology* in October 2009 (Bazarkina E.F., Pokrovski G.S., Zotov A.V., Hazemann J.-L. "Structure and stability of cadmium chloride complexes in hydrothermal fluids"). If accepted, the full text of article will be published in English presented below. Keywords proposed in the submitted version are ***cadmium; chloride complexes; hydrothermal fluid; X-ray absorption spectroscopy; solubility; stability constant; Cd/Zn ratio.***

ABSTRACT

The identity and stability of aqueous species formed by cadmium in H_2O-Na/LiCl-HCl-HNO$_3$ solutions were investigated using in-situ X-ray absorption spectroscopy (XANES and EXAFS) at 20-450°C and 1-600 bar, combined with solubility measurements of CdO and CdS solids at 350-400°C and 300-600 bar. Results show that aqueous Cd speciation is dominated by the cation $Cd(H_2O)_6^{2+}$ in acidic Cl-free solutions, and by chloride species $CdCl_m(H_2O)_n^{2-m}$ over a wide range of temperature ($20 \leq T \leq 450$°C), acidity ($1 \leq pH \leq 8$), and chloride concentration ($0.04 \leq m_{Cl} \leq 18$ mol/kg H_2O). EXAFS spectra from chloride solutions show that with increasing T and m_{Cl} the average number of Cl atoms increases from 1 to ~3 (±0.6), accompanied by a decrease of the number of O from 6 to ~1 (±0.7) in the nearest coordination sphere around Cd. Average Cd-Cl distances in Cd complexes vary in the range 2.41-2.52 (±0.02) Å, increasing with increasing m_{Cl} and decreasing with increasing T, while Cd-O distances remain constant within errors at 2.30 (±0.05) Å in the whole T and m_{Cl} range investigated. This evolution of the Cd atomic environment is accompanied by changes in geometry of the dominant Cd-O/Cl species from octahedral-like to tetrahedral-like with increasing T and m_{Cl}, as shown by XANES spectra analyses. These structural data are consistent with the formation of octahedral $Cd(H_2O)_6^{2+}$ and $Cd(H_2O)_5Cl^+$ and tetrahedral $CdCl_2(H_2O)_2^0$, $CdCl_3(H_2O)^-$ and $CdCl_4^-$ species at $T \leq$ 200-300°C and $m_{Cl} \leq 18$. At $T > 300$°C, aqueous Cd speciation is dominated by two complexes, $CdCl_2(H_2O)_2^0$ and $CdCl_3(H_2O)^-$ in a wide m_{Cl} range (0.04 – 5m). The stability constants of these complexes, derived from solubility measurements at 400°C and 600 bar are ~6 orders of magnitude higher than available HKF-model predictions based on low-T data. The new data on aqueous Cd complexes may be used for interpretation of Cd/Zn ratios measured in natural hydrothermal saline fluids and volcanic vapors in which the greater stability of Cd chloride species as compared to their Zn analogs is likely to be responsible for the elevated Cd/Zn ratios in comparison to crustal rocks and Cl-poor waters.

1. INTRODUCTION

The present study is aimed at better quantifying the identity, stability and structure of cadmium aqueous complexes responsible for Cd transport by hydrothermal fluids. This knowledge is crucial for understanding the behavior of Cd during the formation of ore deposits, for improving ore prospecting and treatment technologies involving hot solutions, and for setting up valuable strategies for remediation of polluted sites, and safe treatment and storage of cadmium industrial wastes. The major source of Cd in the environment is the mining and treatment of Zn-Pb-Cu hydrothermal ores where Cd is commonly present as an isomorphic substitution in Zn-bearing minerals due to the close chemical and crystallographic properties of these metals. The continental crust contains on average 80 ppb of Cd, which is 3 orders of magnitude lower than for Zn, with Cd/Zn mass ratios showing little variations between different rocks (Cd/Zn = 0.001-0.003, Heinrichs et al., 1980; Rudnick and Gao, 2003). However, the behavior of Cd may diverge significantly from that of Zn in hydrothermal processes involving hot aqueous fluids. For example, hydrothermal sphalerites (ZnS) are usually rich in Cd, with Cd/Zn ratios of 0.01 to 0.2, and complete solid solutions CdS-ZnS were described in polymetallic ores and fumarole's minerals (e.g., Axelsson and Rodushkin, 2001; Tombros et al., 2005; Chaplygin et al., 2007; Gottemsmann and Kampe, 2007; Cook et al., 2009). Volcanic gases also selectively concentrate cadmium versus zinc, exhibiting Cd/Zn ratios of 0.1 to 1.0 (Pennisi et al., 1988; Symonds et al., 1993; Rubin, 1997), which is 2 to 3 orders of magnitude higher that the average crustal value cited above. This makes the Cd/Zn ratio a potentially useful geochemical indicator of hydrothermal/volcanic activity and fluid origin, sources, and evolution. However, in contrast with Zn, the Cd behavior in hydrothermal fluids is very poorly known. To interpret rigorously cadmium transport by aqueous fluids at high temperatures and pressures (T-P) and to compare it with Zn we need to know the solubility of Cd-bearing minerals and the chemical status of this metal in the fluid phase.

The main natural ligands capable of transporting Cd under hydrothermal conditions are OH^-/H_2O, Cl^-, and HS^-/H_2S. In aqueous solution, the Cd^{2+} cation undergoes hydrolysis with formation of $Cd(OH)_n^{2-n}$ hydroxide complexes, where $1 \leq n \leq 4$. The stability constants of these species at ambient T-P were extensively studied and reported in numerous thermodynamic reviews (Baes and Mesmer, 1976; Archer, 1998; Martell and Smith, 1998). Based on available data and theoretical correlations with other metals, Shock et al. (1997) reported thermodynamic properties of $Cd(OH)_n^{2-n}$ at elevated T-P. However, the predicted concentrations of Cd hydroxide species in equilibrium with oxy-hydroxide phases at near-neutral pH are unexpectedly high, attaining 10's ppm at elevated T ($\geq 300°C$), which is 1-3 orders of magnitude higher than recent experimental determinations for similar base metals such as Zn (Bénézeth et al., 2002) and Cu (Palmer et al., 2004). The role of sulfur in Cd transport at hydrothermal conditions is not sufficiently known (Rickard and Luther, 2006). Experimental studies on Cd-S systems were performed only at ambient T-P (e.g., Ste-Marie et al., 1963; Daskalakis and Helz, 1992; Wang and Tessier, 1999). Although cadmium has a stronger chemical affinity to the sulfide ligand compared to hydroxide, the abundance of Cd-S complexes at elevated T-P is limited by both the weakening of the sulfide complexes stability with increasing T (Rickard and Luther, 2006; Tagirov et al., 2007), and the low sulfur concentrations, typically less than 0.1-0.5 wt% in most hydrothermal fluids (Barnes, 1979). In contrast, chloride is a far more abundant ligand in

hydrothermal fluids, with concentrations attaining 10-30 wt% (Barnes, 1979). Thus, it is very likely that chloride complexes play a dominant role in the Cd transport in hydrothermal-magmatic settings, similarly to other major base metals like Zn, Fe, Pb, and Ag.

Many experimental and computational studies have demonstrated the formation in aqueous solution of chloride complexes $CdCl_n^{2-n}$, where $1 \leq n \leq 4$. Experimental data for these complexes have been obtained at $T \leq 100°C$ mostly using potentiometry, and well consistent stability constants for Cd chloride complexes at near-ambient temperatures are reported (see reviews of Sverjensky et al., 1997; Archer, 1998; Martell and Smith, 1998; references therein). The distribution of Cd-Cl species as a function of Cl concentration at 20°C and 1 bar calculated using these data is shown in Fig. 1a. In contrast, at high T-P the thermodynamic properties of cadmium chloride complexes are very poorly constrained. To the best of our knowledge, only one experimental work on $CdCl^+$ at $T \leq 250°C$ in weakly saline solutions was published (Palmer et al., 2000). As for the stability constants of Cd-Cl complexes at supercritical temperatures, only theoretical predictions from low-T data using the HKF model are available (Fig. 1b, Sverjensky et al., 1997).

The structures of cadmium chloride complexes in aqueous solution were studied at ambient T-P using X-ray diffraction (XRD), Nuclear Magnetic Resonance (NMR), Raman, Infrared, and X-ray absorption spectroscopy (e.g., Bol et al., 1970, Waters et al., 1973; Drakenberg et al., 1978; Ackerman et al., 1979; Caminiti et al., 1980; Paschina et al., 1983; Mosselmans et al., 1996; Seward and Driesner, 2004). Most of these studies agree about *a)* the presence of water molecules in the first coordination shell of Cd in its chloride species $CdCl_nH_2O_m^{2-n}$, and *b)* Cd coordination change from octahedral to tetrahedral with increasing Cl concentration in solution. It follows from these studies that the cadmium cation (Cd^{2+}) and low-ligand number Cl complexes ($CdCl^+$) are octahedral, and $CdCl_4^{2-}$ is likely to be tetrahedral. The octahedral-to-tetrahedral transition occurs upon the formation of the second ($CdCl_2^0$) or third ($CdCl_3^-$) chloride complex, depending on the solvent medium (Ahrland, 1979; Paschina et al., 1983). Very scarce structural data are, however, available for Cd-Cl complexes at T above ambient. The existing reports using X-ray absorption spectroscopy (XAS) have explored very limited T and Cl concentration ranges ($mCl \leq 1$ mol/kg H_2O, $T \leq 250°C$, Mosselmans et al., 1996; Seward and Driesner, 2004), and do not allow derivation of the identity and stability of the dominant Cd-Cl complexes over the range of hydrothermal T-P-pH conditions and fluid compositions.

Here we combined in situ XAS and solubility measurements to study systematically Cd-Cl complexing over a wide T-P and Cl concentration range (20-450°C, 1-600 bar, 0-18 mol Cl/kg H_2O). Our results provide new insights into the identity, stability and structure of aqueous chloride complexes responsible for Cd transport by hydrothermal fluids.
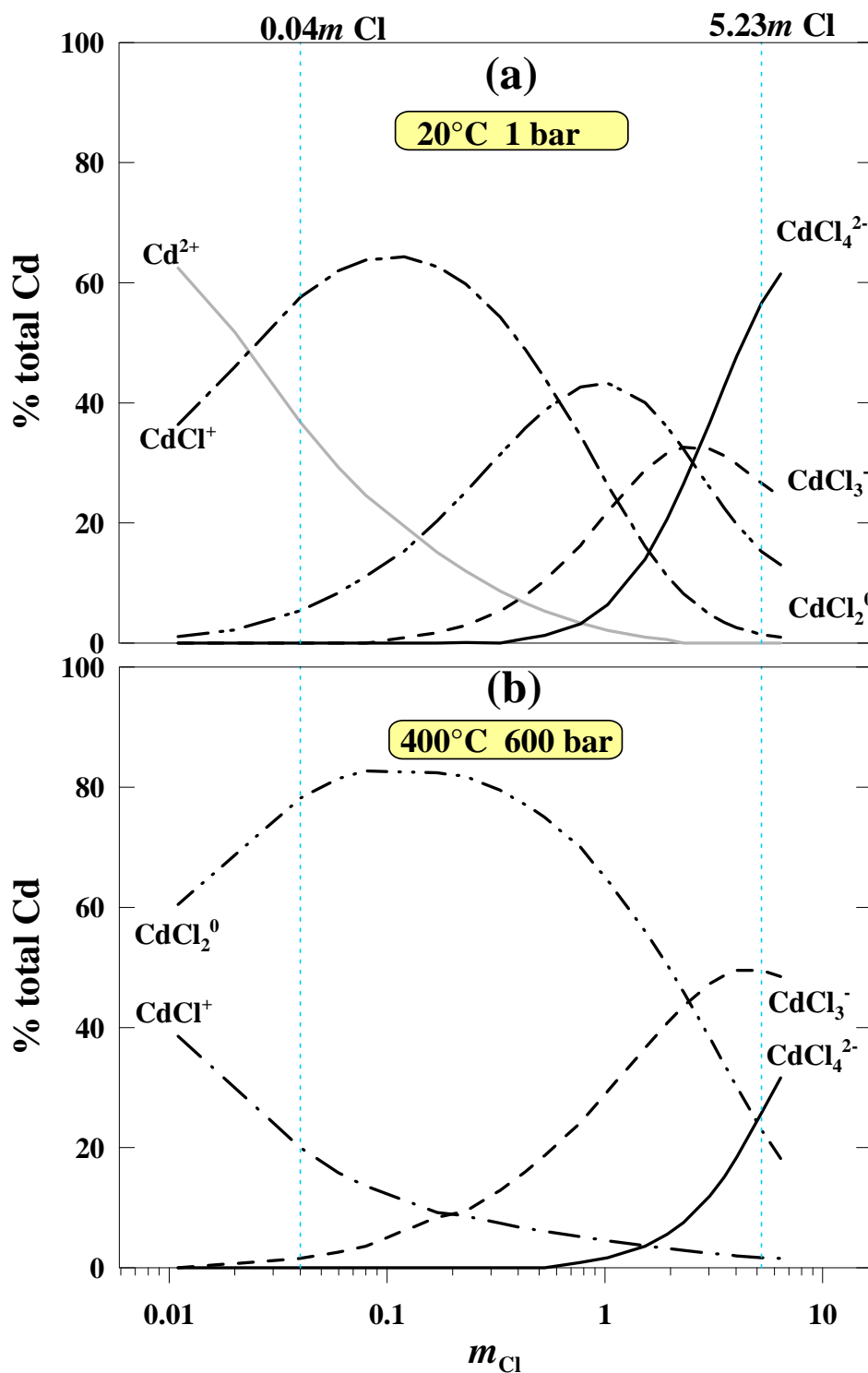
Figure 1. Distribution of Cd species in sodium chloride aqueous solution at 600 bar as a function of m_{Cl} at 20°C (a) and 400°C (b) calculated using the HKF-model parameters from Sverjensky et al. (1997). The vertical dashed lines correspond to the minimum and maximum Cl concentrations in the NaCl-HCl solutions studied in this work.

2. MATERIALS AND METHODS

2.1. Experimental samples, conditions and analytical techniques

In situ XAS measurements were performed on two nitrate $Cd(NO_3)_2$-HNO_3 and six chloride $CdCl_2$-HCl-NaCl aqueous solutions at T = 20-450°C and P = 1-600 bar. In addition, several concentrated $CdCl_2$-HCl-LiCl aqueous solutions (up to 18m Cl) were measured at 20°C and 1 bar. All solutions were prepared by weight from $Cd(NO_3)_2 \times 4H_2O$, $CdCl_2 \times H_2O$, NaCl, LiCl, HNO_3, HCl and deionized water. Solution compositions are reported in Tables 1, 2 and 3 in molality units (m = number of moles of each solute per kg of water). Spectroscopic experiments were complemented by batch-reactor solubility measurements of monteponite (CdO, cubic) and greenockite (CdS, hexagonal) in pure water and similar NaCl-HCl-H_2O solutions at 350-400°C and 300-600 bar. A commercial CdO solid (Fluka, $\geq$ 99%) was treated before experiments. First, the initial powder was washed several times with deionized water to remove ultrafine particles. Then, the slurry was aged in water at 350°C and saturated vapor pressure (P_{sat}) for a month in a titanium autoclave quenched at the end of the run. The solid was recovered and dried at 100°C for 24h. Scanning electron microscopy (SEM) performed on the initial and final CdO product showed that such a treatment was extremely beneficial, resulting in significant crystallinity improvement (typical size of crystals 1-2 μm) and elimination of surface defects and ultrafine particles ($\leq$ 0.1 μm) that could bias solubility determinations (e.g., Pokrovski and Schott, 1998). During the reactor quench, the formation of $Cd(OH)_2$(s) which is thermodynamically stable at $T \leq$ 150°C (Naumov et al., 1974; Wagman et al., 1982) could not be avoided completely, however, and the resulting solid contained about 10% of the hydroxide phase as detected by X-ray diffraction. A commercial CdS powder (Merck, $\geq$ 99%) showed a good crystallinity (crystal size 0.5-2 μm) and, consequently, was used as received. The solids were pressed in pellets for solubility experiments. Aqueous samples from these experiments with concentrations above 0.05 ppm were analyzed for Cd and Na (if present) by atomic absorption spectroscopy (AAS), and by ICP-MS for concentrations below 0.05 ppb. In addition, in batch-reactor experiments Cd concentrations were independently controlled by weight loss of the solid phase (see section 2.4).

2.2. X-ray absorption spectra acquisition

XAS spectra of Cd aqueous solutions were collected at Cd K-edge (~26.7 keV) over the energy range 26.5-27.6 keV on BM30B-FAME bending-magnet beamline (Proux et al., 2005) at the European Synchrotron Radiation Facility (ESRF, Grenoble, France). The storage ring was operated at 6 GeV with a ~200 mA current. The beam energy was selected using a Si (220) double-crystal monochromator with sagittal focusing. The energy was constantly calibrated using a cadmium metal foil; its K-edge position was set at 26,711 eV as the maximum of the first derivative of the main-edge spectrum. The beam size was 1000 μm horizontal $\times$ 300 μm vertical. X-ray photon flux on the sample was about 10^{12} photons/s. Contributions of higher-order harmonics from the Si (220) double-crystal within the FAME optics configuration do not exceed 1% of the total photon flux in the energy range of our experiments (Proux et al., 2006). XAS experiments were carried out using a high T-P cell developed at the Institute Néel (Grenoble) and recently described in detail elsewhere (Pokrovski et al., 2005, 2006, 2009a,b; Testemale et al., 2005). Acquisition time for each XAS scan was ~30 min. Transmission spectra were recorded using silicon diodes collecting scattered radiation from a Kapton

foil placed in the incidental and transmitted X-ray beam. Fluorescence spectra were collected in the 90° geometry using a Canberra solid-state multi-element germanium detector (energy resolution ~300 eV, shaping time 125 ns).

2.3. X-ray absorption spectra analysis

Data reduction and modeling were performed with the Athena and Artemis packages (Ravel and Newville, 2005) based on the IFEFFIT program (Newville, 2001). Details about the reduction procedure can be found elsewhere (Pokrovski et al., 2005, 2006, 2009a,b). Briefly, energies were recalculated into k-space (Å^{-1}) with E^0 (i.e., the energy at which k is zero) chosen as the maximum of the first derivative of the main-edge spectrum. Spectra were normalized to the absorption edge height, background removed, weighted by k^n, where n = 1, 2 and 3, and Fourier transformed (FT) over the k range 2.1-10 Å^{-1} for all aqueous samples for consistency. Larger k-ranges (up to 14 Å^{-1}) were also explored for some low-noisy spectra; they produced no changes in the derived structural parameters within errors. EXAFS fits were performed in the R-space on both real and imaginary parts of FT contributions to obtain the identity of neighbor atoms, Cd-neighbor distance (R), coordination number (N), and Debye-Waller factor (σ^2) for each scattering path (see Tables 1-4). A single nonstructural parameter Δe was varied to account for the difference between the experimental absorption-edge energy and its estimate made by FEFF. To diminish correlations between N and σ^2, and better account for light vs heavy neighbors (O vs Cl), fits were performed simultaneously with k-weighting of 1, 2 and 3. The fitted values of structural parameters were identical within errors, with comparable fit qualities at each k-weighting. This is an additional demonstration of both the validity of the chosen structural models and the accuracy of the EXAFS background removal procedure (Ravel and Newville, 2005). Theoretical backscattering amplitude and phase-shift functions for Cd-O and Cd-Cl single and multiple scattering paths were computed using FEFF6 *ab-initio* code (Zabinski et al., 1995) using CdO and $CdCl_2$ crystal structures. The amplitude reduction factor (S_0^2) was set at 1.00±0.05 as found by fitting spectra of CdO, CdS, $CdCl_2 \times H_2O$, and $Cd(NO_3)_2 \times 4H_2O$ solids. The influence of anharmonic disorder in determining structural parameters was checked using the cumulant expansion method. The values of third- and fourth-order cumulants (c_3 and c_4) found when fitting the signal from Cd 1st coordination shell always converged to zero within ±10^{-4} and did not affect R and N values derived from fits without cumulants. The influence of possible multiple scattering (MS) events within the Cd first coordination shell was also tested using the FEFF code, assuming tetrahedral and octahedral geometries around Cd as found in the model compounds investigated.

In addition to classical EXAFS analysis, XANES spectra of different $Cd-Cl-H_2O$ aqueous species were modeled ab-initio based on the experimental EXAFS-derived Cd-Cl and Cd-O distances and defined species geometries and using the FDMNES computer code (Joly, 2001). Details about this approach for aqueous species can be found elsewhere (e.g., Testemale et al., 2004; Pokrovski et al., 2009a). Very briefly, calculations of theoretical XANES spectra were performed using the Finite Difference Method (FDM) where the electron potential is calculated by resolving the Schrödinger equation on the node points of a three-dimensional grid (Kimball and Shortley, 1934). The obtained raw calculations represent the evolution of the photo-absorption cross-section of Cd as a function of X-ray photon energy and correspond to the transition amplitude between the initial and final states with an energy resolution of the FD method (< 0.1 eV). These spectra, which display almost all possible electronic transitions, are further convoluted with a Lorentzian function with a full width Γ_h

of 7.3 eV to account for the core-hole lifetime at Cd K-edge, and a Gaussian function to account for the experimental resolution assumed to be equal to the intrinsic resolution of the monochromator (Γ_{exp} = 1.4 eV, Proux et al., 2006). The convolution parameters were fixed in all subsequent analyses. Because the electronic states below the Fermi level are occupied, the absorption cross section was set to zero below the Fermi energy prior to the convolution. All calculations were performed in the FDM mode in order to test different clusters symmetries and geometric configurations (note that in case of low symmetry, the muffin-tin approximation is not sufficient in the near-edge energy range; Joly, 2001). The value of energy for the Fermi level (E_{fermi}) was fixed to -3.0 eV, as deduced by examination of the density of state (DOS) evolution of the different electronic states. Changing the values of E_{fermi} from -9 to +3 eV produced only minor effects on the calculated XANES spectra.

2.4. Solubility experiments

Two types of solubility techniques were employed: *a)* batch autoclaves quenched after the run, and *b)* a flexible-cell reactor Coretest® allowing multiple samples of the fluid phase at given *T-P* conditions. Batch autoclaves, made of a Ti alloy, were used for monteponite (CdO cubic) and greenockite (CdS hexagonal) solubility measurements at 400°C and 600 bar in NaCl-HCl-H_2O solutions containing up to 5.23m NaCl and up to 0.13m HCl. Details about this technique may be found elsewhere (Pokrovski et al., 2002a). Briefly, the solid phase was placed in a titanium holder, which is fixed in the upper part of the reactor so that it does not contact the solution at ambient *T-P*, and the reactor is put vertically in a *T* controlled (±1°C) furnace. Experimental *P* was calculated from the degree of filling of the autoclave using the *PVTX* properties of the H_2O-NaCl system at 400°C and 600 bar (Anderko and Pitzer, 1993; Bakker, 2003) and assuming that low concentrations of HCl (m_{HCl} ≤ 0.13m) and dissolved Cd (m_{Cd} ≤ 0.15m) do not significantly modify these properties. The maximum error of *P* estimations does not exceed ±50 bar. At the end of the run, the reactor was quenched in cold water to rapidly separate the solid from solution.

The dissolved Cd contents were determined by AAS in quenched solutions and by weight loss of the solid phase. The batch-reactor quenching technique is pretty efficient for measurements on solids soluble at elevated *T* and in concentrated salt solutions for which sampling techniques (flexible-cell reactor, see below) may fail owing to solute precipitation during the fluid transfer from high *T-P* to ambient conditions. However, the relatively poor reproducibility of the weight-loss method and eventual solid re-crystallization and metal adsorption on the reactor walls inevitably result in elevated detection limits of the quenching technique. These limits were estimated to be ~0.002 m_{Cd} from experiments in pure water and dilute NaCl solutions. Consequently the batch-reactor method was used only for concentrated NaCl solutions (≥ 0.8m NaCl), where CdO and CdS solubility is at least above 0.003m Cd. The weight-loss method failed also for some concentrated NaCl runs (identified by «NA» in Table 7), likely owing to *a)* the precipitation of NaCl crystals in the holder and on the pellet at m_{NaCl} ≥ 1, and *b)* the fragility of the remaining CdS pellet hampering its accurate handling and weighing. In such cases, the solubility was determined only from analyses of Cd of the quenched solution. It was found that steady-state concentrations were attained after 4 and 7 days in CdO and CdS batch-reactor runs, respectively. X-ray diffraction and SEM analyses of solid phases after CdO solubility experiments in HCl solutions (e.g., run O-25, Table 6) showed unidentified Cd oxy-chloride phases together with CdO. Despite the dominant presence of CdO, which likely remains the solubility-controlling phase, the formation of oxy-chlorides may affect significantly Cl concentration and pH in

experimental solutions. Consequently, such runs were not used in further thermodynamic analyses. In contrast, NaCl-bearing CdO- and all CdS-solubility experiments showed the only presence of CdO±NaCl solid phases.

A flexible-cell reactor Coretest was used for CdO solubility measurements in pure H_2O at 350-400°C and 350-400bar. The efficient sampling and clean and inert chemical environment in this reactor enables very low detection limits for Cd, mainly imposed by the limits of analytical techniques (e.g., 1 ppb of Cd in solution for ICP-MS analysis). This allows accurate solubility measurements in pure water, which cannot be assessed using the quenching technique above. The experimental setup was similar to that described elsewhere (Pokrovski et al., 2008). Briefly, the reactor consists of an internal flexible titanium cell (150 mL) inside a large-volume (800 mL) stainless-steel autoclave with water as a pressure medium. The vessel is inserted into a rocking furnace. A pellet of CdO together with deionized water is placed into the cell. During the experiment, small amounts of fluid phase (~2 g) are periodically extracted from the internal cell into a titanium sampling ampoule via titanium tubing and two high pressure valves. The rapid fluid transfer into the ampoule (< 1 s) under experimental *T-P* allows avoiding solute losses from metal precipitation or volatile degassing during sampling at elevated *T* (Pokrovski et al., 2008). It was found that steady-state concentrations were attained in ~2 days after the last *T-P* change. After the experiment, the autoclave is cooled down and the remaining solid is recovered; its XRD and SEM analyses showed the presence of CdO and minor amounts (~10%) of $Cd(OH)_2$ phase that likely to have been formed on cooling.

3. RESULTS FROM XAS EXPERIMENTS

3.1. Cadmium nitrate solutions at 17-300°C

Two nitrate solutions were examined, $0.10m$ $Cd(NO_3)_2 - 0.10m$ HNO_3 and $0.01m$ $Cd(NO_3)_2 - 0.20m$ HNO_3 at $T = 17\text{-}300°C$ and $P = 1\text{-}600$ bar. The XANES spectra of both solutions exhibit identical energy positions and shapes at all temperatures, and are similar to $Cd(NO_3)_2{\times}4H_2O_{(s)}$ in which Cd in the nearest atomic shell is coordinated with 6 O atoms in an octahedral geometry (Macdonald and Sikka, 1969). This suggests a similar octahedral environment for Cd^{2+} in aqueous solution to at least 300°C.

These observations were confirmed by EXAFS modeling. Fits of both transmission and fluorescence spectra yielded identical structural parameters for the first Cd atomic shell for both solutions at all *T* (Table 1). Cadmium was found to be coordinated by 6±0.6 oxygen atoms at 2.28±0.02 Å with no detectable changes of N_O and R_O with increasing *T* and *P*. These findings are in excellent agreement with previous EXAFS, XRD and Raman spectroscopy studies (Bol et al., 1970; Ohtaki et al., 1974; Caminiti and Johanson, 1981 Caminiti et al., 1984; Mosselmans et al., 1996). In contrast, our results are somewhat different from the EXAFS data of Seward and Driesner (2004) who reported a decrease of the $Cd\text{-}O_6$ distance by ~0.04 Å with *T* rise from 25 to 300°C at P_{sat} in similar nitrate solutions. No second shell around Cd was detected over the studied *T* range, suggesting that neither ion pairing nor polymerization took place in such dilute solutions. Thus, our and existing structural data are consistent with the predominance of the octahedral $Cd(H_2O)_6^{2+}$ cation in acidic nitrate solutions.

Table 1. Average cadmium atomic structure in $Cd(NO_3)_2$ – HNO_3 aqueous solutions as a function of Cd concentration and temperature derived from fitting EXAFS spectra at the Cd K-edge.

T°C	P, bar	E°, eV	N_O, atoms	R_O, Å	σ^2_O, Å^2	Δe, eV	$\mathcal{R}$-factor
			Oxygen (O) backscatterrer				
exp #1: 0.100m Cd(NO$_3$)$_2$ – 0.11m HNO$_3$							
17	1	26715.0	6.0	2.29	0.009	3.2	0.014
30	600	26714.8	6.0	2.28	0.008	2.8	0.012
100	600	26714.8	6.0	2.28	0.010	2.7	0.011
300	600	26714.8	5.5	2.29	0.015	2.0	0.040
exp #12: 0.010m Cd(NO$_3$)$_2$ – 0.22m HNO$_3$							
20	600	26714.8	5.9	2.28	0.009	2.7	0.007
100	600	26714.8	6.0	2.28	0.011	2.7	0.005
200	600	26714.8	5.9	2.28	0.013	2.0	0.007
250	600	26714.8	5.9	2.28	0.014	2.0	0.008
300	600	26714.8	5.6	2.30	0.016	1.2	0.010
error	±10	±0.3	±0.6	±0.02	±0.002	±1.0	

m denotes the number of moles of each solute per kg of water (mol/kg H_2O); E° = maximum of the first derivative of the main-edge spectrum; R_O = cadmium-oxygen distance; N_O = number of oxygen atoms; σ^2_O = squared Debye-Waller factor for Cd-O paths; Δe = non structural parameter accounting for energy shift between experimental spectrum and FEFF calculation; $\mathcal{R}$-factor defines goodness of the total fit in R-space as described in IFEFFIT (Newville, 2001). For all samples the fitted k- and R-ranges were respectively 2.1-10.0 Å^{-1} and 1.2-3.0 Å, S^2_0 = 1. The number of variables in the fit N_{var} = 4; the number of independent points N_{ind} ~ 9.

At 300°C the amplitude of the absorption edge decreases rapidly with time indicating a decrease of total Cd concentration in solution, likely due to the enhanced Cd^{2+} hydrolysis and CdO precipitation. This partial precipitation, however, was found to have no influence on XAS spectra from solution. At $T \geq 300°C$, all Cd was completely lost from solution, but with decreasing T below 250°C the precipitate was re-dissolved, yielding identical XAS spectra from solution to those recorded on heating at the corresponding temperature.

3.2. Cadmium chloride solutions at 20-450°C

3.2.1. XANES analysis

At ambient *T-P*, the XANES spectrum of the solution with the lowest chloride concentration investigated (0.04m Cl) exhibits a similar spectral shape as that of nitrate solutions, indicating an octahedral Cd environment. This is in agreement with the predominance of octahedral-like $Cd(H_2O)_6^{2+}$ and $CdCl(H_2O)_5^+$ complexes at such Cl concentrations (Fig. 1a). With increasing m_{Cl}, XANES spectra take progressively a tetrahedral shape (Fig. 2a). This is manifested by *a)* decrease of the white-line amplitude of normalized spectra, *b)* appearance and growth of a new resonance at 26,735 eV, and *c)* disappearance of the resonance at ~26,765 eV, typical of octahedral structures. The main-edge spectral shape at $m_{Cl} \geq$ ~2 m is similar to those of tetrahedral-like complexes of many metals and metalloids in aqueous solution (e.g., $Ge(OH)_4$, Pokrovski et al., 2000; $Ga(OH)_4^-$, Pokrovski et al., 2002b; $FeCl_4^{2-}$,

Testemale et al., 2009). Linear combination fits (LCF) demonstrate that XANES spectra of all Cl-bearing solutions may be reasonably described as the sum of fractions of spectra from the solutions with the lowest (0.04m, 'octahedral') and highest (18.2m, 'tetrahedral') Cl concentration (Supplementary Table EA1-1). This is also in agreement with the results of principal component analysis (PCA) using the ITFA program (Rossberg et al., 2003), which identified only 2 independent components in the nine spectra examined at 20°C, despite the presence of at least 5 Cd chemical species in the investigated Cl-concentration range (Fig. 1a). The stepwise formation of Cd chloride complexes results in smooth and gradual changes in the spectral signature with increasing Cl concentration (Fig. 2). Thus, in the absence of spectral standards for each species in a mixture, neither LCF nor PCA allow accurate and unambiguous extraction of individual species fractions. More quantitative details on these analyses are given in Electronic Annex 1.

With increasing T at the same m_{Cl}, XANES spectra show a similar octahedral-to-tetrahedral transition. For dilute solutions (0.04m and 0.12m Cl), these changes are gradual, occurring over a wide T range, at least from 100 to 300°C (Fig. 2b), whereas for concentrated solutions (0.77 – 5.23m Cl), the T range of transition is narrower, with almost all octahedral features disappearing between 100 and 200°C (Fig. 2c). At $T \geq 400$°C, XANES spectra of all Cl-bearing solutions exhibit typical tetrahedral shapes (Fig. 2d). Pressure changes from 268 to 600 bar at 400°C have no detectable effect on the XANES spectrum of the 0.04m Cl solution indicating that dominant species fractions do not change significantly at least in the studied P range. Like for ambient-temperature solutions, LCF modeling of both XANES and EXAFS spectra at $T \geq 100$°C shows that the whole series of solutions at a given T may be matched within errors by the sum of different fractions of the spectra from two solutions of the lowest and highest Cl concentration. Moreover, spectra at $T \geq 300$°C may be matched equally by the sum of fractions of the 'octahedral' Cd^{2+} from Cl-free nitrate solutions and the 'tetrahedral' [$CdCl_3^-$ +$CdCl_4^{2-}$] from 5.2m - 18.2m Cl solutions (see EA1 for further details). Such LCF models yield, however, too high fractions of octahedral Cd^{2+} + $CdCl^+$ (up to ~30-40% of total Cd) at Cl concentrations of 0.1-1.0m at and above 300°C (see EA-1). The significant amounts of such species at supercritical T disagree, however, with a) HKF-model predictions indicating less than 10-15% of Cd^{2+} + $CdCl^+$ species fraction (Fig. 1b); b) general tendency to form low-coordinated and weakly charged or uncharged complexes at high T (Crerar et al., 1985); c) our solubility results, implying negligible amounts of Cd^{2+} at 350-400°C. Again, this analysis demonstrates the difficulty for identifying the spectra of individual species and quantifying unambiguously their fractions in case of a mixture of complexes exhibiting gradual spectra changes upon the increase of ligation number (N_{Cl}) in the complex with increasing Cl concentration.
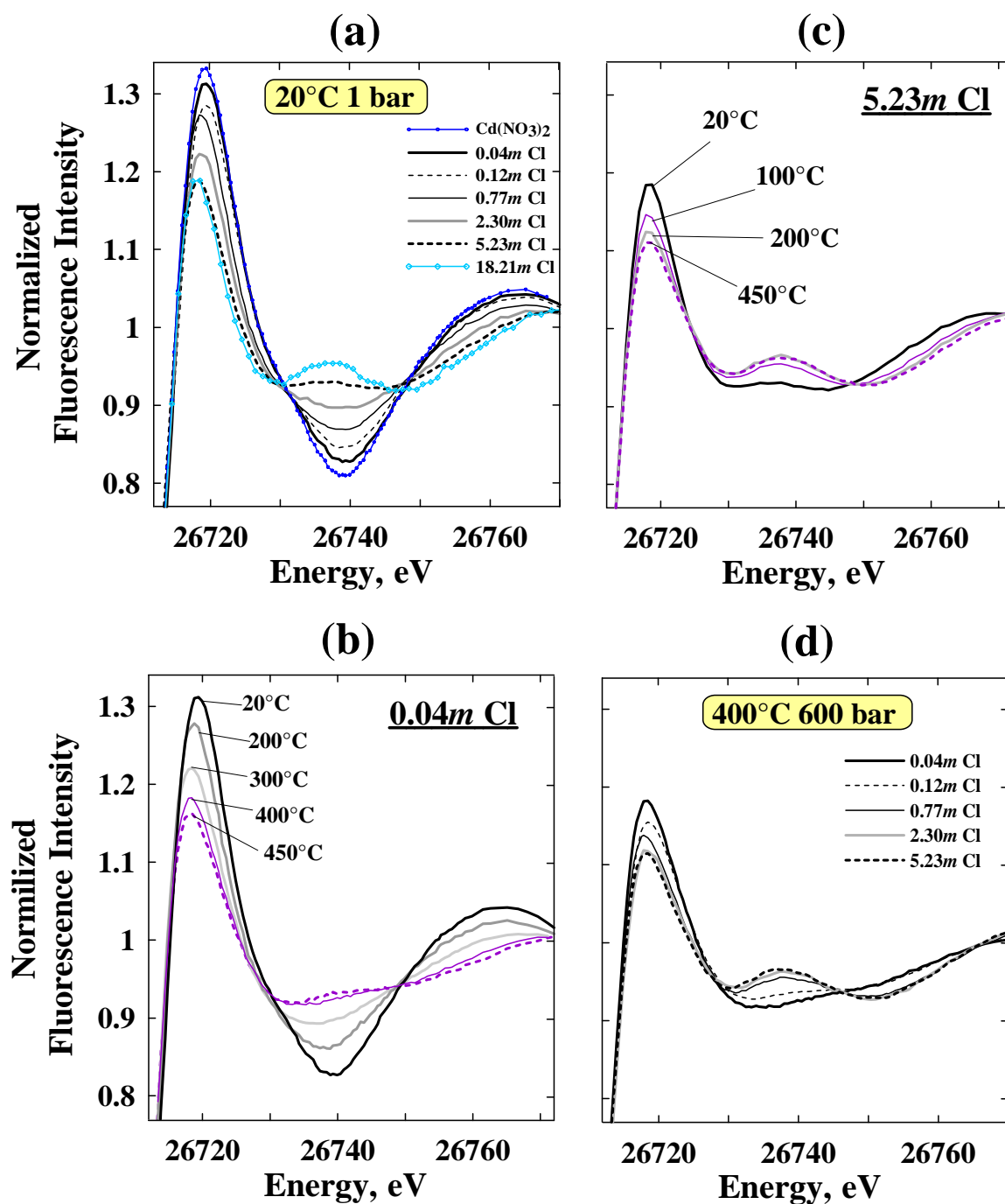
Figure 2. Evolution of XANES spectra of Cd-Cl aqueous solutions as a function of chloride concentration at 20°C and 1 bar (a), 400°C and 600 bar (d), and as a function of temperature at 600 bar for 0.04m (b) and 5.23m (c) of total Cl in solution.

3.2.2. EXAFS analysis

Our conclusions from XANES spectra are compatible with results of EXAFS analyses (Tables 2-4). At ambient T in the solution with the lowest Cl concentration (0.04m), the 1st Cd atomic shell contains ~0.8±0.7 Cl and ~5.5±0.7 O atoms with Cd-Cl and Cd-O distances of 2.48±0.05 Å and 2.30±0.05 Å, respectively. The signal from oxygen backscatterrers largely dominates the EXAFS spectrum of this most dilute chloride solution, thus yielding large uncertainties when extracting the Cl parameters. The value of N_{Cl} reported above may thus be regarded as a 'detection limit' imposed by the spectral statistics (see EA2 for quantitative statistical analysis). Despite large uncertainties, the number of Cl around Cd in this solution is in decent agreement with that predicted from thermodynamic calculations, assuming that all Cd-Cl complexes are inner-sphere (N_{Cl} = 0.6, corresponding to ~60% of CdCl^{+} in this solution, Fig. 1a). With increasing m_{Cl} at 20°C, the number of Cl increases and the number of O decreases (Fig. 3a). This is accompanied by a slight increase of Cd-Cl distances (from 2.48 Å at 0.04m Cl to 2.53 Å at 18.2m Cl, Table 2), whereas Cd-O distances remain constant within errors over the whole range of Cl concentration (2.30±0.05 Å, Table 2). With increasing m_{Cl} and T, the overall EXAFS signal becomes dominated by Cl backscatterrers; consequently, EXAFS fits yield large uncertainties on the oxygen parameters in solutions with $\geq 1m$ Cl at 20°C and in all solutions at $T \geq 200$°C. Thus, potential changes in Cd-O distances in these solutions with T might be hidden behind the uncertainties. Nevertheless, the presence of O in the first coordination shell of Cd of all studied solutions has been further supported by Cauchy Wavelet Transform analyses (see EA3 and Munoz et al., 2003) and by EXAFS statistics (see EA2 and Kelly et al., 2008). The inclusion of O in the model, even for the most concentrated solution (18.2m Cl), significantly improves both the $\mathcal{R}$-factor and reduced chi square χ_ν^2 of all fits (Table EA2-1). As a result, "purely chloride" complexes having no water molecules in the first coordination shell of Cd are unlikely to be dominant even in highly concentrated Cl solutions.

Table 2 Average cadmium atomic structure in $CdCl_2$ – NaCl – HCl aqueous solutions at 600 bar as a function of solution composition and temperature derived from fitting EXAFS spectra at the Cd K-edge.

T°C	E°, eV	Chlorine (Cl) backscatterer			Oxygen (O) backscatterer			Δe, eV	$\mathcal{R}$-factor
		N_{Cl}, atoms	R_{Cl}, Å	σ^2_{Cl}, Å^2	N_O, atoms	R_O, Å	σ^2_O, Å^2		
exp #9&11: 0.005m CdCl$_2$-0.02m NaCl-0.01m HCl (total Cl = 0.04m)									
20	26714.8	0.8	2.48[a]	0.011	5.7	2.30	0.011	3.4	0.005
100	26714.8	1.2	2.47[a]	0.013	5.2	2.30	0.010	3.3	0.004
200	26714.3	1.3	2.43[a]	0.010	4.5	2.30	0.010	3.7	0.007
300	26713.8	2.2	2.42[a]	0.010	3.4	2.30	0.011	3.1	0.003
400	26713.8	2.3	2.41[a]	0.010	2.2	2.30	0.009	3.4	0.005
450	26713.4	2.3	2.41[a]	0.013	2.2	2.30	0.008	3.2	0.009
exp #3: 0.010m CdCl$_2$-0.1m HCl (total Cl = 0.12m)									
20	26714.8	1.0	2.49[b]	0.013	4.8	2.30	0.008	3.5	0.001
100	26714.7	1.3	2.46[b]	0.015	4.6	2.30	0.008	3.5	0.002
200	26714.6	1.6	2.44[b]	0.011	3.8	2.30	0.009	3.5	0.002
300	26714.0	2.5	2.43[b]	0.012	3.0	2.30	0.011	3.0	0.002
400	26713.9	2.5	2.43[b]	0.011	2.1	2.30	0.009	3.2	0.002
450	26713.7	2.5	2.41[b]	0.009	2.1	2.30	0.01	3.4	0.001
exp #7: 0.016m CdCl$_2$-0.73m NaCl-0.01m HCl (total Cl = 0.77m)									
20	26714.3	1.6	2.52	0.015	4.0	2.30	0.008	3.3	0.001
100	26714.2	2.1	2.49	0.011	3.2	2.30	0.008	3.5	0.002
200	26714.0	2.6	2.46	0.010	2.1	2.30	0.010	3.6	0.001
300	26713.6	3.2	2.45	0.009	1.5	2.30	0.010	3.4	0.002
400	26713.6	3.3	2.44	0.010	1.1	2.30	0.009	3.3	0.003
450	26713.3	3.3	2.44	0.010	1.2	2.30	0.009	3.2	0.003
exp #4: 0.013m CdCl$_2$-2.27m NaCl (total Cl = 2.30m)									
20	26714.2	2.6	2.51	0.010	3.2	2.30	0.009	2.9	0.003
100	26713.9	3.1	2.48	0.011	2.1	2.30	0.006	3.3	0.003
200	26713.6	3.4	2.46	0.008	1.4	2.30	0.008	3.6	0.004
300	26713.6	3.4	2.46	0.008	1.1	2.30	0.009	3.6	0.001
400	26713.6	3.4	2.46	0.009	1.1	2.30	0.010	3.8	0.001
exp #2: 0.115m CdCl$_2$-2.32m NaCl-0.12m HCl (total Cl = 2.67m)									
20	26714.2	2.8	2.52	0.012	3.1	2.30	0.010	3.1	0.003
100	26714.0	3.1	2.48	0.011	1.9	2.30	0.008	3.2	0.005
200	26713.9	3.2	2.47	0.010	1.3	2.30	0.007	3.6	0.002
300	26713.7	3.2	2.46	0.011	1.2	2.30	0.008	3.8	0.002
400	26713.6	2.9	2.46	0.010	1.0	2.30	0.007	3.6	0.019
450	26713.6	3.0	2.46	0.010	1.0	2.30	0.007	2.9	0.011
exp #5: 0.022m CdCl$_2$-5.17m NaCl-0.01m HCl (total Cl = 5.23m)									
20	26713.9	3.0	2.52	0.009	2.0	2.30	0.009	3.1	0.004
100	26713.7	3.1	2.48	0.009	1.3	2.30	0.009	3.2	0.003
200	26713.6	3.3	2.47	0.009	1.0	2.30	0.009	3.6	0.003
300	26713.5	3.0	2.46	0.009	1.0	2.30	0.010	3.6	0.001
400	26713.6	3.4	2.46	0.011	1.1	2.30	0.008	3.4	0.003
450	26713.6	3.4	2.46	0.009	1.0	2.30	0.008	3.4	0.004
Error*	±0.3	±0.6	±0.01	±0.004	±0.6	±0.05	±0.004	±1.0	

See footnote of Table 1. Number of variables in the fit N_{var} = 7; number of independent points N_{ind} ~ 9.

* error on each EXAFS parameter for all experiments, unless indicated:

(a) error on Cd-Cl distance decreases from ±0.05 Å at 20°C to ±0.01 Å at 450°C

(b) error on Cd-Cl distance decreases from ±0.03 Å at 20°C to ±0.01 Å at 450°C

Table 3. Average cadmium atomic structure in concentrated CdCl$_2$-LiCl-HCl solutions at 20°C and 1 bar as a function of chloride concentration derived from fitting EXAFS spectra at the Cd K-edge.

T°C	E°, eV	Chlorine (Cl)			Oxygen (O)			Δe, eV	$\mathcal{R}$-factor
		N$_{Cl}$, atoms	R$_{Cl}$, Å	σ$^2_{Cl}$, Å^2	N$_O$, atoms	R$_O$, Å	σ^2_O, Å^2		
exp #13: 0.26m CdCl$_2$-6.63m LiCl-0.14m HCl (total Cl = 7.29m)									
20	26713.8	3.5	2.50	0.008	0.9	2.30	0.006	2.0	0.002
exp #14: 0.34m CdCl$_2$-10.69m LiCl-0.16m HCl (total Cl = 11.53m)									
20	26713.6	3.7	2.51	0.008	0.9	2.30	0.008	3.3	0.003
exp #15: 0.34m CdCl$_2$-17.35m LiCl-0.18m HCl (total Cl = 18.21m)									
20	26713.6	4.1	2.53	0.011	0.9	2.30	0.007	3.0	0.005
Error	±0.3	±0.7	±0.02	±0.004	±0.7	±0.05	±0.004	±1.0	

See footnote of Table 1.

Number of variables in the fit N$_{var}$ = 7; number of independent points N$_{ind}$ ~ 9.

Table 4. Average cadmium atomic structure in a 0.04m Cl solution at 400°C as a function of pressure derived from fitting EXAFS spectra at the Cd K-edge.

P, bar	E°, eV	Chlorine (Cl)			Oxygen (O)			Δe, eV	$\mathcal{R}$-factor
		N$_{Cl}$, atoms	R$_{Cl}$, Å	σ$^2_{Cl}$, Å^2	N$_O$, atoms	R$_O$, Å	σ^2_O, Å^2		
600	26713.8	2.3	2.41	0.010	2.2	2.30	0.009	3.4	0.005
408	26713.5	2.1	2.42	0.011	1.8	2.30	0.010	3.3	0.006
310	26713.5	2.0	2.41	0.011	1.8	2.30	0.009	3.4	0.008
268	26713.5	1.7	2.41	0.010	2.1	2.30	0.010	3.4	0.008
Error	±0.3	±0.7	±0.01	±0.004	±0.7	±0.05	±0.004	±1.0	

See footnote of Table 1.

At the same Cl concentration with increasing *T*, the average Cd-Cl distance systematically decreases, whereas the Cd-O distance remains constant within errors to at least 450°C (Table 2). At the same *T*, above 100°C, with increasing m_{Cl}, Cd-O distances remain the same whereas Cd-Cl distances increase slightly, similarly to the findings at ambient *T* (e.g., at 450°C, R$_{Cd-Cl}$ = 2.41±0.01 and 2.46±0.01 Å at 0.04 and 5.23m Cl, respectively, Fig. 3b). Normalized EXAFS spectra and their corresponding Fourier Transforms at 300°C (exp #3, 4 and 7) are shown in Fig. 4 and the derived structural parameters are reported in Tables 1 and 2. Pressure variations between 600 and 270 bar at 400°C for the 0.04m Cl solution yielded no detectable changes in structural parameters, with Cd coordinated by ~2±0.7 Cl atoms at 2.41±0.01 Å and ~2±0.7 O atoms at 2.30±0.05 Å (Table 4). At *T* above 300°C structural parameters derived from EXAFS modeling for 2-5m Cl solutions are identical, with 3.0±0.7 Cl atoms at 2.46±0.01 Å and 1.0±0.7 O atoms at 2.30±0.05 Å (Table 2). Examples of experimental and modeled EXAFS spectra for 0.04m Cl and 5.23m Cl solutions at 400°C and 600 bar are presented in Fig. 5. The constancy of Cd neighbor numbers and distances, derived from EXAFS in a wide range of m_{Cl} above 300°C, is in a good agreement with the absence of significant changes in the corresponding XANES spectra (Fig. 2d). Despite the large uncertainties on numbers of neighbors intrinsic to the EXAFS method, their average values are consistent with the likely predominance at supercritical *T* of the tetrahedral uncharged CdCl$_2$ complex hydrated by ~2 water molecules and the

negatively charged $CdCl_3^-$ hydrated by ~1 water molecule in the first coordination shell of Cd. It should be noted that the XANES part of the spectrum is far more sensitive than EXAFS to the cluster geometry and symmetry (section 3.3 below) and thus provides an independent confirmation of our EXAFS interpretations.
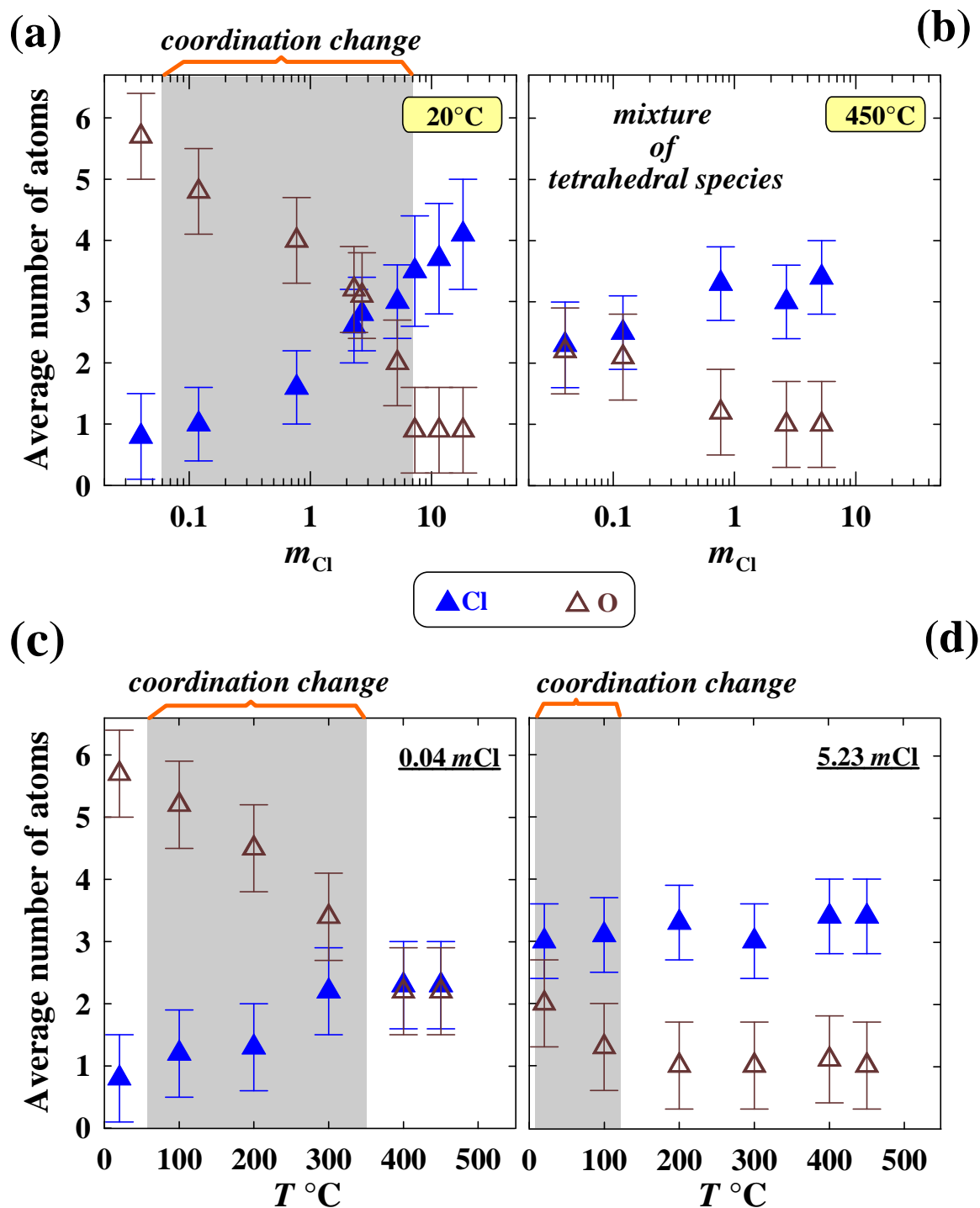
Figure 3. Average numbers of Cl and O atoms as a function of m_{Cl} at 20°C (a) and 450°C (b), and as a function of temperature for 0.04m Cl (c) and 5.23m Cl (d) solutions. Shaded areas indicate the coordination change in the dominant Cd species from octahedral to tetrahedral as found from XANES spectra analysis.

Our results at ambient T are in good agreement with previous EXAFS and XRD studies. At higher T ($\geq$ 200°C) our data may indicate the predominance of $CdCl_2(H_2O)_2^0$ in weakly saline fluids and $CdCl_3(H_2O)^-$ in highly saline solutions. Our average R and N values for Cd neighbors are in good agreement with those for ~$1m$ Cl solutions to 200°C reported by Mosselmans et al. (1996). Their interpretation of those data in terms of Cd aqueous species is, however, quite different from that of our study, suggesting the formation of only two species, Cd^{2+} and $CdCl_4^{2-}$ in their solutions. Although such a scheme does not contradict to LCF analyses in terms of the sum of these two end-member spectra (see section 3.2.1 and EA1), it does contradict to the available stability constants for Cd-Cl species (Sverjensky et al., 1997), which show that Cd speciation at these conditions is dominated by at least three chloride complexes, $CdCl^+$, $CdCl_2^0$ and $CdCl_3^-$. Furthermore, as it was shown by the experiments in Cl-free systems, at T above 300°C the Cd^{2+} is likely to be not stable (see section 3.1). Moreover, existence of Cd^{2+} and $CdCl_4^{2-}$ as the major species in a same solution disagrees with general physical-chemical principles of stepwise chloride complexing of many similar metals. Our structural results are also different from those of Seward and Driesner (2004) who reported, from limited measurements at 250°C in a $0.01m$ $CdCl_2$ solution, shorter Cd-O distances (2.1 Å) and larger average numbers of Cl atoms (N_{Cl} ~3) around Cd than those found in this study for a $0.04m$ Cl solution. Their values of N_{Cl} contradict to the Cl/Cd atomic ratio of two in their studied solution. Note, however, that uncertainties on N_{Cl} may be as large as ±30-50% of the N_{Cl} value in such dilute solutions as shown in our study. A comparison of our derived average numbers of Cl atoms with those calculated using available HKF parameters for the four Cd-Cl complexes (Sverjensky et al., 1997) demonstrates that EXAFS-derived N_{Cl} are systematically higher at all T above 20°C (Table EA1-7). It means that at elevated T the concentrations of such species as Cd^{2+} and $CdCl^+$ in the studied m_{Cl} range solutions are lower than those theoretically predicted. These species are minor at elevated T, and the Cd speciation is likely to be dominated by higher-order chloride complexes.
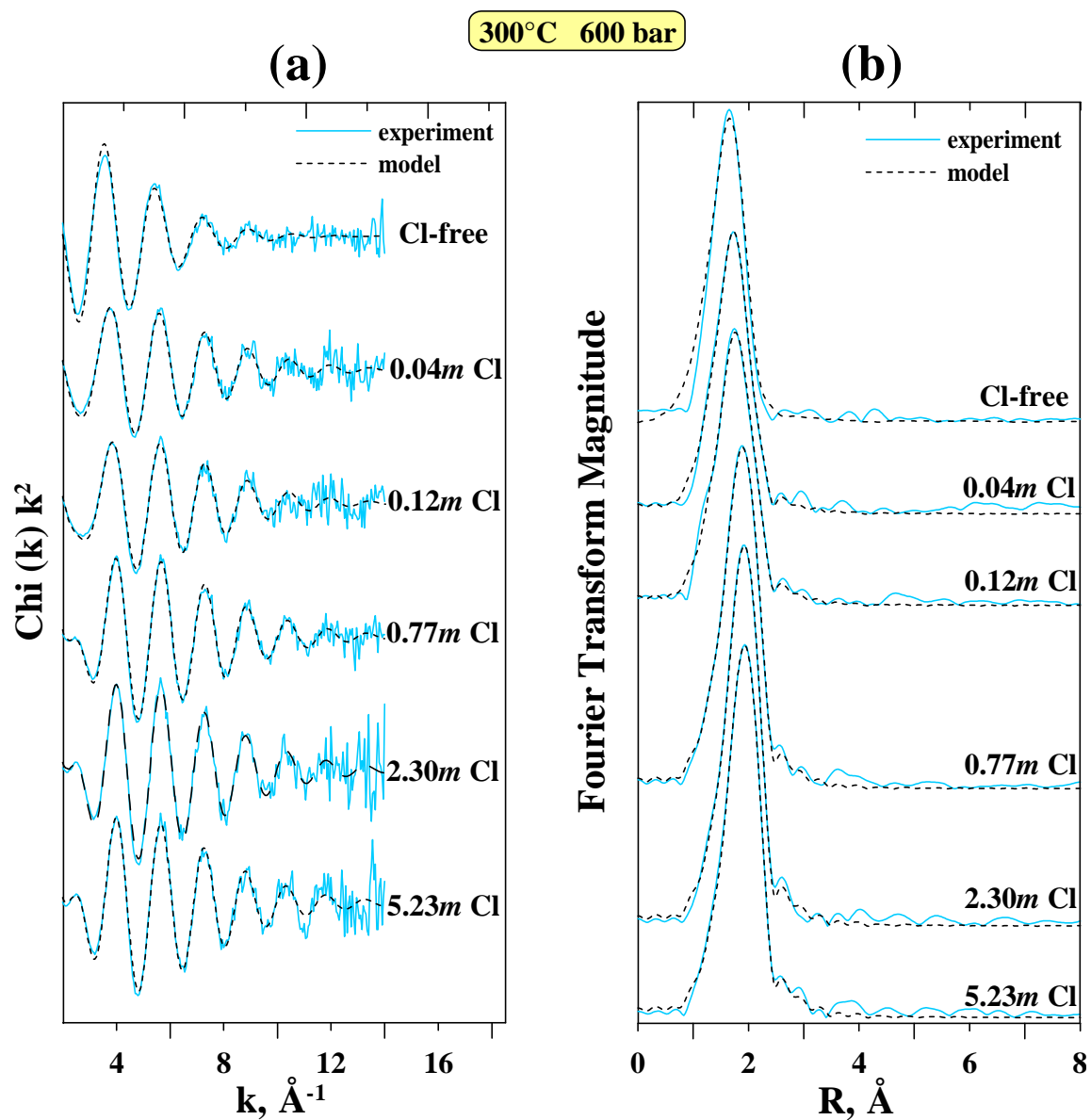
Figure 4. Normalized k^2-weighted EXAFS spectra from Cd-bearing NaCl-HCl aqueous solutions at 300°C and 600 bar (a), and their corresponding Fourier Transform magnitudes (b).
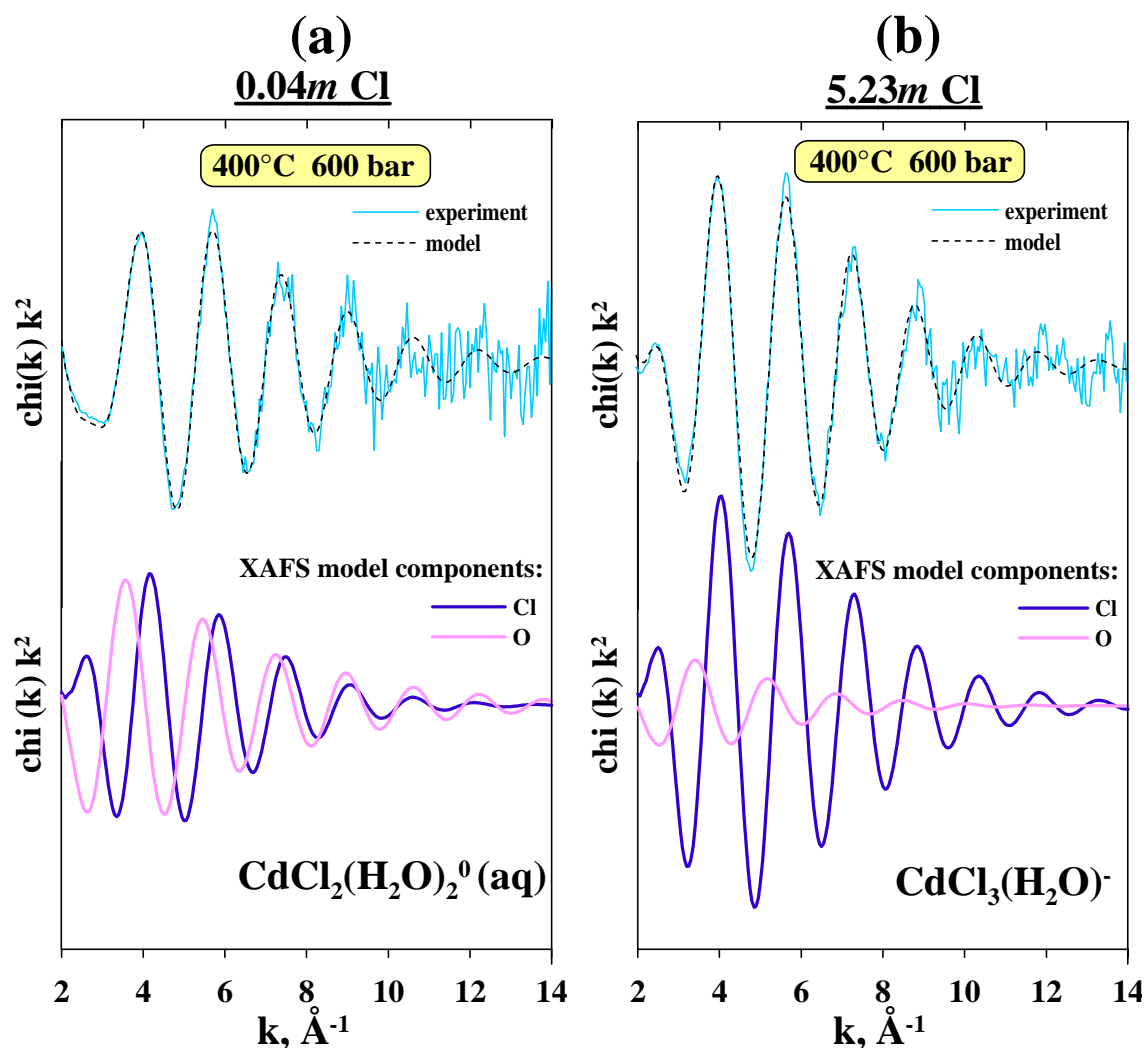
Figure 5. Normalized EXAFS spectra and their fits of two representative experimental solutions at 400°C and 600 bar with 0.04m Cl (a) and 5.23m Cl (b), showing the contributions of O and Cl in the EXAFS signal.

3.3. Quantum-chemical modeling of XANES spectra

Theoretical XANES spectra of different CdO_mCl_n clusters were calculated ab-initio using the FD method of the FDMNES program and assuming octahedral or tetrahedral O/Cl geometries around the Cd atom with 2.30 Å for Cd-O and 2.40 Å Cd-Cl mean distances, according to EXAFS analyses. Variations in Cd-O/Cl distances within ~0.1 Å and in convolution parameters (experimental resolution, Fermi energy, convolution functions, see also section 2.3) yielded only minor changes in the width and amplitude of calculated spectra, without altering significantly the shapes and energy positions of main resonances. The effect of H atoms (from H_2O molecules) on the calculated XANES spectra was found to be too weak to affect their major features and thus was neglected in the further analysis.

Representative spectra are displayed in Fig. 6 for selected CdO_mCl_n clusters of different symmetry and O/Cl numbers ($CdO_{4-m}Cl_m$ = tetrahedral, $CdO_{6-m}Cl_m$ = octahedral, $0 \leq m \leq 6$). Four main features are apparent in this figure as indicated by vertical dashed lines. *a)* The major change is a sharp decrease of the amplitude and a broadening of the white-line (at ~26,718 eV, feature A, Fig. 6) when changing from octahedral to tetrahedral geometry, whatever the number of Cl or O atoms. This evolution is very similar to that of experimental XANES spectra with increasing T and m_{Cl} (Fig. 2). *b)* The white-line changes induced by the octahedral-to-tetrahedral transition are accompanied by a shift of the value of E^0 (~26,713 eV, feature B, Fig. 6) by ~1-2 eV toward lower energies. This is comparable with the experiment which shows a systematic decrease of E^0 by 0.5-1.5 eV with increasing T, particularly pronounced at low and moderate m_{Cl} (Table 2). *c)* With increasing the number of Cl atoms in the cluster, large changes concern the growth of a resonance at ~26,735 eV, particularly pronounced in the tetrahedral geometry (feature C, Fig. 6). The growth of the feature C with T and m_{Cl} is also characteristic of the experimental spectra (Fig. 2) and is consistent with the increase of the number of Cl atoms revealed independently by EXAFS modeling (Table 2). *d)* Within the same geometry (octahedral or tetrahedral), substitution of O by Cl in the cluster results in a relatively minor decrease of the white-line amplitude and width. In contrast, clusters containing 2 to 3 O/Cl ligands, like trigonal pyramidal $CdCl_3$ or linear or angular $Cd(Cl/O)_2$ (not shown) are characterized by spectra with distinctly lower amplitudes of the main-edge resonance (feature A, Fig. 6) than those of tetrahedral-like clusters and all experimental samples. Thus, the main features of theoretical spectra corroborate nicely both the experimental XANES observations and quantitative EXAFS analyses, confirming a coordination change of Cd in its Cl complexes from octahedral to tetrahedral with increasing T and m_{Cl}, and the increase of the number of Cl atoms in the dominant tetrahedral-like species with increasing m_{Cl}.
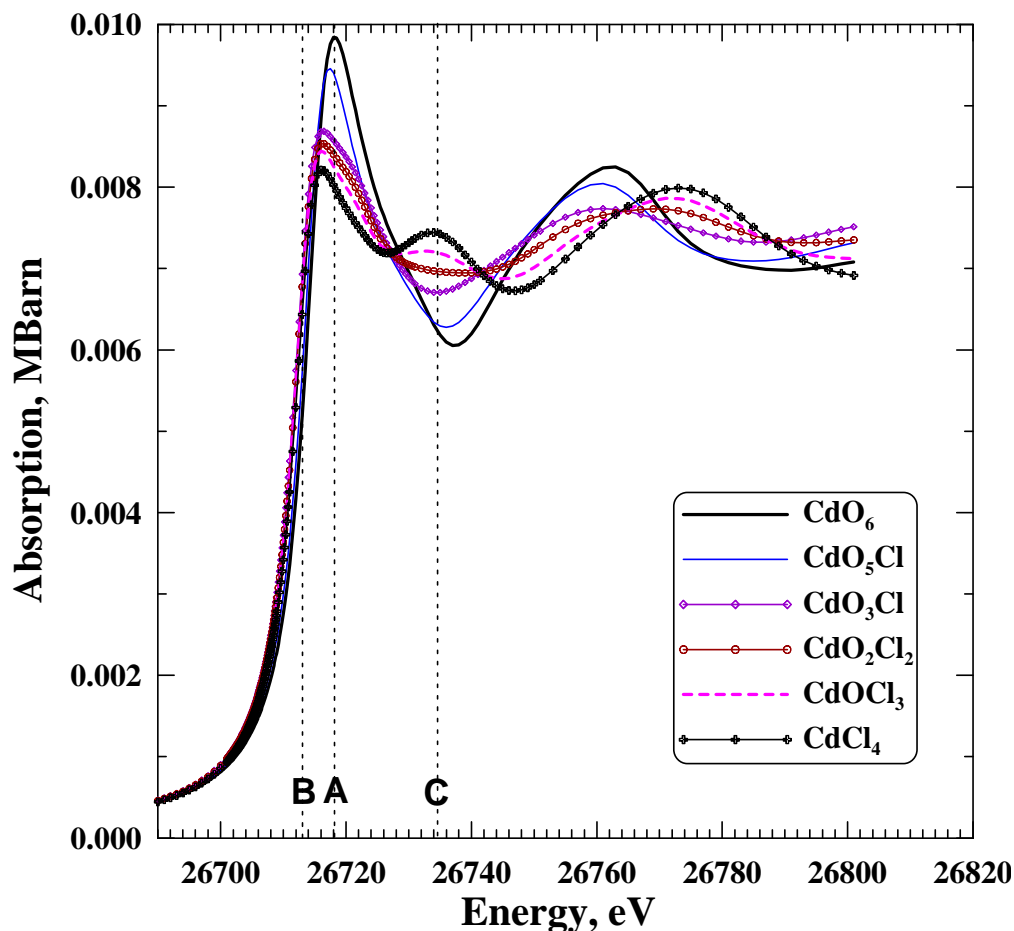
Figure 6. XANES spectra of selected [CdO_mCl_n] clusters, calculated using the FDMNES code and assuming octahedral or tetrahedral cluster geometries, with Cd-O and Cd-Cl average distances of 2.30 and 2.40 Å, respectively. Vertical dashed lines labeled A, B and C indicate the major spectra changes discussed in the text (section 3.3).

3.4. Stoichiometry and structure of Cd-Cl complexes derived from XANES and EXAFS results

Results from both experimental and theoretical XANES and EXAFS spectra, together with LCF and PCA analyses (see EA1), allow new constraints to the identity of the dominant Cd species in Cl-bearing solutions. Although an experimental XANES spectrum at given T and m_{Cl} may be a sum of two or more species simultaneously present in the solution as showed our LCF modeling, it is tempting to compare it with calculated spectra of *individual* Cd-O/Cl clusters. The experimental spectra of nitrate solutions (exp #12) at 20°C and low-concentrated Cl solutions at $T \geq 400$°C (exp #9&11) are strikingly similar to those calculated for the octahedral CdO_6 and tetrahedral CdO_2Cl_2 clusters, respectively, both in shape and amplitude of the white line (feature A, Fig. 7) and the second resonance at 26,735 eV (feature C, Fig. 7). This cluster stoichiometry is also in agreement with the numbers of Cl and O deduced from EXAFS modeling (Table 2). The experimental spectrum of the

18.2m Cl solution at 20°C (exp #15) and the theoretical spectrum of the [CdCl$_4$] cluster have similar energy positions of features A and C (Fig. 7) but different amplitudes. Thus, the presence of octahedral CdCl$_5$(H$_2$O)$^{3-}$ and/or pentahedral CdCl$_5$$^{3-}$/CdCl$_4$(H$_2$O)$^{2-}$ cannot be excluded in this solution. The detection of oxygen atoms by EXAFS and Wavelet analyses in this solution seems to corroborate this hypothesis.

Figure 7. Comparison of selected experimental XANES spectra indicated in the figure with those of different cadmium chloride hydrated complexes calculated using the FDMNES code (see also Fig. 6). Calculated spectra are corrected by 1-2 eV on the energy scale to facilitate the comparison with experiment. Vertical dashed lines labeled A and C indicate the major spectral features discussed in the text (sections 3.3 and 3.4).

The experimental XANES spectra of the most concentrated NaCl solution at $T \geq 200°C$ (m_{Cl} = 5.2m, exp #5, Fig. 7) and moderately concentrated solutions at $T \geq 300°C$ ($m_{Cl} \geq 0.8m$, exp #2, 4, 7, not shown) are very similar to that of the $CdOCl_3$ cluster both in white-line shape and amplitude of the 26,735-eV feature (Feature C, Fig. 7). However, these features are different both for any octahedral-like cluster and the tetrahedral $CdCl_4$ cluster that shows a far more pronounced 26,735-eV resonance (Fig. 7). Although the experimental spectra may be interpreted equally as a sum of CdO_2Cl_2 and $CdCl_4$ clusters, the striking constancy of the experimental spectra, from ~300 to 450°C, for the concentrated Cl solution above 200°C apparent in Fig. 2b,c, is unlikely to be interpreted by the simultaneous presence of two or more species. This is because the species fractions in a mixture should be expected to evolve significantly in such a wide T and m_{Cl} range, which would result in substantial changes in the overall spectral shape. Rather, this constancy points out to the dominant presence of a *single species*, very likely $Cd(H_2O)Cl_3^-$, in all solutions at $m_{Cl} \geq$ ~ 1m and $T > 200°C$. Similarly, the strong resemblance of the spectra of low-concentrated solutions at 400°C (exp #9&11 and 3, $m_{Cl} \leq$ ~0.1m) to that of the tetrahedral CdO_2Cl_2 (Fig. 7) and the absence of evolution in the experimental spectra at $T \geq$ 400°C (Fig. 2b) both indicate the predominance of a single species, most likely $Cd(H_2O)_2Cl_2^0$. This is also in agreement with the constancy within errors of the EXAFS-derived average values of N and R for O/Cl neighbors around Cd in these low-Cl solutions at 400°C, corresponding to the average stoichiometry $CdCl_2O_2$ (Table 2, Fig. 3c, 5a).

Note, however, that the absolute values of $N_{Cl/O}$ derived from EXAFS fits exhibit large uncertainties (at least ~20-30% of the N value, Tables 1-4) prohibiting unambiguous conclusions about the stoichiometry of dominant species on the sole basis of EXAFS results. Consequently, the absolute number of neighbors derived from EXAFS should be taken with care and the major support of the Cd speciation scheme in Cl-bearing solutions stems from the XANES spectra analysis, which is far more sensitive to the cluster stoichiometry and geometry than EXAFS. The 'apparent' simplicity of the Cd speciation scheme at supercritical temperatures (400 and 450°C) inferred in this study, with the dominant presence of tetrahedral $Cd(H_2O)_2Cl_2^0$ and $Cd(H_2O)Cl_3^-$, is also in agreement with the general tendencies of metal-chloride complexation at elevated temperatures driven by the decrease of dielectric constant and increase of thermal vibration that reinforce the stability of neutral and low-charged compact species for most metals (e.g., Crerar et al., 1985; Wood and Samson, 1998; references therein). Consequently, based on the arguments discussed in this section, we assumed the di- and tri-chloride Cd species as the main contributors to the Cd speciation at $T \geq 400°C$. This speciation model has been adopted in the analysis of solubility data below.

4. RESULTS FROM SOLUBILITY EXPERIMENTS

4.1. Solubility in pure water at 350-400°C

The solubilities of monteponite (CdO) measured in pure water using the flexible-cell reactor at 350 and 400°C and pressures 300-400 bar are reported in Table 5. Our solubility values cluster around $10^{-7}m$ Cd and show no significant trends in the investigated T and P ranges. They are ~2 orders of magnitude lower than theoretical predictions based on ambient T-P data and HKF-model correlations for Cd^{2+} and its hydroxide species (Shock et al., 1997). Similar discrepancies between experiment and HKF model predictions were recently found for the solubilities of ZnO, Cu_2O and CuO solids in H_2O

at $T \geq 300°C$ (Bénézeth et al., 2002; Palmer et al., 2004). The low Cd solubilities found in this study demonstrate that Cd^{2+} and its hydroxide complexes are likely to be negligible in most high T-P hydrothermal solutions of near-neutral pH containing chloride ligands, in good agreement with the XAS results of our study. Consequently, Cd^{2+} and its hydroxide complexes were not considered in the further thermodynamic analysis of data in Cl-bearing solutions where solubilities are at least 3 orders of magnitude higher.

Table 5. Solubility of monteponite (CdO, cubic) in pure water measured using the flexible-cell reactor sampling technique.

Run	Duration (days)	T°C	P, bar	m_{Cd} (mol/kg H_2O)
CT350-A1	2	350	400	1.3×10^{-7}
CT350-A3	4	350	400	1.3×10^{-7}
CT350-A4	4	350	400	6.2×10^{-8}
CT350-A5	7	350	400	1.1×10^{-7}
CT350-A6	7	350	400	1.1×10^{-7}
CT400-A7	9	400	400	2.0×10^{-7}
CT400-A8	11	400	400	7.9×10^{-8}
CT400-A9	14	400	300	1.1×10^{-7}

4.2. Solubility in Cl-bearing solutions at 400°C and 600 bar

Solubilities of CdO and CdS in concentrated NaCl-HCl solutions measured using the batch-reactor quenching technique are reported in Tables 6 and 7. In HCl-free runs, the CdO solubility increases from ~0.004 to 0.06 m_{Cd} with increasing NaCl concentration from ~0.1 to ~5m. These solubility values in near-neutral NaCl solutions are 3-5 orders of magnitude higher than those in pure water demonstrating the formation of stable Cd chloride complexes. As demontrated in Fig. 8, our measured values of solubility in HCl-free solutions are at least two orders of magnitude higher than HKF-model predictions based on the stability constants of Cd-Cl complexes at low T-P (Sverjensky et al., 1997). In HCl-bearing runs CdO solubilities are systematically higher in comparison to HCl-free solutions, but are much less sensitive to the total Cl concentration. For example, in runs with 0.10-0.13m HCl, with increasing NaCl concentration from 0.1 to 4.6m the CdO solubility increases by only a factor of two (from 0.05 to 0.1m Cd, Table 6). In addition, the solubilities measured in HCl-bearing runs are somewhat closer to the HKF-model predictions (Sverjensky et al., 1997). This apparent 'discrepancy' with the HCl-free runs is unlikely to be related to eventual differences in the Cd speciation, since XAS analyses yield identical results in HCl-free and HCl-bearing NaCl solutions (Table 2). Rather it is related to the high solubilities of CdO at acidic conditions, comparable to the initial HCl concentrations (Table 6). As a result, CdO dissolution "neutralizes" almost all initial HCl, so that the Cd_{total}/$H^+_{initial}$ ratio in solution in equilibrium with $CdO_{(s)}$ is close to ~0.5 (Table 6) over a wide m_{Cl} range, and is thus only weakly dependent on the variations of ligand number and stability of Cd complexes formed. This was demonstrated by equilibrium calculations in the system $CdO_{(s)}$-HCl-NaCl-H_2O showing that the measured solubilities in HCl-rich runs may be described within experimental uncertainties using a wide range of stability constant values for a given Cd-Cl complex. Consequently, the HCl-rich runs yield larger uncertainties than those from HCl-free solutions when deriving Cd-Cl stability constants (see Tables EA4-2).

Table 6. Solubility of monteponite (CdO, cubic) in H_2O-NaCl-HCl solutions at 400°C and 600 bar measured using the batch-reactor quenching technique.

Run	Duration (days)	m_{NaCl}	m_{HCl}	Mass of fluid (g)	Weight loss CdO (g)	m_{Cd} (WL)	m_{Cd} (AAS)	m_{Cd} (mean)
H-101	*10*	*0*	*0*	*11.566*	*0.0115*	*0.0077*	*0.00045*	*0.0041*
F-104	*7*	*0.12*	*0*	*13.780*	*0.0116*	*0.0066*	*0.0009*	*0.0038*
F-101	7	0.77	0	12.838	0.0581	0.0370	0.0082	0.0226
O-1	13	2.26	0	16.920	0.0588	0.0308	0.0270	0.0289
F-4	7	5.13	0	19.609	0.1237	0.0643	0.0621	0.0632
O-25*	13	0	0.10	10.390	0.0062	0.0047	0.0191	0.0119
O-24	13	0.10	0.10	10.330	0.0619	0.0472	0.0451	0.0462
O-5	13	1.08	0.11	15.060	0.1263	0.0699	0.0552	0.0626
O-4	13	2.31	0.11	16.750	0.1395	0.0741	0.0783	0.0762
O-101	4	2.31	0.12	14.380	0.1929	0.1200	0.0828	0.1014
O-23	13	4.63	0.13	14.100	0.1070	0.0755	0.1085	0.0920

WL = solubility determination by weight-loss of the solid after experiment; AAS = solubility determination by atomic absorption analyses of Cd concentration in the quenched solution after experiment; m_{Cd} (mean) = average value between WL and AAS methods.

Runs *in italic* show the detection limit of the technique.

*This run was not included in the analysis because it showed secondary solid phases formation (see text).

Figure 8. Solubility of monteponite (CdO, cubic) solubility in aqueous solution at 400°C and 600 bar as a function of NaCl concentration. Symbols denote experimental data points of this study; solid curve corresponds to the solubility generated using $CdCl_2^0$ and $CdCl_3^-$ stability constants derived in this study (Table 8); dashed curve stands for the calculated solubility using the HKF parameters for Cd-Cl species from Sverjensky et al. (1997).

The solubility of greenockite (CdS) measured in similar HCl-free NaCl-bearing solutions is ~10 times lower than that of montepomite (Table 7). Note, however, that CdS solubilities in these solutions are close to the detection limit of the technique (section 2.4) and thus are a subject of larger uncertainties than those for CdO. Nevertheless, the measured solubilities are at least 100 times higher than theoretical predictions (Sverjensky et al., 1997). In HCl-bearing solutions, CdS solubilities are still 10-50 times higher than those in HCl-free solutions and closer to those of CdO. This shows again that the solubility in acidic solutions is imposed by initial H^+ concentration, thus rendering these experiments little sensitive to the exact stoichiometry and stability of Cd-Cl species formed in solution. Despite these limitations, both CdO and CdS solubilities measured in Cl-bearing aqueous solutions at 400°C differ significantly from the existing predictions and thus require revision of the available thermodynamic properties of Cd-Cl species. This was achieved by combining bulk solubility data with the XAS results obtained in this study on the stoichiometries of the dominant aqueous Cd-Cl complexes.

Table 7. Solubility of greenockite (CdS, hexagonal) in H_2O-NaCl-HCl solutions at 400°C and 600 bar measured using the batch-reactor quenching technique.

Run	Duration (days)	m_{NaCl}	m_{HCl}	Mass of fluid (g)	Weight loss CdS (g)	m_{Cd} (WL)	m_{Cd} (AAS)	m_{Cd} (mean)
F-24	*7*	*0*	*0*	*10.086*	*0.0018*	*0.0012*	*0.0011*	*0.0011*
F-25	*7*	*0.12*	*0*	*10.301*	*0.0042*	*0.0028*	*0.0019*	*0.0023*
F-1	*7*	*0.77*	*0*	*15.105*	*0.0041*	*0.0020*	*0.0010*	*0.0015*
S-1	13	1.06	0	15.497	NA	NA	0.0037	0.0037
S-23	13	2.27	0	12.107	NA	NA	0.0042	0.0042
F-23	7	2.29	0	12.113	0.0039	0.0025	0.0018	0.0022
F-103	7	5.13	0	18.091	0.0076	0.0038	0.0020	0.0029
S-4	13	5.23	0	19.601	NA	NA	0.0081	0.0081
S-25	13	2.27	0.02	12.603	NA	NA	0.0096	0.0096
S-5	13	2.28	0.11	16.385	NA	NA	0.0401	0.0401
S-101	13	0	0.10	11.823	NA	NA	0.0445	0.0445
S-103	13	0.10	0.10	12.008	NA	NA	0.0303	0.0303

See footnote of Table 6. NA = not available.

5. DERIVATION OF THE STABILITY CONSTANTS OF CADMIUM CHLORIDE COMPLEXES AT 400°C

5.1. Thermodynamic conventions, standard states, and databases

The standard state of solid phases and H_2O is unit activity for the pure phase at all *T* and *P*. For aqueous species, the reference state convention corresponds to unit activity coefficient for a hypothetical 1*m* solution whose behavior is ideal. All concentrations are expressed as the number of moles of each solute per one kg of water (mol/kg H_2O), and equilibrium constants are given on the molality scale. Activity coefficients of charged species are calculated using the Debye-Hückel

equation with the extended term parameter b_{NaCl}, which is a function of T and P (Oelkers and Helgeson, 1990), those of uncharged complexes were assumed to be one. Calculations of solid phase solubilities and aqueous species distribution and stabilities were performed using the HCh software package (Shvarov and Bastrakov, 1999; Shvarov, 2008) based on the minimization of the Gibbs free energy of the system. The HKF equation-of-state parameters of the main fluid constituents H_2O, H^+, OH^-, Na^+, Cl^-, $NaCl^0$ and $NaOH^0$ were adopted from the SUPCRT database (Johnson et al., 1992, http://geopig.asu.edu); and those for HCl^0 and H_2S^0/HS^- were taken from Tagirov et al. (1997) and Akinfiev et al. (2008), respectively. The thermodynamic properties of monteponite (CdO, cubic) were taken from Naumov et al. (1974) and Wagman et al. (1982) and those of greenockite (CdS, hexagonal) from Robie and Hemingway (1995). The ion Cd^{2+} and hydroxide complexes $Cd(OH)_n^{2-n}$ were excluded from modeling of experiments in Cl-bearing solutions because of their negligible contribution ($< 10^{-6}m$ Cd), as shown by our solubility measurements (section 4.1).

5.2. Calculation of the stability constants of $CdCl_2^0$ and $CdCl_3^-$ aqueous complexes at 400°C and 600 bar

The limited number of solubility runs and the low sensitivity of the solubility to Cl concentrations do not allow direct identification of the dominant Cd-Cl complexes from these experiments (see section 4.2.). The choice of Cd aqueous species for the description of measured solubilities was thus guided by our XANES and EXAFS results (see section 3.4), which indicate the dominant presence of $CdCl_2^0$ and $CdCl_3^-$ at $T \geq 300$°C in the wide range of Cl concentrations. In accordance with these findings, at 400°C/600 bar and Cl concentrations below $0.2m$, CdO and CdS solubilities may be described by the formation of the neutral $CdCl_2^0$ complex according to:

$$CdO_{(s)} + 2HCl^0(aq) = CdCl_2^0(aq) + H_2O \qquad K_1 \qquad (1)$$
$$CdS_{(s)} + 2HCl^0(aq) = CdCl_2^0(aq) + H_2S^0(aq) \qquad K_2 \qquad (2)$$

Water molecules identified by XAS analyses in this species are omitted in these equations because they have no effect on solubilities in solutions with water activity close to 1. Unfortunately, the close to the detection limit solubility of both CdO and CdS in dilute Cl solutions in batch-reactor experiments does not allow accurate derivation of equilibrium constants of reactions (1) and (2). Alternatively, these values may be obtained from XAS data and the stability of $CdCl_3^-$ derived from solubility data below.

For concentrated Cl solutions ($> 0.8m$), a single dominant species, $CdCl_3^-$, was chosen in accordance with our XANES and EXAFS results. Its stability constants were calculated from 14 batch-reactor solubility experiments on CdO and CdS in solutions with $m_{Cl} \geq \sim 0.8$ (Tables 6, 7, EA4-2, EA4-3) adopting the following reactions:

$$CdO_{(s)} + 2HCl^0(aq) + Cl^- = CdCl_3^- + H_2O \qquad K_3 \qquad (3)$$
$$CdS_{(s)} + 2HCl^0(aq) + Cl^- = CdCl_3^- + H_2S^0(aq) \qquad K_4 \qquad (4)$$

The calculated values of $\log_{10}K_3$ and $\log_{10}K_4$ are 13.9±0.6 and 6.6±1.0, respectively. Both constants are ~6 orders of magnitude greater than existing HKF predictions (Sverjensky et al., 1997). Note that the derived K_3 and K_4 values yield similar Gibbs free energies for $CdCl_3^-$, thus further confirming the validity of our measurements yielding self-consistent results on the dominant $CdCl_3^-$ complex in H_2O-

Cl-S-bearing solutions at $m_{Cl} > 0.8$ from independent solubility measurements of two different solid phases (CdO and CdS).

The amounts of $CdCl_3^-$ and $CdCl_2^0$ species obtained from LCF analyses of XANES spectra of Cl-bearing solutions (Table EA4-1) allow calculation of the stability constant of the reaction:

$$CdCl_2^0(aq) + Cl^- = CdCl_3^- \qquad\qquad K_5 \qquad\qquad (5)$$
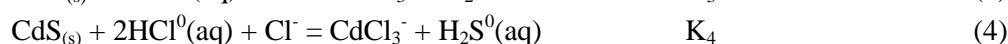
The derived value of $\log_{10}K_5$ is 1.0±0.2 and almost independent of ionic strength because the activity coefficients of the two charged species, Cl^- and $CdCl_3^-$ cancel in this reaction. This value is one order of magnitude higher than HKF-model predictions ($\log_{10}K_5$= -0.003 at 400°C/600 bar, Sverjensky et al., 1997). The latter theoretical value implies the predominance of $CdCl_2^0$ in concentrated Cl solutions (Fig. 1b), which is inconsistent with both XANES and solubility data of this study. Using the values of K_3, K_4 and K_5 derived in this study, the equilibrium constants of reactions (1) and (2) may be calculated, $\log_{10}K_1 = 12.9\pm0.8$, $\log_{10}K_2 = 5.6\pm1.2$ at 400°C/600 bar (Table 8). Again, these values are ~5 orders of magnitude higher than the HKF estimations.

Table 8. Stability constants of cadmium chloride complexes derived in this study.

Reaction		T°C	P, bar	$\log_{10}$ K
$CdO_{(s)} + 2HCl^0(aq) = CdCl_2^0(aq) + H_2O$	(1)	400	600	12.9±0.8[a]
$CdS_{(s)} + 2HCl^0(aq) = CdCl_2^0(aq) + H_2S^0(aq)$	(2)	400	600	5.6±1.2[a]
$CdO_{(s)} + 2HCl^0(aq) + Cl^- = CdCl_3^- + H_2O$	(3)	400	600	13.9±0.6[b]
$CdS_{(s)} + 2HCl^0(aq) + Cl^- = CdCl_3^- + H_2S^0(aq)$	(4)	400	600	6.6±1.0[b]
$CdCl_2^0(aq) + Cl^- = CdCl_3^-$	(5)	400	600	1.0±0.2[c]

[a] Calculated from (b) and (c).
[b] Derived from solubility measurements.
[c] Derived from LCF modeling of XANES spectra.

The derived stability constants of the major $CdCl_2^0$ and $CdCl_3^-$ species allow predictions of Cd-bearing minerals solubilities in supercritical hydrothermal fluids over a wide salinity range. It can be seen in Fig. 8 that the solubility of $CdO_{(s)}$ in a NaCl solution at 400°C/600 bar calculated using our stability constants is at least 1.5 orders of magnitude higher than the HKF-model predictions, which are based on stability constants of Cd-Cl species below 100°C and theoretical correlations amongst thermodynamic parameters (Sverjensky et al., 1997). Consequently, we do not recommend using the available HKF equation-of-state parameters for estimating the Cd speciation and solubility at supercritical *T-P* even for dilute solutions. The XAS data obtained in this study also indicate that these low-temperature based HKF predictions are not satisfactory even at low-to-moderate temperatures (*T* ~ 100-300°C) leading to underestimation of the $CdCl_2^0$ and $CdCl_3^-$ (section 3.2). It is clear, however, that more experimental data on Cd speciation and solubility in a wide *T-P* range are required to provide a self consistent set of data for the major Cd chloride complexes and to accurately model the transport of this metal by hydrothermal fluids.

5.3. Computational uncertainties

The derivation of stability constants of Cd-Cl species in saline supercritical fluids is a subject of different types of uncertainties whose principal sources are briefly addressed below. The first source of uncertainties on the equilibrium constants values reported in Table 8 stems from solubility determinations. Errors on CdO solubilities in concentrated NaCl solutions (> $1m$ Cl) do not exceed 10% of the total dissolved Cd, which corresponds to < 0.1 unit of log K. This uncertainty mostly reflects the variations between the weight-loss method and AAS analyses of Cd in the quenched solutions. The uncertainty increases significantly at lower NaCl concentrations where CdO solubilities approach the detection limit of the quenching technique, and errors may attain ~0.5 log units of m_{Cd} for some runs (e.g., run F-101, Table 6; S-1, Table 7). These uncertainties are also elevated for all CdS runs because of the lower CdS solubility.

The second source of errors stems from the derivation of Cd species identities and fractions from XANES spectra. Only major species could be identified from both LCF fits of experimental XANES spectra and their comparisons with theoretical spectra calculated using quantum-chemistry methods. From XANES spectra analysis, the maximal contribution of species like $CdCl^+$ and $CdCl_4^{2-}$ in our solutions at 400°C is expected to be < 10% of total Cd for each complex. Errors of LCF for the spectra of 0.1-2.6m Cl solutions at 400°C using the $CdCl_2$ and $CdCl_3^-$ spectra from the low (0.04m) and high (5.2m) concentrated solutions as end-members are typically 5-10% of the species fraction. These variations, put together, result in an error of 0.2-0.4 log unit for the value of K_5.

The third potential source of uncertainties stems from the choice of the major species thermodynamics and the activity coefficients of neutral and charged species in H_2O-NaCl/LiCl-HCl-$CdCl_2$ solutions. At ambient T-P, the contribution of this type of error is weak for dilute solutions (< 1m Cl). However, it increases dramatically at high ionic strength for concentrated LiCl solutions (7-18m Cl), attaining errors of more than 30% of the species fraction when computing the Cd species distribution using the extended Debye-Hückel model for activity coefficients (e.g., Fig. 1a). Errors in calculated activity coefficients were discussed in detail by Pokrovski et al. (2006) in their work of Sb speciation and solubility at conditions similar to our study. For high T-P solutions, the domain of applicability of the Debye-Hückel model is wider than at ambient conditions (e.g., Oelkers and Helgeson, 1990). In addition, the activity coefficients of charged species (Cl^- and $CdCl_3^-$) are almost canceled in reactions (3), (4), and (5), so that corresponding constants are only weakly dependent to the ionic strength. Although the activity coefficients of most neutral species are virtually unknown in supercritical saline fluids, they are expected to cancel, at least partly, in reactions (1) and (2). This source of uncertainties remains, however, poorly constrained and, following Pokrovski et al. (2006), we thus expect an additional potential error of the order of ±~0.2 log units for the K values reported in Table 8.

6. COMPARISON WITH ZINC AND GEOLOGICAL IMPLICATIONS

The speciation of cadmium in Cl-bearing hydrothermal fluids investigated in this study may be compared with that of its chemical analog, zinc, which was a subject of many solubility and spectroscopic studies. Although zinc is also transported in the form of tetrahedral-like chloride complexes in saline solutions at elevated T (Buback, 1983; Marley and Gaffney, 1990; Anderson et al., 1995; Mayanovic et al., 1999; Bassett et al, 2000; Liu et al., 2007), there exist significant differences as to the stoichiometry and stability of Zn and Cd chloride complexes. The major Zn-Cl

complexes identified by Raman and X-ray absorption spectroscopy at T above 300°C are $ZnCl_2(H_2O)_2^0$ and $ZnCl_4^{2-}$ (Buback, 1983; Mayanovic et al., 1999; Bassett et al., 2000; Liu et al., 2007), whereas $CdCl_2(H_2O)_2^0$ and $CdCl_3(H_2O)^-$ are the dominant Cd forms as shows this study. Considering the higher affinity of Cd than Zn for the chloride ligand particularly at elevated T (Arhlard, 1979; Crerar et al., 1985), the "absence" of tetrachloride water-free complex for Cd may seem somewhat strange. However, our both XANES and EXAFS analyses reveal unambiguously the presence of oxygen in the first coordination shell of Cd even in highly concentrated Cl solutions and the number of chlorine atoms systematically less than 4 over the wide range of T and m_{Cl}. This strongly suggests that the $CdCl_4^{2-}$ complex is never a dominant Cd species in high T-P solutions. The weak stability of this doubly charged species at elevated temperatures is in line with the general tendency to form compact and uncharged or weakly charged chloride complexes with lower ligand numbers with increasing T and decreasing the fluid dielectric constant (e.g., Brimhall and Crerar, 1987). It should be noted here that the available in situ spectroscopic data for Zn-Cl complexes at elevated T are rather scarce and do not cover systematically the sufficient range of m_{Cl} and T to reveal unambiguously changes in species structures and stoichiometries as a function of these parameters. One of the major limitations is the difficulty to detect, using EXAFS spectroscopy, the presence of oxygen atoms (i.e., water or hydroxide ligands) in the first coordination shell of the metal in its chloride complexes. In addition, the interpretation of XAS spectra using LCF and PCA approaches in case of a mixture of species in solution is rather delicate, and should be confirmed by thermodynamic analyses as it is shown in this study. In view of these limitations, the interpretation of spectroscopic results in terms of $ZnCl_4^{2-}$ at T above 300°C would require more support from further systematic studies. The existence of $ZnCl_4^{2-}$ species as the major form of Zn in high-T Cl-bearing solutions is also questioned by available solubility data (Ruaya and Seward, 1986; Bourcier and Barnes, 1987; Plyasunov and Ivanov, 1991; Cygan at al., 1994; Wesolowski et al., 1998). Consequently, because of large uncertainties on the $ZnCl_4^{2-}$ stability and structure in high T-P hydrothermal fluids, we ignored this complex and adopted in further analyses the thermodynamic properties of the much better known mono-, di- and tri-chloride species as compiled by Sverjensky et al. (1997) and reported in the SUPCRT database (Jonhson et al., 1992, http://geopig.asu.edu/).

The combination of these data with those obtained in this study for Cd-Cl complexing provides new insights about the behavior and fractionation of these metals in hydrothermal systems. Despite large similarities in the identity and structure of the major di- and tri- chloride Zn and Cd complexes, the stability of Cd-Cl species are significantly greater than that of their Zn analogs, particularly at elevated T. This may lead to preferential fluid enrichment by Cd compared to Zn at high T and salt contents. This is demonstrated by calculations of Zn and Cd concentrations in a NaCl-bearing fluid at 400°C and 600 bar in equilibrium with a Cd-bearing sphalerite containing 0.01 wt% of CdS in isomorphic substitution (Fig. 9). These calculations were performed using the thermodynamic properties of Zn-Cl complexes discussed above, those of Cd-Cl species from this study, and assuming an ideal solid solution between shpalerite ZnS and greenockite CdS. It can be seen in Fig. 9 that the Cd/Zn weight ratio in the fluid phase increases from ~0.001 to 1 when the fluid salinity increases from ~0.001m to 1m NaCl. This systematic increase is consistent with observations of Cd *vs* Zn enrichments in volcanic gases (e.g., Symonds et al., 1993) and hydrothermal minerals precipitated from base-metal ore forming saline fluids (e.g., Cook et al., 2009). Although the *absolute* values of Cd/Zn ratios in the fluid phase from our model cannot be compared directly with those found in

natural systems, because the latter depend on many factors like the Cd content in the solubility-controlling minerals, the nature of Cd-bearing minerals, or the fluid sources, the *relative changes* of Cd/Zn ratio calculated with increasing NaCl concentration in the fluid are very similar to those found in natural systems. For example, the range of the Cd/Zn fluid ratios predicted by our model is fairly comparable to that between the mean crustal value (Cd/Zn ~ 0.001-0.003, Rudnick and Gao, 2003) and high-temperature HCl-rich volcanic gases that show the highest Cd enrichment (Cd/Zn ~ 0.1-1.0, Pennisi et al., 1988; Symonds et al., 1993). Thus, the Cd/Zn ratio in fluids and hydrothermal minerals might be a useful indicator of chloride content and salinity during the evolution of hydrothermal-volcanic fluids. More data on Cd contents from natural fluid inclusions and ore deposits are required for the quantitative use of this potential geochemical tracer.
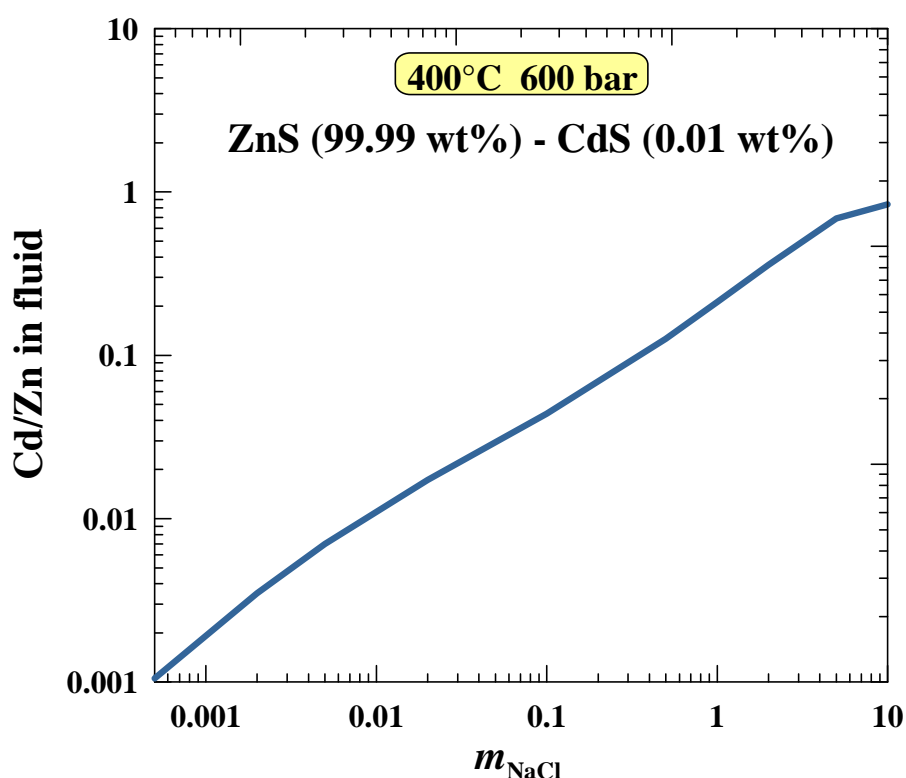
Figure 9. Cd/Zn mass ratio in a fluid in equilibrium with a Cd-bearing sphalerite as a function of NaCl concentration at 400°C and 600 bar. Calculations were performed using the stability constants of Zn-Cl and Cd-Cl species from Sverjensky et al. (1997) and this study, respectively.

7. CONCLUDING REMARKS

In this work we combined in situ XAS spectroscopy with solubility measurements to characterize systematically over a wide T-P range (20 - 450°C, 1 - 600 bar), acidity ($1 \leq pH \leq 8$), and chloride concentration ($0.01 \leq m_{Cl} \leq 18$) the identity and stability of aqueous Cd complexes responsible for the Cd transport by saline hydrothermal fluids. Results show that the Cd speciation in acidic to neutral aqueous chloride solutions at low and moderate temperatures ($T \leq 300°C$) is dominated by a range of octahedral $CdCl_m(H_2O)_{6-m}^{2-m}$ ($0 \leq m \leq 1$-2) and tetrahedral $CdCl_m(H_2O)_{4-m}^{2-m}$ ($2 \leq m \leq 3$-4) species, with the latter complexes becoming predominant with increasing T and m_{Cl}. The average number of Cl atoms in the dominant complexes derived from our XAS data demonstrates reasonable agreement with thermodynamic calculations performed with reported in literature stability constants of cadmium chloride complexes for ambient T, but is systematically higher for elevated T. At supercritical T-P in a wide range of Cl concentrations (to at least ~5m NaCl), the Cd aqueous speciation is controlled by two tetrahedral-like species, $CdCl_2(H_2O)_2^0$ and $CdCl_3(H_2O)^-$, having average interatomic Cd-Cl distances of 2.41±0.02 and 2.46±0.03 Å, respectively, and Cd-O distances of 2.30±0.05Å.

The stoichiometry and structure of these Cd complexes are similar to their base metal analogs Pb, Ni, Co, Cu, Ag forming tetrahedral-like weakly charged or neutral chloride species having 1 to 3 Cl ligands, which is in agreement with the general tendencies of metal-chloride complexing with increasing T (e.g., Seward, 1984; Susak and Crerar, 1985; Brimhall and Crerar, 1987; Berry et al., 2007). The predominance of low-charged low-Cl ligand number species for Cd found in our study disagrees with the dominant formation of $ZnCl_4^{2-}$ and $FeCl_4^{2-}$ suggested from XAS measurements in supercritical NaCl solutions (Mayanovic et al., 1999; Testemale et al., 2009). This discrepancy might reflect both physical limitations of X-ray absorption spectroscopy for analyzing light and disordered atomic shells, composed of light atoms (O vs Cl) and the lack of extensive solubility data for Cd and many other metals in supcritical NaCl-rich solutions that are the main transporting media for these metals.

The stability constants of $CdCl_2(H_2O)_2^0$ and $CdCl_3(H_2O)^-$ species derived via combination of XAS and solubility data at 400°C and 600 bar are ~6 orders of magnitude greater than theoretical predictions from low-temperature data (Sverjensky et al., 1997). Our new data were used to model Cd/Zn ratios in hydrothermal fluids. The modeling shows that at 400°C and 600 bar the Zn/Cd ratio in a fluid in equilibrium with a Cd-bearing sphalerite increases by ~3 orders of magnitude with increasing NaCl concentration from 0.001 to 1.0m. Thus, the Cd/Zn ratio might be a sensitive indicator of salinity changes in hydrothermal processes.

In this study, the combination of complementary in situ spectroscopy and solubility methods with quantum-chemistry and thermodynamic modeling has allowed generation of new data on Cd speciation and solubility in high-T hydrothermal fluids, which is difficult to obtain using a single approach. These first data will be helpful for improving thermodynamic models for high T-P fluids and for better interpreting Cd behavior in hydrothermal-volcanic environments. Work is currently in progress to obtain more experimental and natural data for both Cd and Zn, and to develop a physical-chemical and geochemical basis for the use of Cd/Zn ratios as a tracer of hydrothermal and volcanic processes.

References

Ackerman, J.J.H., Orr, T.V., Bartushka, V.J., Maciel, G.E., 1979. Effect of halide complexation of cadmium (II) on cadmium-113 chemical shifts. J. Am. Chem. Soc.101, 341-347.

Akinfiev, N.N., Baranova, N.N., Zotov, A.V. and Tagirov, B.R., 2008. Thermodynamic description of aqueous components in the system Cu-Ag-Au-S-Se-O-H in the range of temperatures 0-600°C and pressures 1-3000 bars. In: Ryabchikov, I. D., Shapovalov, Yu. B., Osadchii, E. G. (Eds.), Experimental Studies of Endogenic Processes. Publishing Office of the Institute of the Problems of Chemical Physics, Chernogolovka, Russia, pp. 184-203 (in Russian).

Anderko, A., Pitzer, K.S., 1993. Equation-of-state representation of phase equilibria and volumetric properties of the system NaCl-H$_2$O above 573K. Geochim. Cosmochim. Acta 57, 1657-1680.

Anderson, A.J., Mayanovic, R.A., Bajt, S., 1995. Determination of the local structure and speciation of zinc in individual hypersaline fluid inclusions by micro-XAFS. The Can. Minaral. 33, 499-508.

Anderson, B.G., Irish, D.E., 1988. Vibration spectral studies of solutions at elevated temperatures and pressures. X. Raman spectral study of aqueous bromide solutions at 25°C and 200°C. J. Sol. Chem. 17, 763-775.

Archer, D.A., 1998. Thermodynamic properties of import to environmental processes and remediation. I. Previous thermodynamic property values for cadmium and some of its compounds. J. Phys. Chem. Ref. Data 27, 915-946.

Arhland, S., 1979. Complex formation in protic and aprotic media. Pure Appl. Chem. 51, 2019-2039.

Axelsson, M.D., Rodushkin, I., 2001. Determination of major and trace elements in sphalerite using laser ablation double focusing sector field ICP-MS. J. Geochem. Explor. 72, 81-89.

Baes, C.F., Mesmer, R.E. Jr., 1976. The Hydrolysis of Cations. Wiley, New York, 489.

Bakker, R.J., 2003. Package FLUIDS 1. Computer programs for analyses of fluid inclusions data and for modelling bulk fluid properties. Chem. Geol. 194, 3-23.

Barnes, H.L., 1979. Solubilities of Ore Minerals. In: Barrnes, H.L. (Ed.), Geochemistry of Hydrothermal Ore Deposits, 2nd edition. Wiley, pp. 404-459.

Bassett, W.A., Anderson A.J., Mayanovic R.A., Chou I.M., 2000. Hydrothermal diamond anvil cell for XAFS studies of first-row transition elements in aqueous solution up to supercritical conditions. Chem. Geol. 167, 3-10.

Bénézeth, P., Palmer, D., Wesolowski, D.J., Xiao, C., 2002. New measurements of zinc oxide from 150 to 350°C. J. Solution Chem. 31, 947-973.

Berry, A.J., Harris, A. C., Kamenetsky, V.S., Newville, M., Sutton, S. R., 2009.The speciation of copper in natural fluid inclusions at temperatures up to 700°C. Chem. Geol. 259, 2-7.

Bol, W., Gerrits, G.J.A., van Panthaleon van Eck, C.L., 1970. The hydration of divalent cations in aqueous solutions. An X-ray investigation with isomorphous replacement. J. Appl. Cryst. 3, 486-492.

Bourcier, W. L., Barnes, H. L., 1987. Ore solution chemistry-VII. Stabilities of chloride and bisulfide complexes of zinc to 350°C. Econ. Geol. 82, 1839–1863.

Brimhall, G.H., Crerar, D.A., 1987. Ore fluids: magmatic to supergene. Rev. Miner. 17, 235-321.

Brugger, J., Etschmann, B., Liu, W., Testemale, D., Hazemann, J.L., Emerich, H., Van Beek, W., Proux, O., 2007. An XAS study of the structure and thermodynamics of Cu(I) chloride complexes in brines up to high temperature (400°C, 600 bar). Geochim. Cosmochim. Acta 71, 4920-4941

Buback, M., 1983. The vibration spectrum of pure water and aqueous solutions to high pressure and temperatures. In: Somiya, S. (Ed.), Proceedings of the First International Symposium on Hydrothermal Reactions. Gakuzyutu Bunken Fukyukai, Tokyo, pp. 24-36.

Caminiti, R., Johanson, G., 1981. On the structures of cadmium sulphate complexes in aqueous solutions. Acta Chem. Scand. A 35, 373-381.

Caminiti, R., Licheri, G., Paschina, G. Piccaluga, G., Pinna, G., 1980. X-ray diffraction and structural properties of aqueous solutions of divalent metal-chlorides. Z. Naturforsch 35, 1361-1367.

Caminiti, R., Cuca, P., Radnai, T., 1984. Investigation on the structure of cadmium nitrate aqueous solutions by X-ray diffraction and Raman spectroscopy. J. Phys. Chem., 88, 2382-2386.

Chapligin, I.V., Mozgova, N.N., Mozhov, A.V., Koporulina, E.V., Bernhardt, H.J., Bryzgalov, I.A., 2007. Minerals of the system ZnS-CdS from fumaroles of the Kudriavy volcano, Iturup Island, Kuriles, Russia. Can. Mineral. 45, 709-722.

Cook, N.J., Ciobanu, C.L., Pring, A., Skinner, W., Shimizu M., Danyushevsky, L., Saini-Eidukat, B., Melcher, F., 2009. Trace and minor elements in sphalerite: A LA-ICPMS study. Geochim. Cosmochim. Acta. 73, 4761-4791.

Crerar, D., Wood, S., Brantley, S., 1985. Chemical controls on solubility of ore-forming minerals in hydrothermal solutions. Can. Miner. 23, 333-352.

Cygan, G. L., Hemley, J. J., D'Angelo, W. M., 1994. An experimental study of zinc chloride speciation from 300 to 600°C and 0.5–2.0 kbar in buffered hydrothermal solutions. Geochim. Cosmochim. Acta 58, 4841–4855.

Daskalakis, K.D., Helz, G.R., 1992. Solubility of cadmium sulphide, greenockite. in sulfidic waters at 25°C. Environ. Sci. Technol. 26, 2462-2468.

Drakenberg T., Björk N.O., Portanova R., 1978. Cadmium-113 nuclear magnetic resonance study of cadmium (II) halide complexes in water and dimethyl sulfoxide. Phys. Chem., 82, 2423-2426.

Gottesmann, W., Kampe, A., 2007. Zn/Cd ratios in calsilicate-hosted sphalerite ores at Tumurtijn-ovoo, Mongolia. Chem. Erde – Geochim. 67, 323-328.

Heinrichs, H., Schulz-Dobrick, B., Wedepohl K.L., 1980. Terrestrial geochemistry of Cd, Bi, Tl, Pb, Zn and Rb. Geochim. Cosmochim. Acta 44, 1519–1533.

Johnson, J.W., Oelkers, E.H., Helgeson, H.C., 1992. SUPCRT92: a software package for calculating the standard molal thermodynamic properties of minerals, gases, aqueous species, and reactions from 1 to 5000 bar and 0 to 1000°C. Comput. Geosci. 18, 899-947; http://geopig.asu.edu/index.html/.

Joly, Y., 2001. X-ray absorption near-edge structure calculations beyond the muffin tin approximation. Phys. Rev. B63, 125120.

Kelly, S.D., Hesterberg, D., Ravel, B., 2008. Analysis of soils and minerals using X-ray absorption specroscopy. Methods of Soil Analysis. Part 5. Mineralogical Methods, p. 387-463, Soil Sci. Soc. Am., Madison, USA.

Kimball, G. E., Shortley, G.H., 1934. The numerical solution of Schrödinger's equation. Phys. Rev. 45, 815-820.

Liu, W., Etschmann, B., Foran, G., Shelley, M., Brugger, J., 2007. Deriving formation constants for aqueous metal complexes from XANES spectra: Zn^{2+} and Fe^{2+} chloride complexes in hypersaline solutions. Amer. Mineral. 92, 761-770.

Macdonald, A.C., Sikka, S.K., 1969. The determination of the crystal structure of cadmium nitrate tetradeuterate by means of neutron anomalous dispersion measurements. Acta Cryst. B 25, 1804-1811.

Malinowski E.R., 1977. Depermination of the number of factors and the experimental error in a data matrix. Anal. Chem 49, 612-317.

Malinowski E.R., 1991. Factor Analysis in Chemistry. 2nd Edition, Wiley.

Marley, N.A., Gaffney, J.S., 1990. Laser Raman spectral determination of zinc halide complexes in aqueous solutions as a function of temperature and pressure. Applied Spectroscopy 44, 469-476.

Martell, E., Smith, R.M., 1998. Critically Selected Stability Constants of Metal Complexes, NIST Standard Reference Database 46, Version 5.0, NIST, Gaithersburg, MD 20899.

Mayanovic, R.A., Anderson, A.J., Bassett, W.A., Chou I.-M., 1999. XAFS measurements on zinc chloride aqueous solutions from ambient to supercritical conditions using the diamond anvil cell. J. Synchrotron Rad. 6, 195-197.

Mosselmans, J.F.W., Schofield, P.F., Charnock, J.M., Garner, C.D., Pattrick, R.A.D., Vaughan, D.J., 1996. X-ray absorption studies of metal complexes in aqueous solution at elevated temperatures. Chem. Geol. 127, 339-350.

Munoz, M., Argoul, P., Farges F., 2003. Continuous cauchy wavelet transform analyses of EXAFS spectra: a qualitative approach. Amer. Mineral. 88, 694-700.

Naumov, G. B., Ryzhenko, B. N., Khodakovskii, I. L., 1974. Handbook of Thermodynamic Data. U.S Geol. Surv. Rep. USGS-WRD-74-001.

Newville, M., 2001. IFEFFIT: interactive XAFS analysis and FEFF fitting. J. Synchrotron Radiat. 8, 322–324.

Oelkers, E.H., Helgeson, H.C, 1990. Triple-ion anions and polynuclear complexing in supercritical electrolyte solutions. Geochim. Cosmochim. Acta 54, 727-738.

Ohtaki, H., Maeda, M., Ito, S., 1974. X-ray diffraction studies of aqueous solutions of cadmium perchlorate and sodium tetraiodocadmate. Bull. Chem. Soc. Jpn. 47, 2217-2221.

Palmer, D.A., Bénézeth, P., Simonson, J.M., 2004. The solubility of copper oxides around the water/steam cycle. Power Plant Chem. 6, 81-88.

Palmer, D.A., Corti, H.R., Groteword, A., Hyde K. E., 2000. Potentiometric measurements of the thermodynamics of cadmium(II) chloride complexes to high temperatures. In: Steam, Water, and Hydrothermal Systems: Physics and Chemistry Meeting the Needs of Industry. Proceedings of the 13th International Conference on the Properties of Water and Steam (eds P.R. Tremaine, P.G.Hill, P.V. Balakrishnan), NRC Research Press, Ottawa.

Paschina, G., Piccaluga, G., Pinna, G., Magini, M., 1983. Chloro-complexes formation in $ZnCl_2$-$CdCl_2$ aqueous solutions: An X-ray diffraction study. J. Chem. Phys. 78, 5745-5749.

Pennisi, M., LeCloarec, M.F., Lambert, G., Le Roulley, J.C., 1988. Fractionation of metal in volcanic emissions. Earth Planet. Sci. Lett. 88, 284-288.

Plyasunov, A.V., Ivanov, I.P., 1991. The solubility of zinc oxide in sodium chloride solutions up to 600°C and 1000 bar. Geochem. Int. 28, 77-90.

Pokrovski, G.S., Schott, J., 1998. Experimental study of the complexation of silicon and germanium with aqueous organic species: implications for germanium and silicon transport and Ge/Si ratio in natural waters. Geochim. Cosmochim. Acta 62, 3413-3428.

Pokrovski, G.S., Martin, F., Hazemann, J.-L., Schott, J., 2000. An X-ray absorption fine structure spectroscopy study of germanium-organic ligand complexes in aqueous solution. Chem. Geol. 163, 151-165.

Pokrovski, G.S., Kara, S., Roux, J., 2002a. Stability and solubility of arsenopyrite, FeAsS, in crustal fluids. Geochim. Cosmochim. Acta 66, 2361-2378.

Pokrovski, G.S., Schott, J., Hazemann, J.-L., Farges, F., Pokrovsky, O.S, 2002b. An X-ray absorption fine structure and nuclear magnetic resonance spectroscopy study of gallium-silica complexes in aqueous solution. Geochim. Cosmochim. Acta 66, 4203-4322.

Pokrovski, G.S., Roux, J., Hazemann, JL., Testemale, D., 2005. An X-ray absorption spectroscopy study of argutite solubility and aqueous Ge(IV) speciation in hydrothermal fluids to 500°C and 400 bar. Chem. Geol. 217, 127-145.

Pokrovski, G.S., Borisova, A.Y., Roux, J., Hazemann, J.-L., Petdang, A., Tella, M., Testemale, D., 2006. Antimony speciation in saline hydrothermal fluids: A combined X-ray absorption fine structure spectroscopy and solubility study. Geochim. Cosmochim. Acta 70, 4196-4214.

Pokrovski, G.S., Borisova, A.Y., Harrichoury, J.C., 2008 The effect of sulfur on vapor–liquid fractionation of metals in hydrothermal systems. Earth Planet. Sci. Lett. 266, 345-362.

Pokrovski, G.S., Tagirov, B.R., Schott, J., Bazarkina, E.F., Hazemann, J.L., Proux, O., 2009a. An in situ X-ray absorption spectroscopy study of gold-chloride complexing in hydrothermal fluids. Chem. Geol. 259, 17-29.

Pokrovski, G.S., Tagirov, B.R., Schott, J., Hazemann, J.L., Proux, O., 2009b. A new view on gold speciation in sulfur-bearing hydrothermal fluids from in situ X-ray absorption spectroscopy and quantum-chemical modeling. Geochim. Cosmochim. Acta 73, 5406-5427.

Proux, O., Biquard, X., Lahera, E., Menthonnex, J.-J., Prat, A., Ulrich, O., Soldo, Y., Trevisson, P., Kapoujyan, G., Perroux, G., Taunier, P., Grand, D., Jeantet, P., Deleglise, M., Roux, J.-P., Hazemann, J-L., 2005. FAME: a new beamline for X-ray absorption investigations of very diluted systems of environmental, material and biological interests. Phys. Scripta T 115, 970-973.

Proux, O., Nassif, V., Prat, A., Ulrich, O., Lahera, E., Biquard, X., Menthonnex, J.-J., Hazemann, J.-L., 2006. Feedback system of a liquid-nitrogen-cooled double-crystal monochromator: design and performances. J. Synchrotron Radiat. 13, 59–68.

Ravel, B., Newville, M., 2005. ATHENA, ARTEMIS, HEPHAESTUS: data analysis for X-ray absorption spectroscopy using IFEFFIT. J. Synchrotron Radiat. 12, 537–541.

Rickard, D., Luther III, G.W., 2006. Metal sulfide complexes and clusters. Rev. Miner. Geochem. 61, 421-504.

Robie, R.A., Hemingway, B.S., 1995. Thermodynamic Properties of Minerals and Related Substances at 298.15 K and 1 bar (10^5 pascals) pressure and at high temperatures. U. S. Geol. Surv. Bull. 2131, 461.

Rossberg, A., Reich, T., Bernhard G., 2003. Complexation of uranium(VI) with protocatechuic acid – application of iterative transformation factor analysis to EXAFS spectroscopy. Anal. Bioanal. Chem., 376, 631-638.

Ruaya, J. R., Seward, T. M., 1986. The stability of chloro-zinc (II) complexes in hydrothermal solutions up to 350°C. Geochim. Cosmochim. Acta 50, 651–662.

Rubin, K., 1997. Degassing of metals and metalloids from erupting seamount and mid-ocean ridge volcanoes: Observations and predictions. Geochim. Cosmochim. Acta 61, 3525-3542.

Rudnick, R.L., Gao, S., 2003. Composition of the Continental Crust. In: Holland, H.D., Turekian, K.K. (Eds.), Treatise on Geochemistry, Elsevier, Amsterdam.

Rudolph, W.W., Pye, C.C., 1998. Raman spectroscopic measurements and ab initio molecular orbital studies of cadmium(II) hydration in aqueous solution. J. Phys. Chem. B, 102, 3564-3573.

Seward, T.M., 1984. The formation of lead(II) chloride complexes to 300°C: A spectrophotometric study. Geochim. Cosmochim. Acta 48, 121-134.

Seward, T.M., Driesner, T., 2004. Hydrothermal solution structure: experiments and computer simulations. In: Palmer, D.A., Fernández-Prini, R., Harvey, A.H. (Eds.), Aqueous Systems at Elevated Temperatures and Pressures: Physical Chemistry in Water, Steam and Hydrothermal Solutions. Elsevies Ltd., pp. 149-182.

Sharps, J.A., Brown Jr., G.E., Stebbins J.F., 1993. Kinetics and mechanism of ligand exchange of Au(III), Zn(II), and Cd(II) chlorides in aqueous solutions: An NMR study from 28-98°C. Geochim. Cosmochim. Acta 57, 721-731.

Shock, E.L., Sassani, D.C., Willis, M., Sverjensky, D.A., 1997. Inorganic species in geological fluids: Correlations among standard molal thermodynamic properties of aqueous ions and hydroxide complexes. Geochim. Cosmochim. Acta 61, 907-950; http://geopig.asu.edu/index.html/.

Shvarov, Yu. S., 2008. HCh: New potentialities for the thermodynamic simulation of geochemical systems offered by windows. Geochem. Intl. 46, 834-839; http://www.geol.msu.ru/deps/geochems/soft/index.html/

Shvarov, Yu. S., Bastrakov, E.N., 1999. HCh: a software package for geochemical equilibrium modelling. User's Guide. Australian Geological Survey Organization, Record 199/25.

Ste-Marie, J., Torma, A.E., Gübeli, A.O., 1964. The stability of thiocomplexes and solubility products of metal sulphides. Can. J. Chem. 42, 662-668.

Susak, N.J., Crerar, D.A., 1985. Spectra and coordination changes of transition metals in hydrothermal solutions: Implication for ore genesis. Geochim. Cosmochim. Acta 49, 555-564.

Sverjensky, D.A., Shock, E.L. Helgeson, H.C., 1997. Prediction of the thermodynamic properties of aqueous metal complexes to 1000°C and 5 kb. Geochim. Cosmochim. Acta 61, 1359-1412; http://geopig.asu.edu/index.html/.

Symonds, R.B., Reed, M.H., 1993. Calculation of multicomponent chemical equilibria in gas-solid-liquid systems: calculation methods, thermochemical data, and applications to studies of high-temperature volcanic gases with examples from Mount St. Helen. Amer. J. Sci. 293, 758-864.

Tagirov, B.R., Suleimenov O.M., Seward, T.M., 2007. Zinc complexation in aqueous sulfide solutions: Determination of the stoichiometry and stability of complexes via ZnS(cr) solubility measurements at 100°C and 150 bars. Geochim. Cosmochim. Acta 71, 4942-4953.

Tagirov, B.R., Zotov, A.V., Akinfiev, N.N., 1997. Experimental study of the dissociation of HCl from 350 to 500°C and from 500 to 2500 bar. Thermodynamic properties of HCl^0 (aq). Geochim. Cosmochim. Acta 61, 4267-4280.

Testemale, D., Argoud, R., Geaymond, O., Hazemann, J-L., 2005. High pressure/high temperature cell for X-ray absorption and scattering techniques. Rev. Sci. Instrum. 76, 043905-043909.

Testemale, D., Brugger, J., Liu, W., Etschmann, B., Hazemann, J-L., 2009. In-situ X-ray absorption study of iron(II) speciation in brines up to supercritical conditions. Chem. Geol. 264, 295-310.

Testemale, D., Hazemann, JL., Pokrovski, G.S., Joly, Y., Roux, J., Argoud, R., Geaymond, O., 2004. Structural and electronic evolution of As(III) atomic environment in hydrothermal solutions: an EXAFS and XANES investigation, J. Phys. Chem. 121, 8973–8982.

Tombros, S., St. Seymour, K., Spry, P.G., Williams-Jones, A., 2005. Greenockite and zincian greenockite in epithermal polymetallic Ag-Au-Te mineralization, Tinos Island, Hellas: description and conditions of formation. Neues Jahrb. Mineral., Abh. 182, 1-9.

Wagman, D.B., Evans, W.H., Parker, V.B., Schumm, R.H., Halow, I., Bailey, S.M., Shurney, K.L., and Nuttall, R.L., 1982. The NBS tables of chemical thermodynamic properties. J. Phys. Chem. Ref. Data 11, Supplement 2.

Wang, F., Tessier, A., 1999. Cadmium complexation with bisulfide. Environ. Sci. Technol. 33, 4270-4277.

Waters, D.N., Short, E.L., Tharwat, M., Morris, D.F.C., 1973. Vibrational spectra of some halide complexes of zinc(II), cadmium(II), and mercury(II) in solution in tri-n-butyl phosphate. J. Molec. Struc. 17, 389-400.

Wesolowski, D. J., Bénézeth, P., Palmer, D. A., 1998. ZnO solubility and Zn^{2+} complexation by chloride and sulfate in acidic solutions to 290°C with in-situ pH measurement. Geochim. Cosmochim. Acta 62, 971–984.

Wood, S.A., Samson I.M., 1998. Solubility of ore minerals and complexation of ore metals in hydrothermal solutions: Rev. Econ. Geol. 10, 33-77.

Zabinsky, S.I., Rehr, J.J., Ankudinov, A., Albers, R.S., Eller, M.J., 1995. Multiple scattering calculations of X-ray absorption spectra. Phys. Rev. B 52, 2995-3009.

Supplementary Electronic Information

Electronic annex 1

Results of LCF and PCA modeling of XANES spectra derived in this study and their comparison with available thermodynamic predictions (Sverjensky et al., 1997) at 20, 100, 200, 300, and 400°C

1.1. XANES spectra of Cl-bearing solutions at ambient conditions

Linear combination fit (LCF) analyses of experimental XANES spectra were performed using the Athena program (Ravel and Newville, 2005) and different spectral standards chosen amongst the experimental solutions (see below). The LCF modeling was complemented by principal component analysis (PCA) using the ITFA program (Rossberg et al., 2003) on different series of XANES spectra.

LCF analyses demonstrate that XANES spectra of all Cl-bearing solutions at 20°C may be described as the sum of fractions of spectra from the solutions with the lowest (0.04m, 'octahedral') and highest (18.2m, 'tetrahedral') Cl concentration (Table EA1-1). This is also in agreement with the results of principal component analysis (PCA, Rossberg et al., 2003), which identified only 2 independent components in the nine spectra examined at 20°C, despite the presence of at least 5 chemical species in the investigated Cl-concentration range (Fig. 1a, main text). The fractions of 'octahedral' *vs.* 'tetrahedral' group of species derived from LCF and PCA for dilute ($m_{Cl} \leq 0.12m$) and concentrated solutions ($m_{Cl} \geq 5.2m$) are in good agreement, within ~10% of species fraction, with those corresponding to the sum of [Cd^{2+} + $CdCl^{+}$] and [$CdCl_3^{-}$ + $CdCl_4^{-}$] calculated using the available stability constants for these species (see Fig. 1a in the main text; Table EA1-1). This confirms the observations in previous studies of octahedral-to-tetrahedral changes of cadmium chloride complexes geometry with increasing m_{Cl}, with Cd^{2+} and $CdCl^{+}$ being octahedral and $CdCl_3^{-}$ and $CdCl_4^{-}$ tetrahedral (e.g., Drakenberg et al., 1978; Arhland, 1979; Paschina et al., 1983; Sharps et al., 1993). The agreement between species fractions from LCF and thermodynamics is, however, worse at intermediate Cl contents ($0.7 \leq m_{Cl} \leq 5.23m$) in the domain of the $CdCl_2^{0}$ species predominance (Fig. 1a; Table EA1-1). It may be due to the simultaneous existence in solution of both octahedral and tetrahedral configurations for the $CdCl_2^{0}$ species and thus partly explain the disagreement among available studies as to the geometry of the $CdCl_2^{0}$ complex at ambient conditions (Arhland, 1979; Caminiti et al., 1980; Paschina et al., 1983; Anderson and Irish, 1988). It should be noted, however, that the choice of the "tetrahedral" standard may also impact the LCF results. It can be seen in Fig. 2 of the main text that the XANES spectra of the octahedral species Cd^{2+} and $CdCl^{+}$ are very similar, but the spectral differences amongst $CdCl_2^{0}$, $CdCl_3^{-}$, and $CdCl_4^{2-}$ are much more significant (see also section 3.3 in the main text). Thus, the LCF results depend weakly on the octahedral standard, but may be affected significantly by the chosen tetrahedral standard. For example, the use of the 5.23m Cl solution (exp #5) with the dominant $CdCl_2^{0}$ + $CdCl_3^{-}$ + $CdCl_4^{2-}$ species (Fig. 1a of the main text) as the tetrahedral end-member instead of the 18.2m Cl solution (exp #15) with the dominant $CdCl_4^{2-}$, yields better agreement between LCF-derived and thermodynamically predicted octahedral versus tetrahedral species fractions, if $CdCl_2^{0}$ is assumed to be tetrahedral. It should be noted however, that the stepwise

formation of complexes results in very smooth spectral changes. Consequently, in the absence of spectral standards for each Cd-Cl species neither LCF nor PCA allow accurate extraction of individual species fractions from a mixture of complexes.

1.2. XANES spectra of Cl-bearing solutions at elevated temperatures

Similarly to the ambient-temperature solutions, LCF modeling of both XANES and EXAFS spectra *at moderate temperatures (100°C ≤ T ≤ 300°C)* shows that the whole series of solutions at each *T* may be described by the sum of two end-members, the solution with the lowest Cl concentration or the Cl-free nitrate solution which represents the standard for the 'octahedral' species such as Cd^{2+} or $CdCl^+$ having very similar XANES spectra, and the concentrated Cl solution (5.2*m* - 18.2*m* Cl), which is used as the 'tetrahedral' standard, with $CdCl_3^-$ and $CdCl_4^{2-}$ as the dominant species, according to HKF model predictions. Despite the uncertainties as to the choice of tetrahedral end-member spectra, we observed systematically a higher fraction of tetrahedral species at *T* ~ 100-300°C derived from LCF modeling as compared to HKF predictions (Sverjensky et al., 1997; Tables EA1-1,-2,-3,-4). This indicates that the stabilities of octahedral species Cd^{2+} and $CdCl^+$ according to Sverjensky et al. (1997) are likely to be overestimated at *T ≥* 100°C.

Like their lower temperature analogs, the spectra *at supercritical temperatures (400°C and 450°C)* can also be described as a sum of those from the nitrate solution as the "octahedral" standard and the 5.2*m* NaCl solution as the "tetrahedral" standard. Such fits yield, however, too high fractions of octahedral $Cd^{2+}/CdCl^+$ (up to 35% of total Cd) at Cl concentrations of 0.1-1.0*m* (Table EA1-5). The elevated amounts of such species at supercritical *T* disagree with *a)* HKF-model predictions indicating less than 10-15% of $CdCl^+$ species fraction (Fig. 1b) whereas our average N_{Cl} values found from EXAFS spectra are systematically higher than these predictions (Table EA1-7); *b)* general tendency to form low-coordinated and weakly charged or uncharged complexes at high *T* (Crerar et al., 1985); *c)* our solubility results, implying negligible amounts of Cd^{2+} at 350-400°C; *d)* tetrahedral-like shapes of all solutions at *T ≥* 300°C (see Fig. 2 in the main text). Again, this analysis demonstrates the difficulty of identifying spectra of individual species and quantifying unambiguously their fractions in the case of species mixture exhibiting gradual spectra changes upon the increase of ligation number (N_{Cl}) in the complex.

Alternatively, both XANES and EXAFS spectra of all Cl solutions *at 400 and 450°C* can be accurately described (within ±5-10% of each species fraction) as a sum of different fractions of two 'tetrahedral' spectra from solutions with 0.04*m* and 5.23*m* Cl (Table EA1-6). A sharp change from the predominance of the 0.04*m* 'end-member' (≥ 70% of total Cd) to the predominance of the 5.23*m* 'end-member' takes place between ~0.1 and 0.8*m* Cl in solution (Table EA1-6). Above 2*m* Cl, all investigated solutions demonstrate very similar XANES spectra (90±10% of the 5.23*m* standard, Table EA1-6). As explained in the main text, this observation together with the striking similitude of ab-initio calculated spectra of [CdO_2Cl_2] and [$CdOCl_3$] clusters with the experimental spectra from low-Cl and high-Cl solutions at 400 and 450°C strongly suggests that the Cd speciation at supercritical temperatures (400 and 450°C) is likely to be dominated by tetrahedral $Cd(H_2O)_2Cl_2^0$ and $Cd(H_2O)Cl_3^-$.

This simplicity might be 'questioned' by PCA analyses using the IND function (Malinowski, 1977; Rossberg et al., 2003), which yields 4 'independent' factors in the Cd-Cl XANES data matrix at

400-450°C. However, any attempt to isolate these components from XANES spectra using PCA algorithms failed, likely because of *a)* the insufficient contrast between different XANES spectra exhibiting very smooth changes as a function of m_{Cl} at these *T*, *b)* the presence of small fractions of other complexes, and *c)* the increasing spectral noise at high *T* and eventual minor amplitude and energy shifts between spectra during their acquisition which might result in an overestimation of the number of independent factors by PCA (e.g., Malinowski, 1991). In contrast, simple LCF analyses with XANES spectra of the most dilute (0.04*m* Cl) and most concentrated (5.2*m* Cl) solutions as the independent components allowed description within errors of the whole spectral set at these *T* (Table EA1-6).

Supplementary Table EA1-1. Linear combination fits of Cd-bearing solutions **at 20°C** and their comparison with the distribution of $CdCl_{1-4}$ complexes according to Sverjensky et al. (1997)*.

exp#	mCl	LCF of XANESspectra		mol % of total Cd*				
		% «octa»	% «tetra»	Cd^{2+}	$CdCl_1^+$	$CdCl_2^0$	$CdCl_3^-$	$CdCl_4^{2-}$
12	0.00	100	0	100	0	0	0	0
9, 11	0.04	89	11	37	58	5	<1	<1
3	0.12	78	22	20	64	15	1	<1
7	0.77	61	39	3	35	43	16	3
4	2.30	38	62	<1	8	32	33	27
2	2.67	31	69	<1	8	32	32	28
5	5.23	18	82	<1	1	15	27	57
13	7.29	7	93	<1	<1	5	14	81
14	11.52	3	97	<1	<1	2	8	90
15	18.21	0	100	<1	<1	1	6	93
error		±10	±10					

LCF=linear combination fits of XANES spectra; %«octa»= fraction of the octahedral standard with $Cd(H_2O)_6^{2+}$ from the spectrum of $Cd(NO_3)_2$-HNO_3 solution, exp #12 at 20°C; %«tetra»= fraction of the tetrahedral standard, presumably $CdCl_3^-$ + $CdCl_4^{2-}$, from the spectrum of 18.2*m* Cl solution, exp #15 at 20°C;
*Mole fractions (in mol %) of $CdCl_n^{2-n}$ in experimental Cd-bearing Na/LiCl-HCl aqueous solutions are calculated using HKF model parameters of Sverjensky et al. (1997).

Supplementary Table EA1-2. Linear combination fits of Cd-bearing solutions **at 100°C** and their comparison with the distribution of $CdCl_{1-4}$ complexes according to Sverjensky et al. (1997).

exp#	m_{Cl}	LCF of XANESspectra		mol % of total Cd*				
		% «octa»	% «tetra»	Cd^{2+}	$CdCl_1^+$	$CdCl_2^0$	$CdCl_3^-$	$CdCl_4^{2-}$
12	0.00	100	0	100	0	0	0	0
9, 11	0.04	86	14	39	57	4	<1	<1
3	0.12	71	29	19	64	16	1	<1
7	0.77	46	54	6	49	38	8	<1
4	2.30	16	84	2	26	45	24	3
2	2.67	9	91	2	25	45	25	4
5	5.23	0	100	1	13	37	38	11
error		±10	±10					

%«octa»= fraction of the octahedral standard with $Cd(H_2O)_6^{2+}$ from the spectrum of the $Cd(NO_3)_2$-HNO_3 solution, exp #12 at 100°C; %«tetra»= fraction of the tetrahedral standard, presumably $CdCl_2^0$ + $CdCl_3^-$ + $CdCl_4^{2-}$, taken from the spectrum of the 5.23*m* Cl solution, exp #5 at 100°C.

Supplementary Table EA1-3. Linear combination fits of Cd-bearing solutions **at 200°C** and their comparison with the distribution of $CdCl_{1-4}$ complexes according to Sverjensky et al. (1997).

exp#	m_{Cl}	LCF of XANESspectra		mol % of total Cd*				
		% «octa»	% «tetra»	Cd^{2+}	$CdCl_1^+$	$CdCl_2^0$	$CdCl_3^-$	$CdCl_4^{2-}$
12	0.00	100	0	100	0	0	0	0
9, 11	0.04	76	24	17	72	11	<1	<1
3	0.12	57	43	8	66	25	1	<1
7	0.77	24	76	2	37	51	10	<1
4	2.30	5	95	1	19	52	26	2
2	2.67	0	100	1	18	52	27	2
5	5.23	0	100	<1	10	44	40	6
error		±5	±5					

%«octa»= fraction of the octahedral standard with $Cd(H_2O)_6^{2+}$ from the spectrum of $Cd(NO_3)_2$-HNO_3 solution, exp #12 at 200°C; %«tetra»= fraction of the tetrahedral standard, presumably $CdCl_2^0$ + $CdCl_3^-$ + $CdCl_4^{2-}$, taken from the spectrum of 5.23m Cl solution, exp #5 at 200°C.

Supplementary Table EA1-4. Linear combination fits of Cd-bearing solutions **at 300°C** and their comparison with the distribution of $CdCl_{1-4}$ complexes according to Sverjensky et al. (1997).

exp#	m_{Cl}	LCF of XANES spectra		mol % of total Cd				
		% «octa»	% «tetra»	Cd^{2+}	$CdCl_1^+$	$CdCl_2^0$	$CdCl_3^-$	$CdCl_4^{2-}$
12	0.00	100	0	100	0	0	0	0
9, 11	0.04	54	46	3	58	39	1	<1
3	0.12	38	62	1	40	56	3	<1
7	0.77	15	85	<1	15	66	18	<1
4	2.30	5	95	<1	7	55	36	2
2	2.67	< 5	> 95	<1	7	54	37	2
5	5.23	0	100	<1	4	42	48	7
error		±5	±5					

%«octa»= fraction of the octahedral standard with $Cd(H_2O)_6^{2+}$ from the spectrum of $Cd(NO_3)_2$-HNO_3 solution, exp #12 at 300°C; %«tetra»= fraction of the tetrahedral standard, presumably $CdCl_3^-$, taken from the spectrum of 5.23m Cl solution, exp #5 at 300°C.

Supplementary Table EA1-5. Linear combination fits **"Octa + Tetra"**of Cd-bearing solutions **at 400°C** and their comparison with the distribution of $CdCl_{1-4}$ complexes according to Sverjensky et al. (1997).

exp#	m_{Cl}	LCF of XANES spectra		mol % of total Cd				
		% «octa»	% «tetra»	Cd^{2+}	$CdCl_1^+$	$CdCl_2^0$	$CdCl_3^-$	$CdCl_4^{2-}$
12**	0.00	100	0	100	0	0	0	0
9, 11	0.04	35	65	<1	20	78	2	<1
3	0.12	24	76	<1	15	82	3	<1
7	0.77	11	89	<1	5	70	24	1
4	2.30	< 5	> 95	<1	3	46	44	8
2	2.67	0	100	<1	2	43	44	10
5	5.23	0	100	<1	1	23	50	26
error		±5	±5					

%«octa»= fraction of the octahedral standard, $Cd(H_2O)_6^{2+}$ from the spectrum of the $Cd(NO_3)_2$-HNO_3 solution, exp #12 at 300°C; %«tetra»= fraction of the tetrahedral standard, presumably $CdCl_3^-$, taken from the spectrum of the 5.23m Cl solution, exp #5 at 400°C.
**at 300°C

Supplementary Table EA1-6. Linear combination fits **"Tetra + Tetra"** of Cd-bearing solutions **at 400°C** and their comparison with the distribution of $CdCl_{1-4}$ complexes according to Sverjensky et al. (1997).

exp#	m_{Cl}	LCF of XANES spectra		mol % of total Cd*				
		%«tetra-1»	%«tetra-2»	Cd^{2+}	$CdCl_1^+$	$CdCl_2^0$	$CdCl_3^-$	$CdCl_4^{2-}$
9, 11	0.04	100	0	<1	20	78	2	<1
3	0.12	70	30	<1	15	82	3	<1
7	0.77	25	75	<1	5	70	24	1
4	2.30	10	90	<1	3	46	44	8
2	2.67	10	90	<1	2	43	44	10
5	5.23	0	100	<1	1	23	50	26
error		±10	±10					

«tetra-1»= fraction of the tetrahedral species $CdCl_2^0$ standard taken from the spectrum of 0.04m Cl solution, exp #9,11 at 400°C; %«tetra-2»= fraction of the tetrahedral species $CdCl_3^-$ standard taken from the spectrum of 5.23m Cl solution, exp #5 at 400°C. The results of this LCF modeling were used in the derivation of the stability constant of the reaction: $CdCl_2^0(aq) + Cl^- = CdCl_3^-$. The details are given in Electronic Annex 4.

Supplementary Table EA1-7. Average number of chloride atoms around Cd in NaCl-HCl-CdCl$_2$ aqueous solutions **at 20, 200, 300, and 400°C** derived from EXAFS analysis, compared with the average Cl ligation number calculated according to Sverjensky et al. (1997).

exp#	m_{Cl}	N_{Cl}, 20°C		N_{Cl}, 100°C		N_{Cl}, 200°C		N_{Cl}, 300°C		N_{Cl}, 400°C	
		EXAFS	HKF	EXAFS	HKF	EXAFS	HKF	EXAFS	HKF	EXAFS	HKF
9,11	0.04	0.8	0.7	1.2	0.7	1.3	0.9	2.2	1.4	2.3	1.8
3	0.12	1.0	1.0	1.3	1.0	1.6	1.2	2.5	1.7	2.5	1.9
7	0.77	1.6	1.8	2.1	1.5	2.6	1.7	3.2	2.0	3.3	2.2
4	2.30	2.6	2.8	3.1	2.0	3.4	2.1	3.4	2.3	3.4	2.6
2	2.67	2.8	2.8	3.1	2.1	3.2	2.1	3.2	2.3	2.9	2.6
5	5.23	3.0	3.4	3.1	2.5	3.3	2.4	3.0	2.6	3.4	3.0
error		±0.6		±0.6		±0.6		±0.6		±0.6	

Electronic annex 2

Statistical analysis of O/Cl and O+Cl models of EXAFS spectra of selected experimental solutions at 20 and 400°C

The EXAFS statistical parameters for evaluating the goodness of fit are $\mathcal{R}$-factor, which is the fraction of misfit between experiment and model, and reduced chi square χ_ν^2, which takes into account the degree of freedom and uncertainties of each data point (see Kelly et al., 2008 for details). The statistical significance of a model including both O and Cl in the first Cd shell in comparison with a model containing a single shell of O or Cl was analyzed using the equation of Kelly et al. (2008):

$$\frac{\chi_{\nu i}^2}{\chi_{\nu f}^2} - 1 \geq 2 \cdot \sqrt{\frac{2}{\nu}}$$

where $\chi_{\nu i}^2$ = reduced-chi-square of the single-shell model (only Cl or O); $\chi_{\nu f}^2$ = reduced-chi-square of the mixed-shell model (Cl +O); ν = degree of freedom in the fit (N_{ind} - N_{var} ≈ 3 for all spectra). For the EXAFS spectra derived in this study this equation corresponds to:

$$\frac{\chi_{\nu i}^2}{\chi_{\nu f}^2} - 1 \geq 1.6$$

Thus, all the EXAFS fits with a single (O or Cl only) atomic shell were compared with the corresponding fit using a mixed O+Cl atomic shell. It can be seen in the last column of Table EA2-1 that the inclusion of both Cl and O atoms in the fit results in statistically significant improvement of the EXAFS model for all studied solutions, except that of the lowest Cl concentration (0.04m) at ambient temperature (see section 3.2.2 in the main text for discussion).

Supplementary Table EA2-1. Comparison of structural and statistical parameters of EXAFS fits with a single (O or Cl only) and mixed (O+Cl) first atomic shell around Cd for selected solutions.

	Atom	N, atoms	R, Å	σ^2, Å^2	Δe, eV	$\mathcal{R}$-factor	χ_v^2	$\dfrac{\chi_{vi}^2}{\chi_{vf}^2}$
exp #9&11 (total Cl = 0.04m) 20°C								
Model-1 (Cl only)	Cl	9.1±1.5	2.43±0.02	0.007	-12.1	0.020	205	7.1
Model-2 (O only)	O	5.5±0.7	2.30±0.05	0.007	3.2	0.010	89	1.3
Model-3 (Cl + O)	Cl	0.8±0.7	2.48±0.05	0.010	3.4	0.005	77	
	O	5.7±0.7	2.30±0.05	0.010				
exp #9&11 (total Cl = 0.04m) 450°C								
Model-1 (Cl only)	Cl	1.8±0.7	2.36±0.03	0.006	-8.9	0.095	779	143.6
Model-2 (Cl + O)	Cl	2.3±0.7	2.41±0.01	0.010	3.2	0.009	65	
	O	2.2±0.7	2.30±0.05	0.010				
exp #5 (total Cl = 5.23m) 20°C								
Model-1 (Cl only)	Cl	3.3±0.8	2.49±0.02	0.010	-2.9	0.035	963	109.6
Model-2 (Cl + O)	Cl	3.0±0.6	2.52±0.01	0.009	3.1	0.004	92	
	O	2.0±0.7	2.30±0.05	0.009				
exp #5 (total Cl = 5.23m) 450°C								
Model-1 (Cl only)	Cl	3.0±0.7	2.46±0.01	0.009	2.4	0.021	325	33.7
Model-2 (Cl + O)	Cl	3.4±0.6	2.46±0.01	0.011	3.4	0.004	56	
	O	1.0±0.7	2.30±0.05	0.008				
exp #15(total Cl =18.21m) 20°C								
Model-1 (Cl only)	Cl	3.8±0.5	2.53±0.02	0.009		0.020	136	8.7
Model-2 (Cl + O)	Cl	4.1±0.6	2.53±0.02	0.011	3.0	0.005	46	
	O	0.9±0.7	2.30±0.05	0.007				

See footnote of Tables 1 and 2 in the main text for explanation of EXAFS parameters.

Electronic annex 3

Continuous Cauchy Wavelet Transform analysis of EXAFS spectra of selected Cd-Cl solutions

Supplementary Figure 1. Continuous Cauchy Wavelet Transform (CCWT, Munoz et al., 2003) of Cd K-edge EXAFS spectra of 0.04m and 5.2m of total Cl solutions at 20 and 450°C and 600 bar, and of 7.3m and 18.2m of total Cl solutions at 20°C and 1 bar. Each graph represents k^2-weighted experimental spectrum, its Fourier Transform magnitude, and CCWT modulus showing the localization of each EXAFS contribution in (k, R) space. The color intensity is proportional to the magnitude of the CCWT modulus (blue=low, red to brown=high). The vertical lines indicate the maximum intensity positions for O and Cl neighbors around the Cd absorber. It can be seen that except the 0.04m Cl solution at 20°C where the Cl contribution is weak (< 1 Cl atom, see Table 2 in the main text and Electronic Annex 2 above), all other spectra clearly indicate the presence of both O and Cl atoms in the first atomic shell of Cd aqueous complexes.
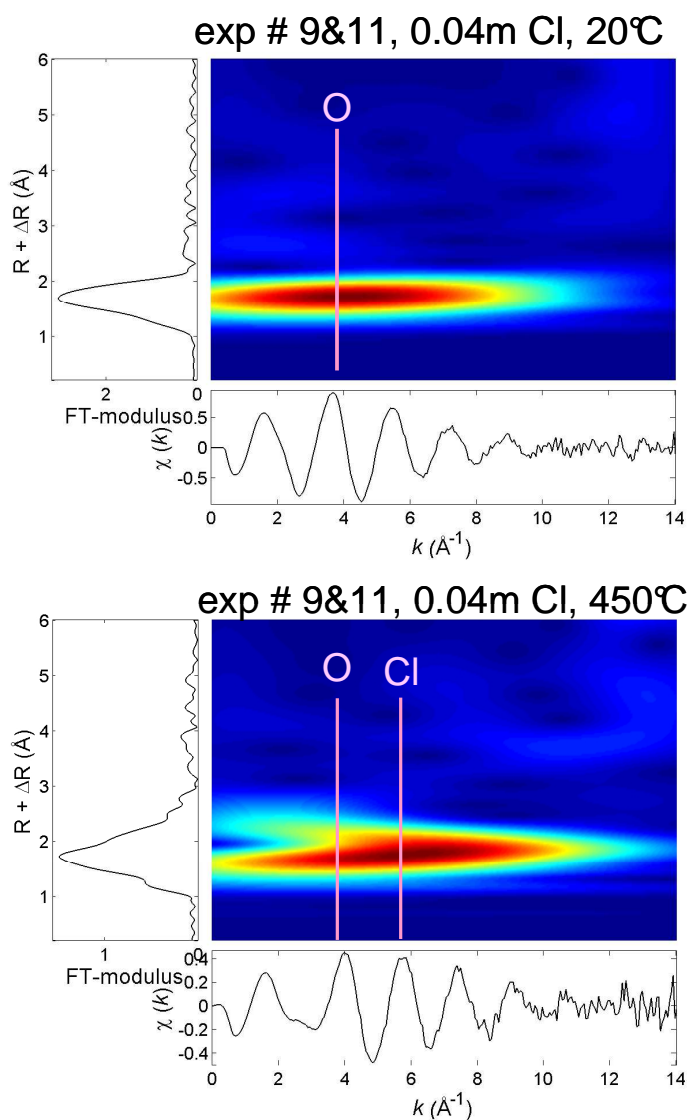
exp # 5, 5.2m Cl, 20°C
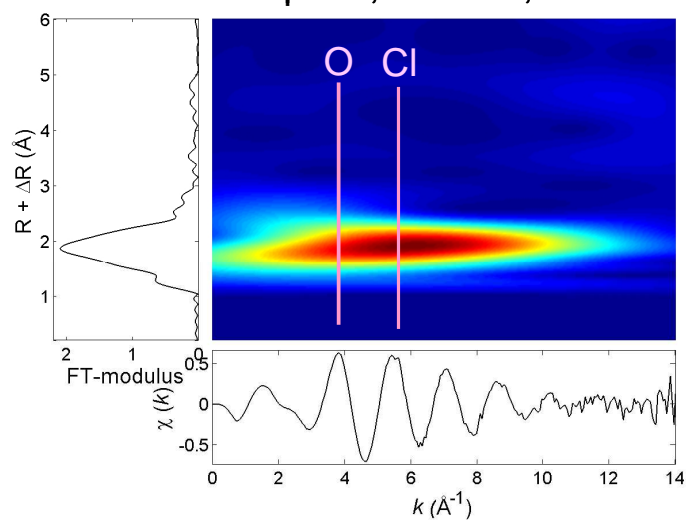
exp # 5, 5.2m Cl, 450°C
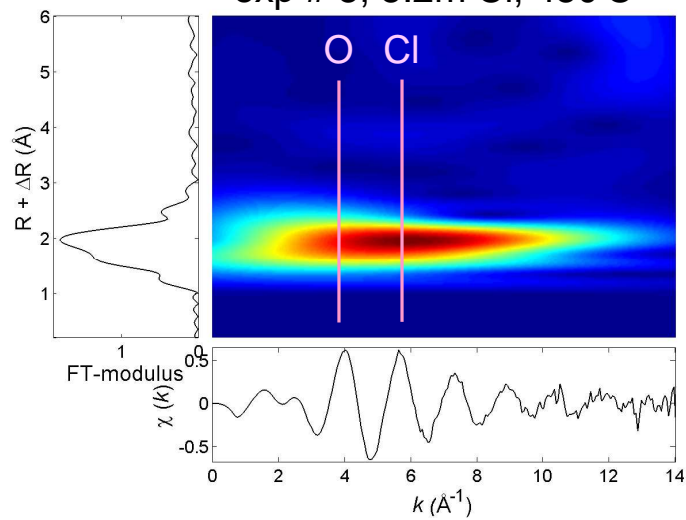
exp # 13, 7.3m Cl, 20°C
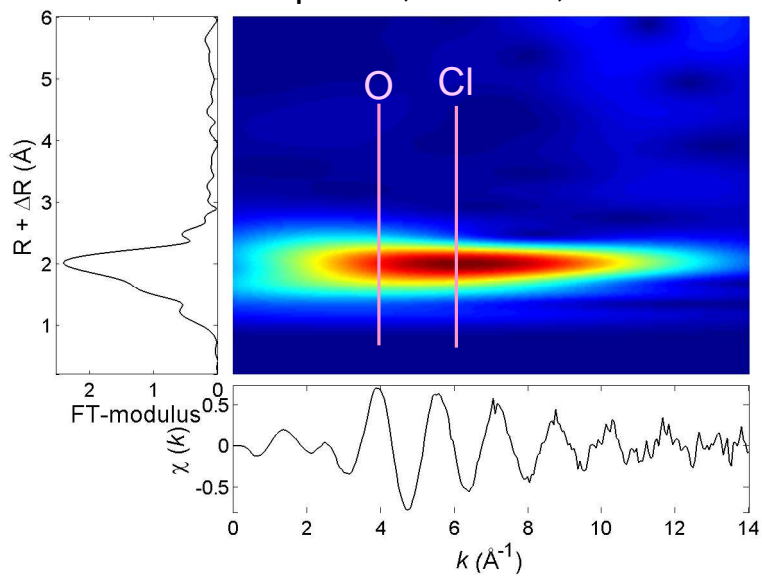
exp # 15, 18.2m Cl, 20°C
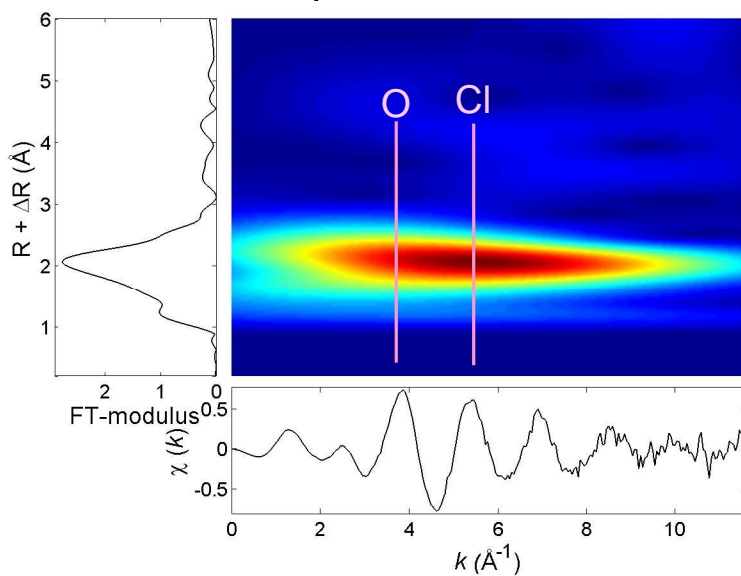
Electronic annex 4

Derivation of $CdCl_2^0$ and $CdCl_3^-$ stability constants at 400°C and 600 bar

The derivation of stability constants at 400°C and 600 bar were performed using the results of LCF of XANES spectra for Cl-bearing solutions and CdO and CdS solubility measurements. Calculations of m_{Cl^-} and optimizations of individual values Gibbs free energy of aqueous cadmium chloride complexes were performed with the HCh program package (Shvarov, 2008) was used. This was achieved by adjusting the Gibbs free energy values of each chosen species at 400°C and 600 bar to match the experimental solubility values. Details about the choice of the dominant species can be found in the in main text (section 3); they correspond to the following reactions:

$$CdO_{(s)} + 2HCl^0(aq) = CdCl_2(aq) + H_2O \qquad (1)$$

$$CdS_{(s)} + 2HCl^0(aq) = CdCl_2(aq) + H_2S^0(aq) \qquad (2)$$

$$CdO_{(s)} + 2HCl^0(aq) + Cl^- = CdCl_3^- + H_2O \qquad (3)$$

$$CdO_{(s)} + 2HCl^0(aq) + Cl^- = CdCl_3^- + H_2S^0(aq) \qquad (4)$$
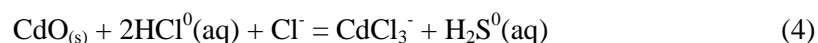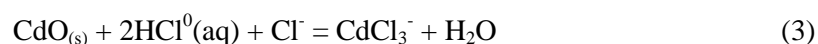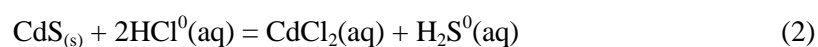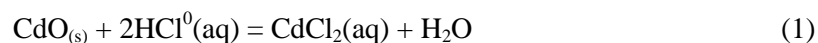
$$CdCl_2^0(aq) + Cl^- = CdCl_3^- \qquad (5)$$

Supplementary Table EA4-1. Derivation of the stability of reaction (5) from LCF fractions of $CdCl_2^0$ and $CdCl_3^-$ in XAS experiments

					LCF of XANES spectra		$CdCl_2^0 + Cl^- = CdCl_3^-$
exp #	m_{Cl}	T°C	P, bar	m_{Cl^-}	%$CdCl_2^0$	%$CdCl_3^-$	$\log_{10} K(5)$
3	0.12	400	600	0.03	70	30	1.10±0.20
7	0.77	400	600	0.35	25	75	0.96±0.30
4	2.30	400	600	1.01	10	90	0.97±0.30
2	2.67	400	600	1.00	10	90	0.97±0.30
error					±10	±10	

LCF=linear combination fit modeling of XANES and EXAFS spectra; %$CdCl_2^0$ = the fraction of standard for $CdCl_2^0$ (0.04 mCl solution spectrum at 400°C); %$CdCl_3^-$=the fraction of standard for $CdCl_3^-$ (5.23m Cl solution spectrum at 400°C).

Supplementary Table EA4-2. Derivation of the stability constants of reactions (1) and (3) from CdO solubility measurements

Run	m_{NaCl}	m_{HCl}	Measured solubility, m_{Cd}			$\Delta G°$, kJ/mol		$\log_{10}K(1)$	$\log_{10}K(3)$
			(WL)	(AAS)	average	$CdCl_2^0(aq)$	$CdCl_3^-$		
F-104	*0.12*	*0*	*0.0066*	*0.0009*	*0.0038*	*≥-472*	*-*	*<13.8*	*-*
F-101	0.77	0	0.0370	0.0082	0.0226	-	-605±10	-	14.3±0.8
O-1	2.26	0	0.0308	0.0270	0.0289	-	-599±3	-	13.9±0.2
F-4	5.13	0	0.0643	0.0621	0.0632	-	-599±1	-	13.9±0.1
O-25*	0	0.10	0.0047	0.0191	0.0119	-	-	-	-
O-24	0.10	0.10	0.0472	0.0451	0.0462	-400±70	-	8.3±5.4	-
O-5	1.08	0.11	0.0699	0.0552	0.0626	-	-595±15	-	13.6±1.2
O-4	2.31	0.11	0.0741	0.0783	0.0762	-	-600±10	-	14.0±0.8
O-101	2.31	0.12	0.1200	0.0828	0.1014	-	-610±10	-	14.7±0.8
O-23	4.63	0.13	0.0755	0.1085	0.0920	-	-590±10	-	13.2±0.8

See footnote of Table 6.

$\Delta G°$ is the apparent molal Gibbs free energy of the species at 400°C and 600 bar as defined in Sverjensky et al. (1997).

*this run was excluded from thermodynamic analysis becaused showed secondary Cd-Cl-OH solid phases.

Supplementary Table EA4-3. Derivation of the stability of reactions (2) and (4) from CdS solubility measurements

Run	m_{NaCl}	m_{HCl}	Measured solubility, m_{Cd}			$\Delta G°$, kJ/mol		$\log_{10}K(2)$	$\log_{10}K(4)$
			(WL)	(AAS)	average	$CdCl_2^0$	$CdCl_3^-$		
F-1	*0.77*	*0*	*0.002*	*0.0010*	*0.0015*	*>-495*	*-*	*<7.9*	*-*
S-1	1.06	0	-	0.0037	0.0037	-	-618±20	-	7.6±1.6
S-23	2.27	0	-	0.0042	0.0042	-	-610±10	-	7.0±0.8
F-23	2.29	0	0.0025	0.0018	0.0022	-	-608±10	-	6.8±0.8
F-103	5.13	0	0.0038	0.0020	0.0029	-	-595±10	-	5.8±0.8
S-4	5.23	0	-	0.0081	0.0081	-	-610±10	-	7.0±0.8
S-25	2.27	0.02	-	0.0096	0.0096	-	-600±20	-	7.0±1.6
S-5	2.28	0.11	-	0.0401	0.0401	-	-580±30	-	4.7±2.3
S-101*	0	0.10	-	0.0445	0.0445	≤-410*	-	≥1.3*	-
S-103*	0.10	0.10	-	0.0303	0.0303	≤-390*	-	≥-0.3*	-

See footnote of Table 7.

*Only a minimal value of ΔG of the dominant cadmium chloride complex can be estimated from these runs (see in the main text for details).

References for Electronic annexes

Anderson, B.G., Irish, D.E., 1988. Vibrational spectral studies of solutions at elevated temperatures and pressures. X. Raman spectral study of aqueous cadmium bromide solutions at 25 and 200°C. J. Solution Chem. 17, 763-775.

Arhland, S., 1979. Complex formation in protic and aprotic media. Pure Appl. Chem. 51, 2019-2039.

Caminiti, R., Licheri, G., Paschina, G. Piccaluga, G., Pinna, G., 1980. X-ray diffraction and structural properties of aqueous solutions of divalent metal-chlorides. Z. Naturforsch 35, 1361-1367.

Crerar, D., Wood, S., Brantley, S., 1985. Chemical controls on solubility of ore-forming minerals in hydrothermal solutions. Can. Miner. 23, 333-352.

Drakenberg T., Björk N.O., Portanova R., 1978. Cadmium-113 nuclear magnetic resonance study of cadmium (II) halide complexes in water and dimethyl sulfoxide. Phys. Chem., 82, 2423-2426.

Kelly, S.D., Hesterberg, D., Ravel, B., 2008. Analysis of soils and minerals using X-ray absorption specroscopy. Methods of Soil Analysis. Part 5. Mineralogical Methods, p. 387-463, Soil Sci. Soc. Am., Madison, USA.

Malinowski, E.R., 1977. Depermination of the number of factors and the experimental error in a data matrix. Anal. Chem 49, 612-317.

Malinowski, E.R., 1991. Factor Analysis in Chemistry. 2nd Edition, Wiley.

Munoz, M., Argoul, P., Farges F., 2003. Continuous cauchy wavelet transform analyses of EXAFS spectra: a qualitative approach. Amer. Mineral. 88, 694-700.

Paschina, G., Piccaluga, G., Pinna, G., Magini, M., 1983. Chloro-complexes formation in $ZnCl_2$-$CdCl_2$ aqueous solutions: An X-ray diffraction study. J. Chem. Phys. 78, 5745-5749.

Ravel, B., Newville, M., 2005. ATHENA, ARTEMIS, HEPHAESTUS: data analysis for X-ray absorption spectroscopy using IFEFFIT. J. Synchrotron Radiat. 12, 537–541.

Rossberg, A., Reich, T., Bernhard G., 2003. Complexation of uranium(VI) with protocatechuic acid – application of iterative transformation factor analysis to EXAFS spectroscopy. Anal. Bioanal. Chem., 376, 631-638.

Sharps, J.A., Brown Jr., G.E., Stebbins J.F., 1993. Kinetics and mechanism of ligand exchange of Au(III), Zn(II), and Cd(II) chlorides in aqueous solutions: An NMR study from 28-98°C. Geochim. Cosmochim. Acta 57, 721-731.

Shvarov, Yu. S., 2008. HCh: New potentialities for the thermodynamic simulation of geochemical systems offered by windows. Geochem. Intl. 46, 834-839; http://www.geol.msu.ru/deps/geochems/soft/index.html/

Sverjensky, D.A., Shock, E.L. Helgeson, H.C., 1997. Prediction of the thermodynamic properties of aqueous metal complexes to 1000°C and 5 kb. Geochim. Cosmochim. Acta 61, 1359-1412; http://geopig.asu.edu/index.html/

Chapter V. MODELING OF Cd/Zn RATIOS IN HYDROTHERMAL FLUIDS AND VAPORS AND COMPARISON WITH NATURAL OBSERVATIONS

This chapter is devoted to the analysis of Cd/Zn ratios in model systems pertinent to base-metal bearing hydrothermal solutions described in details in previous chapters. In addition, this chapter presents results on Zn and Cd solubility and partitioning in low-density hydrothermal vapors (density < ~0.4 g/cm^3) and during immiscibility phenomena in a water-salt system. Finally, it analyses the data on Zn/Cd ratios in high-temperature volcanic condensates of Kudryavy volcano as an example of natural high-T vapor phases. This chapter consists of four sections. First, we present, based on data reported in previous chapters, the revised thermodynamic properties of Cd and Zn chloride complexes, and use them to model Cd/Zn ratios as a function of T, P and Cl content in dense hydrothermal fluids (section V-1). Second, we present the results of a pilot experiment on ZnO and CdO solubilities in pure water and low saline hydrothermal vapors (section V-2). Third, we report the results of vapor-liquid partitioning measurements for Cd and Zn in the H$_2$O-NaCl-HCl two-phase system and use these data to predict the evolution of Cd/Zn ratios in boiling hydrothermal fluids (section V-3). Finally, we briefly describe analytical results of our field work at the Kudryavy volcano, in an attempt to provide a physical-chemical interpretation of Cd/Zn ratios in volcanic gases (section V-4). The experimental, analytical and field sampling techniques used in this part of the thesis are presented in detail in Chapter I. A part of experimental data from vapor-liquid experiments and details of volcanic condensates analyses are given in Supplementary Tables for Chapters V.

V-1. Derivation of thermodynamic properties for Cd and Zn chloride complexes and modeling of Cd/Zn ratios in dense saline hydrothermal fluids

The prediction of Cd and Zn transport and fractionation in high T-P geological fluids requires knowledge of thermodynamic properties of their chloride complexes, which are the major carriers of these metals in natural fluids in a wide T-P range. The ensemble of experimental results reported in previous chapters of the manuscript, together with a critical analysis of available literature data allows derivation of the thermodynamic parameters of Cd-Cl complexes within the framework of the revised HKF equation of state. The derivation procedure is briefly outlined below.

The values of standard partial Gibbs free energy of formation $\Delta_f G^0_{298}$ and entropies S^0_{298} for CdCl$^+$, CdCl$_2^0$(aq) and CdCl$_3^-$ were taken from the review of Archer (1998) as discussed in Chapter III. The corresponding enthalpies of formation $\Delta_f H^0_{298}$ for these three complexes were calculated from values of $\Delta_f G^0_{298.15}$ and $S^0_{298.15}$ and using entropy values from CODATA (1989) for simple compounds whose $\Delta_f G^0_{298}$ and $\Delta_f H^0_{298}$ are equal to zero by definition (Cd(metal), Cl$_2$(gas), H$_2$(gas), H$^+$). The standard partial molal volumes V^0_{298} and associated a_1 - a_4 HKF parameters of all four cadmium chloride complexes were derived from the pressure dependence of complex stabilities from our potentiometric measurements at 25°C and pressures 1-1000 bar, as detailed in Chapter III. The Born coefficients ω were calculated with the UT-HEL program (Shvarov, 2008) using the correlation

between ω and S^0_{298} (Shock et al., 1989). The standard partial molal heat capacities $C^0_{p\,298.15}$ and associated HKF parameters c_1 and c_2 for the first three Cd-Cl complexes were regressed with the UT-HEL using the stability constants for $CdCl_2^0(aq)$ and $CdCl_3^-$ at 400°C and 600 bar derived from our XAFS and solubility data (Chapter IV), and the stability constant for $CdCl^+$ at 10-250°C and P_{sat} according to Palmer et al. (2000). For $CdCl_4^{2-}$, the $\Delta_f G^0_{298.15}$ value was determined from our potentiometric measurements (Chapter III). The entropy $S^0_{298.15}$ was estimated using the theoretical method proposed by Hovey (1988). This method is based on the linear correlation between the nonsolvation (nonelectrostatical) contribution to the standard entropy ($\Delta_n S^0_{298.15}$) for the Cd^{2+} ion and its three chloride complexes and the number of the ligands (chloride ions) in the complex. This non-electrostatical contribution ($\Delta_n S^0_{298.15}$) to the standard entropy ($S^0_{298.15}$) is calculated as

$$\Delta_n S^0_{298.15} = S^0_{298.15} - \Delta_s S^0_{298.15} \qquad (V\text{-}1)$$

where $\Delta_s S^0_{298.15}$ is the electrostatic contribution to the standard entropy calculated as $\Delta_s S^0_{298.15} = \omega \cdot Y$, where ω is a Born coefficient and Y is a Born function for entropy ($Y = -5.81 \cdot 10^5$, Tanger and Helgeson, 1988). The Born coefficient was determined using the total entropy values for all Cd-Cl complexes as adopted above and a correlation between $S^0_{298.15}$ and ω from Shock et al. (1989). For Cd^{2+}, the values of ω and $S^0_{298.15}$ were taken from Shock et al. (1997) and CODATA (1989), respectively. Our XAFS and solubility data at 400°C and 600 bar (Chapter IV; Bazarkina et al., 2009) show that at these T-P even in concentrated NaCl ($5m$) solutions, the amount of $CdCl_4^{2-}$ does not exceed 10% of total dissolved Cd (Chapter IV). Consequently, this amount was used to estimate the highest possible value of $CdCl_4^{2-}$ stability constant at 400°C/600 bar, and to derive its corresponding heat capacity $C^0_{p\,298.15}$ and c_1 and c_2 parameters using the procedure described above. Thus, these values should be considered as maximum estimates, and more measurements are required to provide an accurate set of HKF parameters for the $CdCl_4^{2-}$ species. The thermodynamic parameters of Cd-Cl species derived in this study are reported in Table V-1.

A detailed literature analysis of Zn-Cl complexes is given in Chapter I, and their stoichiometries and structures reported from spectroscopic works are compared with those found for Cd-Cl species in Chapter IV. This analysis suggests that the dominant zinc chloride complexes in high temperature ($T > 200\text{-}300$°C) hydrothermal solutions are $ZnCl^+$, $ZnCl_2^0(aq)$ and $ZnCl_3^-$. $ZnCl_4^{2-}$ is likely to be very weak. Despite some discrepancies in the stability constants for these species from different authors, the dataset proposed in the review of Sverjensky et al. (1997) seems to provide the best agreement with this speciation scheme, and thus this set was adopted in the further analysis. It should be noted, however, that accurate spectroscopic and solubility data are necessary to resolve the current discrepancies among the Zn-Cl complexes. The estimations of Cd/Zn ratios in hydrothermal fluids that follow should thus be regarded as semi-quantitative, but they nevertheless provide useful insights into the potential use of the Cd/Zn ratio as a tracer of fluid composition and evolution.

Table V-1. HKF parameters for cadmium chloride complexes used or determined in this study.

HKF parameters		$CdCl^+$	$CdCl_2^0(aq)$	$CdCl_3^-$	$CdCl_4^{2-}$
$\Delta_fG^0_{298.15}$	(cal · mol^{-1})	-52629[1]	-84883[1]	-115399[1]	**-145583**[2]
$\Delta_fH^0_{298.15}$	(cal · mol^{-1})	-57508[3]	92023[3]	134131[3]	156589[3]
$S^0_{298.15}$	(cal · mol^{-1}·K^{-1})	7.06[1]	25.72[1]	45.15[1]	**50.61**[4]
$C_p^0{}_{298.15}$	(cal · mol^{-1}·K^{-1})	**11.1**[5]	**116.0**[5]	**97.8**[5]	*42.5*[5]
$V^0_{298.15}$	(cm^3 · mol^{-1})	**2.28**[2]	**42.21**[2]	**63.47**[2]	**81.35**[2]
$a_1\cdot10$	(cal ·mol^{-1}·bar^{-1})	**2.2303**[2]	**7.5221**[2]	**10.8045**[2]	**13.8329**[2]
$a_2\cdot10^{-2}$	(cal · mol^{-1})	**-2.3357**[2]	**10.5852**[2]	**18.5994**[2]	**25.9938**[2]
a_3	(cal ·K· mol^{-1}·bar^{-1})	**6.6681**[2]	**1.5895**[2]	**-1.5605**[2]	**-4.4669**[2]
$a_4\cdot10^{-4}$	(cal ·K· mol^{-1})	**-2.6824**[2]	**-3.2166**[2]	**-3.5479**[2]	**-3.8536**[2]
c_1	(cal ·mol^{-1}·K^{-1})	**16.6729**[5]	**73.7011**[5]	**72.0276**[5]	*53.6809*[5]
$c_2\cdot10^{-4}$	(cal ·K· mol^{-1})	**-0.7693**[5]	**20.5956**[5]	**16.8832**[5]	*5.6267*[5]
$\omega\cdot10^{-5}$	(cal ·mol^{-1})	**0.4372**[6]	**-0.0495**[6]	**0.9378**[6]	**2.4766**[6]

In bold – values derived in this study, in bold-italic – preliminary estimates (see text).
[1] Taken from Archer's review of NBS data (Archer, 1998);
[2] Determined from potentiometric measurements;
[3] Calculated using $\Delta_fG^0_{298.15}$ and $S^0_{298.15}$ and entropy values of Cd(metal), Cl$_2$(gas), H$_2$(gas), H$^+$ from CODATA (1998);
[4] Calculated from linear correlation between non-electrostatic contribution of entropy $\Delta_nS^\circ_{298.15}$ ($\Delta_nS^0_{298.15} = S^0_{298.15} - \Delta_sS^0_{298.15}$) and ligand number ($n$) for $n = 0$ to 3 (Cd^{2+}, CdCl$^+$, CdCl$_2$(aq), and extrapolated to $n = 4$ (CdCl$_4^{2-}$);
[5] Calculated from XAFS and solubility data at 400°C and 600 bar (see text for details).
[6] Calculated using the correlation of ω· with $S^0_{298.15}$ (Shock et al, 1989).

Table V-2. HKF parameters for zinc chloride complexes from Sverjensky et al. (1997), http://geopig.asu.edu/index.html/

HKF parameters (units)		$ZnCl^+$	$ZnCl_2^0(aq)$	$ZnCl_3^-$
$\Delta_fG^0_{298.15}$	(cal · mol^{-1})	-66850	-98300	-129310
$\Delta_fH^0_{298.15}$	(cal · mol^{-1})	-66240	-109080	-151060
$S^0_{298.15}$	(cal · mol^{-1}·K^{-1})	23.00	27.03	25
$C_p^0{}_{298.15}$	(cal · mol^{-1}·K^{-1})	19.9	34.7	41.97
$V^0_{298.15}$	(cm^3· mol^{-1})	-1.28	24.82	53.9
$a_1\cdot10$	(cal ·mol^{-1}·bar^{-1})	1.6583	5.1486	9.5636
$a_2\cdot10^{-2}$	(cal · mol^{-1})	-3.7293	4.7929	15.5732
a_3	(cal ·K· mol^{-1}·bar^{-1})	7.2088	3.8592	-0.3779
$a_4\cdot10^{-4}$	(cal ·K· mol^{-1})	-2.6248	-2.9771	-3.4227
c_1	(cal ·mol^{-1}·K^{-1})	19.6947	26.1528	42.2912
$c_2\cdot10^{-4}$	(cal ·K· mol^{-1})	1.0191	4.0338	5.5147
$\omega\cdot10^{-5}$	(cal ·mol^{-1})	0.2025	-0.038	1.2513

The results of our modeling of the Cd/Zn ratio in hydrothermal fluids in equilibrium with Cd-bearing sphalerite as a function of m_{Cl}, T, P are presented in Fig. V-1. These calculations performed with HKF parameters for Cd-Cl and Zn-Cl complexes reported above (Tab. V-1, V-2) show that increasing temperature and chloride content with decreasing pressure results in highest Cd/Zn ratios. The effects of temperature and chloride concentration (fluid salinity) are much stronger than that of pressure and can result in changes in Cd/Zn ratio in fluid of up to 4-5 orders of magnitude (Fig. V-1). It should be noted of course, that composition of initial sphalerite affect significantly these diagrams resulting in increasing Cd/Zn ratio with increasing of Cd content in shpalerite in equilibrium with fluid. Thus, it can be assumed that the *absolute* values of Cd/Zn ratios in different natural settings cannot be compared directly without analyses of fluid sources. In the same time, the *relative changes* of Cd/Zn ratio within one geological object may indicate changing T-P-m_{Cl} parameters during fluid evolution. This conclusion can be confirmed by natural data with wide variations of Cd/Zn ratio in hydrothermal ores, modern hydrothermal solutions and volcanic gases (e.g., Qian, 1987; Metz and Trefry, 2000; Schvartz, 2000; Gottemsmann and Kampe, 2007; Cook et al., 2009) in contrast with rather constant Cd/Zn ratio in the hosted rocks of the Eath's crust (e.g., Rudnick and Gao, 2003).
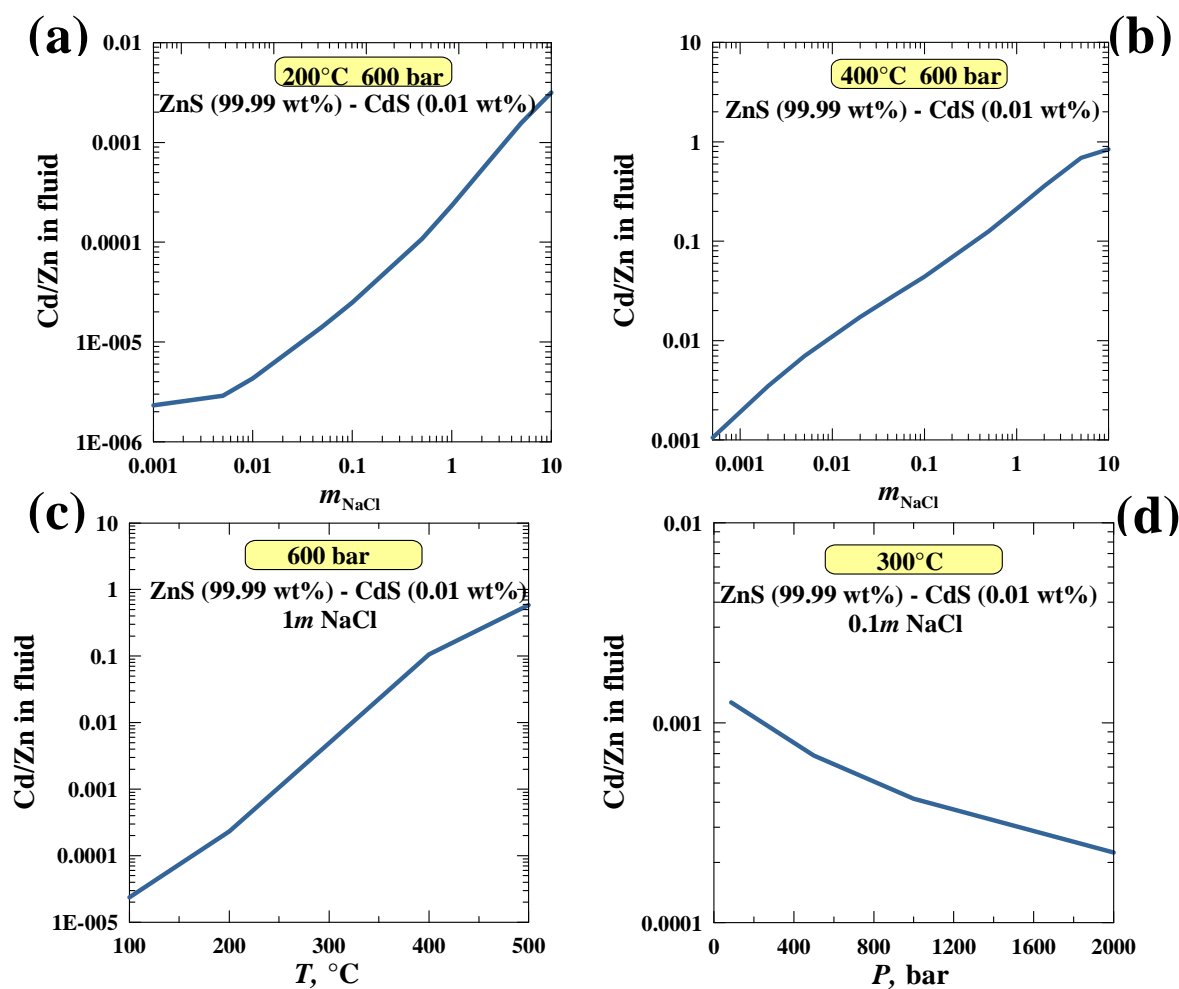
Figure V-1. *Cd/Zn ratio in a hydrothermal fluid as a function of fluid salinity at 200°C and 600 bar (a) and at 400°C and 600 bar (b), as a function of temperature at 600 bar and 1m NaCl fluid salinity (c) and as a function of pressure at 300°C at 0.1m NaCl fluid salinity (d).*

V-2. Solubility of CdO and ZnO at 350-400°C and 220-400 bar

Although the thermodynamic properties of Cd and Zn chloride complexes obtained above can be applied for modeling of Cd and Zn transport and solubilities in dense saline fluids (typical density above 0.5 g/cm^3), they cannot be applied to low-density aqueous hydrothermal vapors because of the physical limitations of the HKF model (e.g., Plyasunov and Shock, 2001). In this part of work, we attempted to provide the first experimental data for CdO and ZnO solubilities in low-density vapor (density < 0.3 g/cm^3) at 400°C. In addition, we measured the oxide solubilities in pure water at 350 and 400°C to assess the importance of hydroxide complexes of these metals. All measurements were performed using the flexible-cell Coretest reactor with rapid sampling (see Chapter I for details). The experimental results and their analysis in terms of Zn/Cd ratios are briefly presented below.

Results from measurements in pure water

Although the solubility of CdO in pure water at 350-400°C and 300-400 bar was already briefly mentioned in chapter IV (Bazarkina et al., 2009, submitted), here we complete these data with ZnO solubility results and compare both metals. Both CdO and ZnO solubilities in pure water are given in Table V-3 and displayed in Fig. V-2. The measured solubilities are $1.0 \times 10^{-7} m$ ($\pm\ 0.3 \times 10^{-7} m$) for Cd and $2.0 \times 10^{-6} m$ ($\pm\ 2.5 \times 10^{-6} m$) for Zn on average and show no detectable evolution within the studied *T-P*-density range. Our ZnO solubilities are in decent agreement with those recently reported by Bénézeth at al. (2002) at 350°C and 175-268 bar (Fig. V-2). For CdO, there are no published data at high *T*, to the best of our knowledge, and thus our measurements provide the first pioneering results. Both ZnO and CdO data may be compared only with theoretical HKF model predictions given by Shock et al. (1997), which are based on ambient-temperature data for Cd and Zn hydroxide complexes, theoretical correlations between HKF-model parameters, and empirical correlations between different metals. It can be seen in Fig. V-2 that our solubilities are at least 1 and 2 orders of magnitude lower than these HKF predictions for Zn and Cd, respectively. Our low solubilities of Cd and Zn are also in harmony with recent high-*T* measurements for CuO (Palmer at al., 2001; Palmer at al., 2004). Our results in pure water thus demonstrate that hydroxide complexes of both cadmium and zinc are very weak and may account for only trace metal concentrations in the fluid phase ($<10^{-5}\ m$) and, consequently, do not play an important role in most natural ore-forming hydrothermal fluids.

Table V-3. Solubility of CdO and ZnO in pure H$_2$O measures in experiments with Coretest reactor.

Sample	T,°C	P, bar	Days	*m*Zn	*m*Cd
CT350-A1	350	400	2	$3.1 \cdot 10^{-06}$	$1.3 \cdot 10^{-07}$
CT350-A3	350	400	4	$1.7 \cdot 10^{-06}$	$1.3 \cdot 10^{-07}$
CT350-A4	350	400	4	$2.6 \cdot 10^{-06}$	$6.6 \cdot 10^{-08}$
CT350-A5	350	400	7	$2.7 \cdot 10^{-06}$	$1.1 \cdot 10^{-07}$
CT350-A6	350	400	7	$2.4 \cdot 10^{-06}$	$1.1 \cdot 10^{-07}$
CT400-A7	400	400	9	$3.8 \cdot 10^{-06}$	$2.0 \cdot 10^{-07}$
CT400-A8	400	400	11	$4.9 \cdot 10^{-07}$	$7.9 \cdot 10^{-08}$
CT400-A9	400	300	14	$1.4 \cdot 10^{-06}$	$1.1 \cdot 10^{-07}$
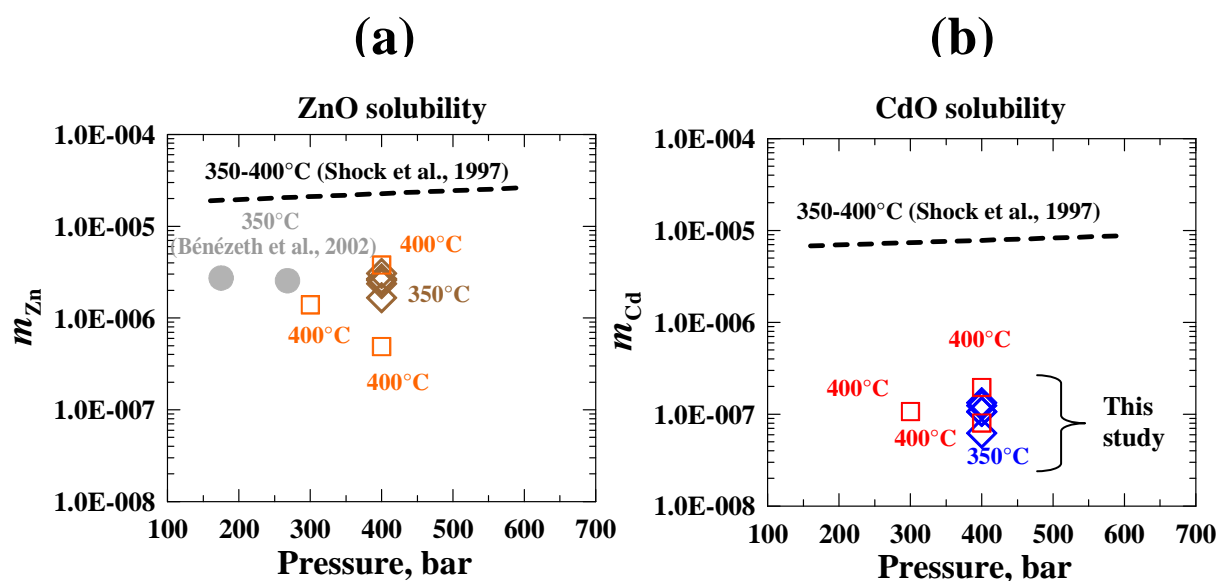
Figure V-2. *Solubility of ZnO (a) and CdO (b) in pure water at 350-400°C and 300-400 bar. Squares and diamonds = experimental data derived in this study at 350°C and 400°C, respectively; circles = the experimental data of Bénézeth et al. (2002) for ZnO; curves = HKF predictions of Shock et al. (1997) from low-T data.*

Results from measurements in Cl-bearing low-density supercritical fluids

The solubilities of CdO and ZnO in the low-saline and low-density (up to 0.05m of total Cl, 0.35-0.15g/cm^3) fluid phase at 400°C and pressures between 220 and 300 bar are reported in Table V-3. The experiment was started at 300 bar and the pressure was lowered by steps to 220 bar when a steady state concentrations are attained for both metals. This attainment was found to be rapid, in less than 1 day at all pressures investigated. At the end of the run, pressure was increased again to 250 and when to 300 bar to check for chemical reversibility. At 250 bar, after attainment of Cd and Zn steady state, NaCl or HCl solutions were injected into the reactor (as indicated in Table V-4).

Table V-4. Solubility of CdO and ZnO in NaCl-HCl aqueous solutions at 400°C and 220-300 bar.

Sample	P, bar	Days	mNaCl (inj.)	mHCl (inj.)	mCl (HPLC)	mNa (AAS)	mZn (AAS)	mCd (AAS)	mHCl (calc.)	mCl (calc.)
CT-A10	300	17	0.0020	0.0020	NA	0.0021	$3.4 \cdot 10^{-5}$	$5.9 \cdot 10^{-4}$	0.0020	0.0040
CT-A11	300	21			NA	0.0021	$2.6 \cdot 10^{-5}$	$6.4 \cdot 10^{-4}$	0.0020	0.0040
CT-A12	280	23			NA	0.0021	$2.5 \cdot 10^{-5}$	$5.6 \cdot 10^{-4}$	0.0020	0.0040
CT-A13	280	24			NA	0.0022	$2.6 \cdot 10^{-5}$	$6.4 \cdot 10^{-4}$	0.0020	0.0040
CT-A14	265	25			NA	0.0022	$2.4 \cdot 10^{-5}$	$6.3 \cdot 10^{-4}$	0.0020	0.0040
CT-A15	250	28			NA	0.0021	$9.9 \cdot 10^{-6}$	$4.3 \cdot 10^{-4}$	0	0.0020
CT-A16	250	37	0.0021	0.0021	NA	0.0022	$6.9 \cdot 10^{-6}$	$4.6 \cdot 10^{-4}$	0	0.0021
CT-A17	220	42			0.0014	0.0017	$8.8 \cdot 10^{-6}$	$1.1 \cdot 10^{-4}$	0	0.0021
CT-A18	250	44	0.0020	0.0072	0.0026	0.0023	$1.1 \cdot 10^{-5}$	$4.8 \cdot 10^{-4}$	0	0.0020
CT-A19	250	46			NA	0.0023	$5.8 \cdot 10^{-6}$	$4.4 \cdot 10^{-4}$	0	0.0020
CT-A20	250	49	0.0021	0.0322	NA	0.0025	$1.3 \cdot 10^{-5}$	$5.4 \cdot 10^{-4}$	0	0.0021
CT-A21	250	51			0.0023	0.0024	$8.4 \cdot 10^{-6}$	$4.6 \cdot 10^{-4}$	0	0.0021
CT-A22	220	56			NA	0.0019	$1.7 \cdot 10^{-6}$	$1.3 \cdot 10^{-4}$	0	0.0021
CT-A23	220	57			0.0026	0.0019	$3.4 \cdot 10^{-6}$	$2.3 \cdot 10^{-4}$	0	0.0021
CT-A24	250	57	0.0232	0.0163	0.0242	0.0200	$1.3 \cdot 10^{-5}$	$1.6 \cdot 10^{-3}$	0	0.023
CT-A25	250	58			0.0227	0.0180	$1.4 \cdot 10^{-5}$	$1.9 \cdot 10^{-3}$	0	0.023
CT-A26	250	59			0.0223	0.0180	$1.3 \cdot 10^{-5}$	$2.1 \cdot 10^{-3}$	0	0.023
CT-A27	300	61	0.0232	0.0049	0.0431	0.0270	$4.2 \cdot 10^{-5}$	$6.8 \cdot 10^{-3}$	0.020	0.043
CT-A28	300	64			0.0517	0.0260	$5.8 \cdot 10^{-5}$	$9.6 \cdot 10^{-3}$	0.029	0.052

inj. = concentrations injected to the experimental solution during the run; calc. = calculated based on the mass balance and the total Cl concentrations measured by HPLC and assuming that at $P < 300$ bar all HCl was consumed by formation of cadmium hydroxychlorides (see text); NA = not analyzed.

At pressures below 300 bars, HPLC analyses of total Cl in the sampled fluid indicated significant losses of Cl, whereas Na concentrations remained constant. This is a strong indication of the reaction of HCl with Cd or Zn oxides at low pressures. Injections of additional HCl amounts into the reactor resulted in a rapid loss from the fluid of Cl corresponding to the fraction of HCl. In addition, SEM analyses of solid phases after the experiment have shown the presence of well-crystalline Cd-Cl-O-bearing phases (Fig. V-3a) that are likely to have formed at experimental T-P and survived the cooling to ambient conditions. The presence of H in these phases could not be determined by SEM analyses, and their quantities were also too small for XRD analyses. Neo-formed phases of similar Cd-O-Cl compositions (Fig. V-3b) were also observed in our solubility experiments in acidic NaCl solutions at higher pressures (600 bar, see Chapter IV). The data available in the literature on the Cd-Cl-O solids (e.g., Walter-Lévy and Groult, 1970; Cudennec et al., 1997) let us to suggest that our neo-formed solids are likely to be of cadmium hydroxyl-chlorides of the composition $Cd(OH)_mCl_n$. The thermodynamic properties of these solids are not known, and thus do not allow analyses of our low-pressure experiments in terms of equilibrium thermodynamics.
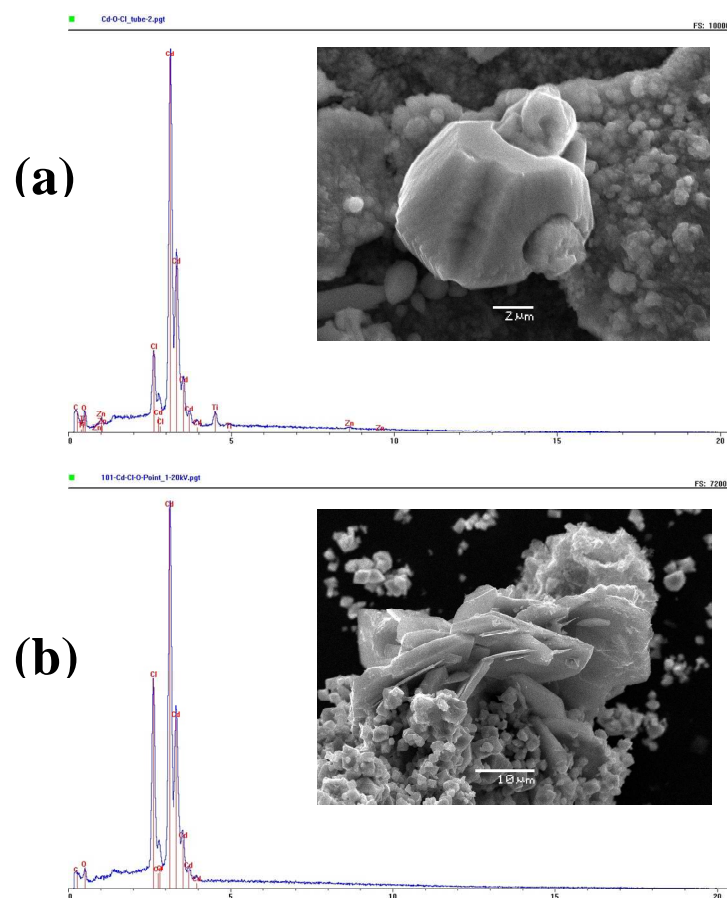
Figure V-3. *Solid phases of Cd-Cl-O composition detected by SEM after experiments. (a) the solid phase found after Coretest runs, supposed to be stable in low-density HCl-bearing fluids; (b) the solid phase found in HCl-free runs in batch-reactor, supposed to be not stable at 400°C and 600 bar and to occur only at ambient T-P during quenching.*

Despite these limitations intrinsic to the chemical system under investigation, these first measurements do allow interesting qualitative comparisons of the behavior of Zn and Cd chloride complexes in low-density supercritical fluids; they complement our results in dense saline fluids. The major results are briefly presented below.

First, our results further confirm the major control of the chloride ligands on both Zn and Cd mobility in the vapor phase, similar to that found in denser fluids (see Chapter IV). For example, at 300 bar in the presence of only 0.004m Cl in the vapor phase, the solubilities of CdO and ZnO increase ~4 and ~1 orders of magnitude, respectively, in comparison to those in pure water. Cd and Zn concentrations in these low-Cl fluids are far above those in Cl-free fluids, thus confirming again that hydroxide complexes formed in the absence of Cl provide a very little contribution to Cd and Zn transport.

Second, the effect of chloride is much stronger for Cd than for Zn. For example, with increasing Cl concentration from $0.004m$ to $0.05m$, the solubility of CdO increases by almost 1.5 orders of magnitude (from $6 \times 10^{-4}m$ to 1×10^{-2} m), whereas that of ZnO rises only by a factor of 2 (from $\sim 3 \times 10^{-5}m$ to $\sim 6 \times 10^{-5}m$, samples CT-A10, CT-A11, CT-A27 and CT-A28 in Table V-4). The greater affinity of Cd to Cl in the vapor phase is also manifested by the formation of Cd hydroxy-chloride solid phases at the expense of CdO, whereas ZnO is likely to remain the stable solubility-controlling solid phase for Zn (see above).

Third, the greater Cd than Zn affinity to the Cl ligand results in a large increase, in the presence of CdO and ZnO solids, of the Cd/Zn ratio in the vapor phase with increasing Cl content. For example, at 400°C/ 300 bar, the Cd/Zn mass ratio increases from ~0.1 in pure water to ~300 at $0.05m$ Cl (Fig. V-2a). This observation is in line with the data presented in chapters III and IV for dense aqueous solutions. Unfortunately, the evolution of Cd/Zn vapor-phase ratios as a function of pressure or density could not be inferred unambiguously because of the increasing loss of HCl upon the formation of Cd hydroxy-chloride phases with decreasing pressure below 300 bar (Fig. V-2b). Thus the formation of such phases may occur in volcanic gases at very low pressures and high HCl content, and thus should be taken into account while interpreting Cd/Zn ratios in such natural fluids. Laboratory solubility measurements of cadmium sulfide which is expected to by far more stable than oxide and oxy-chlorides in S-bearing systems, are necessary to make definitive conclusions about the change of Cd/Zn ratios as a function of fluid density.

(a)   **(b)**
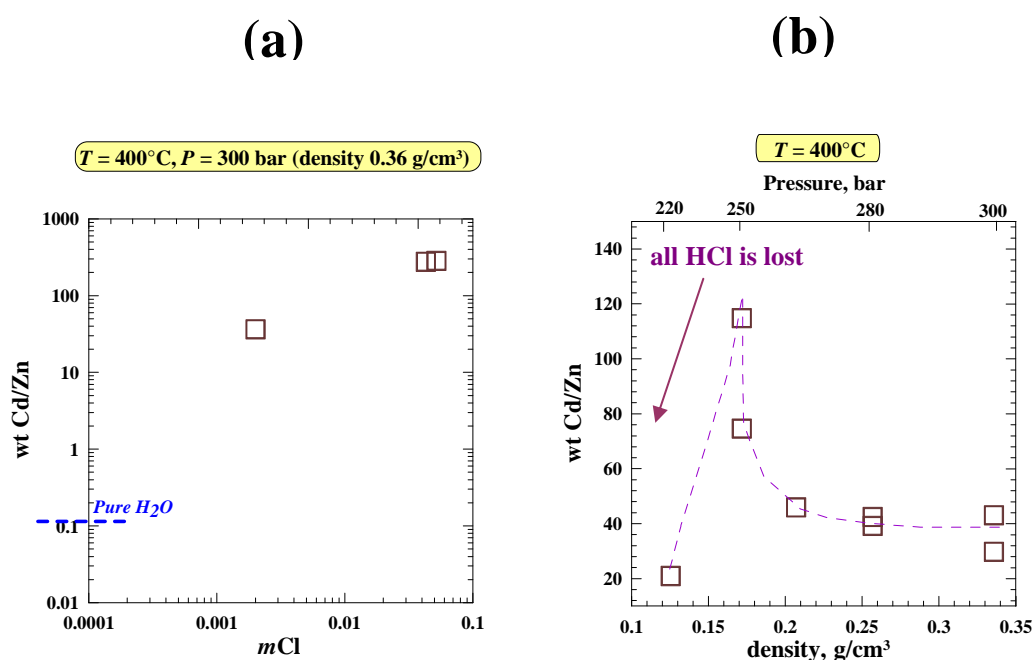
Figure V-4. *Cd/Zn mass ratios in hydrothermal vapors as a function of chloride content at 400°C and 300 bar (a) and as a function of pressure and density (b). At pressures below 300 bar the initially injected HCl is partly lost due to the formation of new Cd-Cl-O-H phases. Between 250 and 220 bar, all HCl is lost from the solution, these losses affect significantly the Cd/Zn ratio in the vapor. The Cd and Zn concentrations used for the Cd/Zn ratio calculation is given in Table V-4.*

V-3. Distribution of Cd and Zn between the coexisting vapor and liquid phases in the water-salt system

The results of the previous chapter in a solid-vapor system demonstrate that in addition to the chemical-speciation control in the fluid phase, the nature and changes of Cd and Zn-bearing solid phases in equilibrium with the low-density fluid may significantly alter the Cd/Zn ratios. Many high-temperature magmatic fluids carrying metals and salts are however often undersaturated with respect to Zn and Cd minerals upon their separation from a magmatic intrusion and further accent. They often undergo boiling and vapor-brine separation on their route to metal deposition at shallow depth. It is thus important to know the fractionation of Zn and Cd in such boiling fluids in the two-phase (vapor-liquid) water-salt system.

We thus measured the distribution of Cd and Zn between the coexisting vapor and liquid phases in the H_2O-NaCl-HCl system at 400 and 450°C at the pressure of the vapor-liquid equilibrium. In this system, the pressure decrease below the critical point results in the decrease of both density and NaCl content in the vapor, accompanied by the concomitant increase of both parameters in the coexisting liquid (or brine) phase (see Fig. II-7, chapter II). The whole set of raw experimental data points from two experiments at 400°C and one experiment at 450°C are given in Supplementary Tables 1 and 2. All studied metals fractionate largely in favor of the Cl-rich liquid phase. This fractionation increases in the order Na < Zn < Cd.

The vapor-liquid partitioning of dissolved compounds can be treated in the framework of the density model (Styrikovich et al., 1955), recently extended for many economically relevant metals in the water-salt system (Pokrovski et al., 2005). This model operates with individual apparent vapor-liquid partitioning coefficients (K_m) for each metal defined as

$$\log_{10} K_m = \log_{10} \frac{m_{vapor}}{m_{liquid}} \qquad \text{(V-2)}$$

where m is the molality (i.e., the number of moles of metal per kg of water in each coexisting phase). This partition coefficient may be linearly related to the densities of each coexisting phase, in the logarithmic scale:

$$\log_{10} K_m = n_i \cdot \log_{10} (\frac{density_{vapor}}{density_{liquid}}) \qquad \text{(V-3)}$$

where n_i is the empirical coefficient for each metal. Positive values of n_i correspond to preferential partitioning into the liquid phase; negative values, typical of gases, indicate partitioning in favor of the vapor.

The values of n_i for Cd, Zn and Na partitioning at 400°C an 450°C obtained by a regression of experimental data points and using the densities in the H_2O-NaCl system according to Bischoff (1991) are listed in Table V-5 for each temperature, and displayed in Fig. V-5. It can be seen that the n_i values increase in the order Na < Zn < Cd, indicating the increasing affinity of Cd for the Cl-rich liquid

phase. These values for each of the three studied metals are constant within errors for all runs and both temperatures, confirming that an average value can be reliably used, thus providing a temperature-independent equation for predicting metal vapor-liquid partitioning over a wide T-P-X_{NaCl} range. Our average n_i values for Na are in good agreement with the numerous data for NaCl (see compilation of Bischoff, 1991) and for Na and Zn in fair agreement, within errors, with those of Pokrovski et al. (2005) (Tab. V-5).

The simple equation of state involving densities of the coexisting vapor and liquid, which are well known in the water-salt systems, allows reliable predictions of Cd and Zn behavior in boiling saline fluids. Thus, during the fluid boiling, Cd will have a greater tendency than Zn to concentrate into the brine phase, resulting in an increase of Cd/Zn ratios in the brine with the fluid accent and decreasing pressure. On contrary, the corresponding Cd/Zn ratios will decrease in the vapor phase. Thus, low Cd/Zn ratios will be more typical for low-Cl vapor-like fluids produced upon boiling and separation and accent of the vapor from the saline brine. This tendency is somewhat opposite to that in solid-vapor systems studied above, which are more pertinent to magma degassing in the form of low-density aqueous volcanic vapor phase, and in which Cd/Zn ratios increase with increasing Cl in the vapor and, probably, decreasing density. Thus, Cd/Zn ratios might probably be indicative of the fluid origin (boiling and brine-vapor separation versus direct magma degassing). This hypothesis requires, of course, verification using natural geological information. Unfortunately, almost no data exists on Cd concentrations in the coexisting vapor and brine fluid inclusions from magmatic-hydrothermal deposits, whereas data of Zn are abundant (e.g., Yardley, 2005, Philippot et al., 2001). In contrast, Cd and Zn data in fumarole's condensates and sublimates from modern volcanic areas have been reported in the literature and thus may be used to track the evolution of Cd/Zn ratios provided that these analyses are reliable. These issues will be treated briefly in the last subchapter below.

Table V-5. Values of the parameter n_i (molality scale) in the framework of the density model, from our experiments 1, 2, 4, and their comparison with literature data.

	This study				Bischoff, 1991		Pokrovski et al., 2005
	400°C, exp1	400°C, exp2	450°C, exp4	Average	400°C	450°C	300-450°C
Na	3.54	3.66	3.48	3.56±0.18	3.54	3.41	3.93±0.06
Zn	4.08	4.16	4.11	4.10±0.08	-	-	4.37±0.11
Cd	4.78	4.81	4.80	4.80±0.03	-	-	-
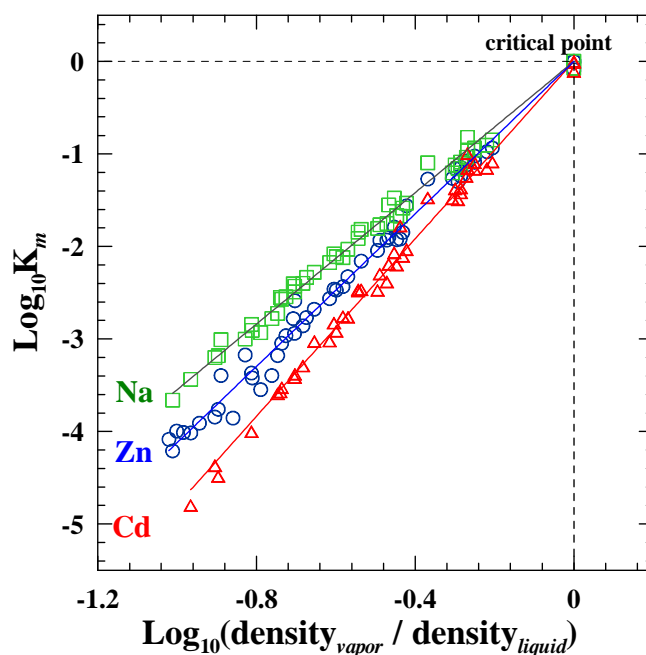
Figure V-5. *Density model for Na, Zn and Cd partitioning between the coexisting vapor and liquid phases in the H_2O-NaCl-HCl system at 400-450°C. The symbols denote the experimental data points from Supplementary Tables 1 and 2, but the solid lines represent the linear regressions for each metal using the n_i values from Table V-5.*

V-4. Cd and Zn in volcanic gases of Kudryavy volcano: brief results of a field work in September 2006

A part of this thesis has been devoted to a field study of volcanic gases from the active Kudryavy volcano, Iturup, Kuril Islands, carried out in September 2006. The goals of this work were: *1)* to sample high-temperature fumaroles and to measure metal and volatile concentrations in the condensates with a particular emphasis on Cd and Zn and their major ligands Cl and S; *2)* to develop a new technique for condensate sampling allowing to quantify the possible losses of metals during high-temperature sampling; and *3)* to confront these natural data with our experimental and modeling results on Zn and Cd.

The results show that our new technique for condensate sampling, discussed in details in Chapter II, enables very efficient sampling and estimation of possible metals losses not accounted for when using classical techniques (e.g., "Giggenbach bottles"). The element concentrations in volcanic condensate samples are compared in Supplementary Tables 3-7 between different chemical treatments and analytical techniques. For the majority of analyzed major elements and volatiles, including sulfur, we have found very good agreement between different analytical techniques like ICP-AES, ICP-MS and HPLC (performed at LMTG, Toulouse, France) and total gas chromatography (carried out at IVIS DVO RAS, Petropavlovsk-Kamchatsky, Russia). The samples with the ammonia matrix after oxidation by H_2O_2 analyzed by ICP-AES and HPLC yield total sulfur concentrations identical within

±5% to those analyzed in "Giggenbach bottles" and those reported elsewhere for similar fumaroles of Kudryavy volcano (e.g., Taran et al., 1995; Yudovskaya et al., 2006). The matrix-free samples analyzed by ICP AES have shown sulfur concentrations 50-100% less than simultaneous samples with ammonia matrix. Thus, the presence of ammonia matrix results in efficient sampling of volcanic gases with very minor losses of total sulfur (≤5%). The chloride concentrations analyzed by HPLC in the samples with ammonia matrix after oxidation by H_2O_2 are 15-30% higher than those analyzed by total gas chromatography in "Giggenbach bottles". The possible total gas chromatography analytical problems for samples from "Giggenbach bottles" were discussed in Taran et al. (1995). Consequently, in this study we used the chloride concentrations from HPLC analyses.

Table V-6. Selected metals and volatiles concentrations in fumaroles condensates of the sampled points of Kudryavy volcano in September 2006 (see supplementary tables 3-7 for the full set of data).

	Rhenium field T=550°C Sampling points 1,2			Dome field T=700°C Sampling point 3			Main field T=820°C Sampling point 4		
	Cond.	**Precip.**	**Total**	**Cond.**	**Precip.**	**Total**	**Cond.**	**Precip.**	**Total**
S, ppm	13000	100	13100	30000	500	30500	40000	400	40400
Cl, ppm	2500	-	2500	10000	-	10000	8500	-	8500
Cu, ppm	0.020	0.050	0.070	0.040	0.110	0.15	1.500	0.100	1.600
Zn, ppm	0.30	0.20	0.50	2.400	1.000	3.40	1.400	1.500	3.000
As, ppm	2.20	0.30	2.50	3.500	2.500	5.00	3.000	1.600	3.600
Mo, ppm	0.15	0.005	0.15	2.00	1.00	3.00	0.150	0.650	0.800
Cd, ppm	0.010	0.090	0.10	0.050	0.040	0.09	0.055	0.005	0.060
Sn, ppm	0.030	0.020	0.050	0.24	0.020	0.26	0.200	0.020	0.220
Sb, ppm	0.020	0.005	0.025	0.065	0.005	0.07	0.057	0.003	0.060
Re, ppm	0.0030	0.0030	0.0060	0.050	0.060	0.11	0.005	0.020	0.025
Pb, ppm	0.20	0.100	0.30	0.800	0.300	1.10	0.500	0.200	0.700
Bi, ppm	0.020	0.090	0.11	0.15	0.10	0.25	0.150	0.040	0.190

«Cond.» = condensates; «Precipit.» = precipitations in the sampling tube; «Total» = «Cond.» + «Precipit.»; « - » not analyzed.

Our measured total concentrations of Pb and As trace metals demonstrate an excellent agreement between different sampling, treatment and analytical techniques (see Supplementary Tables V-6 and V-7). For other trace metals, including Cd and Zn, variations between different techniques and analytical treatments are somewhat greater. For example, S-rich samples posed matrix problems when analyzing some trace metals (e.g., Cd and Cu) at ppb levels. This was particularly pronounced for the ICP-MS technique which may yield incorrect results because of the strong influence of Cl and S on the measured signal. Thus, for ICP-MS analyses sulfur-rich samples in the ammonia matrix were diluted 2 to 10 times more than ammonia-free samples in which 50-90% of sulfur was lost during sampling due to high volatility of sulfur species. Consequently, the concentrations in these diluted samples have elevated uncertainties. In the case of disagreement with ICP-MS analyses, ICP-AES data were assumed to be more accurate. Summarized data for selected metals and volatiles are reported in Table V-6. All performed analyses are given in Supplementary Tables for Chapter V.

Our analyses of both condensates and precipitations during sampling have demonstrate that up to 90-99% of some metals can be lost during sampling due to the precipitation in the sampling tubes (e.g., Cd in sample point 1, Table V-6, Fig. V-6). Different metals demonstrate different tendencies with temperature. As it can be seen from the Fig. V-6, the precipitation in the sampling tube of such metals as Cd, Cu, Sn, Sb and Bi decreases with increasing temperature, whereas for such metals as Zn, As, Mo, Re, precipitation, in contrast, increases with increasing temperature. The amount of Pb precipitated in the sampling tube is constantly ~30% of the total Pb (TableV-6, FigV-6b). It should be noted that possible losses of metals during sampling was often ignored in previous studies. Work is currently in progress to revise the existing volcanic gas data and compare them with the data obtained in this work. This part is out of the scope of the present thesis. The total metal concentrations in the fumaroles vapor corresponds to the sum of amounts measured in the condensate and precipitated in the tube, as shown in Table V-5 and in Fig. V-7.
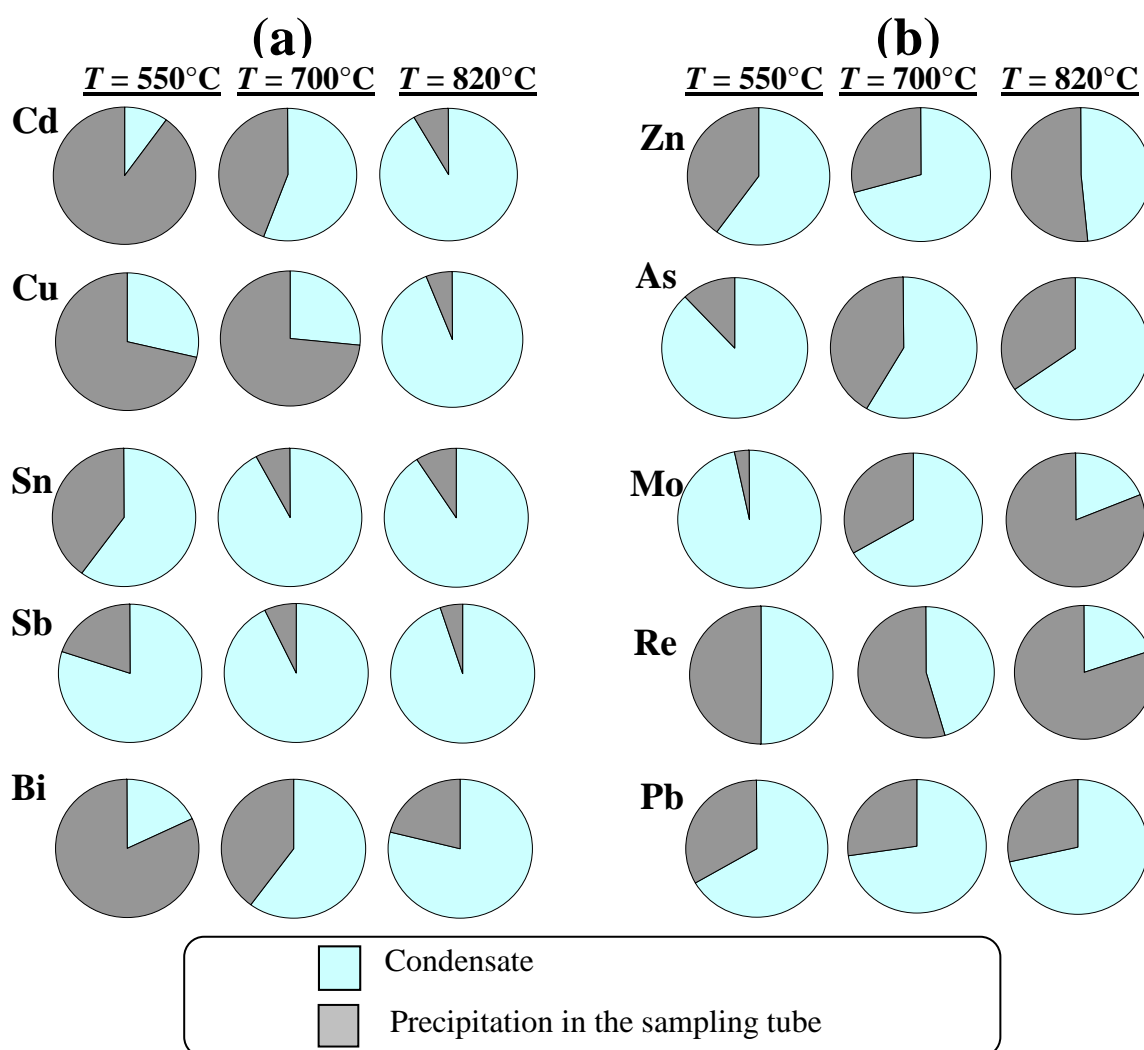
Figure V-6. *Metals distribution between condensates and precipitations in the corresponding sampling tube at 550°C (sampling point 1,2, Rhenium field), 700°C (sampling point 3, Dome field) and 800°C (sampling point 4, Main field). (a) Precipitation increases with increasing temperature; (b) precipitation decreases with increasing temperature. Pb demonstrates no tendencies with temperature. The values of all concentrations are given in Table V-6.*
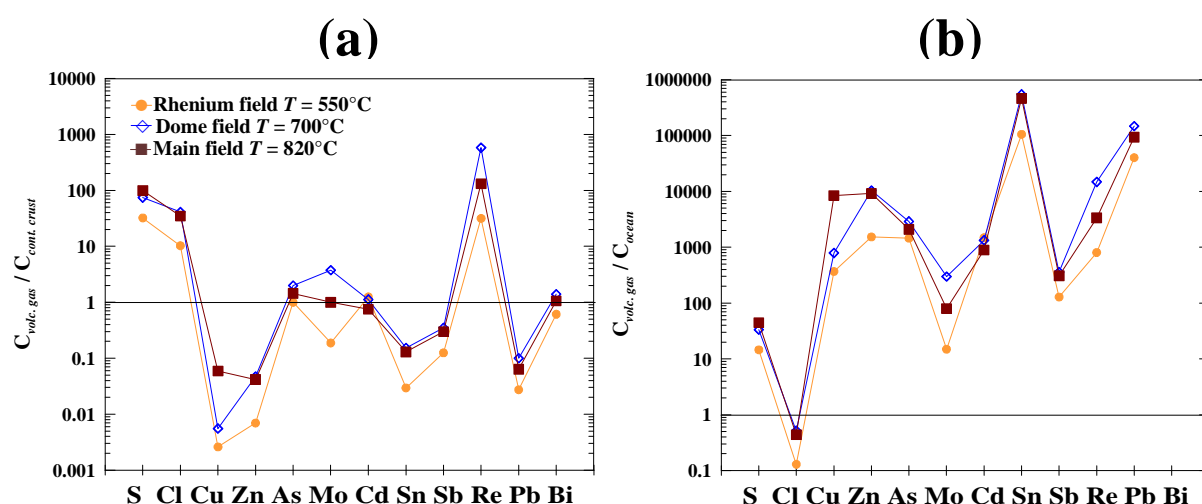
Figure V-7. *Chemical composition of the volcanic gases at 550°C, 700°C and 820°C. All concentrations are normalized to the average concentrations in the continental crust (a) and in the ocean (b). The values of the concentrations correspond to "Total" in the Table V-6. The average concentrations in the continental crust are from Rudnick and Gao (2003) and in the ocean – from Bruland and Lohan (2003).*

Despite the scarcity of the complete set of data on Cd, Zn and sulfur and chloride forms, it is tempting however, to examine the evolution of Cd/Zn ratios in the fumaroles as a function of concentration of the main ligands of these metals, H_2S and HCl. The major reactions controlling Cd and Zn transport in fumaroles gases are likely the following:

$$CdCl_2 + H_2S^0 = CdS + 2HCl^0 \qquad\qquad (V-4)$$
$$ZnCl_2 + H_2S^0 = ZnS + 2HCl^0 \qquad\qquad (V-5)$$

Both CdS and ZnS were found in the fumaroles sublimates in previous studies (e.g., Chaplygin et al., 2007), suggesting that they might be the solubility controlling phases. The neutral gaseous Cd and Zn chloride species are likely to dominate the metal speciation in these very low-density and dielectric constant media, which greatly favor uncharged species stabilities. Hydrochloric acid is the major Cl-bearing compound of volcanic gases. The full thermodynamic description of gas-solid reactions is out of scope of this work, so only rough concentration trends will be discussed here.

In Fig. V-8 the Cd/Zn mass ratio measured in our samples and rare published work (Taran et al., 1995) is plotted as a function of total Cl concentration. It can be seen that, despite the large data scatter, there is a general tendency of increasing the Cd/Zn ratio in the gas with increasing HCl ligand concentration. This again confirms the higher affinity of Cd that Zn to Cl ligands in the vapor phase. However, the stability of CdS versus ZnS solids and the concentration of H_2S which is involved in the solubility controlling reactions V-4 and V-5 should be also taken into account. It can be seen in Fig.

V-6b that again there is a vague but positive correlation between Cd/Zn and HCl/H$_2$S in the fumaroles. The data scatter is the result of a number of factors like temperature differences between different samples, solid-gas equilibration kinetics and possible variations of gas composition with time and place. This very rough geochemical analysis is just intended to provide ideas for the potential use of Cd/Zn ratios as a geochemical tracer in volcanic gases. It is clear that an integrated approach combining full geological information with thermodynamic modeling will allow to do so in the future.
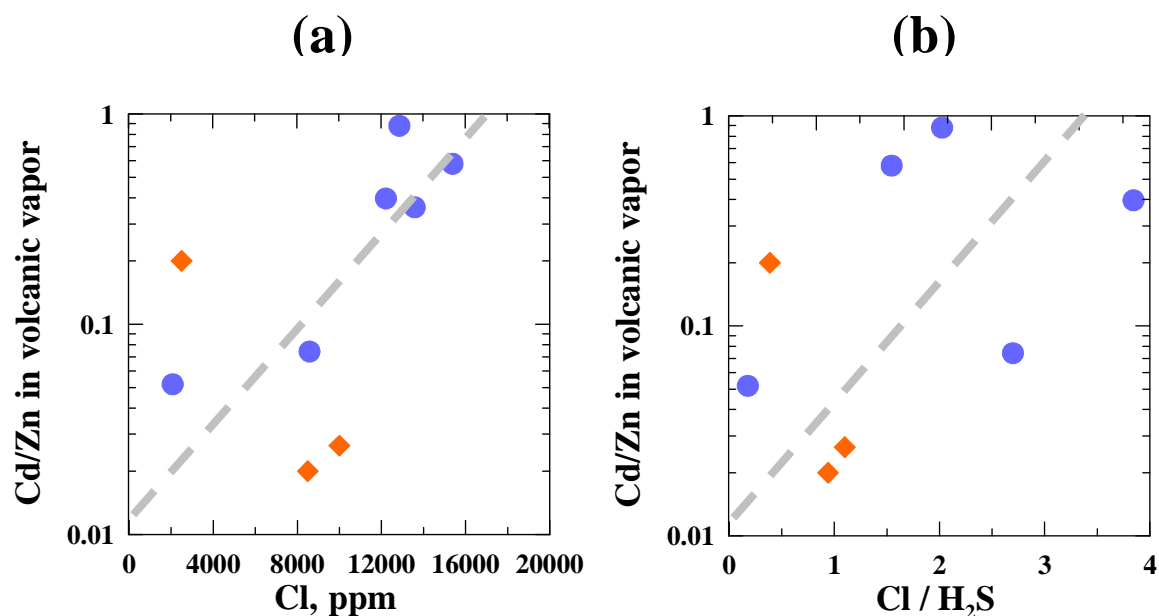
Figure V-8. *Cd/Zn weight ratio in Kudryavy volcano gases as a function of Cl concentration (a) and HCl/H$_2$S weight ratio (b). Diamonds = our data (Tab. V-6), circles = data of Taran et al. (1995); curves represent linear regression of all data.*

Supplementary Tables for Chapter V.

Supplementary Table V-1. Vapor-liquid partitioning of Na, Zn and Cd in the H_2O-NaCl-HCl system at 400°C and 450°C.

Sample	P, bar	Vapor, measured				Liquid, interpolated using data of Supplementary Table V-2				$\log_{10}$dens	$\log_{10}K_m$		
		Density	mNa	mZn	mCd	Density	mNa	mZn	mCd	V/L	Na	Zn	Cd
Experiment #1, *T* = 400°C													
I-4u	278.1	0.293	1.17E-01	2.46E-03	1.80E-03	0.520	1.07	3.03E-02	2.64E-02	-0.25	-0.96	-1.09	-1.17
I-1u(a)	278.1	0.293	1.24E-01	2.87E-03	2.13E-03	0.520	1.07	3.03E-02	2.64E-02	-0.25	-0.94	-1.02	-1.09
I-2u(a)	277.6	0.286	1.23E-01	2.68E-03	1.94E-03	0.529	1.12	3.18E-02	2.78E-02	-0.27	-0.96	-1.07	-1.16
I-5u	276.7	0.274	9.24E-02	2.40E-03	1.28E-03	0.545	1.22	3.45E-02	3.04E-02	-0.30	-1.12	-1.16	-1.38
I-6u	276.5	0.271	7.75E-02	1.91E-03	1.02E-03	0.549	1.24	3.52E-02	3.10E-02	-0.31	-1.20	-1.26	-1.48
I-7u	266.6	0.214	3.73E-02	7.09E-04	2.81E-04	0.661	2.17	6.08E-02	5.58E-02	-0.49	-1.77	-1.93	-2.30
I-10V	267.8	0.219	3.64E-02	6.74E-04	2.18E-04	0.649	2.05	5.76E-02	5.26E-02	-0.47	-1.75	-1.93	-2.38
I-11V	266.2	0.213	3.46E-02	5.62E-04	1.91E-04	0.665	2.21	6.19E-02	5.69E-02	-0.49	-1.81	-2.04	-2.47
I-8V	262.3	0.199	3.14E-02		2.20E-04	0.698	2.57	7.17E-02	6.65E-02	-0.54	-1.91		-2.48
I-9V(a)	262.3	0.199	3.67E-02		2.26E-04	0.698	2.57	7.17E-02	6.65E-02	-0.54	-1.85		-2.47
I-13V	245.8	0.159	1.51E-02	2.90E-04	4.45E-05	0.801	4.05	1.12E-01	1.07E-01	-0.70	-2.43		-3.38
I-13L	244.3	0.158	1.62E-02	1.88E-04		0.803	4.10	1.13E-01	1.08E-01	-0.71	-2.40	-2.78	
I-15V	240.8	0.150	1.26E-02		3.19E-05	0.825	4.50	1.24E-01	1.19E-01	-0.74	-2.55		-3.57
I-15L	238.8	0.149	8.68E-03	8.37E-05	3.11E-05	0.830	4.59	1.27E-01	1.22E-01	-0.75	-2.72	-3.18	-3.59
I-17V	218.0	0.119	6.59E-03		2.43E-05	0.920	6.72	1.84E-01	1.81E-01	-0.89	-3.01	-3.40	
I-17L	215.5	0.116	4.40E-03	2.74E-05	8.06E-06	0.929	7.00	1.92E-01	1.89E-01	-0.91	-3.20	-3.84	-4.37
I-18V	196.6	0.098	2.09E-03	1.61E-05		1.002	9.62	2.62E-01	2.62E-01	-1.01	-3.66	-4.21	
Experiment #2, *T* = 400°C													
II-1V	279.4	0.310	1.32E-01	1.38E-03	8.38E-04	0.498	0.93	1.19E-02	1.03E-02	-0.206	-0.849	-0.936	-1.088
II-2V	277.5	0.285	1.04E-01	1.08E-03	7.14E-04	0.531	1.12	1.42E-02	1.25E-02	-0.271	-1.035	-1.120	-1.243
II-3V(a)	279.0	0.305	1.21E-01	1.31E-03	7.48E-04	0.505	0.97	1.23E-02	1.07E-02	-0.219	-0.905	-0.976	-1.156
II-4V(a)	277.1	0.279	8.69E-02	1.05E-03	5.57E-04	0.538	1.17	1.48E-02	1.30E-02	-0.285	-1.128	-1.147	-1.368
II-6V	277.1	0.279	9.53E-02	8.52E-04	4.93E-04	0.538	1.17	1.48E-02	1.30E-02	-0.285	-1.088	-1.239	-1.420
II-7V	276.9	0.276	8.28E-02	7.55E-04	4.23E-04	0.542	1.19	1.51E-02	1.33E-02	-0.292	-1.157	-1.300	-1.496
II-9V	271.1	0.233	5.09E-02	5.98E-04	1.82E-04	0.616	1.73	2.18E-02	1.97E-02	-0.422	-1.532	-1.561	-2.033
II-10V	270.5	0.230	4.64E-02	3.18E-04	1.59E-04	0.622	1.79	2.24E-02	2.03E-02	-0.431	-1.585	-1.848	-2.106
II-12V(a)	270.1	0.228	3.88E-02	2.76E-04	3.45E-04	0.626	1.82	2.29E-02	2.07E-02	-0.438	-1.672	-1.919	-1.779

II-11V	269.5	0.226	4.03E-02	2.78E-04	1.35E-04	0.632	1.88	2.35E-02	2.14E-02	-0.447	-1.668	-1.927	-2.200
II-14V	260.1	0.192	2.55E-02	1.60E-04	5.45E-05	0.714	2.74	3.40E-02	3.17E-02	-0.570	-2.031	-2.327	-2.765
II-15V(a)	259.0	0.189	2.14E-02	1.29E-04	5.74E-05	0.722	2.83	3.52E-02	3.29E-02	-0.582	-2.121	-2.434	-2.758
II-16V	257.5	0.185	2.30E-02	1.24E-04	4.18E-05	0.733	2.97	3.68E-02	3.45E-02	-0.599	-2.110	-2.472	-2.916
II-17V	256.0	0.180	2.08E-02	1.05E-04	3.44E-05	0.743	3.10	3.85E-02	3.62E-02	-0.616	-2.174	-2.564	-3.023
II-20V	237.7	0.145	7.74E-03	2.30E-05		0.839	4.65	5.73E-02	5.52E-02	-0.761	-2.779	-3.395	
II-21V	233.6	0.139	5.86E-03	1.74E-05		0.856	5.00	6.15E-02	5.95E-02	-0.789	-2.932	-3.548	
II-22V	230.4	0.135	6.56E-03	2.47E-05		0.870	5.30	6.51E-02	6.33E-02	-0.811	-2.908	-3.421	
II-23V (a)	227.7	0.131	5.53E-03	4.57E-05		0.881	5.55	6.81E-02	6.63E-02	-0.829	-3.002	-3.173	
II-24V	222.9	0.124		1.03E-05		0.900	6.01	7.36E-02	7.20E-02	-0.859		-3.855	
II-26V	208.7	0.109		1.13E-05		0.955	7.54	9.20E-02	9.11E-02	-0.944		-3.911	
II-27V	201.5	0.102		1.01E-05		0.985	8.55	1.04E-01	1.04E-01	-0.984		-4.011	
II-28V	198.4	0.099		1.10E-05		0.997	8.97	1.09E-01	1.09E-01	-1.001		-3.996	
II-26L-V	195.0	0.096		9.37E-06		1.007	9.37	1.14E-01	1.14E-01	-1.021		-4.085	

Experiment #4, $T = 450°C$

4-1V	470.0	0.54	1.6096	5.76E-02	5.95E-02	0.54	1.61	5.75E-02	6.09E-02	0	0	0	-0.01
4-2V	424.0	0.535	1.4877	5.14E-02	5.12E-02	0.535	1.77	6.32E-02	6.56E-02	0	-0.07	-0.09	-0.11
4-3V	416.0	0.360	0.3754	1.81E-02	9.99E-03	0.667	2.49	9.28E-02	9.87E-02	-0.27	-0.82		-1.00
4-4V	406.0	0.310	0.2541	6.17E-03	4.14E-03	0.723	3.17	1.15E-01	1.24E-01	-0.37	-1.10	-1.27	-1.47
4-5V	392.8	0.270	0.1333	2.42E-03	1.36E-03	0.765	3.99	1.50E-01	1.59E-01	-0.45	-1.48	-1.79	-2.07
4-6V	390.1	0.263	0.1170	1.97E-03	1.07E-03	0.771	4.17	1.58E-01	1.67E-01	-0.47	-1.55	-1.90	-2.19
4-7V	376.8	0.238	0.0774	1.25E-03	6.53E-04	0.817	5.07	1.80E-01	1.92E-01	-0.54	-1.82	-2.16	-2.47
4-7Lvap	360.5	0.215	0.0524	7.44E-04	3.42E-04	0.864	6.32	2.16E-01	2.31E-01	-0.60	-2.08	-2.46	-2.83
4-8V	347.9	0.199	0.0389	5.19E-04	2.51E-04	0.898	7.41	2.48E-01	2.67E-01	-0.65	-2.28	-2.68	-3.03
4-9V(a)	342.6	0.193	0.0355	4.68E-04		0.912	7.69	2.75E-01	2.92E-01	-0.67	-2.34	-2.77	
4-9Lvap	340.2	0.190	0.0314	3.90E-04	1.52E-04	0.917	7.88	2.81E-01	2.99E-01	-0.68	-2.40	-2.86	-3.29
4-10V	335.0	0.184	0.0267	3.40E-04	1.21E-04	0.931	8.28	2.96E-01	3.14E-01	-0.70	-2.49	-2.94	-3.42
4-10Lvap	329.3	0.177	0.0249	3.39E-04		0.943	8.74	3.12E-01	3.32E-01	-0.73	-2.54	-2.96	
4-11V	326.5	0.175	0.0242	2.89E-04	1.02E-04	0.952	9.00	3.22E-01	3.42E-01	-0.74	-2.57	-3.05	-3.53
4-11Lvap	305.7	0.154	0.0154	1.64E-04	4.06E-05	0.998	10.75	3.84E-01	4.08E-01	-0.81	-2.84	-3.37	-4.00
4-12V	281.8	0.132	0.0085	7.99E-05	1.60E-05	1.043	12.88	4.60E-01	4.89E-01	-0.90	-3.18	-3.76	-4.49
4-13V	261.6	0.117	0.0054	5.10E-05	8.91E-06	1.084	14.83	5.30E-01	5.63E-01	-0.97	-3.44	-4.02	-4.80

Supplementary Table V-2. Measured concentrations of Na, Zn, Cd in the liquid phase of our vapor-liquid partitioning experiments.

Sample	P, bar	Liquid density, g/cm^3	mNa	mZn	mCd
Experiment #1, $T = 400°C$					
I-4d	283.5	0.492	0.752	2.42E-02	2.16E-02
I-5d	277.2	0.536	1.363	4.31E-02	3.85E-02
I-6d	275.4	0.568	1.335	4.00E-02	3.57E-02
I-7d	266.3	0.664	2.059	5.43E-02	4.94E-02
I-8L	265.5	0.672	1.785	5.68E-02	4.41E-02
I-10L	267.8	0.649	2.612	7.11E-02	6.33E-02
I-11L	265.5	0.672	2.222	6.67E-02	5.94E-02
I-12L(a)	265.8	0.669	2.649	7.24E-02	6.85E-02
Experiment #2, $T = 400°C$					
II-1L	279.4	0.498	1.648	1.74E-02	1.12E-02
II-2L	276.5	0.549	1.154	1.47E-02	0.00E+00
II-6L	276.4	0.550	1.270	1.70E-02	1.34E-02
II-7L	276.1	0.556	1.308	1.66E-02	1.36E-02
II-9L	269.3	0.634	1.889	2.23E-02	2.02E-02
II-10L	269.9	0.628	1.878	2.26E-02	2.11E-02
II-11L	268.3	0.644	2.035	2.52E-02	2.54E-02
II-14L	255.4	0.730	2.924	3.61E-02	3.53E-02
II-16L	254.1	0.739	3.044	3.77E-02	3.75E-02
II-17L	252.6	0.749	3.144	4.05E-02	3.37E-02
II-20L	229.9	0.855	5.067	6.24E-02	5.64E-02
II-21L	230.7	0.851	4.874	6.17E-02	5.82E-02
II-22L	224.0	0.880	5.474	6.56E-02	6.92E-02
II-24L	221.2	0.891	5.721	7.08E-02	6.90E-02
Experiment #4, $T = 450°C$					
4-1L	470.0	0.540	1.61	5.75E-02	6.09E-02
4-2L	424.0	0.535	1.77	6.32E-02	6.56E-02
4-3L	415.5	0.674	2.54	9.48E-02	1.01E-01
4-4L	406.0	0.723	3.17	1.15E-01	1.24E-01
4-5L	389.5	0.773	4.21	1.59E-01	1.69E-01
4-6L	371.6	0.833	5.45	1.89E-01	2.02E-01
4-8L(a)	343.1	0.911	7.86	2.61E-01	2.81E-01

Supplementary Table V-3. Anions concentrations in volcanic condensates from HPLC analyses.

Sample point	Field name	T,°C	F⁻, ppm	Cl⁻, ppm	SO_4^{2-}, ppm	S, ppm (recalculated)
1	Rhenium	550-350	152	2216	32998	11773
2	Rhenium	550-351	239	2856	41948	14966
3	Dome	700-465	-	10077	81618	29120
4	Main	820-620	-	8485	89870	32064

"-" = below detection limits (< 0.1 ppm)

Supplementary Table V-4. Gas chromatography analyses of fumarolic gases sampled with "Giggenbach bottles", analyses performed by V. Shapar and I. Timofeeva at the Institute of Volcanology and Seismology (IVIS DVO RAS, Petropavlovsk-Kamchatsky, Russia).

	Rhenium	Dome	Main (Fracture)	Main	Molybdenum
T, °C	550	725	744	820	613
date	27/09/06	07/09/06	21/09/06	30/09/06	09/09/06
H_2O, mol %	98.38	96.60	94.57	94.68	96.80
CO_2, mol %	0.63	0.58	0.90	2.14	0.92
H_2S, mol %	0.35	0.51	0.78	0.52	0.49
SO_2, mol %	0.43	1.60	2.69	1.85	1.26
HCl, mol %	0.099	0.337	0.382	0.098	0.313
CO, mol %	6.5E-04	6.2E-03	7.1E-03	0.015	2.0E-03
CH_4, mol %	2.1E-04	3.6E-05	2.6E-05	3.2E-04	9.1E-05
H_2, mol %	0.095	0.335	0.602	0.631	0.178
N_2, mol %	0.025	0.037	0.067	0.063	0.031
O_2, mol %	3.5E-04	3.7E-04	3.4E-03	4.4E-03	4.9E-04
Ar, mol %	6.8E-05	1.2E-04	2.2E-04	1.1E-04	1.4E-04
He, mol %	0	5.3E-06	0	0	3.0E-06
C_2H_6, mol %	4.0E-07	4.5E-08	4.1E-08	3.5E-07	1.1E-07
C_2H_4, mol %	2.5E-07	1.5E-06	1.3E-06	1.2E-06	1.2E-06

Supplementary Table V-5. Total sulfur and chlorine concentration in the samples from "Giggenbach bottles". Recalculated from Supplementary Table V-4.

Field name	T°C	date	Cl, ppm	S, ppm
Rhenium	550	27/09/06	1907	13442
Dome	725	07/09/06	6288	35491
Main (Fracture)	744	21/09/06	6911	56752
Main	820	30/09/06	1788	39025
Molybdenium	613	09/09/06	5861	29590

Supplementary Table V-6. ICP-AES analyses of volcanic condensate samples.

	No matrix			3M NH$_4$OH matrix			
	Condensate (Aqua regia)	Precipitation (Aqua regia)	Total	Condensate (Aqua regia)	(H$_2$O$_2$)	Precipitation (Aqua regia)	Total
Sample point 1, T=550-350°C, Rhenium field, 26/09/2006							
As, ppm	2.3	0.63	**2.9**	2.1	1.9	0.40	**2.5**
B, ppm	28	16	**44**	17	16	6.7	**23**
Ca, ppm	1.90	1.2	**3.1**	0.59	0.58	0.86	**1.5**
Cd, ppm	0.0093	0.088	**0.10**	0.0071		0.049	**0.056**
Cu, ppm						0.033	**0.033**
Fe, ppm	1.69	0.88	**2.6**	0.88	0.79	0.94	**1.8**
K, ppm		13	**13**		0.27	5.3	**5.3**
Mg, ppm	0.50	0.24	**0.74**	0.42	0.37	0.43	**0.85**
Na, ppm	11	8.4	**19**		0.15	3.6	**3.6**
Pb, ppm	0.13	0.30	**0.44**	0.14	0.14	0.13	**0.27**
S, ppm	6952	70	**7022**	11680	10850	55	**11735**
Zn, ppm	0.89	0.20	**1.1**	0.34	0.31	0.18	**0.52**
Sample point 2, T=550-350°C, Rhenium field, 27/09/2006							
As, ppm	1.6			2.2	2.1	0.2	**2.4**
B, ppm	27			16	16	0.018	**16**
Ca, ppm	8.1			0.16	0.22	0.70	**0.86**
Cd, ppm	0.019			0.012	0.011	0.022	**0.034**
Cu, ppm						0.051	**0.051**
Fe, ppm	2.2			0.23	0.20	0.52	**0.75**
K, ppm						1.3	**1.3**
Mg, ppm	0.54			0.044	0.042	0.18	**0.22**
Na, ppm	12					0.35	**0.35**
Pb, ppm	0.31			0.23	0.22	0.064	**0.30**
S, ppm	9979			14120	14115	92	**14211**
Zn, ppm	4.0			0.13	0.14	0.32	**0.45**
Sample point 3, T=700-465°C, Dome field, 27/09/2006							
As, ppm	1.2	3.7	**4.8**	3.4	3.2	2.4	**5.8**
B, ppm	59	11	**70**	17	19	17	**34**
Ca, ppm	8.8	2.3	**11**	3.9	4.5	1.6	**5.5**
Cd, ppm	0.051	0.036	**0.087**	0.038	0.038	0.024	**0.061**
Cu, ppm	0.038	0.11	**0.15**			0.068	**0.068**
Fe, ppm	21	23	**44**	16	15	13	**30**
K, ppm	12	14	**26**	8.5	7.1	16	**24**
Mg, ppm	4.7	4.31	**9.0**	4.3	4.1	2.2	**6.6**
Na, ppm	41	10	**51**	8.5	8.1	12	**20**
Pb, ppm	0.90	0.62	**1.5**	0.76	0.73	0.34	**1.1**
S, ppm	2461	720	**3181**	29552	33231	673	**30225**
Zn, ppm	4.3	0.92	**5.2**	2.4	2.3	1.0	**3.4**
Sample point 4, T=820-620°C, Main field, 30/09/2006							
As, ppm				3.0	2.7	1.6	**4.5**
B, ppm				18	17	36	**54**
Ca, ppm				0.9	1.0	3.6	**4.5**
Cd, ppm				0.055	0.050	0.005	**0.061**
Cu, ppm				1.5	1.3	0.081	**1.6**

Fe, ppm	2.1	2.0	1.8	**4.0**
K, ppm	4.7	4.0	26	**31**
Mg, ppm	0.32	0.29	0.39	**0.70**
Na, ppm	4.3	3.0	19	**23**
Pb, ppm	0.54	0.48	0.15	**0.7**
S, ppm	33720	32451	349	**34068**
Zn, ppm	1.4	1.3	1.5	**2.9**

"Condensate" corresponds to the analyses of condensated volcanic gases; "Precipitation" corresponds to the analyses of sampling tubes for corresponding condensate; "No matrix" means that condensates were sampled without ammonia matrix; "3M NH$_4$OH matrix" means that condensate samples were collected to ammonia matrix; "Aqua regia" means that samples were treated using aqua regia; "H$_2$O$_2$" means that samples were treated with H$_2$O$_2$ (only samples with ammonia matrix).

Supplementary Table V-7. ICP-MS analyses of volcanic condensate samples.

	No matrix			3M NH$_4$OH matrix			
	Condensate (Aqua regia)	Precipitation (Aqua regia)	Total	Condensate (Aqua Regia)	Condensate (H$_2$O$_2$)	Precipitation (Aqua regia)	Total
Sample point 1, T=550-350°C, Rhenium field, 26/09/2006							
Cu, ppm	0.0048	0.013	**0.018**	0.016	0.020	0.039	**0.055**
Zn, ppm	0.61	0.13	**0.74**	0.23	0.23	0.094	**0.319**
As, ppm	2.2	0.50	**2.7**	2.0	1.7	0.26	**2.27**
Se, ppm	0.67	0.063	**0.73**	0.50	0.52	0.042	**0.54**
Mo, ppm	0.040	0.017	**0.057**	0.15	0.15	0.0053	**0.155**
Ag, ppm							
Cd, ppm	0.0077	0.067	**0.075**			0.033	**0.033**
Sn, ppm	0.026	0.020	**0.046**	0.044	0.044	0.013	**0.057**
Sb, ppm	0.020	0.002	**0.023**	0.019	0.019	0.0017	**0.021**
Te, ppm	0.10	0.018	**0.12**	0.078	0.081	0.015	**0.09**
Ba, ppm	0.051	0.260	**0.31**	0.10	0.11	0.12	**0.23**
W, ppm						0.00076	**0.00076**
Re, ppm	0.0031	0.0029	**0.0060**			0.00077	**0.00077**
Tl, ppm	0.030			0.024	0.024	0.0027	
Pb, ppm	0.171	0.26	**0.43**	0.17	0.17	0.10	**0.27**
Bi, ppm	0.035	0.20	**0.24**	0.022	0.022	0.092	**0.11**
Sample point 2, T=550-350°C, Rhenium field, 27/09/2006							
Cu, ppm	0.010			0.064	0.091	0.092	**0.155**
Zn, ppm	3.0			0.068	0.072	0.28	**0.35**
As, ppm	1.6			2.3	2.2	0.13	**2.39**
Se, ppm	0.46			0.44	0.42	0.25	**0.69**
Mo, ppm	0.032			0.0050		0.020	**0.025**
Ag, ppm	0.035			0.0019		0.0043	**0.0063**
Cd, ppm	0.047			0.0050		0.019	**0.024**
Sn, ppm	0.039			0.035	0.027	0.012	**0.047**
Sb, ppm				0.018	0.015	0.0066	**0.025**
Te, ppm				0.055	0.049	0.051	**0.11**
Ba, ppm				0.0065	0.0075	0.0022	**0.0088**
W, ppm				0.012		0.0016	**0.013**
Re, ppm							
Tl, ppm	0.034			0.030	0.033	0.0031	**0.033**
Pb, ppm	0.379			0.28	0.28	0.065	**0.344**
Bi, ppm	0.016			0.011	0.020	0.058	**0.069**

Sample point 3, *T*=700-465°C, Dome field, 27/09/2006

Cu, ppm	0.062	0.067	**0.13**	0.11	0.13	0.058	**0.17**
Zn, ppm	3.1	0.29	**3.4**	1.9	1.7	0.44	**2.3**
As, ppm	0.93	1.4	**2.3**	3.1	3.3	1.3	**4.4**
Se, ppm	1.3	1.0	**2.3**	0.72	0.63	1.2	**1.9**
Mo, ppm	5.1	0.9	**6.0**	1.9	2.2	1.0	**2.9**
Ag, ppm	0.0034	0.0031	**0.007**	0.0029	0.0021	0.002	**0.0047**
Cd, ppm	0.037	0.014	**0.051**	0.025	0.022	0.014	**0.039**
Sn, ppm	0.243	0.044	**0.29**	0.23	0.25	0.015	**0.25**
Sb, ppm	0.083	0.0025	**0.086**	0.058	0.063	0.0039	**0.062**
Te, ppm	0.13	0.17	**0.30**	0.066	0.066	0.17	**0.23**
Ba, ppm	0.12	0.10	**0.22**	0.058	0.068	0.22	**0.27**
W, ppm		0.015	**0.015**	0.067	0.076	0.030	**0.10**
Re, ppm	0.051	0.058	**0.11**	0.0073	0.0071	0.078	**0.086**
Tl, ppm	0.078	0.032	**0.11**	0.082	0.090	0.018	**0.10**
Pb, ppm	0.88	0.35	**1.2**	0.84	0.92	0.26	**1.10**
Bi, ppm	0.16	0.083	**0.25**	0.15	0.16	0.061	**0.21**

Sample point 4, *T*=820-620°C, Main field, 30/09/2006

Cu, ppm				1.60	2.02	0.21	**1.8**
Zn, ppm				1.13	1.1	1.3	**2.4**
As, ppm				2.93	3.1	1.5	**4.4**
Se, ppm				1.2	1.4	0.47	**1.7**
Mo, ppm				0.14	0.13	0.64	**0.79**
Ag, ppm						0.0016	**0.0016**
Cd, ppm				0.042	0.045	0.0039	**0.046**
Sn, ppm				0.19	0.20	0.024	**0.22**
Sb, ppm				0.056	0.054	0.0028	**0.059**
Te, ppm				0.14	0.16	0.11	**0.26**
Ba, ppm				0.014	0.018	0.78	**0.79**
W, ppm				0.018	0.013	0.020	**0.038**
Re, ppm				0.0048	0.0062	0.021	**0.026**
Tl, ppm				0.073	0.088	0.011	**0.085**
Pb, ppm				0.63	0.67	0.17	**0.79**
Bi, ppm				0.15	0.17	0.044	**0.19**

See footnote of Supplementary Table V-6.

Chapter VI. CONCLUSIONS AND PERSPECTIVES

The hydrothermal fluids and volcanic vapors concentrate and fractionate Cd and Zn, in some cases dramatically affecting Cd/Zn ratios. Although, many experimental studies were conducted by previous authors on Zn aqueous speciation and mineral solubilities, our study provides the first systematic structural and thermodynamic data for Cd at temperatures and pressures above ambient. Thus, the major part of our experimental work was devoted to the identity, structure and stability of the main aqueous species transporting cadmium in hydrothermal fluids and vapors in a wide range of T-P-mCl. We have used a combination of different complementary laboratory methods like potentiometry, solubility, and in situ X-ray absorption spectroscopy. In addition, for both Cd and Zn we performed solubility measurements in high-T aqueous Cl-bearing vapors and vapor-brine partitioning measurements in the two-phase H_2O-NaCl-HCl system. These experimental laboratory data were compared with our analyses of volcanic fumaroles at the Kudryavy volcano (Kuril Islands, Russia) and available literature data for modern hydrothermal systems and hydrothermal ore deposits in an attempt to correlate the Cd/Zn ratios in fluids and minerals with physical-chemical parameters and fluid compositions.

Our potentiometric measurements performed in Cd-bearing chloride aqueous solutions as a function of pressure at 25°C allowed the derivation of individual molal volumes of four cadmium chloride complexes. Our data demonstrate a good linear correlation between the non-electrostatic contribution to the standard molal volume and the ligand number in the complex for $CdCl_2^0$(aq), $CdCl_3^-$, and $CdCl_4^{2-}$ but this linearity breaks up for Cd^{2+} and $CdCl^+$. This corresponds to the coordination change from octahedral (for $Cd(H_2O)_6^{2+}$ and $CdCl(H_2O)_5^+$ species) to tetrahedral structures (for $CdCl_2(H_2O)_2^0$, $CdCl_3(H_2O)^-$, $CdCl_4^{2-}$ species). This observation is in agreement with our direct XAFS spectroscopy data. The values of the standard volumes were used in the framework of the revised HKF equation of state to provide improved pressure-dependent HKF parameters for each Cd-Cl species, thus allowing calculations of their thermodynamic properties at pressures up to 5000 bar. The thermodynamic modeling performed using these new data for Cd and available literature data for Zn (Sverjensky et al., 1997) demonstrates that in hydrothermal fluids the increase of pressure results in an increase of the Cd content in sphalerite in equilibrium with a hydrothermal saline fluid. The results of this part of our work constitute a research article submitted to *Geology of Ore Deposits* in August 2009 (Bazarkina et al., 2009a).

In situ X-ray absorption spectroscopy in Cd-bearing solutions together with $CdO_{(s)}$ and $CdS_{(s)}$ solubility measurements were used to investigate the stoichiometry, structure and stability of the dominant cadmium chloride aqueous complexes in aqueous solution to 450°C and 600 bar. Results show that Cd aqueous speciation is dominated by the cation $Cd(H_2O)_6^{2+}$ in acidic Cl-free solutions, and by chloride species $CdCl_m(H_2O)_n^{2-m}$ over a wide range of temperature (20 – 450°C), acidity (1 – 8 pH), and chloride concentration (0.04 – 18m). Our spectroscopic data are consistent with the formation of octahedral $Cd(H_2O)_6^{2+}$ and $Cd(H_2O)_5Cl^+$ species and tetrahedral $CdCl_2(H_2O)_2^0$, $CdCl_3(H_2O)^-$ and $CdCl_4^-$ species at $T \leq$ 200-300°C and $m_{Cl} \leq$ 18. At ambient T-P our XANES and EXAFS results are in good agreement with stability constants for the four cadmium chloride complexes reported in the literature. At $T >$ 300°C, aqueous Cd speciation is dominated by two complexes, $CdCl_2(H_2O)_2^0$ and $CdCl_3(H_2O)^-$ in a wide m_{Cl} range (0.04 – 5m). The stability constants of these complexes, derived from

solubility measurements at 400°C and 600 bar are ~6 orders of magnitude higher than available HKF-model predictions which are based on low-T data. These new data were compared with the available structural and thermodynamic information about major Zn-Cl complexes, and a new potential geochemical tracer of the fluid composition using the Zn/Cd ratio has been proposed. These results are presented in a research article submitted to *Chemical Geology* in October 2009 (Bazarkina et al., 2009b).

Our accurate CdO and CdS solubility measurements in pure water and low-saline vapors at 400°C confirmed the findings in dense saline solutions. The higher affinity of Cd than Zn to the chloride ligand is responsible for the strong increase of the Cd/Zn ratio with increasing Cl concentration. These results are in line with our measured partitioning coefficients of Cd and Zn between coexisting vapor and liquid phases in the H_2O-NaCl-HCl system. Both Cd and Zn, together with Na, fractionate largely in favor of the Cl-rich liquid phase. This fractionation increases in the order Na - Zn - Cd. Consequently, during the fluid boiling, Cd will have a greater tendency than Zn to concentrate into the brine phase, resulting in an increase of Cd/Zn ratios in the Cl-rich brine during the fluid accent and pressure decrease. These data, combined with thermodynamic calculations of CdS and ZnS solubilities, where compared with natural analyses of Zn, Cd, associated metals and main volatile ligands S and Cl in high T-P fumaroles of the Kudryavy volcano, sampled and analyzed during this study. Our samples of volcanic condensates together with previous data of Taran et al. (1995) reported for the Kudryavy volcano demonstrate that despite the large data scatter, the Cd/Zn ratio has a tendency to increase with increasing Cl concentration. The Cd/Zn ratio can thus be used to trace the fluid evolution and composition.

PERSPECTIVES

A combination of different experimental and theoretical approaches was developed to study the identity, structure and stability of the dominant aqueous species responsible for Cd and Zn transport and precipitation in hydrothermal processes. Our study allowed obtaining new data about the behavior of these metals in a wide range of T-P-density-m_{Cl}-pH conditions, typical of hydrothermal-volcanic settings. At the same time, of course, our study indicated a number of new important near-future scientific challenges. Some of these new issues are discussed below.

- First, the inconsistency among the available in the literature solubility, potentiometric, spectroscopic and theoretical studies both on Cd and Zn speciation in the fluid phase should be emphasized. Despite numerous reported experimental studies on aqueous Zn-Cl complexes, the identity, structure and stability of the main Zn-Cl complexes in hydrothermal solutions should be carefully revised and existing discrepancies should be resolved. As it was done in our work for Cd chloride complexes, complementary experimental approaches should be applied to unambiguously resolve the stoichiometries and stabilities of main aqueous species of Zn. Different approaches should yield consistent data. For example, indirect methods like correlations between molal volumes and ligand number confirm nicely more direct spectroscopic findings as it was demonstrated in this work. Only ensemble of different experimental approaches together with thermodynamic analyses can help to understand, explain, and quantitatively model the metal behavior in hydrothermal fluids in a wide range of salinity and T-P- pH conditions.

- Second, it should be mentioned that more data on Cd contents in natural hydrothermal fluids and vapors are required. To the best of our knowledge, there are no reported data on Cd concentrations measured in individual fluid inclusions. It should be noted that simultaneous Cd and Zn measurements in fluid inclusions using such analytical techniques like laser ablation ICP-MS will provide the necessary information about the true concentrations of these metals in natural fluids. Unfortunately, almost no data exists on Cd concentrations in the coexisting vapor and brine fluid inclusions from magmatic-hydrothermal deposits, whereas data of Zn are abundant (e.g., Heinrich, 2007; Yardley, 2005; Philippot et al., 2001). It is clear also that for better understanding of the sources of Cd and Zn in hydrothermal fluids and tendencies of Cd/Zn ratios in Nature (Fig. VI-1) we need to know how these metals fractionate during crystallization of magmatic rocks, pegmatite and skarn formation, and their partitioning between magma and fluid phases. Both natural and experimental data are required to resolve this issue.
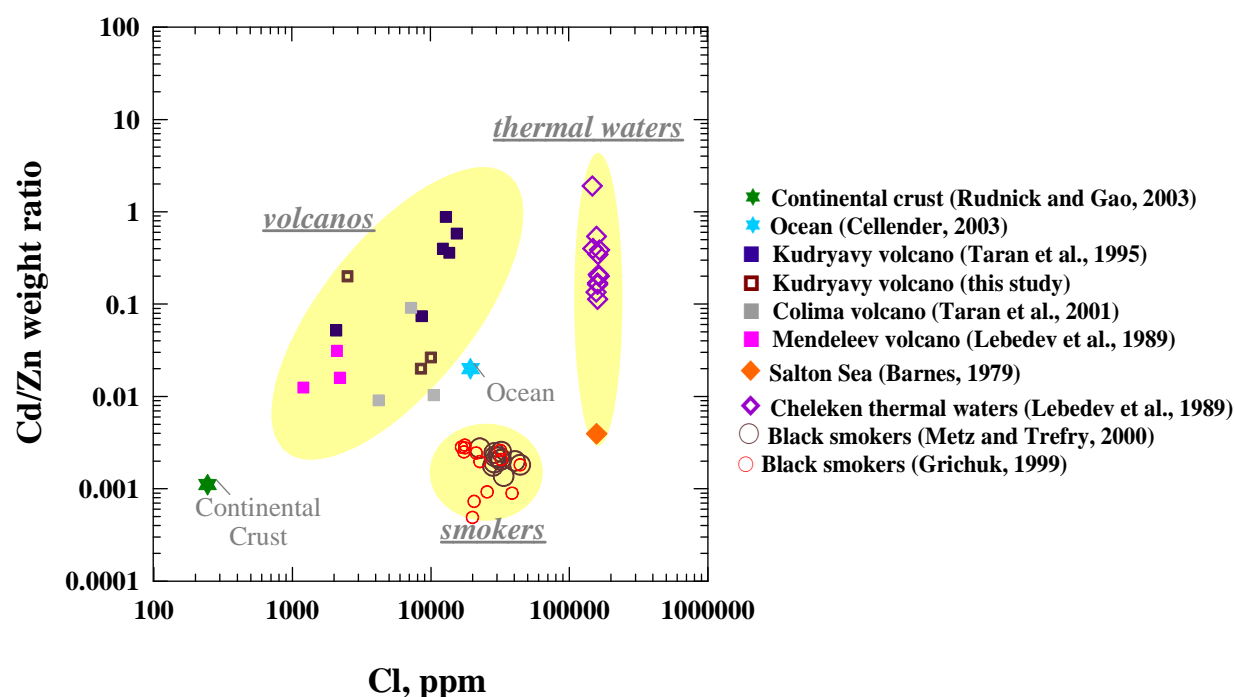
Figure VI-1. *The Cd/Zn ratio plotted as a function of Cl concentration observed in Nature. Three main trends are marked: volcanos, thermal waters and smokers.*

- Third, it should be mentioned that there are only few studies of complexing of Cd and Zn with ligands other than Cl and OH/H_2O, which are minor in the majority of natural hydrothermal fluids. The first ligand in this list is sulfur. For the moment, there are very limited experimental data for Zn complexation with sulfur ligands only at $T \leq 100°C$ (e.g., Tagirov et al., 2007) and there is no experimental data on Cd complexation with sulfur ligands at T-P above ambient. However, as it was mentioned by Rickard and Luther (2006), sulfide chemistry of Cd may be somewhat different from that of Zn. Thus, there is an important lack in our knowledge of Cd and Zn geochemistry. It should be mentioned also that our knowledge of the role of such minor ligands as NH_3^-, PO_4^{3-}, F^-, BO_3^{3-} in the behavior of both Cd and Zn is also very limited.

- Another interesting point is how the discussed in this study difference in the chemical speciation of Cd and Zn may affect the isotopic fractionation of these metals. Some limited data for Cd and Zn stable isotopes in natural samples have recently been reported in the literature (e.g., Lacan et al., 2006; Ripperger et al., 2007; Wombacher et al., 2008). However, there is no experimental data about this issue, but only an experimental approach at carefully controlled laboratory conditions may help to discriminate the numerous thermodynamic, kinetic and geochemical factors responsible for the isotope variations in complex natural systems.

This short analysis implies that the same conclusions and perspectives are certainly applicable to many other economically and geochemically important similar elements (e.g., Pb, Cu, Fe, Ag). A combination of experimental, modeling and analytical approaches is necessary to better understand their transport and precipitation by high-temperature geological fluids responsible for the formation of the majority of these metal resources on our planet.

References

Ackerman, J.J.H., Orr, T.V., Bartushka, V.J., Maciel, G.E., 1979. Effect of halide complexation of cadmium (II) on cadmium-113 chemical shifts. J. Am. Chem. Soc.101, 341-347.

Adriano, D. C., 1986. Trace Elements in the Terrestrial Environment. Springer, New York.

Akinfiev N.N., Baranova N.N., Zotov A.V. and Tagirov B.R., 2008. Thermodynamic description of aqueous components in the system Cu-Ag-Au-S-Se-O-H in the range of temperatures 0-600°C and pressures 1-3000 bars. In: *Experimental studies of endogenic processes* (eds. I. D. Ryabchikov, Yu. B. Shapovalov, E. G. Osadchii). Publishing Office of the Institute of the Problems of Chemical Physics, Chernogolovka, Russia, pp. 184-203 (in Russian).

Allen, R.L., Weihed, P. and Global VMS Research Project Team, 2002. Global comparisons of volcanic-associated massive sulphide districts, in Blundell, D.J., Neubauer, F., and Von Quadt, A., eds., The Timing and Location of Major Ore Deposits in an Evolving Orogen: Geological Society of London Special Publication 204, p. 13-37.

Anderko, A., Pitzer, K.S., 1993. Equation-of-state representation of phase equilibria and volumetric properties of the system NaCl-H_2O above 573K. Geochim. Cosmochim. Acta 57, 1657-1680.

Anderko, A., Pitzer, K.S., 1993. Equation-of-state representation of phase equilibria and volumetric properties of the system NaCl-H_2O above 573K. Geochim. Cosmochim. Acta 57, 1657-1680.

Anderson, A.J., Mayanovic, R.A., Bajt, S., 1995. Determination of the local structure and speciation of zinc in individual hypersaline fluid inclusions by micro-XAFS. The Can. Mineral. 33, 499-508.

Anderson, B.G., Irish, D.E., 1988. Vibration spectral studies of solutions at Elevated Temperatures and Pressures. X. Raman spectral study of aqueous bromide solutions at 25°C and 200°C. J. Sol. Chem. 17, 763-775.

Anderson, B.G., Irish, D.E., 1988. Vibration spectral studies of solutions at elevated temperatures and pressures. X. Raman spectral study of aqueous bromide solutions at 25°C and 200°C. J. Sol. Chem. 17, 763-775.

Anderson, B.G., Irish, D.E., 1988. Vibrational spectral studies of solutions at elevated temperatures and pressures. X. Raman spectral study of aqueous cadmium bromide solutions at 25 and 200°C. J. Solution Chem. 17, 763-775.

Archer, D.A., 1998. Thermodynamic properties of import to environmental processes and remediation. I. Previous thermodynamic property values for cadmium and some of its compounds. J. Phys. Chem. Ref. Data 27, 915-946.

Arhland, S., 1979. Complex formation in protic and aprotic media. Pure Appl. Chem. 51, 2019-2039.

Axelsson, M.D., Rodushkin, I., 2001. Determination of major and trace elements in sphalerite using laser ablation double focusing sector field ICP-MS. J. Geochem. Explor. 72, 81-89.

Baes, C.F., Mesmer, R.E. Jr., 1976. The Hydrolysis of Cations. Wiley, New York, 489.

Bailey, R.A., Clark H.M., Ferris J.P, Krause S., Strong R.L., 2002. Chemistry of the Environment, 2nd Ed., San Diego, USA: Academic Press.

Bakker, R.J., 2003. Package FLUIDS 1. Computer programs for analyses of fluid inclusions data and for modelling bulk fluid properties. Chem. Geol. 194, 3-23.

Barnes, H.L., 1979. Solubilities of Ore Minerals. In: Geochemistry of Hydrothermal Ore Deposits, ed. H.L. Barrnes, 2nd edition. Wiley, pp. 404-459.

Bassett, W.A., Anderson A.J., Mayanovic R.A., Chou I.M., 2000. Hydrothermal diamond anvil cell for XAFS studies of first-row transition elements in aqueous solution up to supercritical conditions. Chem. Geol. 167, 3-10.

Baumann, E.W., 1971. Sesitivity of the fluoride-selective electrode below micromolar range. Analyt. Chim. Acta 54, 189-197.

Bazarkina, E.F., Zotov, A.V., Akinfiev, N.N., 2009a. Potentiomentric study of cadmium chloride complexes from 1 to 1000 bar at 25°C. Submitted to Geology of Ore Deposits in August 2009.

Bazarkina, E.F., Pokrovski, G.S., Zotov, A.V., Hazemann, J.-L., 2009b. Structure and stability of cadmium chloride complexes in hydrothermal fluids. Submitted to Chemical Geology in October 2009.

Bénézeth, P., Palmer, D., Wesolowski, D.J., Xiao, C., 2002. New measurements of zinc oxide from 150 to 350°C. J. Solution Chem. 31, 947-973.

Berry, A.J., Harris, A. C., Kamenetsky, V.S., Newville, M., Sutton, S. R., 2009.The speciation of copper in natural fluid inclusions at temperatures up to 700°C. Chem. Geol. 259, 2-7.

Bischoff, J.L., 1991. Densities of liquids and vapors in boiling NaCl–H2O solutions: a PVTX summary from 300 to 500 °C. Am. J. Sci. 291, 309–338.

Bol, W., Gerrits, G.J.A., van Panthaleon van Eck, C.L., 1970. The hydration of divalent cations in aqueous solutions. An X-ray investigation with isomorphous replacement. J. Appl. Cryst. 3, 486-492.

Botcharnikov, R.E., Knyazik, V.A., Steinberg, A.S., Steinberg, G.S., 1998. Emission of gases, rock- and ore-forming components on Kudriavy volcano, Iturup Island, Kurile Islands. Dokl. Ross. Akad. Nauk 361, 671- 674 (in Russ.).

Botcharnikov, R.E., Shmulovich, K.I., Tkachenko, S.I., Korzhinsky, M.A., Rybin, A.V., 2003. Hydrogen isotope geochemistry and heat balance of a fumarolic system: Kudriavy volcano, Kuriles. J. Volcanol. Geotherm. Res. 124, 45–66.

Bourcier, W. L., Barnes, H. L., 1987. Ore solution chemistry-VII. Stabilities of chloride and bisulfide complexes of zinc to 350°C. Econ. Geol. 82, 1839–1863.

Brimhall, G.H., Crerar, D.A., 1987. Ore fluids: magmatic to supergene. Rev. Miner. 17, 235-321.

Brugger, J., Etschmann, B., Liu, W., Testemale, D., Hazemann, J.L., Emerich, H., Van Beek, W., Proux, O., 2007. An XAS study of the structure and thermodynamics of Cu(I) chloride complexes in brines up to high temperature (400°C, 600 bar). Geochim. Cosmochim. Acta 71, 4920-4941

Bruland, K.W., Lohan, M.C., 2003. 6.02. Controls of trace metals in seawater. In: Holland, H.D., Turekian, K.K. (Eds.), Treatise on Geochemistry, Elsevier, Amsterdam.

Buback, M., 1983. The vibration spectrum of pure water and aqueous solutions to high pressure and temperatures. In: Somiya, S. (Ed.), Proceedings of the First International Symposium on Hydrothermal Reactions. Gakuzyutu Bunken Fukyukai, Tokyo, pp. 24-36.

Butterworth, P., Hillier, I.H., Burton, N.A., Vaughan D.J., Guest, M.F., Tossell J.A., 1992. Calculations of the structures, stabilities, Raman Spectra, and NMR spectra of $CdCl_n(OH_2)_a^{2-n}$, $CdBr_n(OH_2)_a^{2-n}$, and $ZnCl_n(OH_2)_a^{2-n}$ species in aqueous solution. J. Phys. Chem. 96, 6494-6500.

Callender, E., 2003. Heavy metals in the environment – historical trands. In: Treatise on Geochemistry (ed. by Holland H.D., Turekian K.K.), Elsevier, Amsterdam. Volume 9 (ed. Lollara B.S.), 67-105.

Caminiti, R., Licheri, G., Paschina, G. Piccaluga, G., Pinna, G., 1980. X-ray diffraction and structural properties of aqueous solutions of divalent metal-chlorides. Z. Naturforsch 35, 1361-1367.

Caminiti, R., Johanson, G., 1981. On the structures of cadmium sulphate complexes in aqueous solutions. Acta Chem. Scand. A 35, 373-381.

Caminiti, R., Cuca, P., Radnai, T., 1984. Investigation on the structure of cadmium nitrate aqueous solutions by X-ray diffraction and Raman spectroscopy. J. Phys. Chem., 88, 2382-2386.

Chaplygin, I.V., Mozgova, N.N., Mozhov, A.V., Koporulina, E.V., Bernhardt, H.J., Bryzgalov, I.A., 2007. Minerals of the system ZnS-CdS from fumaroles of the Kudriavy volcano, Iturup Island, Kuriles, Russia. Can. Mineral. 45, 709-722.

CODATA, 1989. CODATA key values for thermodynamics, ed. Cox, J. D., Wagman, D. D., and Medvedev, V. A., Hemisphere Publishing Corp., New York USA, 1989.

Cook, N.J., Ciobanu C.L., Pring, A., Skinner, W., Shimizu, M., Danyushevsky, L., Saini-Eidukat, B., Melcher, F., 2009. Trace and minor elements in sphalerite: A LA-ICPMS study. Geochim. Cosmochim. Acta 73, 4761-4791.

Crerar, D., Wood, S., Brantley, S., 1985. Chemical controls on solubility of ore-forming minerals in hydrothermal solutions. Can. Miner. 23, 333-352.

Cudennec, Y, Gerault, Y., Lecerf, A., 1997. Synthesis and crystal structure of β-$Cd_2(OH)_3Cl$. Solid state chemistry and crystal chemistry 324, 457-466.

Cygan, G. L., Hemley, J. J., D'Angelo, W. M., 1994. An experimental study of zinc chloride speciation from 300 to 600°C and 0.5–2.0 kbar in buffered hydrothermal solutions. Geochim. Cosmochim. Acta 58, 4841–4855.

Daskalakis, K.D., Helz, G.R., 1992. Solubility of cadmium sulphide, greenockite. in sulfidic waters at 25°C. Environ. Sci. Technol. 26, 2462-2468.

Decrée, S., Marignac, C., De Putter, T., Deloule, E., Liégois, J.-P., Demaiffe, D., 2008. Pb-Zn mineralisation in a Miocene regional extensional context : The case of the Sidi Driss and Douahria ore deposits (Nefza mining district, northern Tunisia). Ore Geol. Rev. 34, 285-303.

Drakenberg T., Björk N.O., Portanova R., 1978. Cadmium-113 nuclear magnetic resonance study of cadmium (II) halide complexes in water and dimethyl sulfoxide. Phys. Chem., 82, 2423-2426.

Elderfield, H., Rickaby, R. E. M., 2000. Oceanic Cd/P ratio and nutrient utilization in the glacial Southern Ocean. Nature 405, 305–310.

Eriksson, L., 1953. The complexity constants of cadmium chloride and bromide. Acta Chem. Scand. 7, 1146-1154.

Ermakov, V.A., Steinberg, G.S., 1999. Kudryavyi volcano and evolution of Medvezhiya caldera (Iturup Isl., Kurile Ils.). Volcanol. Seismol. 3, 19–40 (in Russian).

Ferri, D., Salvatore, F., 1988. Ann. Chim. Roma 78, p. 497.

Fischer, T.P., Giggenbach, W.F., Sano, Y., Williams, S.N., 1998a. Fluxes and sources of volatiles discharged from Kudryavy, a subduction zone volcano, Kurile Islands. Earth Planet. Sci. Lett. 160, 81–96.

Fischer, T.P., Shuttleworth, S., O'Day, P.A., 1998b. Determination of trace and platinum-group elements in high ionic-strength volcanic fluids by sector-field inductively coupled plasma mass spectrometry (ICP-MS). Fresenius J. Anal. Chem. 362, 457–464.

Galley, A.G., Hannington, M.D., Jonasson, I.R., 2007. Volcanogenic massive sulphide deposits. In: Mineral Deposits of Canada: A Synthesis of Major Deposit-Types, District Metallogeny, the Evolution of Geological Provinces, and Exploration Methods. Ed. By Goodfellow, W.D. Geol. Ass. of Can., Mineral Deposits Division, Special Publication No. 5, 141-161.

Giggenbach, W.F., 1975. A simple method for the collection and analysis of volcanic gas samples. Bull. Volcanol. 39, 135–145.

Giggenbach, W.F., Goguel, R.L., 1989. Collection and analysis of geothermal and volcanic water and gas discharges. New Zeland DSIR Chemistry Div. Rprt., CD 2401, 81.

Glushko, V.P. (ed.), 1972. Thermal Constants of Substances (translated from Russian Termicheskie Konstanti Vechestv). Moscow, VINITI, 367. Availible online at http://www.chem.msu/sgi-bin/tkv.pl (in Russian). The English Edition was published by Wiley & Sons in 1999.

Goldschmidt, V.M., 1958. Geochemistry. London: Oxford University Press, Amen House.

Goodfellow, W.D., 2007. Base metal metallogeny of the Selwyn Basin, Canada. In: A Synthesis of Major Deposit-Types, District Metallogeny, the Evolution of Geological Provinces, and Exploration Methods. Ed. by Goodfellow W.D. Mineral Deposits of Canada, Special Publication 5, 553-579.

Gottesmann, W., Kampe, A., 2007. Zn/Cd ratios in calsilicate-hosted sphalerite ores at Tumurtijn-ovoo, Mongolia. Chem. Erde – Geochim. 67, 323-328.

Grichuk, D.V., 2005. The Cd/Zn ratio as an indicator of the magmatic fluids input to the hydrothermal systems. Proceedings of the VII International Conference "New Ideas in the Earth Sciences", 85. KDU, Moscow (in Russian).

Heinrich, C.A., 2007. Fluid–fluid interactions in magmatic–hydrothermal ore formation, Rev. Mineral. Geochem. 65, pp. 363–387.

Heinrichs, H., Schulz-Dobrick, B., Wedepohl K.L., 1980. Terrestrial geochemistry of Cd, Bi, Tl, Pb, Zn and Rb. Geochim. Cosmochim. Acta 44, 1519–1533.

Helgeson, H. C., Kirkham, D. H., 1974. Theoretical prediction of the thermodynamic behavior of aqueous electrolytes at high pressures and temperatures. I. Summary of the thermodynamic/electrostatic properties of the solvent. Amer. J. Sci. 274, 1089-1198.

Helgeson, H.C., Kirkham, D.H., Flowers, G.C., 1981. Theoretical prediction of the thermodynamic behaviour of aqueous electrolytes at high pressures and temperatures: IV. Calculation of activity coefficients, osmotic coefficients, and apparent molal and standard and relative partial molal properties to 600°C and 5 kbar. Amer. J. Sci. 281, 1249-1561.

Hemley, J.J., Cygan, G.L., Fein, J.B., Robinson, G.R., D'Angelo, W.M., 1992. Hydrothermal ore-forming processes in the light of studies in rock-buffered systems. Econ. Geol. 87, 1-43.

Hitzman, M.W., Redmond, P. B., Beaty, D.W., 2002. The Carbonate-Hosted Lisheen Zn-Pb-Ag Deposit, County Tipperary, Ireland. Econ. Geol. 97, 1627-1655.

Hovey, J.K., 1988. Thermodynamics of aqueous solutions: Ph. D. dissertation. Edmonton, Canada, Univ. Albertta.

International cadmium association, 2003. http://www.cadmium.org/

Ivanov, V.V., 1997. Ecological geochemistry of elements. Ecology, Moscow (in Russian).

Johnson, J.W., Oelkers, E.H., Helgeson, H.C., 1992. SUPCRT92: a software package for calculating the standard molal thermodynamic properties of minerals, gases, aqueous species, and reactions from 1 to 5000 bar and 0 to 1000°C. Comput. Geosci. 18, 899-947; http://geopig.asu.edu/index.html/.

Joly, Y., 2001. X-ray absorption near-edge structure calculations beyond the muffin tin approximation. Phys. Rev. B63, 125120.

Jonasson, I.R., Sangster, D.F., 1978. Zn:Cd ratios for sphalerites separated from some Canadian sulphide ore samples. Paper Geol. Surv. Can., 78-1B, 195-201.

Kelly, S.D., Hesterberg, D., Ravel, B., 2008. Analysis of soils and minerals using X-ray absorption specroscopy. Methods of Soil Analysis. Part 5. Mineralogical Methods, p. 387-463, Soil Sci. Soc. Am., Madison, USA.

Kimball, G. E., Shortley, G.H., 1934. The numerical solution of Schrödinger's equation. Phys. Rev. 45, 815-820.

King, E.L., 1949. Thermodynamic data on the cadmium chloride complexes determined from the solubility of cadmium ferricyanide. J. Am. Chem. Soc. 71, 319-322.

Korzhinsky, M.A., Tkachenko, S.I., Bulgakov, R.F., Shmulovich, K.L., 1996. Condensate compositions and native metals in sublimates of high-temperature gas streams of Kudryavy Volcano, Iturup Island, Kuril Islands. Geochem. Int. 36, 1175–1182.

Korzhinsky, M.A., Botcharnikov, R.E., Tkachenko, S.I., Steinberg, G.S., 2002. Decade-long study of degassing at Kudriavy volcano, Iturup, Kurile Islands (1990–1999): gas temperature and composition variations, and occurrence of 1999 phreatic eruption. Earth Planets Space 54, 337-347.

Kovalenker, V.A., Laputina, LP., Znamenskii, V.S., Zotov I.A., 1993. Indium mineralization of the Great Kuril Island arc. Geol. Ore Deposits, 35, 491-495 (translated from Geololia. Rudnykh Mestorozhdenii, 35, 547- 552).

Lacan, F., Francois R., Ji, Y., Sherrell, R.M. Cadmium isotopic composition in the ocean. Geochim. Cosmochim. Acta 70, 5104-5118.

Latimer, W. M. (Ed.), 1952. The Oxidation States of the Elements and their Potentials in Aqueous Solutions. New York, Prentice-Hall. 2nd Edn., p. 245.

Leach, D.L., Bradley, D., Lewchuk, M.T., Symons, D.T.A., de Marsily, G., and Brannon, J., 2001. Mississippi Valley-type lead-zinc deposits through geological time: Implications from recent age-dating research: Mineralium Deposita, v. 36, p. 711–740.

Leach, D.L., Sangster, 1993. Mississippi Valley-type lead-zinc deposits. In: Mineral Deposit Modelling. Ed. by Kirkham, R.V., Sinclair, W.D., Thorpe, R.I., and Duke, J.M. Geological Association of Canada Special Paper 40, 289-314.

Leach, D.L., Viets, J.B., Foley-Ayuso, N., Klein, D.P., 1995, Mississippi Valley-Type Pb-Zn deposits (Models 32a, b; Briskey, 1986 a, b). In: Preliminary Compilation of Descriptive Geoenvironmental Mineral Deposit Models. Ed. by Du Bray, E. A. U.S. Government Consulting Group, Open File Report 95-831, 234-243.

Lide D.R. (Ed.), 2004. Handbook of geochemistry and physics. Boca Raton: CRS Press, 84th edition.

Liu, W., Etschmann, B., Foran, G., Shelley, M., Brugger, J., 2007. Deriving formation constants for aqueous metal complexes from XANES spectra: Zn^{2+} and Fe^{2+} chloride complexes in hypersaline solutions. Amer. Mineral. 92, 761-770.

Lydon, J.W., Paakki, J.J., Anderson, H.E., Reardon, N.C., 2000. An overview of the geology and geochemistry of the Sullivan Deposit. In: The geological environment of the Sullivan Deposit, British Columbia: Ed. by Lydon, J.W., Höy, T., Slack, J.F., and Knapp, M.E., Geological Association of Canada, Mineral Deposits Division, Special Publication 1, 505-522.

Lynch-Strieglitz, J., 2003. Tracers of past ocean circulation. In: Treatise on Geochemistry (Eds. Holland, H.D., Turekian, K.K.), Elsevier, Amsterdam. Volume 6 (Ed. Elderfield, H.), 433-451.

Macdonald, A.C., Sikka, S.K., 1969. The determination of the crystal structure of cadmium nitrate tetradeuterate by means of neutron anomalous dispersion measurements. Acta Cryst. B 25, 1804-1811.

Makeev, A.B., 1985. Isomorphism of cadmium and manganese in sphalerite. Nauka, Leningrad (in Russian).

Malinowski, E.R., 1977. Determination of the number of factors and the experimental error in a data matrix. Anal. Chem 49, 612-317.

Malinowski, E.R., 1991. Factor Analysis in Chemistry. 2nd Edition, Wiley.

Marley, N.A., Gaffney, J.S., 1990. Laser Raman spectral determination of zinc halide complexes in aqueous solutions as a function of temperature and pressure. Applied Spectroscopy 44, 469-476.

Martell, E., Smith, R.M., 1998. Critically Selected Stability Constants of Metal Complexes, NIST Standard Reference Database 46, Version 5.0, NIST, Gaithersburg, MD 20899.

Metz, S., Trefry, J.H., 2000. Chemical and mineralogical influences on concentrations of trace metals in hydrothermal fluids. Geochim. Cosmochim. Acta 64, 2267-2279.

Mayanovic, R.A., Anderson, A.J., Bassett, W.A., Chou I.-M., 1999. XAFS measurements on zinc chloride aqueous solutions from ambient to supercritical conditions using the diamond anvil cell. J. Synchrotron Rad. 6, 195-197.

Metal prices, http://www.metalprices.com/

Mosselmans, J.F.W., Schofield, P.F., Charnock, J.M., Garner, C.D., Pattrick, R.A.D., Vaughan, D.J., 1996. X-ray absorption studies of metal complexes in aqueous solution at elevated temperatures. Chem. Geol. 127, 339-350.

Moore, D.W., Young, L.E., Modene, J.S., Plahuta, J.T., 1986. Geological setting and genesis of the Red Dog zinc-lead-silver deposit, Western Brooks Range, Alaska. Economic Geology 81, 1696-1727.

Munoz, M., Argoul, P., Farges F., 2003. Continuous cauchy wavelet transform analyses of EXAFS spectra: a qualitative approach. Amer. Mineral. 88, 694-700.

Naumov, G. B., Ryzhenko, B. N., Khodakovskii, I. L., 1974. Handbook of Thermodynamic Data. U.S Geol. Surv. Rep. USGS-WRD-74-001.

Nelson, J., Paradis, S., Christensen, J., and Gabites, J., 2002. Canadian Cordilleran Mississippi Valley-type deposits; a case for Devonian-Mississippi back-arc hydrothermal origin: Economic Geology 97, 1013-1036.

Newville, M., 2001. IFEFFIT: interactive XAFS analysis and FEFF fitting. J. Synchrotron Radiat. 8, 322–324.

Newville, M., 2004. Fundamentals of XAFS. Consortium for advanced Radiation Sources, University of Chicago, Chicago, IL.

Nogawa, K., Kido, T., 1996. Itai-Itai disease and health effects of cadmium. In: L.W. Chang, Editor, Toxicology of Metals, CRC Press, Boca Raton, USA, 353–369.

Nriagu, J. O., 1988. A silent epidemic of environmental metal poisoning? Environ. Pollut. 50, 139–161.

Nriagu, J. O., 1990. Global metal pollution. Environment 32, 7–33.

Oelkers, E.H., Helgeson, H.C, 1990. Triple-ion anions and polynuclear complexing in supercritical electrolyte solutions. Geochim. Cosmochim. Acta 54, 727-738.

Ohtaki, H., Maeda, M., Ito, S., 1974. X-ray diffraction studies of aqueous solutions of cadmium perchlorate and sodium tetraiodocadmate. Bull. Chem. Soc. Jpn. 47, 2217-2221.

Oliveria, W.A., 1979. Ebulliometric determination of step stability constants. J. Coord. Chem. 9, 7-11.

Palmer, D.A., Corti, H.R., Groteword, A., Hyde K. E., 2000. Potentiometric measurements of the thermodynamics of cadmium(II) chloride complexes to high temperatures. In: Steam, water, and hydrothermal systems: physics and chemistry meeting the needs of industry. Proceedings of the 13th International Conference on the Properties of Water and Steam (Toronto, Canada, 1999). Ed. by Tramaine P.R., Hill P.G., Irish, D. E., Balakrishnan, P. V. NRC Research Press, Ottawa 2000, 736-743.

Palmer, D.A., Bénézeth, P., Petrov, A. Yu., Simonson, J.M., 2001. Behavior of aqueous electrolytes in steam cycles: the solubility and volatility of copper (I) and copper(II) oxides. Palo Alto, Calif.: Electric Power Research Institute, December 2001. TR-1003993.

Palmer, D.A., Bénézeth, P., Simonson, J.M., 2004. The solubility of copper oxides around the water/steam cycle. Power Plant Chem. 6, 81-88.

Paradis, S., Hannigan, P., and Dewing, K., 2007. Mississippi Valley-type lead-zinc deposits. In: Mineral Deposits of Canada: A Synthesis of Major Deposit-Types, District Metallogeny, the Evolution of Geological Provinces, and Exploration Methods. Ed. by Goodfellow, W.D. Geol. Ass. of Can., Mineral Deposits Division, Special Publication No. 5, 185-203.

Paschina, G., Piccaluga, G., Pinna, G., Magini, M., 1983. Chloro-complexes formation in $ZnCl_2$-$CdCl_2$ aqueous solutions: An X-ray diffraction study. J. Chem. Phys. 78, 5745-5749.

Pearson, R.G., 1963. Hard and soft acids and bases. J. Amer. Chem. Soc .85, 3533-3539.

Pennisi, M., LeCloarec, M.F., Lambert, G., Le Roulley, J.C., 1988. Fractionation of metal in volcanic emissions. Earth Planet. Sci. Lett. 88, 284-288.

Philippot, P., Ménez B., Drakopoulos, M., A. Simionovici, Snigirev A., Snigireva I., 2001. Mapping trace-metal (Cu, Zn, As) distribution in a single fluid inclusion using a 3rd generation synchrotron light source. Chem. Geol. 173, 151-158.

Pivovarov, S., 2005. Modeling of ionic equilibria of trace metals (Cu^{2+}, Zn^{2+}, Cd^{2+}) in concentrated aqueous electrolyte solutions at 25°C. J. Colloid. Interface Sci. 291, 421-432.

Plyasunov, A.V., Ivanov, I.P., 1991. The solubility of zinc oxide in sodium chloride solutions up to 600°C and 1000 bar. Geochem. Int. 28, 77-90.

Plyasunov, A. V., Shock, E. L., 2001. Correlation strategy for determining the parameters of the revised Helgeson-Kirkham-Flowers model for aqueous nonelectrolytes. Geochim. Cosmochim. Acta 65, 3879–3900.

Pokrovski, G.S., Schott, J., 1998. Experimental study of the complexation of silicon and germanium with aqueous organic species: implications for germanium and silicon transport and Ge/Si ratio in natural waters. Geochim. Cosmochim. Acta 62, 3413-3428.

Pokrovski, G.S., Martin, F., Hazemann, J.-L., Schott, J., 2000. An X-ray absorption fine structure spectroscopy study of germanium-organic ligand complexes in aqueous solution. Chem. Geol. 163, 151-165.

Pokrovski, G.S., Kara, S., Roux, J., 2002a. Stability and solubility of arsenopyrite, FeAsS, in crustal fluids. Geochim. Cosmochim. Acta 66, 2361-2378.

Pokrovski, G.S., Schott, J., Hazemann, J.-L., Farges, F., Pokrovsky, O.S, 2002b. An X-ray absorption fine structure and nuclear magnetic resonance spectroscopy study of gallium-silica complexes in aqueous solution. Geochim. Cosmochim. Acta 66, 4203-4322.

Pokrovski, G.S., Roux, J., Hazemann, JL., Testemale, D., 2005. An X-ray absorption spectroscopy study of argutite solubility and aqueous Ge(IV) speciation in hydrothermal fluids to 500°C and 400 bar. Chem. Geol. 217, 127-145.

Pokrovski, G.S., Borisova, A.Y., Roux, J., Hazemann, J.-L., Petdang, A., Tella, M., Testemale, D., 2006. Antimony speciation in saline hydrothermal fluids: A combined X-ray absorption fine structure spectroscopy and solubility study. Geochim. Cosmochim. Acta 70, 4196-4214.

Pokrovski, G.S., Borisova, A.Y., Harrichoury, J.C., 2008 The effect of sulfur on vapor–liquid fractionation of metals in hydrothermal systems. Earth Planet. Sci. Lett. 266, 345-362.

Pokrovski, G.S., Tagirov, B.R., Schott, J., Bazarkina, E.F., Hazemann, J.L., Proux, O., 2009a. An in situ X-ray absorption spectroscopy study of gold-chloride complexing in hydrothermal fluids. Chem. Geol. 259, 17-29.

Pokrovski, G.S., Tagirov, B.R., Schott, J., Hazemann, J.L., Proux, O., 2009b. A new view on gold speciation in sulfur-bearing hydrothermal fluids from in situ X-ray absorption spectroscopy and quantum-chemical modeling. Geochim. Cosmochim. Acta 73, 5406-5427.

Proux, O., Biquard, X., Lahera, E., Menthonnex, J.-J., Prat, A., Ulrich, O., Soldo, Y., Trevisson, P., Kapoujyan, G., Perroux, G., Taunier, P., Grand, D., Jeantet, P., Deleglise, M., Roux, J.-P., Hazemann, J-L., 2005. FAME: a new beamline for X-ray absorption investigations of very diluted systems of environmental, material and biological interests. Phys. Scripta T 115, 970-973.

Proux, O., Nassif, V., Prat, A., Ulrich, O., Lahera, E., Biquard, X., Menthonnex, J.-J., Hazemann, J.-L., 2006. Feedback system of a liquid-nitrogen-cooled double-crystal monochromator: design and performances. J. Synchrotron Radiat. 13, 59–68.

Qian, X., 1987. Trace elements in galena and sphalerite and their geochemical significance in distinguishing the genetic types of Pb-Zn ore deposits. Chin. J. Goechem. 6, 177-190.

Ravel, B., Newville, M., 2005. ATHENA, ARTEMIS, HEPHAESTUS: data analysis for X-ray absorption spectroscopy using IFEFFIT. J. Synchrotron Radiat. 12, 537–541.

Reilly, P.J., Stokes, R.H., 1970. The activity coefficients of cadmium chloride in water and sodium chloride solutions at 25°C. Aust. J. Chem. 23, 1397-1405.

Rickard, D., Luther III, G.W., 2006. Metal sulfide complexes and clusters. Rev. Miner. Geochem. 61, 421-504.

Ripperger, S., Rehkämper, M., Porcelli, D., Halliday, A.N., 2007. Cadmium isotope fractionation in seawater – A signature of biological activity. Earth Planet. Sci. Lett. 261, 670-684.

Ryzhenko, B.N., Bryzgalin, O.V., 1987. Dissociation of acids under hydrothermal conditions. Geokhimiya 1, 137–142 (in Russian).

Robie, R.A., Hemingway, B.S., 1995. Thermodynamic properties of minerals and related substances at 298.15 and 1 bar (10^5 pascals) pressure and at high temperatures. U. S. Geol. Surv. Bull. 2131, 461.

Rossberg, A., Reich, T., Bernhard G., 2003. Complexation of uranium(VI) with protocatechuic acid – application of iterative transformation factor analysis to EXAFS spectroscopy. Anal. Bioanal. Chem., 376, 631-638.

Rozhkova, D.V., Zotov A.V., Bazarkina, E.F., 2009. The lowest limit of linearity of the function E-pX for ion-selective electrodes in the presence of complexion ligands (an example of fluorum-selective electrode). Proceedings of the IX International Conference "New Ideas in the Earth Sciences" RGGRU, Moscow, 85.

Ruaya, J. R., Seward, T. M., 1986. The stability of chloro-zinc (II) complexes in hydrothermal solutions up to 350°C. Geochim. Cosmochim. Acta 50, 651–662.

Rubin, K., 1997. Degassing of metals and metalloids from erupting seamount and mid-ocean ridge volcanoes: Observations and predictions. Geochim. Cosmochim. Acta 61, 3525-3542.

Rudnick, R.L., Gao, S., 2003. 3.01. Composition of the continental crust. In: Holland, H.D., Turekian, K.K. (Eds.), Treatise on Geochemistry, Elsevier, Amsterdam.

Rudolph, W.W., Pye, C.C., 1998. Raman spectroscopic measurements and ab initio molecular orbital studies of cadmium(II) hydration in aqueous solution. J. Phys. Chem. B, 102, 3564-3573.

Sangster, D.F., 1990. Mississippi Valley-type and SEDEX lead-zinc deposits: a comparative examination: Institution of Mining and Metallurgy, Transactions, Section B: Applied Earth Science 99, 21-42.

Schwartz, M.O., 2000. Cadmium in Zinc Deposits: Economic Geology of a Polluting Element. Int. Geol. Rev. 42, 445-469.

Seward, T.M., 1984. The formation of lead(II) chloride complexes to 300°C: A spectrophotometric study. Geochim. Cosmochim. Acta 48, 121-134.

Seward, T.M., Driesner, T., 2004. Hydrothermal solution structure: experiments and computer simulations. In: Palmer, D.A., Fernández-Prini, R., Harvey, A.H. (Eds.), Aqueous Systems at Elevated Temperatures and Pressures: Physical Chemistry in Water, Steam and Hydrothermal Solutions. Elsevies Ltd., pp. 149-182.

Sharps, J.A., Brown Jr., G.E., Stebbins J.F., 1993. Kinetics and mechanism of ligand exchange of Au(III), Zn(II), and Cd(II) chlorides in aqueous solutions: An NMR study from 28-98°C. Geochim. Cosmochim. Acta 57, 721-731.

Shmulovich, K.I., Churakov, S.V., 1998. Natural fluid phases at high temperatures and low pressures. J. Geochem. Explor. 62, 183–191.

Shock, E.L., Helgeson, H.C., Sverjensky, D.A., 1989. Calculation of the thermodynamic and transport properties of aqueous species at high pressures and temperatures: standard partial molal properties of inorganic neutral species. Geochim. Cosmochim. Acta. 53, 2157-2183.

Shock, E.T., Helgeson, H.C., 1988. Calculation of the thermodynamic and transport properties of aqueous species at high pressures and temperatures: correlation algorithms for ionic species and equation of state prediction to 5 kb and 1000°C. Geochim. et Cosmochim. Acta. 52, 2009-2036.

Shock, E.L., Sassani, D.C., Willis, M., Sverjensky, D.A., 1997. Inorganic species in geological fluids: Correlations among standard molal thermodynamic properties of aqueous ions and hydroxide complexes. Geochim. Cosmochim. Acta 61, 907-950; http://geopig.asu.edu/index.html/.

Shvarov, Yu. S., 2008. HCh: New potentialities for the thermodynamic simulation of geochemical systems offered by windows. Geochem. Intl. 46, 834-839; http://www.geol.msu.ru/deps/geochems/soft/index.html/

Shvarov, Yu. S., Bastrakov, E.N., 1999. HCh: a software package for geochemical equilibrium modelling. User's Guide. Australian Geological Survey Organization, Record 199/25.

Sillén L.G., Liljeqvist, B., 1944. Sven. Kem. Tidskr. 56, pp. 85–95 (in Swedish).

Smirnov, V.I. (ed.), 1977. Ore Deposits of the USSR. London; San Francisco: Pitman Pub.

Solovov, A.P. (Ed.), 1990. Handbook of Ore Deposits Prospecting. Nedra, Moscow (in Russian).

Ste-Marie, J., Torma, A.E., Gübeli, A.O., 1964. The stability of thiocomplexes and solubility products of metal sulphides. Can. J. Chem. 42, 662-668.

Styrikovich, M.A., Khaibullin, I.K., and Tshvirashvili, D.G., 1955. A study of salt solubility in high-pressure water steam: Akademiya Nauk SSSR Doklady 100, 1123–1126.

Susak, N.J., Crerar, D.A., 1985. Spectra and coordination changes of transition metals in hydrothermal solutions: Implication for ore genesis. Geochim. Cosmochim. Acta 49, 555-564.

Sverjensky, D.A., Shock, E.L. Helgeson, H.C., 1997. Prediction of the thermodynamic properties of aqueous metal complexes to 1000°C and 5 kb. Geochim. Cosmochim. Acta 61, 1359-1412; http://geopig.asu.edu/index.html/.

Swaddle, T.W., Mak, M.S., 1983. The partial molar volumes of aqueous metal cations: their prediction and relation to volumes of activation for water exchange. Canad. J. Chem. 61, 473-480.

Symonds, R.B., Reed, M.H., 1993. Calculation of multicomponent chemical equilibria in gas-solid-liquid systems: calculation methods, thermochemical data, and applications to studies of high-temperature volcanic gases with examples from Mount St. Helen. Amer. J. Sci. 293, 758-864.

Symonds, R.B., Rose, W.I., Gerlach, T.M., Briggs, P.H., Harmon R.S., 1990. Evalution of gases, condensates, and SO2 emission from Augustine volcano, Alaska: the degassing of a Cl-rich volcanic system. Bull. Volcanol. 52, 355-374.

Tagirov, B.R., Zotov, A.V., Akinfiev, N.N., 1997. Experimental study of the dissociation of HCl from 350 to 500°C and from 500 to 2500 bar. Thermodynamic properties of HCl^0 (aq). Geochim. Cosmochim. Acta 61, 4267-4280.

Tagirov, B.R., Suleimenov O.M., Seward, T.M., 2007. Zinc complexation in aqueous sulfide solutions: Determination of the stoichiometry and stability of complexes via ZnS(cr) solubility measurements at 100°C and 150 bars. Geochim. Cosmochim. Acta 71, 4942-4953.

Tanger, J.C., Helgeson, H.C., 1988. Calculation of the thermodynamic and transport properties of aqueous species at high pressures and temperatures: revised equation of state for the standard partial properties of ions and electrolytes. Amer. J. Sci. 288, 19-98.

Taran, Yu.A., Hedenquist, J.W., Korzhinsky, M.A., Tkachenko, S.I., Shmulovich, K.I., 1995. Geochemistry of magmatic gases from Kudryavy volvano, Iturup, Kuril Islands. Geochim. Cosmochim. Acta 59, 1749-1761.

Tauson, V.L., Chernyshev, L.V., 1977. Investigation of phase relations and structural peculiarities of mixed crystals in the ZnS-CdS system. Geochem. Int. 9, 1299-1311.

Testemale, D., Hazemann, JL., Pokrovski, G.S., Joly, Y., Roux, J., Argoud, R., Geaymond, O., 2004. Structural and electronic evolution of As(III) atomic environment in hydrothermal solutions: an EXAFS and XANES investigation, J. Phys. Chem. 121, 8973–8982.

Testemale, D., Argoud, R., Geaymond, O., Hazemann, J-L., 2005. High pressure/high temperature cell for X-ray absorption and scattering techniques. Rev. Sci. Instrum. 76, 043905-043909.

Testemale, D., Brugger, J., Liu, W., Etschmann, B., Hazemann, J-L., 2009. In-situ X-ray absorption study of iron(II) speciation in brines up to supercritical conditions. Chem. Geol. 264, 295-310.

Tkachenko, S.I., Porter, R.P., Korzhinsky, M.A., van Bergen, M.D., Shmulovich, K.I., Shteinberg, G.S., 1999. Mineral- and oreforming processes in high-temperature fumarolic gases at Kudryavy volcano, Iturup Island, Kuril Archipelago. Geochem. Int. 37, 355–366.

Tolcin, A.C. (ed.), 2008. Minerals Yearbook – 2007. Cadmium. U.S. Geological Survey.

Tolcin, A.C. (ed.), 2009. Minerals Yearbook – 2007. Zinc. U.S. Geological Survey.

Tombros, S., St. Seymour, K., Spry, P.G., Williams-Jones, A., 2005. Greenockite and zincian greenockite in epithermal polymetallic Ag-Au-Te mineralization, Tinos Island, Hellas: description and conditions of formation. Neues Jahrb. Mineral., Abh. 182, 1-9.

Turner, D.R., Whifield, M., Dickson, A.G., 1981. The equilibrium speciation of dissolved components in freshwater and seawater at 25°C and 1 atm pressure. Geochim. Cosmochim. Acta 45, 855-881.

U.S. Geological Survey, 2008a, Zinc statistics. In: Historical statistics for mineral and material commodities in the United States: U.S. Geological Survey Data Series 140. Ed. By Kelly, T.D., and Matos, G.R. Available online at http://pubs.usgs.gov/ds/2005/140/.

U.S. Geological Survey, 2008b, Cadmium statistics. In: Historical statistics for mineral and material commodities in the United States: U.S. Geological Survey Data Series 140. Ed. By Kelly, T.D., and Matos, G.R. Available online at http://pubs.usgs.gov/ds/2005/140/.

Valleau, J.P., Turner, S.J., 1964. An ultrasonic study of some of the complexing reactions of chloride with cadmium ion. Can. J. Chem. 42, 1186-1197.

Vanderzee, C.E., Dawson, H.J., 1953. The stability constants of cadmium chloride complexes: variation with temperature and ionic strength. J. Amer. Chem. Soc. 75, 5659-5663.

Von Damm, K.L., 1990. Seafloor hydrothermal activity: black smoker chemistry and chimneys. Ann. Rev. Earth Planet. Sci. 18, 173-204.

Wagman, D.B., Evans, W.H., Parker, V.B., Schumm, R.H., Halow, I., Bailey, S.M., Shurney, K.L., and Nuttall, R.L., 1982. The NBS tables of chemical thermodynamic properties. J. Phys. Chem. Ref. Data 11, Supplement 2.

Wahrenberger, C., Seward, T.M., Dietrich, V., 2002. Volatile traceelement transport in high-temperature gases from Kudryavy volcano (Iturup, Kurile Islands, Russia). In: Hellmann, R.,Wood, S.A. (Eds.), Water–Rock Interaction: a Tribute to David A. Crerar. Geochem. Soc. Spec. Publ, vol. 7, pp. 307–327.

Walter-Lévy, L., Groult, D., 1970. Contribution à l'étude des halogénures basiques de cadmium, I, Sur la formation et les propriétés des chlorures basiques de cadmium. Bull. Soc. Chim. Fr. 11, 3868-3878.

Wang, F., Tessier, A., 1999. Cadmium complexation with bisulfide. Environ. Sci. Technol. 33, 4270-4277.

Waters, D.N., Short, E.L., Tharwat, M., Morris, D.F.C., 1973. Vibrational spectra of some halide complexes of zinc(II), cadmium(II), and mercury(II) in solution in tri-n-butyl phosphate. J. Molec. Struc. 17, 389-400.

Wedepohl, K.H. (ed.), 1972. Handbook of Geochemistry. Springer-Verlag, Heidelberg.

Wesolowski, D. J., Bénézeth, P., Palmer, D. A., 1998. ZnO solubility and Zn^{2+} complexation by chloride and sulfate in acidic solutions to 290°C with in-situ pH measurement. Geochim. Cosmochim. Acta 62, 971–984.

WHO (World Health Organization), 2006. Guidelines for drinking-water quality. Vol.1, Recommendations. – 3rd ed. Geneva, Switzerland: WHO Press. Available online at http://www.who.int.

Wood, S.A., Samson I.M., 1998. Solubility of ore minerals and complexation of ore metals in hydrothermal solutions: Rev. Econ. Geol. 10, 33-77.

Xuexin, S. Minor elements and ore genesis of the Fankou lead-zinc deposits, China. Mineral. Deposita. 1984. V. 19. P. 95-104.

Yardley, 2005. Metal concentrations in crustal fluids and their relationship to ore formation. Economic Geology 100, 613-632.

Yudovskaya, M.A., Tessalina, S., Distler, V.A., Chapligin I.V., Chugaev, A.V., Dikov Y.P., 2008. Behavior of highly-siderophile elements during magma degassing: A case study at the Kudryavy volcano. Chem. Geol. 248, 318-341.

Zabinsky, S.I., Rehr, J.J., Ankudinov, A., Albers, R.S., Eller, M.J., 1995. Multiple scattering calculations of X-ray absorption spectra. Phys. Rev. B 52, 2995-3009.

Zhang, Yu., Muhammed, M., 2001. Critical evaluation of thermodynamics of complex formation of metal ions in aqueous solutions. VI. Hydrolysis and hydroxo-complexes of Zn^{2+} at 298.15K. Hydrometallurgy 60, 215-236.

Zotov, A.V., Koroleva, L.A., Osadchii, E.G., 2006. Potentiometric study of the stability of Eu^{3+} acetate complexes as a function of pressure (1-1000) bar at 25^{0}C. Geochem. Int. 44, 384-394.

An in situ X-ray absorption spectroscopy study of gold-chloride complexing in hydrothermal fluids

Gleb S. Pokrovski [a,*], Boris R. Tagirov [b], Jacques Schott [a], Elena F. Bazarkina [a,b], Jean-Louis Hazemann [c], Olivier Proux [d]

[a] Experimental Geochemistry and Biogeochemistry Group, Laboratoire des Mécanismes et Transferts en Géologie, LMTG - Université de Toulouse - CNRS - IRD - OMP, 14 Av. E. Belin, F-31400 Toulouse, France
[b] Institute of Ore Deposits Geology, IGEM RAS, Staromonetniy per. 35, 119017 Moscow, Russia
[c] Institut Néel, CNRS, 25 avenue des Martyrs, F-38042 Grenoble Cedex 9, France
[d] Laboratoire de Géophysique Interne et Tectonophysique, UMR CNRS - Université Joseph Fourier, 1381 rue de la Piscine, Domaine Universitaire, F-38400 Saint-Martin-d'Hères, France

ARTICLE INFO

ABSTRACT

Despite the growing body of experimental data on gold solubility in hydrothermal fluids, the identity, structure and stoichiometry of Au-bearing aqueous complexes remain poorly known. Here we present the first in situ measurements, using X-ray absorption fine structure (XAFS) spectroscopy, of the stability and structures of Au^{III} and Au^I chloride complexes at elevated temperatures and pressures ($T–P$) typical of natural hydrothermal conditions. The $HAuCl_4$–$NaCl$–HCl–$Au_{(s)}$ and $NaCl$–H_2SO_4–$Au_{(s)}$ systems were investigated to 500 °C and 600 bar using a recently designed X-ray cell which allows simultaneous determination of the absolute concentration of the absorbing atom (Au) and its local atomic environment in the fluid phase. XAFS data combined with Density Functional Theory quantum-chemical calculations of species structures and ab-initio modeling of XANES spectra show that the $Au^{III}Cl_4^-$ species is rapidly reduced to $Au^ICl_2^-$ at temperatures above 100–150 °C in acidic $NaCl$–HCl solutions. In the latter complex, two chlorine atoms are aligned in a linear geometry around Au at an average distance of 2.267±0.004 Å. Our data provide the first direct structural evidence for $AuCl_2^-$, which is the major Au-bearing species in acidic Cl-rich hydrothermal fluids over a wide $T–P$ range, in agreement with previous solubility and Raman spectroscopy data. Total aqueous Au concentrations measured by XAFS in $HAuCl_4$–HCl–$NaCl$ and $NaCl$–H_2SO_4 solutions in the presence of $Au_{(s)}$ are, however, one to two orders of magnitude lower than those predicted by equilibrium thermodynamic calculations. This discrepancy is believed to be due to the combined effects of the cell properties, X-ray beam induced phenomena, and kinetic factors which may complicate the interpretation of high $T–P$ spectroscopic data in redox-sensitive systems.

© 2008 Elsevier B.V. All rights reserved.

1. Introduction

Knowledge of the identity, stability and structure of gold aqueous complexes is indispensable for understanding the transport, distribution and deposition of this precious metal by ore-forming fluids. As a result, many studies have been devoted, over almost 40 years, to quantifying gold interactions with major natural ligands like hydroxide, chloride and sulfide (see Stefánsson and Seward, 2003a,b; Tagirov et al., 2005, 2006; references therein). Most of these studies have been performed using solubility methods or synthetic fluid inclusion techniques in hydrothermal reactors involving high temperature–pressure ($T–P$) fluid sampling or quenching to ambient conditions. However, the "noble" nature of Au resulting in low solubilities and rapid kinetics of reduction of both principal gold forms in solution, monovalent Au^I and trivalent Au^{III}, into native metal poses

a formidable challenge for experimentalists, and is responsible for the large discrepancies affecting both the stability constants and stoichiometries of Au-bearing aqueous species derived from bulk solubility data. Here we report new structural and stability data for Au^{III} and Au^I chloride complexes obtained at elevated temperatures using in situ XAFS spectroscopy, thermodynamic modeling and quantum-chemical calculations.

Auric gold (Au^{III}) chloride complexes are recognized as primary aqueous Au species in oxidizing surficial environments at acidic and neutral conditions, whereas aurous gold (Au^I) chloride species form at elevated temperatures in hydrothermal Cl-rich fluids (e.g., Gammons and Williams-Jones, 1997; Akinfiev and Zotov, 2001; Berrodier et al., 2004). The stoichiometry and stability of Au^{III}–Cl complexes have been studied at ambient conditions using potentiometry (Nikolaeva et al., 1972), Raman (Peck et al., 1991; Murphy and LaGrange, 1998), and XAFS (Farges et al., 1993; Berrodier et al., 2004) spectroscopy which show that the square-plane $AuCl_4^-$ dominates in acidic solutions (pH≤~5) and is progressively replaced by mixed $AuCl_n(OH)_{4-n}$ species

with increasing solution pH. No data are available, however, on the structure of Au^{III}–Cl species at temperatures above ambient.

The formation conditions and structure of Au^{I} chloride complexes are much less constrained owing to their low stability at ambient T–P and weak solubility even at high temperatures. A number of solubility studies have reported the formation constants for the AuCl$_2^-$ species presumed to be dominant in natural acidic chloride-rich fluids at elevated T–P (Henley, 1973; Wood et al., 1987; Zotov and Baranova, 1989; Gammons and Williams-Jones, 1995, 1997; Stefánsson and Seward, 2003b). The agreement between studies carried out since the 1990's is rather good with a scatter of AuCl$_2^-$ formation constant values of less than 0.3 log units to 450 °C and 1500 bar (see Stefánsson and Seward, 2003b for discussion). In addition, a few attempts have been undertaken to detect this species by in situ Raman spectroscopy at temperatures up to 300 °C (Pan and Wood, 1991; Murphy et al., 2000), but they led to somewhat contradictory results regarding both Raman band assignments and Au^{I}–Au^{III} transformation conditions in chloride solutions. Thus, direct evidence for the formation of aurous chloride species is still lacking and their stoichiometry and structure remain poorly constrained. Clearly, more in situ studies are needed to better understand and quantify the stabilities and structures of Au species in the system Au^{I}–Au^{III}–Cl at hydrothermal T–P.

With the advent of in situ spectroscopic methods and improvement of synchrotron radiation sources in the last 10–15 years, it has become possible to rigorously assess the local atomic structures of metals in high T–P aqueous fluids (e.g., see Seward and Driesner, 2004). These in situ data, complemented by quantum-chemical and molecular dynamics calculations (e.g., Sherman, 2001) and ab-initio modeling of X-ray absorption spectra (e.g., see Rehr, 2006 for a recent review), are going to provide unprecedented insights into the identities and structures of metal complexes in hydrothermal fluids. In addition, quite recently, a few in situ spectroscopic studies combining *simultaneous measurement* of mineral solubilities and local atomic structures of solutes have been reported on relatively simple systems containing a mineral and an aqueous fluid phase (e.g., quartz-H$_2$O, Zotov and Keppler, 2002; GeO$_2$–H$_2$O, Pokrovski et al., 2005a; Sb$_2$O$_3$–H$_2$O–NaCl–HCl, Pokrovski et al., 2006a, 2008b; Au–H$_2$O–H$_2$S–NaOH, Schott et al., 2006).

The present study focuses on in situ X-ray absorption spectroscopy measurements of gold speciation, solubility and structure in Cl-bearing aqueous fluids to 500 °C and 600 bar in the model systems Au$_{(s)}$–HAuCl$_4$–NaCl–HCl and Au$_{(s)}$–NaCl–H$_2$SO$_4$. Here we combined in situ XAFS experiments with quantum-chemical optimizations of complex geometries and calculations of near-edge X-ray absorption (XANES) spectra to investigate the stability, transformation kinetics, and structure of the principal Au^{III} and Au^{I} chloride complexes. Our results provide the first direct structural evidence for the AuCl$_2^-$ species in hydrothermal solution and demonstrate the promising potential of combining in situ synchrotron radiation spectroscopy with ab-initio modeling for in situ studies of complex high T–P fluid systems pertinent to Earth's hydrothermal-magmatic settings.

2. Materials and methods

2.1. Experimental design and XAFS spectra acquisition

Three types of aqueous solutions were examined in this study: HAuCl$_4$–NaCl–HCl, Au$_{(s)}$–HAuCl$_4$–NaCl–HCl, and Au$_{(s)}$–2 m NaCl–0.5 m H$_2$SO$_4$. Metallic gold foil was 0.5 mm thick with a purity of 99.99% (GoodFellow). Gold tetrachloride solution (HAuCl$_4$) was prepared by dissolving Au metal in 20% HCl boiling solution. Experimental solutions were prepared from analytical-grade reagents NaCl, HCl, H$_2$SO$_4$ and doubly de-ionized water.

XAFS spectra (including the X-ray absorption near edge structure region or XANES, and the extended X-ray absorption fine structure region or EXAFS) of aqueous Au solutions were collected in both transmission and fluorescence mode at the Au L_3-edge (~11.9 keV) over the energy range 11.7–13.0 keV on BM30B-FAME beamline (Proux et al., 2005) at the European Synchrotron Radiation Facility (ESRF, Grenoble, France). The storage ring was operated at 6 GeV with a ~180 mA current. Energy was selected using a Si(220) double-crystal monochromator with sagittal focusing. Contributions of higher-order harmonics from the Si(220) double-crystal within the FAME optics configuration do not exceed 0.1% of the transmitted intensity in the energy and absorbance ranges of our experiments (Proux et al., 2006). The beam size was focused to 300 μm horizontal × 200 μm vertical yielding an X-ray photon flux on the sample of ~10^{12} photons/s as measured with a calibrated Canberra diode. Silicon diodes collecting scattered radiation from a Kapton foil were employed for measuring the intensities of the incident (I_0) and transmitted (I_1 and I_2) X-ray beams while fluorescence spectra were collected in the 90° geometry using a Canberra solid-state 30-element germanium detector (energy resolution = 300 eV, shaping time = 125 ns). Energy was constantly calibrated using a gold metal foil placed behind the sample (i.e., between the I_1 and I_2 transmission detectors); its L_3 edge energy was set at 11.919 keV as the maximum of the first derivative of the main edge spectrum.

XAFS measurements were carried out using a spectroscopic cell recently described in detail elsewhere (Pokrovski et al., 2005a, 2006a; Testemale et al., 2005). Very briefly, the design includes an inner optical cell (Fig. 1) which is inserted in a high-pressure steel vessel pressurized with helium and having three beryllium windows for X-ray passage. The internal cell consists of a vertically oriented sapphire or glassy-carbon tube polished inside, and two sapphire coaxial rods equipped with Viton O-ring seals and inserted into the tube from each end. The rods delimit the sample space, in which experimental solid and solution are placed, and can move in the tube in response to pressure changes like a piston in a syringe. The volume of the sample space is about 0.1 to 0.2 cm^3 which corresponds to a height of 3 to 6 mm, depending on T–P conditions. Pressure in the sample space is always balanced with that of helium gas and the mobile pistons. The optical path through the vertically oriented cell remains constant owing to the low temperature expansion coefficient of sapphire and glassy carbon. The temperature in the sample space is maintained to ± 0.2 °C by Mo heating resistances and Pt–Pt/Rh thermocouples connected to a Eurotherm® temperature controller. Temperature gradients through the sample space do not exceed 5° at a run temperature of 400 °C. The Viton O-rings are situated outside the heating zone (at <100 °C when the sample-space temperature is 400 °C) to avoid their thermal degradation. This results in a relatively small 'dead-volume' space between the rods and glassy-carbon tube (<20–30% of the total cell volume) that produces minimal solute diffusion and solid precipitation below or above the hot sample space. Helium pressure is monitored using three pressure sensors placed at the cell exit and at the end of the pressure line. Pressure variations between them do not exceed 10 bars; the mean value is adopted. The cell design permits operation up to ~500 °C and ~2000 bar (depending of the amplitude of the fluid expansion and the thickness of Be windows). Additional details about the cell properties and operation limits are given in Pokrovski et al. (2006a).

It should be noted that because of the high external pressure coupled with elevated mobility of helium, partial diffusion of He into the internal cell and its dissolution in aqueous solution cannot be completely avoided. Such effects are expected to be weak at temperatures below 300 °C and experimental He pressures of 600 bar, at which He solubility in water ranges from 0.3 to 4 mol% between 25 and 300 °C as shown by thermodynamic calculations using available Henry constants (e.g., Schulte et al., 2001). However, its solubility might become important at near-critical temperatures, significantly lowering water activity and thus affecting solid phase solubilities. Measurements of He diffusivity into an empty cell through Viton seals at ambient temperature and He pressures above 500 bar
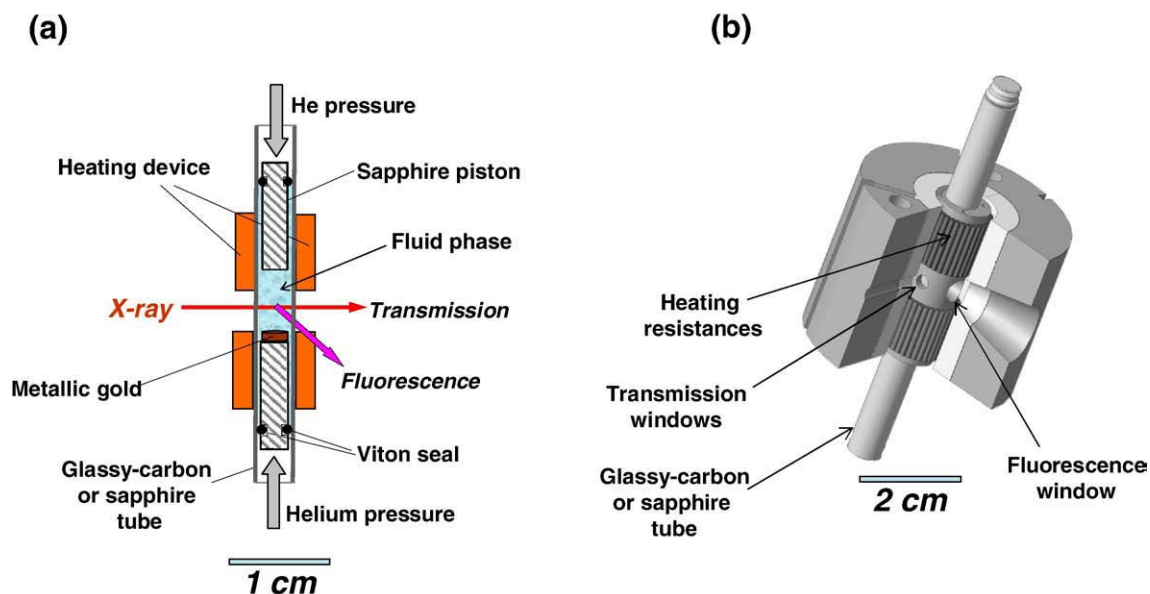
Fig. 1. (a) Details of the internal part of the X-ray cell, and (b) the assembled cell with a heating device used for XAFS measurements in this study.

demonstrated negligible He diffusion within the duration of typical XAFS experiments (1–2 days). Although it is difficult to quantitatively estimate the amplitude and rate of He diffusion at elevated *T–P* into the cell in the presence of a fluid phase, tests involving rapid cell cooling (<15 min) from 450 to 20 °C under 600 bar of He pressure revealed neither changes in the mass of fluid initially loaded nor the appearance of a vapor phase, thus indicating that He dissolution is likely to be insignificant in most experiments. Furthermore, previous solubility measurements in different systems at temperatures above 300 °C using the same cell design demonstrated excellent agreement

with solubility data obtained in batch hydrothermal reactors (e.g., GeO_2–H_2O, Sb_2O_3–NaCl–HCl, Au–NaOH–S, Pokrovski et al., 2005a, 2006a,b, 2008b), thus implying that He dissolution in the experimental fluid (if occurs) has no significant effect on mineral solubilities and solute atomic structures.

A small piece of Au foil (~50 mg, 3 mm in diameter) was placed at the bottom of the sample space (i.e., on the top of the lower sapphire rod) below the beam passage through the aqueous solution. Note that the diameter of the holes (2–3 mm) in the heating assemblage around the cell tube is such that the Au solid at the cell bottom is never
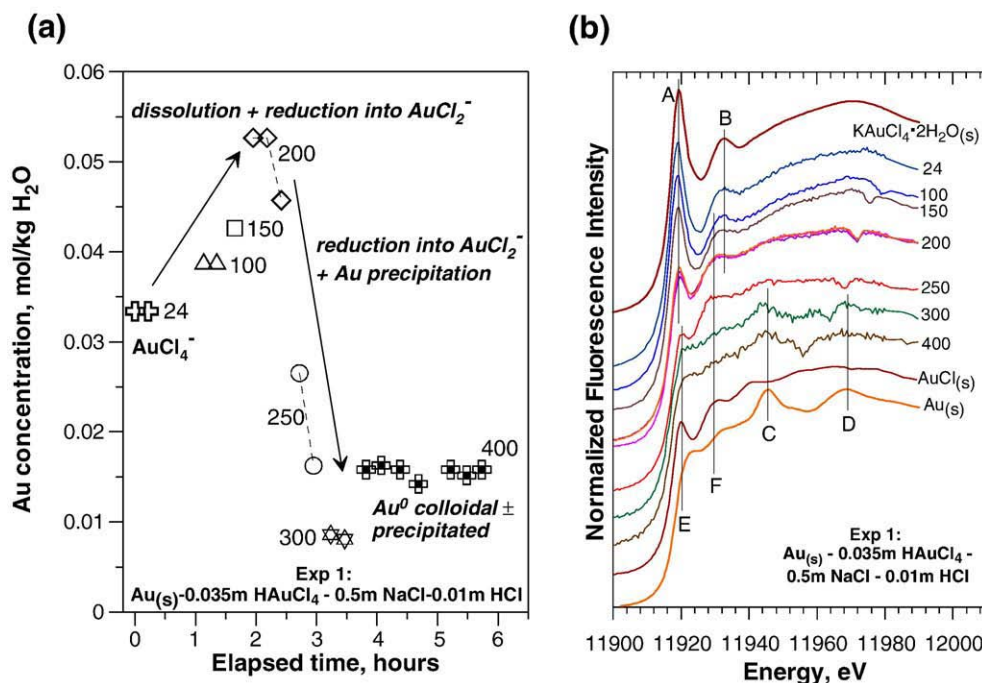
Fig. 2. (a) Evolution of dissolved Au concentration in solution at 600 bar in a mono-crystalline sapphire cell as a function of temperature and time in the system $Au_{(s)}$–$HAuCl_4$–NaCl–HCl for indicated composition and temperatures (in °C), measured by monitoring the absorption edge height in transmission mode. The error is comparable to the symbol size. (b) Normalized Au–L_{III} near-edge (XANES) spectra from the same experiment at indicated temperatures. Vertical lines show features characteristic of the square $AuCl_4^-$ species similar to those in crystalline $KAuCl_4 \cdot 2H_2O$ (A, B), metallic gold (C, D), and the linear [Cl–Au–Cl] unit in $AuCl_{(s)}$ and $AuCl_2^-$ complex (E, F). The glitches apparent in some spectra of solutions between 11,950 and 11,990 eV correspond to diffraction peaks from the sapphire cell walls. The spectrum of $AuCl_{(s)}$ was kindly provided by Doonan and Reith (personal communication).
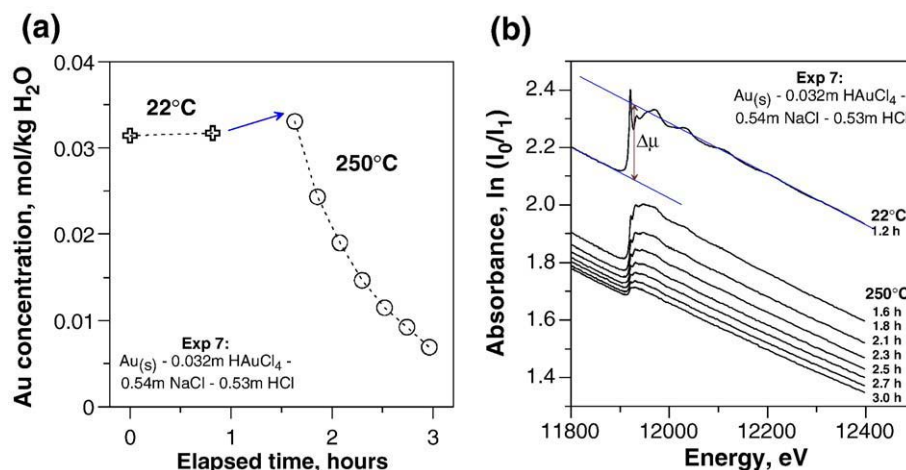
Fig. 3. (a) Evolution of Au dissolved concentration as a function of time in an acid HAuCl$_4$–NaCl–HCl aqueous solution of indicated composition in the presence of native gold (Exp 7), determined from the absorption edge height, $\Delta\mu$, of the transmission spectra shown in (b), and using Eq. (1). The error is comparable to the symbol size. (b) Raw transmission scans at Au–L$_{III}$ edge at 22 and 250 °C and 600 bar for the same experiment, as a function of run duration (in hours from the start of the experiment). The decrease of the total absorbance and absorption edge height at 250 °C demonstrates the precipitation of Au from solution.

exposed to the direct beam which "sees" only the central part of the sample space occupied by the fluid phase (Fig. 1). The cell was pressurized to 600 bars and heated. XAFS spectra were recorded at temperatures from 20 to 500 °C (depending on experiment and solution composition) and as a function of time, allowing the dissolved Au concentration and structural changes to be monitored (e.g., Figs. 2 and 3). The spectral amplitudes both in the XANES and EXAFS regions recorded in transmission and fluorescence modes were found to be identical demonstrating the absence of self-absorption effects in the fluorescence mode, at least at the investigated gold concentrations ($\leq\sim0.05$ m).

2.2. XAFS spectra analysis

Classical EXAFS spectra reduction was performed with the Athena and Artemis packages (Ravel and Newville, 2005) based on the IFEFFIT program (Newville, 2001). Details about the reduction procedure can be found elsewhere (Pokrovski et al., 2005a, 2006a). Briefly, spectra were normalized to the absorption edge height, background-removed using the AUTOBK algorithm, weighted by k^n, where $n = 1$, 2 or 3, and Fourier filtered over the k range from ~3 to 9–12 Å^{-1} (depending on the signal-to-noise ratio) to produce radial structure functions (RSF). Fits were performed in R-space on both the real and imaginary parts of the RSF contributions (Newville, 2001) to obtain the identity of the backscattering atoms, Au-neighbor distance (R), coordination number (N), and the Debye–Waller factor (σ^2) for each scattering path. In addition to these structural parameters, a single nonstructural parameter, Δe, was varied to account for its estimate made by FEFF. To diminish correlations between N and σ^2, and R and Δe, and better account for light versus heavy neighbors and multiple scattering paths, fits were performed simultaneously with k-weightings of 1, 2 and 3. The fitted values of the structural parameters were identical within errors, with similar fit qualities for each k-weighting. This is an additional demonstration of both the validity of the chosen structural models and the accuracy of the EXAFS background removal procedures (Ravel and Newville, 2005). Theoretical backscattering amplitude and phase-shift functions for Au–Cl, Au–O, Au–H, Au–Na/K, Au–Au single and multiple scattering paths were computed using the FEFF6 *ab initio* code (Zabinsky et al., 1995) with Au, AuCl, Au$_2$O$_3$, NaAuCl$_4$, KAuCl$_4\cdot$2H$_2$O, and Na$_3$Au(S$_2$O$_3$)$_3\cdot$2H$_2$O crystal structures. The amplitude reduction factor (S_0^2) was set at 0.85 ± 0.05 as found by fitting spectra of these solid references. This value is identical to that reported previously for Au L$_2$ and L$_3$ edges of different compounds (Benfield et al., 1994). The influence of anharmonic disorder in

determining structural parameters was checked using the cumulant expansion method (e.g., Crozier et al., 1988). The values of third- and fourth-order cumulants (c_3 and c_4) found when fitting the Au first coordination shell always converged to zero within errors ($\pm10^{-4}$) and thus had no influence on the main structural parameters (R, N and σ). The presence of multiple scattering (MS) events within the Au first coordination shell was examined using the FEFF code (see below), assuming local D$_h$ or C$_{4v}$ geometries around Au, as found in the model compounds investigated. Multi-electron excitations (MEE) in the Au L$_3$-edge EXAFS region, like 2p4f which yields additional transitions at $k \sim4$–6 Å^{-1}, may interfere with standard background subtraction procedures and thus influence the analysis (e.g., Benfield et al., 1994). However, these MEE could not be detected unambiguously in most of our Au^I spectra, in agreement with previous findings that showed a negligible impact of these transitions on EXAFS-derived structural parameters for Au^I-bearing compounds (Benfield et al., 1994; Berrodier et al., 2004). For Au^{III} samples, the MEE were identified in the spectra, but were found to be too weak to affect the structural parameters. In addition to the classical EXAFS analysis, XANES spectra of different Au aqueous species potentially present in the experimental solutions were modeled based on species optimized geometries generated using quantum-chemical algorithms and the EXAFS derived Au-ligand distances (see Section 2.4).

2.3. Determination of dissolved Au concentration from the absorption edge height

Dissolved Au concentrations were determined from the amplitude of the absorption edge height over the Au L$_3$-edge of transmission spectra ($\Delta\mu$) using the following equation based on the classical X-ray absorption relation (see Pokrovski et al., 2005a, 2006a; Testemale et al., 2005 for details):

$$C_{Au} = \Delta\mu/(\Delta\sigma_{Au} \times M_{Au} \times l \times d_{fluid})\qquad(1)$$

where C_{Au} is Au aqueous concentration (mol kg^{-1} of fluid), $\Delta\sigma_{Au}$ is the change of the total absorption cross-section of Au over its L$_3$-edge (cm^2 g^{-1}), l is the optical path length inside the cell (cm) which remains constant through the experiment, M_{Au} is Au atomic weight (0.1970 kg mol^{-1}), and d_{fluid} is the density of the aqueous solution (g cm^{-3}) at given T and P.

The absorption cross-sections for Au were taken from the recent compilation of Elam et al. (2002). These values are in close agreement, within $\sim5\%$ below and above the Au L$_3$-edge, with other databases

(e.g., as compiled in the Hephaestus software, Ravel and Newville, 2005). In the absence of direct volumetric data on the system H_2O–$NaCl$–HCl–H_2SO_4–Au at elevated T–P, the fluid density in our XAFS experiments was approximated using the Pressure–Volume–Temperature–Composition (PVTX) properties of the system $NaCl$–H_2O (Anderko and Pitzer, 1993; Bakker, 2003), and assuming that Au/HCl/H_2SO_4 solutes in water yield the same contribution to the fluid density as the equivalent *weight concentration* of NaCl. It is expected that the maximum error of density estimations using this approximation does not exceed 10% at temperatures above 200 °C.

The height of the absorption-edge step ($\Delta\mu$) in each transmission EXAFS scan was determined using a classical 'empirical' normalization technique of the AUTOBK algorithm (Newville, 2001), and an independent Cromer–Liberman normalization (CLnorm, Cromer and Liberman, 1970), both implemented in the Athena software. Values of $\Delta\mu$ found using both approaches were identical within errors, thus confirming the validity of estimates of atomic-like background over the Au L_3-edge. The uncertainty on $\Delta\mu$ determinations, as estimated by changing fitted energy ranges or by comparing different scans for the same Au concentration, is less than 5% for a $\Delta\mu$ amplitude greater than 0.1 (~0.01 m Au), is about 10% for $\Delta\mu$ between 0.01 and 0.1, and reaches 30–50% for $\Delta\mu$ between 0.01 and 0.001 (~10^{-3}–10^{-4} m Au).

2.4. Quantum-chemical calculations of optimized structures and XANES spectra for Au aqueous species

The quantum chemical calculations were performed using the Gaussian 03 program (Frisch et al., 2004) based on Density Functional Theory (DFT) and second order Møller–Plesset (MP2) methods. DFT calculations were carried out using a B3LYP functional (Lee et al., 1988; Becke, 1993) incorporated into Gaussian 03. The 6-311+G(d) basis set was used for Cl, O, and H. The Stuttgart–Dresden (SDD) relativistic effective core potential (RECP) adopted in Schwerdtfeger et al. (1989) was used in most calculations for Au. This potential, combined with [7s-3p-4d] contraction for valence electrons, was used to approximate the Au inner electronic structure consisting of 60 electrons ([Kr]+4d+4f). Previously, the SDD RECP was successfully used to study structures and thermo-chemical properties of $Au^+(H_2O)_n$ clusters (Feller et al., 1999). We denote these theory levels as B3LYP/SDD/6-311+G(d) and MP2/SDD/6-311+G(d) for DFT and MP2 methods, respectively. In addition, a series of calculations for $AuOH(OH_2)^0$ and $AuCl_2^-$ was performed with the LANL2DZ (Hay and Wadt, 1985) and CEP-121G (Stevens et al., 1992) effective core potentials. Besides, to account for the effect of bulk solvent (water at 25 °C, ε=78.36), several calculations were carried out with the aid of a Polarized Continuum Model (PCM/B3LYP/SDD/6-311+G(d) theory level). The normal mode analysis showed that the calculated geometries represent the true minima on the potential energy surface.

XANES spectra of different Au aqueous species were modeled based on the optimized geometries of the predicted species and experimental EXAFS-derived Au-ligand distances, using the FDMNES computer code (Joly, 2001). This program calculates theoretical XANES spectra using two different formalisms, the classical multiple scattering (MS) muffin-tin method (e.g., Rehr et al., 1992) and/or the Finite Difference Method (FDM) where the electron potential is calculated by resolving the Schrödinger equation on the node points of a three-dimensional grid (Kimball and Shortley, 1934). The obtained raw calculations represent the evolution of the photo-absorption cross-section of Au as a function of X-ray photon energy and correspond to the transition amplitude between the initial and final states. The generated raw spectra, which correspond to an energy resolution of the FD method (<0.1 eV) and thus display almost all possible electronic transitions, are further convoluted with a Lorentzian function with a full width Γ_h of 5.41 eV to account for the core hole lifetime at the Au L_3-edge, and a Gaussian function to account for the experimental resolution assumed to be equal to the intrinsic

resolution of the monochromator (Γ_{exp}=0.61 eV, Proux et al., 2006). The convolution parameters were fixed in all subsequent analyses. Because the electronic states below the Fermi level are occupied, the absorption cross section is taken to be equal to zero below the Fermi energy prior to the convolution. All calculations were performed in the FDM mode in order to test different clusters symmetries and geometric configurations (note that in case of low symmetry, the muffin-tin approximation is not sufficient in the near-edge energy range; Joly, 2001). The values of energy for the Fermi level were fixed to −4.0 and −2.9 eV for Au^{III} and Au^I, respectively, as deduced from examination of the density of state (DOS) evolution of the different electronic states.

3. Results

3.1. Evolution of XANES spectra and gold dissolved concentrations in Au^{III}/Au^I acidic chloride solutions

3.1.1. $HAuCl_4$–$NaCl$–HCl system

Two experiments in a glassy-carbon and mono-crystalline sapphire cell were performed on an aqueous solution of the initial composition ~0.035 m $HAuCl_4$–0.50 m $NaCl$–0.01 m HCl at temperatures to 300 °C and pressures of 600 bar (Exp 2 and 3, Table 1). Aqueous gold concentrations derived from transmission spectra by monitoring the absorption edge amplitude as a function of temperature and time are reported in Table 1. It was found that in the carbon cell dissolved Au concentrations remain stable to 100 °C, but decrease rapidly at $T \geq 150$ °C both with time at the same T and with increasing T, whereas in the sapphire cell Au concentrations are identical to the initial value at $T \leq 250$ °C, at least within the time interval passed at each temperature (20 to 80 min, see Table 1). XANES spectra of these solutions (Fig. 4) are the same at $T \leq 100$ and identical to those of crystalline Na and K auric chlorides ($NaAuCl_4$, $KAuCl_4 \cdot 2H_2O$) and acidic (pH ≤ ~5) $HAuCl_4$-bearing solutions over a wide range of Au (10^{-5}–10^{-1} m) and chloride (0.01–1 m) concentrations at ambient T–P reported previously by Berrodier et al. (2004) and Farges et al. (1993). As shown in detail in these works, the XANES spectra of these compounds are dominated by a strong pre-edge feature at ~11919 eV arising from electronic transitions from the 2p ground states to the partially empty 5d states of Au^{3+} (Berrodier et al., 2004). The spectra of aqueous Au^{III} in acidic chloride media below 100 °C recorded in our study are fully consistent with the dominant presence of the square-plane $AuCl_4^-$ complex, in agreement with these XAFS and other independent low-temperature Raman and UV–Vis data (Pan and Wood, 1991; Peck et al., 1991; Murphy et al., 2000).

At temperatures above 150 °C, both in carbon and sapphire cells, the amplitude of the Au^{III} pre-edge feature decreases rapidly with temperature and time, and the shape of XANES spectra indicates the precipitation of metallic gold at $T \geq 200$ °C (Fig. 4). However, the fast spectral evolution together with rapid decrease of Au concentration did not allow accurate assessment of all spectral features within the limited beam time. The major conclusion from these experiments is the instability of $AuCl_4^-$ at temperatures above 150 °C, resulting in rapid transformation to other species followed by metallic gold precipitation. These phenomena are much faster in the carbon cell than the sapphire cell since C is likely to create reducing conditions favorable to Au^{III} reduction. A more quantitative assessment of Au^{III} reduction processes has been obtained from experiments in the presence of metallic gold reported below.

3.1.2. $Au_{(s)}$–$HAuCl_4$–$NaCl$–HCl system

Two experiments were performed in a carbon and sapphire cell on the same initial solution composition as above but in the presence of a piece of metallic Au placed in the cell together with the Au^{III} chloride solution (Exp 1 and 4, Table 1). A third experiment was done in a polycrystalline sapphire cell at more acidic conditions and higher Cl concentrations (Exp 7, $Au_{(s)}$–0.032 m $HAuCl_4$–0.54 m $NaCl$–0.53 m

Table 1
Total dissolved gold concentrations and fraction of the $AuCl_2^-$ species in aqueous solution in the systems $HAuCl_4$–NaCl–HCl, $Au_{(s)}$–$HAuCl_4$–NaCl–HCl, and $Au_{(s)}$–NaCl–H_2SO_4 at 600 bar as a function of temperature, run duration, and cell material

Run/cell	System composition (mol/kg H₂O)	T, °C	Time, hours	m_{Au}	$AuCl_2^-$, mol%
Exp 2 sapphire	0.036 m $HAuCl_4$– 0.50 m NaCl– 0.01 m HCl	24	0.2	0.037	0
		100	1.2	0.036	<3
		150	0.7	0.036	<3
		200	0.3	0.037	24±2
		250	0.3	0.037	86±4
		300	2.4	0.03–0.01	95±5
Exp 3 carbon	0.036 m $HAuCl_4$– 0.50 m NaCl– 0.01 m HCl	30	1.6	0.036	<4
		100	1.4	0.036	10±2
		150	1.4	0.035–0.031	43±3
		175	1.4	0.027–0.015	78±5
		200	1.4	0.008–0.002	Au^0
		225	1.4	<0.002	Au^0
		250	1.0	<0.002	Au^0
Exp 7 sapphire	Au– 0.032 m $HAuCl_4$– 0.54 m NaCl– 0.53 m HCl	22	1.2	0.032	0
		250	1.9	0.033–0.007	100
Exp 1 sapphire	Au– 0.035 m $HAuCl_4$– 0.50 m NaCl– 0.01 m HCl	24	0.7	0.033	<3
		100	0.8	0.039	9.5±3
		150	0.3	0.043	29±2
		200	0.8	0.053–0.046	73±2
		250	0.5	0.027–0.016	97±2
		300	0.6	~0.009	Au^0
		400	2.1	~0.015	Au^0
Exp 4 carbon	Au– 0.036 m $HAuCl_4$– 0.50 m NaCl– 0.01 m HCl	30	1.9	0.037	<3
		100	2.0	0.039–0.037	14±2
		150	2.0	0.039–0.033	41±3
		200	2.6	2.4×10^{-2}–5×10^{-4}	Au^0
		250	0.6	$<5 \times 10^{-4}$	Au^0
Exp 5 carbon	Au–2.6 m NaCl– 0.53 m H_2SO_4	300	0.8	$\leq 10^{-5}$	>95
		400	0.7	$\leq 5 \times 10^{-5}$	>95
		450	0.7	$\sim 2 \times 10^{-3}$	>95
Exp 6 carbon	Au–2.6 m NaCl– 0.53 m H_2SO_4	400	1.4	$\leq 2 \times 10^{-4}$	>95
		500	3.4	$\leq 3 \times 10^{-4}$	>95

$AuCl_2^-$ mole fraction was derived using linear combination analysis (LCA) of normalized XANES spectra which was performed in the range −30 to 60 eV over the Au L_{III}-edge and using the spectra from Exp 7 at 22 and 250 °C as the references for the $AuCl_4^-$ and $AuCl_2^-$ species, respectively, and assuming that $Au_{tot} = AuCl_4^- + AuCl_2^-$.

Au^0 means that almost all Au was lost from solution and metallic gold precipitated, the gold remaining in solution is likely to be in the colloidal form and/or deposited on the cell optical windows.

m_{Au} = total dissolved Au molality derived from the absorption edge amplitude in transmission mode and using Eq. (1), a concentration range denotes the initial and final m_{Au} value at the given T.

Time represents the duration of spectra acquisition (in hours) at each temperature step.

HCl). The run in the carbon cell (Exp 4) yielded similar results to those described above showing a systematic (though somewhat slower than without the metal) decrease of both the Au^{III} pre-edge feature and dissolved Au total concentrations at 100–150 °C, followed by rapid Au precipitation at 200–250 °C (see Fig. 4 for similar experiments).

In contrast, the same run performed in the sapphire cell (Exp 1) showed a higher thermal stability of the studied solution, with significant increase of Au concentrations from 0.035 m (at 30 °C) to a maximum value of 0.053 m with rising temperature to 200 °C (Fig. 2a). Gold dissolution was accompanied by systematic changes in the XANES spectra as manifested by i) a decrease of the Au^{III} pre-edge peak amplitude and ii) energy shifts of the main $Au^{III}Cl_4$ XANES features (identified as A and B in Fig. 2b). At 200 °C, Au concentrations were found to decrease slightly (by ~20%) within an hour, whereas the XANES spectra of three successive scans remained almost identical (Fig. 2b). At 250 °C, Au precipitation was accelerated (Fig. 2a), but successive XANES scans (20 min each) did not show changes within

the experimental resolution. At this temperature, the XANES spectra are characterized by a weak resonance at ~11921 eV (feature E) which is different in energy from the Au^{III} pre-peak (feature A at 11919 eV), and by another resonance at 11929 eV (feature F) not present in the spectra of Au^{III} at T≤ 100 °C (Fig. 2b). Note that a linear combination of Au^{III} and Au^0 spectra could not account for these resonances. These features are very close to those of the XANES spectrum of crystalline $AuCl_{(s)}$ in which Au is linearly coordinated with two Cl atoms (Straehle and Loercher, 1974). The EXAFS part of these spectra could not be examined, however, due to the presence of numerous diffraction peaks arising from the mono-crystalline sapphire tube. At higher temperatures (300 and 400 °C), an extremely rapid (within ~10 min, corresponding to the time necessary to raise temperature) Au precipitation occurred and XANES spectra displayed the major features of metallic gold (features C and D in Fig. 2), without detectable evolution with time (up to 2 h). The gold remaining in solution (<0.01 m) might be present in colloidal form, but some contribution to the spectra from the metal deposited on the cell walls in front of the transmission and fluorescence windows cannot be ruled out. This experiment thus demonstrated that Au^{III} reduction, likely into soluble Au^I chloride complexes, occurs in a limited temperature window (150–250 °C).

A third experiment, carried out at 250 °C for a longer duration in a more acidic and Cl concentrated solution (0.53 m HCl, 0.54 m NaCl, Exp 7) using a poly-crystalline sapphire cell with more tightly adjusted pistons and smaller dead volume (<10% of cell volume), confirms these findings. It can be seen in Fig. 3 that, although total Au concentrations decrease systematically with time, normalized XAFS spectra recorded in successive scans over about 2 h do not show any detectable evolution. They are identical within normalization errors to those recorded at 250 and 300 °C in the other sapphire-cell experiments described above (Exp 1 with $Au_{(s)}$ and Exp 2 without
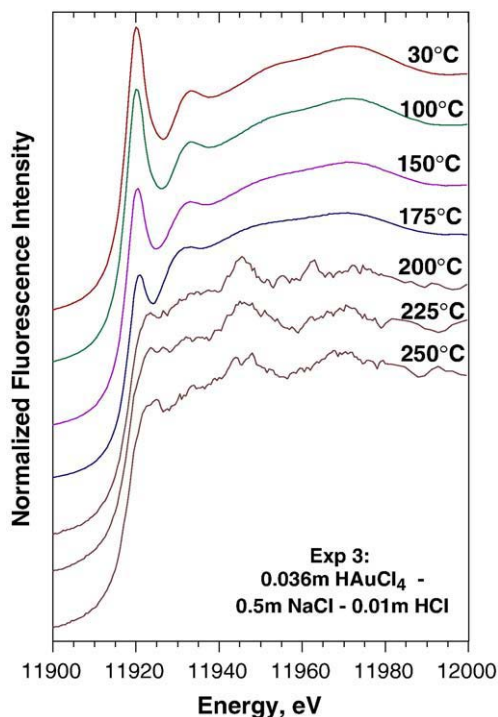

Fig. 4. Normalized Au–L_{III} XANES spectra from Exp 3 in a carbon cell (0.036 m $HAuCl_4$–0.50 m NaCl–0.01 m HCl) at 600 bar and indicated temperatures (spectra at each T are shifted along the vertical axis for clarity). The spectrum at each temperature is the sum of 2 to 3 scans (30 min each) that show only a weak evolution with time. Spectra at T≥200 °C correspond to gold metal, whereas those recorded between 30 and 175 °C are likely to be a mixture of Au^{III} and Au^I chloride species. The high noise of the gold metal spectra is due to the low Au concentration in solution (m_{Au}<0.01, see Table 1). Identical spectra were recorded in Exp 4 in a carbon cell ($Au_{(s)}$–0.036 m $HAuCl_4$–0.50 m NaCl–0.01 m HCl) from 30 to 150 °C (not shown).
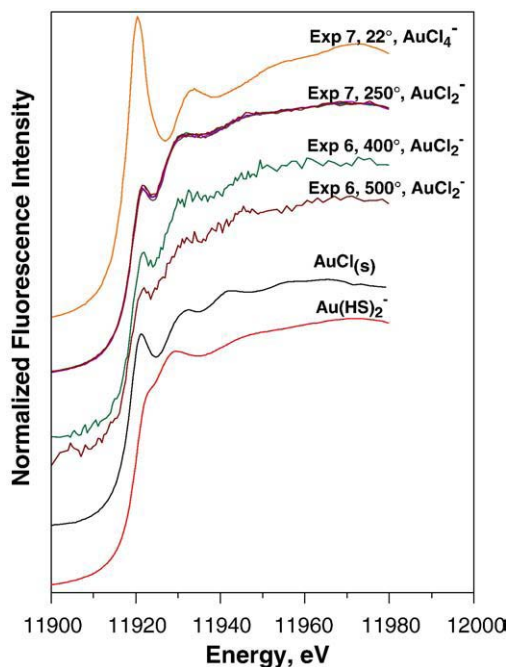
Fig. 5. Normalized Au–L$_{III}$ XANES spectra from selected solutions in the presence of native gold at 600 bar and indicated temperatures (spectra at each T are shifted along the vertical axis for clarity): Exp 7 = Au$_{(s)}$–0.032 m HAuCl$_4$–0.54 m NaCl–0.53 m HCl, Exp 6 = Au$_{(s)}$–2.6 m NaCl–0.53 m H$_2$SO$_4$. In Exp 7 at 250 °C several scans recorded at different times are presented (see Fig. 3), they show no detectable evolution with time. The spectra of crystalline AuCl$_{(s)}$, and the linear Au(HS)$_2^-$ complex at 300 °C/600 bar (Schott et al., 2006), analogous to AuCl$_2^-$, are also shown for comparison. The poor statistics of the spectra in Exp 6 is due to the low Au solution concentration (~10^{-4} m, see Table 1).

Au$_{(s)}$). It is thus very likely that at elevated temperatures AuCl$_4^-$ reduces into Au^I-Cl complexes, presumably AuCl$_2^-$, as suggested both from in situ Raman spectroscopy on similar solutions (Pan and Wood, 1991; Murphy et al., 2000) and solubility measurements in the system Au$_{(s)}$–Au^{III}Cl$_4$–NaCl–HCl (Gammons and Williams-Jones, 1995, 1997), which showed that increasing the temperature in the presence of metallic gold promotes the reduction of AuCl$_4^-$ into AuCl$_2^-$ according to

$$2Au_{(s)} + AuCl_4^- + 2Cl^- = 3AuCl_2^- \qquad (2)$$

3.1.3. Au$_{(s)}$–NaCl–H$_2$SO$_4$ system

Two runs were performed to study Au dissolution in a 2.6 m NaCl–0.53 m H$_2$SO$_4$ solution at temperatures from 300 to 500 °C at 600 bar using a carbon cell (Exp 5 and 6). Dissolved gold concentrations were found to be close to the detection limit of our technique ($<10^{-3}$–10^{-4} m Au) and showed no detectable evolution with time, over at least 3 h (see Table 1). Despite the significant noise affecting the XANES spectra recorded from these Au-poor solutions (Fig. 5), their main features were found to be very similar to those in the Au^{III}–Cl±Au$_{(s)}$ systems at 250 °C and lower Cl concentrations described above. Equilibrium thermodynamic calculations carried out using the available stability constants for Au^{III}Cl$_4^-$ and Au^I chloride and hydroxide complexes (see Appendix) indicate that AuCl$_2^-$ should be by far the dominant Au species in the experimental solutions, with concentrations increasing from 0.001 to 0.1 m Au between 300 and 500 °C. The much lower Au concentrations measured by XAFS in this study are likely due to the presence of carbon whose partial dissolution at $T>300$ °C generates more reducing conditions than those predicted for a NaCl–H$_2$SO$_4$ solution, and thus favors the stability of metallic gold. For example, calculations show that in Exp 5 at 300 °C in the presence of graphite, H$_2$S is the dominant sulfur species, pH becomes less acidic (pH ~3.9 versus ~1.0 without graphite), and Au concentrations decrease ~20 times (to ~3×10^{-5} m), whereas AuCl$_2^-$ largely dominates over AuHS^0 that forms in the presence of H$_2$S at acidic pH. A detectable H$_2$S

smell after our experiments confirms these thermodynamic predictions. Thus, these experiments, together with those described above (Sections 3.1.1 and 3.1.2), provide a further confirmation that similar Au^I–Cl complexes, presumably AuCl$_2^-$, form in acidic chloride solutions over wide temperature (250–500 °C) and Cl concentration (0.5–2.6 m) ranges.

3.2. Local structure of Au chloride complexes in hydrothermal fluids

Normalized EXAFS spectra and their corresponding Fourier Transforms from selected solutions in the system HAuCl$_4$–NaCl–HCl with and without metallic Au obtained in a glassy-carbon or polycrystalline-sapphire cell (Exp 3, 4 and 7) are shown in Fig. 6 and the derived structural parameters are reported in Table 2. In both systems, the spectra at ≤30 °C and pressures 1 and 600 bars are identical and can be accurately modeled with 3.9±0.2 Cl atoms at an average distance of 2.282±0.004 Å around the gold atom, and a very weak thermal and/or structural disorder (DW factor ~0.001 Å^2). The pronounced feature apparent in the Fourier Transform Magnitude of these spectra at ~4 Å (not corrected for phase shift) corresponds to linear multiple scattering paths within the AuCl$_4^-$ cluster. This is supported by their fitted DW factors and path distances which are twice those for the single scattering Au–Cl paths. This feature is a direct indication that Cl atoms are arranged in square-plane geometry around the central Au atom, similar to the crystal structures of tetra-aurates of alkaline metals (e.g., Théobald and Omrani, 1980; Jones et al., 1988), thus confirming that AuCl$_4^-$ is by far the dominant species in our solutions, in full agreement with the previous findings from X-ray diffraction, Raman and XAFS spectroscopy (Maeda et al., 1974; Benfield et al., 1994; Murphy et al., 2000; Berrodier et al., 2004).

It can be seen in Fig. 6 that with increasing temperature the spectral amplitude decreases systematically consistent with quantitative EXAFS modeling which predicts both a decrease of the average number of Cl atoms and an increase of the Au–Cl DW factors which attain values of 1.8±0.3 atoms and ~0.002 Å^2, respectively, with a mean Au–Cl distance of 2.267±0.004 Å at 250 °C and 600 bar. Note that EXAFS spectra in experiments with and without metallic gold in the T range 20–150 °C (Exp 3 and 4) are identical and yield similar structural parameters (Table 2). No changes in spectra were detected below 100 °C demonstrating that the structure and Au–Cl distances in the dominant AuCl$_4^-$ complex do not change significantly at least in this T-range. At $T ≥ 150$ °C, average Au–Cl distances exhibit a slight but detectable decrease (by ~0.01 Å, Table 2). This evolution is likely to reflect a decrease in the proportion of AuCl$_4^-$ versus AuCl$_2^-$ with rising temperature. The amplitude of the MS feature gradually decreases with temperature and is consistent with the multiple scattering paths within the linear Cl–Au–Cl unit, with values of R, N and σ^2 parameters twice as those for the single scattering Au–Cl path. The low DW factors, very weak evolution of Au–Cl distances with temperature, and negligible 3rd- and 4th-order cumulants from anharmonic analyses indicate very little thermal and positional disorder. This reflects the strong covalent character of Au–Cl bonds in gold-chloride complexes and weak interactions of AuCl species with the solvent water molecules (hydration). The weak-to-negligible evolution with T of the structural parameters for AuCl$_4^-$ and AuCl$_2^-$ species is similar to that observed for other strongly covalent and weakly hydrated complexes of soft metals (e.g., As(OH)$_3$, Pokrovski et al., 2002; Testemale et al., 2004; Ge(OH)$_4$, Pokrovski et al., 2005a; Sb(OH)$_3$, Pokrovski et al., 2006a; Au(HS)$_2^-$, Pokrovski et al., 2006b; Schott et al., 2006) whose molecular structure and stability are only slightly sensitive to the changes in the solvent density and dielectric constant (e.g., Pokrovski et al., 1999, 2005b, 2008a).

The EXAFS-derived parameters are in agreement with a progressive reduction of the fraction of AuCl$_4^-$ complexes with increasing temperature in both systems (i.e., with and without metallic Au), consistent with the evolution of the XANES spectra described above (Section 3.1). The
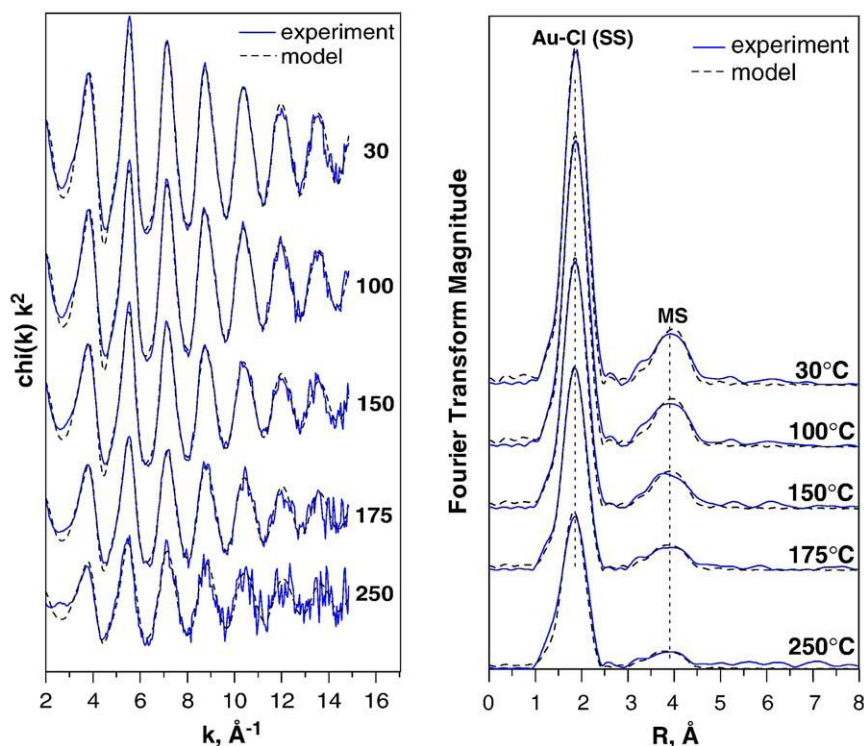
Fig. 6. Normalized k^2-weighted EXAFS spectra from Au-bearing NaCl–HCl aqueous solutions at 600 bar and indicated temperatures (in °C), and their corresponding Fourier Transform magnitudes (not corrected for phase shift). Dashed curves denote fits using the parameters from Table 2; vertical dotted lines indicate the position of Cl neighbors (corresponding to a single scattering path, SS) and linear multiple scattering paths (MS). Spectra at temperatures 30–175 °C are from Exp 3 and 4 with the starting composition 0.036 m HAuCl$_4$–0.50 m NaCl–0.01 m HCl, whereas the spectrum at 250 °C comes from Exp 7 with the starting composition Au$_{(s)}$–0.032 HAuCl$_4$–0.54 m NaCl–0.53 m HCl (see Table 1). The slight mismatch of the experimental spectra by the fit at ~4.5 and ~6.0 is likely to correspond to multi-electron transitions not accounted for by classical EXAFS modeling (Berrodier et al., 2004).

number of Cl neighbors derived from the spectrum at the highest temperature (250 °C) is likely to correspond to the dominant presence of the linear AuCl$_2^-$ complex which should represent at least 90% of the total dissolved Au at these conditions considering the uncertainties of the N$_{Cl}$ values. No neighbors other than Cl (e.g., O, Na) could be detected around Au within the experimental resolution (~10%), suggesting that the sum of

Table 2

Average gold local atomic structure in aqueous solution in the systems HAuCl$_4$–NaCl–HCl and Au$_{(s)}$– HAuCl$_4$–NaCl–HCl, as a function of temperature, pressure and cell material, derived from fitting EXAFS spectra at Au–L$_{III}$ edge

T, °C	P, bar	Atom	N, atoms	R, Å	σ^2, Å^2	$\mathcal{R}$-factor
Exp 7: Au$_{(s)}$–0.032 m HAuCl$_4$–0.54 m NaCl–0.53 m HCl, sapphire cell						
22	600	Cl	3.8	2.281	0.0010	0.016
250	600	Cl	1.8	2.267	0.0024	0.017
Exp 3: 0.036 m HAuCl$_4$–0.50 m NaCl–0.01 m HCl, carbon cell						
30	1	Cl	4.0	2.283	0.0012	0.010
30	600	Cl	3.9	2.282	0.0012	0.014
100	600	Cl	3.6	2.283	0.0016	0.007
150	600	Cl	3.0	2.279	0.0018	0.008
175	600	Cl	2.3	2.273	0.0020	0.006
Exp 4: Au$_{(s)}$–0.036 m HAuCl$_4$–0.50 m NaCl–0.01 m HCl, carbon cell						
30	600	Cl	3.9	2.283	0.0012	0.011
100	600	Cl	3.5	2.283	0.0016	0.010
150	600	Cl	3.0	2.280	0.0017	0.009
Error			±0.3	±0.004	±30%	

R = gold-backscatterer mean distance, N = coordination number, σ^2 = squared Debye–Waller factor (relative to $\sigma^2 = 0$ adopted in the calculation of reference amplitude and phase functions by FEFF), $\mathcal{R}$-factor defines goodness of the total fit in R-space as described in IFEFFIT (Newville et al., 2001). For all samples the fitted k- and R-ranges were respectively 3.0–11.0 Å^{-1} and 1.2–4.8 Å (not corrected for phase shift). Major multiple scattering contributions (MS) within the linear AuCl$_2$ and square plane AuCl$_4$ clusters like Au–Cl1–Cl2–Au ($R_{ms1} = 2 \times R_{Au–Cl}$), and Au–Cl1–Au–Cl2–Au ($R_{ms2} = 2 \times R_{Au–Cl}$) were included in all fits. Their DW factors were found to range between 0.002 and 0.004 Å^2. The number of variables in the fit, N_{var} = 4 to 7, number of independent points, N_{ind} ~17.

the fractions of Au^I hydroxide species (e.g., AuOH(H$_2$O)^0), the hydrated cation (Au(H$_2$O)$_2^+$), and Au^I and Au^{III} hydroxy-chloride complexes (e.g., Au(H$_2$O)Cl^0, Au(OH)Cl$^-$, Au^{III}Cl$_{4-n}$(OH)$_n$) is less than 10% of total dissolved Au at 250 °C. Because EXAFS sees the average atomic environment around the absorbing atom, the presence of some fraction of AuCl$_4^-$ or other eventual AuCl$_n$ complexes having no OH/H$_2$O ligands in the first Au coordination shell cannot be ruled out on the basis of EXAFS spectra only. Independent criteria from thermodynamics and XANES spectra help constrain the Au–Cl speciation model. The dominant presence of AuCl$_2^-$ in solutions above 200–250 °C is in agreement with the equilibrium thermodynamic calculations showing that this species accounts for more than ~70 and 85% of total Au at 250 °C in the systems Au$_{(s)}$–HAuCl$_4$–0.5 m NaCl–0.01 m HCl and Au$_{(s)}$–HAuCl$_4$–0.5 m NaCl–0.5 m HCl, respectively (Supplementary Table). Unlike EXAFS, XANES spectra are particularly sensitive to the absorber oxidation state and cluster symmetry and geometry. As it will be shown below, an independent demonstration that AuCl$_2^-$ is by far the dominant Au species at these conditions is provided by ab-initio XANES spectra modeling using the optimized species geometries calculated by quantum-chemical algorithms and the experimental EXAFS-derived Au–Cl distances.

3.3. Quantum-chemical calculations of Au–Cl species structures and XANES spectra

The optimized Au–O and Au–Cl distances and bond angles for different Au hydroxide and chloride species are listed in Table 3, and selected complexes geometries are shown in Fig. 7. Calculations demonstrate that all Au^I complexes adopt linear configurations, whereas AuCl$_4^-$ has a planar square-like structure, in agreement with general chemical rules and available crystallographic data. The Au–Cl distances calculated at all theory levels are 0.05–0.1 Å longer than the experimental values. The use of different relativistic effective core potentials for Au yields Au–Cl and Au–O distances which agree with

Table 3
Au–O and Au–Cl bond lengths (in angstroms) and ligand–Au–ligand angles (in degrees) for Au–OH–Cl complexes predicted from quantum chemical calculations, and their comparison with EXAFS data

Species	Chemical bond	L–Au–L angle, calculated	R, calculated	R, EXAFS
$Au(OH)(H_2O)^0$, gas[a]	Au–OH	175.9	1.98	
	Au–OH_2		2.18	
$Au(OH)(H_2O)^0$, gas[b]	Au–OH	176.5	1.97	
	Au–OH_2		2.15	
$Au(OH)(H_2O)^0$, gas[c]	Au–OH	175.9	1.99	
	Au–OH_2		2.19	
$Au(OH)(H_2O)^0$, gas[d]	Au–OH	175.7	1.98	
	Au–OH_2		2.19	
$Au(OH)(H_2O)^0$, aq[e]	Au–OH	178.6	2.02	
	Au–OH_2		2.08	
$AuCl(H_2O)^0$, gas[a]	Au–Cl	179.7	2.28	
	Au–OH_2		2.19	
$AuCl(H_2O)^0$, gas[b]	Au–Cl	179.8	2.25	
	Au–OH_2		2.15	
$AuCl(H_2O)^0$, aq[e]	Au–Cl	178.8	2.33	
	Au–OH_2		2.15	
$AuCl_2^-$, gas[a]	Au–Cl	180.0	2.36	
$AuCl_2^-$, gas[b]	Au–Cl	180.0	2.32	
$AuCl_2^-$, gas[c]	Au–Cl	180.0	2.37	
$AuCl_2^-$, gas[d]	Au–Cl	180.0	2.38	
$AuCl_2^-$, aq[e]	Au–Cl	180.0	2.37	2.267±0.004
$AuCl_2^-\cdot2H_2O$, gas[a]	Au–Cl	180.0	2.35	
$AuCl_4^-$, gas[a]	Au–Cl	90.0	2.37	
$AuCl_4^-$, gas[b]	Au–Cl	90.0	2.33	
$AuCl_4^-$, aq[e]	Au–Cl	90.0	2.37	2.282±0.004
$AuCl_4^-\cdot4H_2O$, gas[a]	Au–Cl	90.0	2.36	

[a] B3LYP/SDD/6-311+G(d).
[b] MP2/SDD/6-311+G(d).
[c] B3LYP/CEP-121G/6-311+G(d).
[d] B3LYP/LANL2DZ/6-311+G(d).
[e] PCM/B3LYP/SDD/6-311+G(d).

one another within ~0.02 Å. The solvation of Au complexes by water molecules, with the formation of $AuCl_2^-\cdot2H_2O$ and $AuCl_4^-\cdot4H_2O$ gaseous clusters results in a small (by 0.01 Å) decrease of Au–Cl distances. Changes in $AuCl_2^-$ and $AuCl_4^-$ geometries induced by the

incorporation of bulk solvent effects using the PCM model are also minor (≤0.01 Å, ≤1°). In contrast, solvation of polar molecules $Au(OH)(OH_2)^0$ and $AuCl(OH_2)^0$ results in elongation of Au–OH and Au–Cl distances (by 0.04 and 0.05 Å, respectively), and shortening of Au–OH_2 distances (by 0.10 and 0.04 Å for $Au(OH)(OH_2)^0$ and $AuCl(OH_2)^0$, respectively) compared to the gas phase geometries. These calculations are in qualitative agreement with those of Tossel (1996). Calculations at the MP2 level of theory yield shorter than DFT Au–Cl distances which are closer to those determined from EXAFS experiments, with differences of ~0.05 Å.

The calculated geometries of Au–Cl complexes and EXAFS-derived Au–Cl distances can be used to quantitatively interpret the XANES spectra obtained in this study (e.g., Fig. 2b). It should be remembered that the 'white line' observed in the XANES spectra of most Au^I and Au^{III} compounds results from the 2p to 5d orbital electronic transitions and should be regarded rather as a pre-edge feature (e.g., Benfield et al., 1994; Berrodier et al., 2004; references therein). In Au^{III} compounds like $KAuCl_4\cdot2H_2O_{(s)}$, the 5d orbital is partially empty and such a transition yields a particularly intense feature (labeled A in Fig. 2b). In contrast, for Au^I compounds like $AuCl_{(s)}$, the amplitude of the 'white line' (labeled E in Fig. 2b) is dramatically decreased and slightly shifted to higher energy because only a single electron transition is allowed to the $5d^9$ orbital set. In the case of native gold $Au_{(s)}$, the 5d orbital is filled, having a d^{10} electronic configuration, thus rendering the 2p5d transition impossible. This leads to the disappearance of the 'white line' in its spectrum. Thus, the 'white line' feature allows direct determination of the oxidation state of Au in its aqueous and solid species, which is quantitatively confirmed by XANES ab-initio modeling.

XANES modeling was performed to check the two different model geometries suggested by quantum chemical calculations, i.e. square-plane $Au^{III}Cl_4$ and linear Au^ICl_2 structures, which are inferred for Exp 7 at 22 and 250 °C, respectively, on the basis of XANES spectra comparisons and EXAFS-derived distances and coordination numbers (see Sections 3.1 and 3.2). The calculations were performed for isolated molecules by taking into account only the central Au atom and the first shell composed of Cl atoms, without considering solvation effects in solution. The electronic structures of Au^0, Au^I
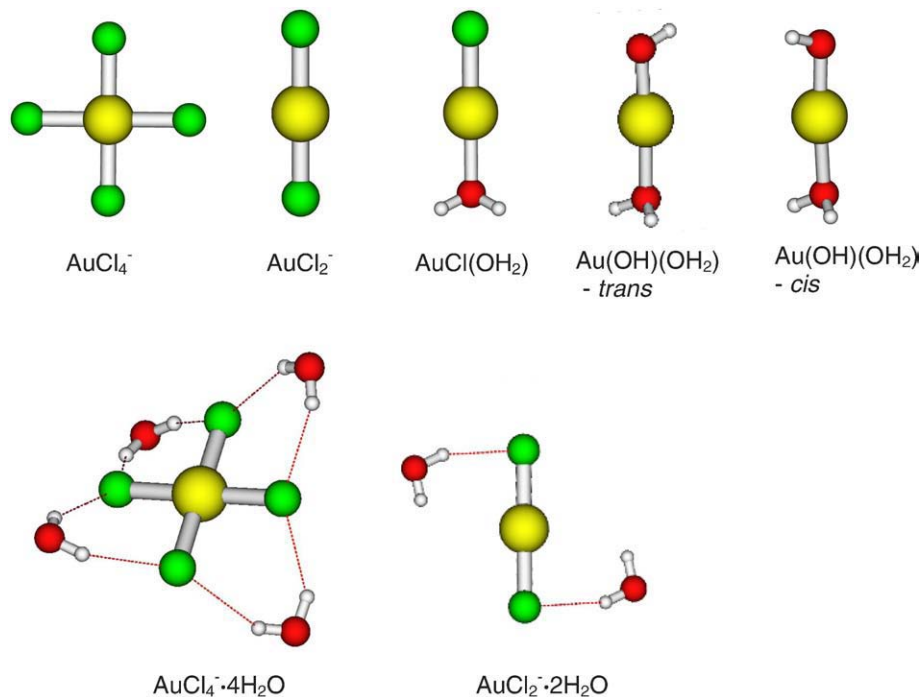

Fig. 7. Optimized gas-phase geometries of Au^{III} and Au^I chloride and hydroxide species calculated using DFT quantum-chemical methods using B3LYP/SDD/6-311+G(d) formalisms.

and Au^{III} were assumed to be respectively $[Xe]4f^{14}5d^{10}6s^1$, $[Xe]$ $4f^{14}5d^96s^1$ and $[Xe]4f^{14}5d^86s^1$. Note that the partial charge on the gold atom is +1 for Au^I and +2 for Au^{III}, because the valence state electron is not completely delocalized, particularly in case of the strongly covalent Au^{III}–Cl compounds; this results in a lower partial charge on the Au^{III} atom than the apparent oxidation state of +3. Calculated and experimental spectra are compared in Fig. 8.

It can be seen that for both structures, the raw calculations reproduce all characteristic features observed in the experimental spectra. The convoluted spectrum for the $Au^{III}Cl_4$ cluster corresponds fairly well to the experimental one at 22 °C where $AuCl_4^-$ is by far the dominant species. For Au^ICl_2, the agreement is less good, particularly in the near-edge energy range. The calculated 'white' line position is shifted by ~2 eV to lower energy and exhibits a lower amplitude

(a)

(b)

Fig. 8. XANES spectra of (a) $AuCl_4^-$ and (b) $AuCl_2^-$ aqueous species modeled using the FDMNES ab-initio code, and their comparison with experimental data (Exp 7 at 22 and 250 °C, 600 bar). The raw calculated spectra are scaled by ×0.4 for clarity. The energy of 0 eV on the X-axis corresponds to the L_{III} absorption edge of metallic Au at 11919 eV. The high-intensity 'spikes' below 0 eV in the raw spectra correspond to predicted electronic transitions that are not resolved in the convoluted spectra, which take into account the core-hole width and experimental resolution (see Section 2.4).

compared to the experimental spectrum. However, all major features in the 20–60 eV range above the edge match correctly the experimental spectrum. Thus, both models are in semi-quantitative agreement with the experimental XANES spectra, confirming that $Au^{III}Cl_4^-$ and $Au^ICl_2^-$ are the dominant Au species in the investigated solution at 22 and 250 °C, respectively. The mismatches between calculated and experimental amplitudes of XANES features might be attributed to the presence of a weak hydration shell around Au complexes in solution that was not considered by the present modeling. Such hydration is expected to have no detectable effect on the EXAFS signal which is poorly sensitive to distant and loosely bound shells, but it may influence the XANES spectra owing to their greater sensitivity than EXAFS to the atomic arrangement and cluster geometry. For example, solvation effects may slightly affect the amplitudes of the main XANES features as shown for the similar $CuCl_2^-$ species having a linear Cl–Cu–Cl geometry (Brügger et al., 2007). Work is currently in progress to explicitly account for the solvation effects on XANES spectra of Au complexes.

4. Discussion

4.1. Au^{III}–Au^I relationships and comparison with available Raman spectroscopy studies

The whole set of XANES and EXAFS results obtained in this study together with available thermodynamic data indicates that $AuCl_4^-$ and $AuCl_2^-$ are by far the dominant Au species in the investigated acidic Cl-bearing systems at $T \leq 100$ °C and $T \geq 250$ °C, respectively. In the intermediate T-range, in the $HAuCl_4$–NaCl–HCl system with and without $Au_{(s)}$, the fraction of each species can be thus quantified from XANES linear combination analyses (LCA) using, as the references, the XANES spectra of $AuCl_4^-$ and $AuCl_2^-$ obtained at 22 and 250 °C, respectively (Exp 7). The fraction of Au present as $AuCl_2^-$ ($Au_{tot} = AuCl_4^- + AuCl_2^-$) derived from the analysis of XANES spectra is reported in Table 1. Note that because of contrasting spectral shapes for Au^{III} and Au^I species, the limit of detection of each species fraction is very low, <3% of total Au, with a typical uncertainly less than 5%. This detection limit is much lower than that derived from the average number of chlorine atoms determined from EXAFS spectra (~10–20%) because of the much greater sensitivity of XANES than EXAFS to Au redox state and species geometry (linear Au^ICl_2 versus plane-square $Au^{III}Cl_4^-$) despite the similarities in Au–Cl bond lengths in both complexes (~2.27–2.28 Å). The accurate match of the experimental XANES spectra with the sum of the two end member species strongly suggests that no other complexes with different XANES signatures (e.g., $AuCl_3^{2-}$, $AuOH^0$) may be present in significant amounts. Thus, both EXAFS and XANES yield identical $AuCl_2^-/AuCl_4^-$ fractions within errors confirming again that these two species are largely dominant in our experimental systems.

It can be seen in Table 1 that in the $HAuCl_4$–NaCl–HCl solutions without gold, the reduction with increasing temperature of Au^{III} to Au^I is much slower in the (more inert) sapphire cell than in the carbon cell (Exp 2 versus Exp 3), but in both cases the precipitation of metallic Au, which starts at 250 and 150 °C, respectively, is always accompanied by the progressive formation of $AuCl_2^-$ at the expense of $AuCl_4^-$. These findings agree with the Raman spectroscopic study of Pan and Wood (1991) carried out on concentrated hydrochloric acid solutions ($m_{HCl} = 2$–5) at P_{sat} using a Pyrex cell, which indicated the appearance of a new band at ~332 cm^{-1} above 100 °C, tentatively attributed to the $AuCl_2^-$ species. This assignment was, however, disputed in the more recent Raman spectroscopic study of Murphy et al. (2000) carried out on less acidic solutions similar to those of our study at comparable T–P conditions and using silica or glass pressure cells. These authors observed rapid Au precipitation at elevated temperatures from $HAuCl_4$–HCl solutions similar to our findings, but did not detect any new bands that might correspond to the $AuCl_2^-$ species, in contrast
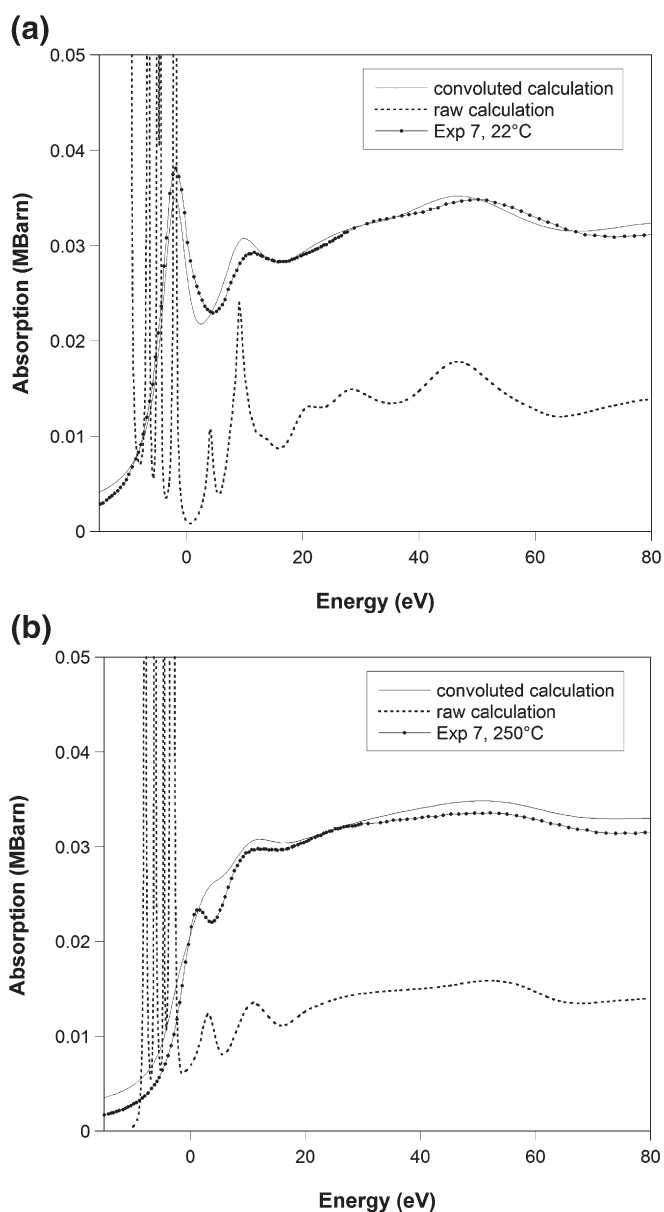
with our XAFS evidence for $AuCl_4^-$ reduction to $AuCl_2^-$. This apparent disagreement might be related to the much lower sensitivity of Raman spectroscopy, in comparison to XAFS, to distinguish between the overlapping Au^{III}–Cl and Au^I–Cl vibrations which are expected to be very close following their almost identical bond lengths (within 0.01 Å) as found in our study (e.g., Raman frequencies for the stretching Au–Cl vibrations at ambient conditions are 324 and 329 cm^{-1}, respectively for $AuCl_4$ and $AuCl_2$ moieties in solid compounds, Braunstein and Clark, 1973; Murphy et al., 2000). Another possibility might be differences in cell-material properties between our and their study resulting in different redox potentials which might favor $AuCl_2^-$ stability in our experiments. A third possibility might be X-ray beam induced reduction, but no convincing demonstration of X-ray beam effects could be done in our study at least within the limited period of beam exposure (up to few hours).

In the presence of an excess of metallic gold in $HAuCl_4$–NaCl–HCl solutions, the fraction of $AuCl_2^-$ in solution increases with the temperature rise and is comparable in both the carbon and sapphire cells (Exp 4 versus Exp 1) at $T \leq 150$ °C, and it is also close to that measured in the absence of gold. At $T > 150$ °C, almost all Au is lost from solution in the carbon cell, but in the sapphire cell, $AuCl_4^-$ reduction to $AuCl_2^-$ increases and is accompanied by Au dissolution between 150 and 200 °C, followed by Au precipitation at $T \geq 250$ °C (Table 1, Figs. 2 and 3). These observations are in agreement with the Raman study of Murphy et al. (2000) which showed, on the basis of peak fitting procedures, a growth at $T \geq 250$ °C of the band at ~326 cm^{-1} tentatively attributed to the $AuCl_2^-$ species. Note, however, that quantification of species distribution and total dissolved Au concentrations was not possible from Raman spectra in contrast with XAFS spectra obtained in this study.

4.2. Comparison with thermodynamic calculations

The Au aqueous concentrations and species distribution obtained from XAFS spectroscopy can be compared with available thermodynamic data for aqueous Au species which are largely based on solubility measurements performed over a wide range of *T–P* and solution compositions. Detailed discussion of the different data sources, derivation of thermodynamic properties for some Au aqueous species, and computational details are reported in the Appendix, whereas calculated Au total concentrations and fractions of the major species in the solutions investigated by XAFS are listed in the Supplementary Table.

4.2.1. Metal-free $HAuCl_4$–NaCl–HCl system

In the metal-free $HAuCl_4$–NaCl–HCl solutions, calculations predict that $AuCl_4^-$ is the dominant species (>90%) and that no Au precipitation occurs to at least 300 °C. In contrast, our experiments show that at least 50% of total dissolved Au is reduced to $AuCl_2^-$ at $T < 250$ °C, and the major part of Au is precipitated above 250 °C both in carbon and sapphire cells. If this discrepancy may be easily explained for experiments in the carbon cell whose minor dissolution at elevated temperatures creates reducing conditions favorable for Au^{III} reduction as shown by thermodynamic calculations, the cause for Au reduction/precipitation phenomena observed in the inert sapphire cell remains unclear. It might result from beam-induced effects, as was observed for sulfite (SO_3) and thiosulfate (S_2O_3) aqueous solutions of monovalent gold at ambient temperature (Pokrovski, personal communication), and NaCl–NaOH solutions of trivalent gold at neutral-to-basic pH (Berrodier et al., 2004; Wang et al., 2007). Such effects were not observed, however, in the acidic Au^{III}–Cl solutions at ambient temperature over at least 2–3 h of beam exposure in this study, where Au^{III} is in the form of the extremely stable $AuCl_4^-$ complex. Similarly, no beam-induced Au precipitation was detected in XAFS experiments with the identical cell configuration in the system Au–S–NaOH where Au^I forms very stable hydrosulfide species (Pokrovski et al., 2006b). Thus, no convincing evidence for beam-induced effects

in the Au^I–Cl system can be provided in this study likely owing to a combination of other factors (e.g., cell material, gas exchange etc.) which further complicate the spectroscopic investigation of certain redox-sensitive systems. Further systematic studies are necessary to quantitatively address the X-ray beam effects.
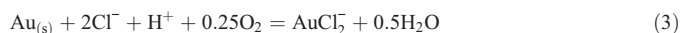
Note that the partial dissolution of He in the fluid at temperatures below 300 °C is too low to significantly affect water activity and thus decrease metal solubilities (see Section 2.1 for details). Assuming, in the worst case, an equilibrium between the experimental solution and helium gas, He solubility in pure water at 600 bar He and 250 °C is <2 mol% and is even less in the presence of electrolytes (NaCl), thus suggesting that He dissolution is unlikely to explain the observed low solubility.

Another possible cause for the observed discrepancy might be the loss of oxygen through the Viton seal rings (e.g., the oxygen fugacity in $AuCl_4^-/AuCl_2^-$ solutions (Exp 2) in the absence of $Au_{(s)}$ at 200 and 300 °C is predicted to be as high as 0.5 and 1 bar, respectively). Note also that the formation of a thin water film between the seal rings and the cell/piston walls may favor the escape of dissolved gas. Oxygen loss, together with fast reduction kinetics of dissolved Au at elevated temperatures may lead to precipitation of small quantities of metallic Au at $T > 100$ °C followed by massive Au precipitation at $T \sim 300$ °C. This could explain why the $AuCl_4^-/AuCl_2^-$ ratio in Exp 2 (initially metal-free) was close to that determined in the presence of metallic Au (Exp 1).

4.2.2. $HAuCl_4$–NaCl–HCl system with native gold at weakly acidic pH

In the weakly acidic (0.01 m HCl) $HAuCl_4$–NaCl–HCl system with an excess of Au metal examined in our study (Exp 1 and 4), thermodynamic calculations predict the formation of the $AuCl_2^-$, $AuOH^0$ and $AuCl^0$ aurous species at the expense of $AuCl_4^-$, and an increase of dissolved Au concentrations from ~0.04 to 0.10 m as temperature is raised from 100 to 300 °C (Supplementary Table). The predicted aqueous distribution of all Au–Cl species is in qualitative agreement with our XAFS findings, as well as the small amount of $AuOH^0$ calculated using gold solubility data from Zotov et al. (1985) and Vlassopoulos and Wood (1990) (see Appendix). Data of Stefánsson and Seward (2003a) yield somewhat higher concentrations of $AuOH^0$ at 100–300 °C (up to 45% of total aqueous Au) in contradiction with our XAFS spectra, which do not show the presence of oxygen atoms in the first coordination sphere of Au (Table 2) within the detection limit of XAFS spectroscopy ($N_O < ~0.1$–0.2 atoms).

Like in the metal-free system, XAFS-measured total Au concentrations at $T \geq 150$ °C are 1–2 orders of magnitude lower than those deduced from thermodynamic calculations. The reasons for that may be i) influence of the cell material (carbon in Exp 4), ii) beam-induced effects, and iii) equilibration of oxygen/hydrogen pressure with the external autoclave volume through the seal rings. Indeed, if the ratio of $AuCl_4^-/AuCl_2^-$ concentrations is independent of redox conditions (Eq. (2)), dissolved Au concentration is controlled by the oxygen (or hydrogen) contents according to the reactions

$$Au_{(s)} + 2Cl^- + H^+ + 0.25O_2 = AuCl_2^- + 0.5H_2O \tag{3}$$

$$Au_{(s)} + 4Cl^- + 3H^+ + 0.75O_2 = AuCl_4^- + 1.5H_2O \tag{4}$$

Thus, the loss of dissolved oxygen from the spectroscopic cell would result both in reduction of Au^{III} and in $Au_{(s)}$ precipitation. Quantification of the contributions of different factors affecting Au behavior in Cl-bearing systems at elevated temperatures will await further studies.

4.2.3. $HAuCl_4$–NaCl–HCl system with native gold at strongly acidic pH

In the more acidic and Cl-rich $HAuCl_4$–NaCl–HCl system (~0.5 m HCl–0.5 m NaCl) with an excess of native gold at 250 °C and 600 bar (Exp 7 in sapphire cell), calculations predict that more than 85% of

total Au is in the form of $AuCl_2^-$, with minor contributions from $AuCl^0$ ($<10\%$) and $AuCl_4^-$ ($<5\%$). This is in quantitative agreement with our EXAFS and XANES results which indicate that $AuCl_2^-$ accounts for more that 90% of total Au, with a possible presence of less than 5-10% of $AuCl^0$ or other species ($AuOH^0$), which is at the limit of spectral resolution. XAFS-derived aqueous Au concentrations are, however, at least an order of magnitude lower than the predicted values (0.05–0.10 m), and show a progressive decrease with time even after 2 h of measurement. Again, we are not able to account for these discrepancies. Considering the inert and tight nature of the Al_2O_3 cell used in this run, the most probable explanation would be Au reduction under the effect of X-ray irradiation which may cause water radiolysis and production of hydrogen radicals and solvated electrons (H^*, e^-) in solution that might be efficient reductants of Au^I species (e.g., Wang et al., 2007). More experiments are needed to quantitatively address this issue.

5. Concluding remarks

To our knowledge, this study provides the first measurements using in situ XAFS spectroscopy of the stability and structure of Au^{III} and Au^I chloride complexes at elevated temperatures and pressures pertinent to natural hydrothermal conditions. It demonstrates that XAFS spectroscopy can be used for direct measurement of both concentrations and the local atomic structures of metals in the complex and rapidly evolving fluid systems ubiquitous in high T–P geological environments.

Combination of classical XAFS spectral analysis with ab-initio quantum-chemical calculations of optimized geometries and XANES spectra of Au aqueous complexes allows accurate characterization of the identities and structures of the Au species responsible for the gold transport by high-temperature hydrothermal fluids. Our data provide direct spectroscopic evidence for the formation of the $AuCl_2^-$ complex in acidic saline hydrothermal fluids. This complex is linear, with Au–Cl distances of 2.267±0.004 Å, in agreement with Au^I crystal chemistry. The structural parameters for this species, derived for the first time, will allow an improved interpretation of Raman spectroscopic data and predictions of solvation effects in high T–P fluids.

This study also shows that the properties of the spectroscopic cell material and X-ray beam-induced effects may exert strong influence on redox-sensitive aqueous systems like that investigated in this study. Explicit account of these effects is required to unambiguously interpret in situ spectroscopic data at elevated T–P.

Acknowledgements

Appendix A. Supplementary data

Supplementary data associated with this article can be found, in the online version, at doi:10.1016/j.chemgeo.2008.09.007.

References

Akinfiev, N.N., Zotov, A.V., 2001. Thermodynamic description of chloride, hydrosulphide, and hydroxo complexes of Ag(I), Cu(I), and Au(I) at temperatures of 25–500 °C and pressures of 1–2000 bar. Geochem. Int. 39 (10), 990–1006.

Anderko, A., Pitzer, K.S., 1993. Equation-of-state representation of phase equilibria and volumetric properties of the system NaCl–H2O above 573 K. Geochim. Cosmochim. Acta 57, 1657–1680.

Bakker, R.J., 2003. Package FLUIDS 1. Computer programs for analysis of fluid inclusion data and for modelling bulk fluid properties. Chem. Geol. 194, 3–23.

Becke, A.D., 1993. Density-functional thermochemistry. III. The role of exact exchange. J. Chem. Phys. 98, 5648–5652.

Benfield, R.E., Filipponi, A., Bowron, D.T., Newport, R.J., Gurman, S.J., 1994. An X-ray absorption study of gold coordination compounds: EXAFS refinements and double-electron excitation background. J. Phys., Condens. Matter 6, 8449–8468.

Berrodier, I., Farges, F., Benedetti, M., Winterer, M., Brown Jr., G.E., Deveughèle, M., 2004. Adsorption mechanisms of trivalent gold on iron- and aluminum-(oxy)hydroxides. Part 1: X-ray absorption and Raman scattering spectroscopic studies of Au(III) adsorbed on ferrihydrite, goethite, and boehmite. Geochim. Cosmochim. Acta 68, 3019–3042.

Braunstein, P., Clark, R.J.H., 1973. The preparation, properties and vibrational spectra of complexes containing the $AuCl_2^-$, $AuBr_2^-$ and AuI_2^- ions. J. Chem. Soc. Dalton Trans. 1845–1848.

Brugger, J., Etschmann, B., Liu, W., Testemale, D., Hazemann, J.-L., Emerich, H., van Beek, W., Proux, O., Tran, C., 2007. An XAS study of the structure and thermodynamics of Cu(I) chloride complexes in brines up to high temperature (400 °C, 600 bars). Geochim. Cosmochim. Acta 71, 4920–4941.

Crozier, E.D., Rehr, J.J., Ingalls, R., 1988. Amorphous and liquid systems. In: Koningsberger, D.C., Prins, R. (Eds.), X-ray Absorption: Principles, Applications, Techniques of EXAFS, SEXAFS and XANES. Wiley-Interscience, New York, pp. 373–442.

Cromer, D.T., Liberman, D., 1970. Relativistic calculations of anomalous scattering factors for X-rays. J. Chem. Phys. 53, 1891–1898.

Elam, W.T., Ravel, B.D., Sieber, J.R., 2002. A new atomic database for X-ray spectroscopic calculations. Radiat. Phys. Chem. 63, 121–128.

Farges, F., Sharps, J.A., Brown Jr., G.E., 1993. Local environment around gold(III) in aqueous chloride solutions: An EXAFS spectroscopy study. Geochim. Cosmochim. Acta 57, 1243–1252.

Feller, D., Glendening, E.D., Jong, W.A., 1999. Structures and binding enthalpies of M^+ $(H_2O)_n$ clusters, M=Cu, Ag, Au. J. Chem. Phys. 110, 1475–1491.

Frisch, M.J., Trucks, G.W., Schlegel, H.B., Scuseria, G.E., Robb, M.A., Cheeseman, J.R., Montgomery Jr., J.A., Vreven, T., Kudin, K.N., Burant, J.C., Millam, J.M., Iyengar, S.S., Tomasi, J., Barone, V., Mennucci, B., Cossi, M., Scalmani, G., Rega, N., Petersson, G.A., Nakatsuji, H., Hada, M., Ehara, M., Toyota, K., Fukuda, R., Hasegawa, J., Ishida, M., Nakajima, T., Honda, Y., Kitao, O., Nakai, H., Klene, M., Li, X., Knox, J.E., Hratchian, H.P., Cross, J.B., Bakken, V., Adamo, C., Jaramillo, J., Gomperts, R., Stratmann, R.E., Yazyev, O., Austin, A.J., Cammi, R., Pomelli, C., Ochterski, J.W., Ayala, P.Y., Morokuma, K., Voth, G.A., Salvador, P., Dannenberg, J.J., Zakrzewski, V.G., Dapprich, S., Daniels, A.D., Strain, M.C., Farkas, O., Malick, D.K., Rabuck, A.D., Raghavachari, K., Foresman, J.B., Ortiz, J.V., Cui, Q., Baboul, A.G., Clifford, S., Cioslowski, J., Stefanov, B.B., Liu, G., Liashenko, A., Piskorz, P., Komaromi, I., Martin, R.L., Fox, D.J., Keith, T., Al-Laham, M.A., Peng, C.Y., Nanayakkara, A., Challacombe, M., Gill, P.M.W., Johnson, B., Chen, W., Wong, M.W., Gonzalez, C., Pople, J.A., 2004. Gaussian 03, Revision C.02. Gaussian, Inc., Wallingford CT.

Gammons, C.H., Williams-Jones, A.E., 1995. The solubility of Au–Ag alloy+AgCl in HCl/NaCl solutions at 300 °C: new data on the stability of Au(I) chloride complexes in hydrothermal fluids. Geochim. Cosmochim. Acta 59, 3453–3468.

Gammons, C.H., Williams-Jones, A.E., 1997. The disproportionation of gold(I) chloride complexes at 25 to 200 °C. Geochim. Cosmochim. Acta 61, 1971–1983.

Hay, P.J., Wadt, R.R., 1985. Ab initio effective core potentials for molecular calculations. Potentials for K to Au including the outermost core orbitals. J. Chem. Phys. 82, 299–310.

Henley, R.W., 1973. Solubility of gold in hydrothermal chlorine solution. Chem. Geol. 11, 73–87.

Joly, Y., 2001. X-ray absorption near-edge structure calculations beyond the muffin tin approximation. Phys. Rev. B 63, 125120.

Jones, P.G., Hohbein, R., Schwarzmann, E., 1988. Anhydrous sodium tetrachloroaurate (III). Acta Crystallogr. C 44, 1164–1166.

Kimball, G.E., Shortley, G.H., 1934. The numerical solution of Schrödinger's equation. Phys. Rev. 45, 815–820.

Lee, C., Yang, W., Parr, R.G., 1988. Development of the Colle–Slavetti correlation-energy formula into a functional of the electron density. Phys. Rev. B 37, 785–789.

Maeda, M., Ohtaki, H., Johansson, G., 1974. An X-ray investigation of the structures of the tetrachloro- and tetrabromoaurate(III) ions in aqueous solution. Bull. Chem. Soc. Japan 47 (9), 2229–2237.

Murphy, P.J., LaGrange, M.S., 1998. Raman spectroscopy of Au chloro-hydroxy speciation in fluids at ambient T and P: a re-evaluation of the effects of pH and chloride concentration. Geochim. Cosmochim. Acta 62, 3515–3526.

Murphy, P.J., Stevens, G., LaGrange, M.S., 2000. The effects of temperature and pressure on gold-chloride speciation in hydrothermal fluids: a Raman spectroscopic study. Geochim. Cosmochim. Acta 64, 479–494.

Newville, M., 2001. IFEFFIT: interactive XAFS analysis and FEFF fitting. J. Synchrotron Radiat. 8, 322–324.

Nikolaeva, N.M., Erenburg, A.M., Antipina, V.A., 1972. About the temperature dependence of the standard potentials of halogenide complexes of gold. Izv. Sibirskogo Otdeleniya AN SSSR, No. 9. Ser. Khim. Nauk, Vip., vol. 4, pp. 126–128 (in Russian).

Pan, P., Wood, S.A., 1991. Gold-chloride complexes in very acidic aqueous solutions and at temperatures 25–300 °C: a laser Raman spectroscopic study. Geochim. Cosmochim. Acta 55, 2365–2371.

Peck, J.A., Tait, C.D., Swanson, B.I., Brown Jr., G.E., 1991. Speciation of aqueous gold(III) chloride from ultraviolet/visible absorption and Raman/resonance Raman spectroscopies. Geochim. Cosmochim. Acta 55, 671–676.

Pokrovski, G.S., Bény, J.-M., Zotov, A.V., 1999. Solubility and Raman spectroscopic study of As(III) speciation in organic compound-water solutions. A hydration approach for aqueous arsenic in complex solutions. J. Solution Chem. 28, 1307–1327.

Pokrovski, G.S., Zakirov, I.V., Roux, J., Testemale, D., Hazemann, J.-L., Bychkov, A.Y., Golikova, G.V., 2002. Experimental study of arsenic speciation in vapor phase to 500 °C: implications for As transport and fractionation in low-density crustal fluids and volcanic gases. Geochim. Cosmochim. Acta 66, 3453–3480.

Pokrovski, G.S., Roux, J., Hazemann, J.-L., Testemale, D., 2005a. An X-ray Absorption spectroscopy study of argutite solubility and germanium aqueous speciation in hydrothermal fluids to 500 °C and 400 bar. Chem. Geol. 217, 127–145.

Pokrovski, G.S., Roux, J., Harrichoury, J.-C., 2005b. Fluid density control on vapor–liquid partitioning of metals in hydrothermal systems. Geology 33, 657–660.

Pokrovski, G.S., Borisova, A.Yu., Roux, J., Hazemann, J.-L., Petdang, A., Tella, M., Testemale, D., 2006a. Antimony speciation in saline hydrothermal fluids: a combined X-ray absorption fine structure and solubility study. Geochim. Cosmochim. Acta 70, 4196–4214.

Pokrovski, G.S., Tagirov, B.R., Schott, J., Hazemann, J.-L., Harrichoury, J-C., Roux, J., 2006b. Speciation of gold and associated metals at hydrothermal conditions: in situ experimental approaches and physical–chemical modeling. Actes du Colloque GDR Transmet — Bilan & Perspectives, Nancy 6–7 juillet 2006, pp. 91–94.

Pokrovski, G.S., Borisova, A.Yu., Harrichoury, J.-C., 2008a. The effect of sulfur on vapor–liquid fractionation of metals in hydrothermal systems. Earth Planet. Sci. Lett. 266, 345–362.

Pokrovski, G.S., Roux, J., Hazemann, J.-L, Borisova, A.Yu., Gonchar, A.A., Lemeshko, M.P., 2008b. In situ X-ray absorption spectroscopy measurement of vapour-brine fractionation of antimony at hydrothermal conditions. Min. Mag. 72 (2), 667–681.

Proux, O., Nassif, V., Prat, A., Ulrich, O., Lahera, E., Biquard, X., Menthonnex, J.-J., Hazemann, J.-L., 2006. Feedback system of a liquid-nitrogen-cooled double-crystal monochromator: design and performances. J. Synchrotron Radiat. 13, 59–68.

Proux, O., Biquard, X., Lahera, E., Menthonnex, J.-J., Prat, A., Ulrich, O., Soldo, Y., Trevisson, P., Kapoujyan, G., Perroux, G., Taunier, P., Grand, D., Jeantet, P., Deleglise, M., Roux, J.-P., Hazemann, J.-L., 2005. FAME: a new beamline for X-ray absorption investigations of very diluted systems of environmental, material and biological interests. Phys. Scripta T115, 970–973.

Ravel, B., Newville, M., 2005. ATHENA, ARTEMIS, HEPHAESTUS: data analysis for X-ray absorption spectroscopy using IFEFFIT. J. Synchrotron Radiat. 12, 537–541.

Rehr, J.J., 2006. Theory and calculations of X-ray spectra: XAS, XES, XRS, and NRIXS. Radiat. Phys. Chem. 75, 1547–1558.

Rehr, J.J., Albers, R.C., Zabinsky, S.I., 1992. High-order multiple-scattering calculations of X-ray-absorption fine structure. Phys. Rev. Lett. 69, 3397–3400.

Schott, J., Pokrovski, G.S., Tagirov, B.R., Hazemann, J.-L., Proux, O., 2006. First in situ XAFS determination of gold solubility and speciation in sulfur-rich hydrothermal solutions. Geochim. Cosmochim. Acta 70 (18A), 13.

Schwerdtfeger, P., Dolg, M., Schwarz, W.H.E., Bowmaker, G.A., Boyd, P.D.W., 1989. Relativistic effects in gold chemistry. I. Diatomic gold compounds. J. Chem. Phys. 91, 1762–1774.

Seward, T.M., Driesner, T., 2004. Hydrothermal solution structure: experiments and computer simulations. In: Palmer, D.A., Fernandez-Prini, R., Harvey, A.H. (Eds.), Aqueous Systems at Elevated Temperatures and Pressures. Elsevier, pp. 149–182.

Schulte, M.D., Shock, E.L., Wood, R.H., 2001. The temperature dependence of the standard-state thermodynamic properties of aqueous nonelectrolytes. Geochim. Cosmochim. Acta 65, 3919–3930.

Sherman, D.M., 2001. Quantum chemistry and classical simulations of metal complexes in aqueous solutions. Rev. Min. Geochem. 42, 273–317.

Stefánsson, A., Seward, T.M., 2003a. The hydrolysis of gold(I) in aqueous solutions to 600 °C and 1500 bar. Geochim. Cosmochim. Acta 67, 1677–1688.

Stefánsson, A., Seward, T.M., 2003b. Stability of chloridogold(I) complexes in aqueous solutions from 300 to 600 °C and from 500 to 1800 bar. Geochim. Cosmochim. Acta 67, 4559–4576.

Stevens, W.J., Krauss, M., Basch, H., Jasien, P.G., 1992. Relativistic compact effective potentials and efficient, shared-exponent basis sets for the third-, fourth-, and fifth-row atoms. Can. J. Chem. 70, 612–630.

Straehle, J., Loercher, K.P., 1974. Die Kristalldaten der Goldhalogenide AuBr$_3$ und AuCl. Zeit. Naturfor. Teil B29, 266–267.

Tagirov, B.R., Salvi, S., Schott, J., Baranova, N.N., 2005. Experimental study of gold-hydrosulphide complexing in aqueous solutions at 350–500 °C, 500 and 1000 bars using mineral buffers. Geochim. Cosmochim. Acta 69, 2119–2132.

Tagirov, B.R., Baranova, N.N., Zotov, A.V., Schott, J., Bannykh, L.N., 2006. Experimental determination of the stabilities Au$_2$S(cr) at 25 °C and Au(HS)$_2^-$ at 25–250 °C. Geochim. Cosmochim. Acta 70, 3689–3701.

Testemale, D., Hazemann, J.-L., Pokrovski, G.S., Joly, Y., Roux, J., Argoud, R., Geaymond, O., 2004. Structural and electronic evolution of As(III) atomic environment in hydrothermal solutions: an EXAFS and XANES investigation. J. Phys. Chem. 121, 8973–8982.

Testemale, D., Argoud, R., Geaymond, O., Hazemann, J.-L., 2005. High pressure/high temperature cell for x-ray absorption and scattering techniques. Rev. Sci. Instrum. 76, 043905–043909.

Théobald, F., Omrani, H., 1980. Structure du tetrachloroaurate(III) de potassium dehydrate. Acta Crystallogr. B36, 2932–2935.

Tossel, J.A., 1996. The speciation of gold in aqueous solution: A theoretical study. Geochim. Cosmochim. Acta 60, 17–29.

Vlassopoulos, D., Wood, S.A., 1990. Gold speciation in natural waters: I. Solubility and hydrolysis reactions of gold in aqueous solution. Geochim. Cosmochim. Acta 54, 3–12.

Wang, C.H., Chien, C.C., Yu, Y.L., Lee, C.J., Lee, C.F., Chen, C.H., Hwu, Y., Yang, C.S., Je, J.H., Margaritondo, G., 2007. Structural properties of 'naked' gold nanoparticles formed by synchrotron X-ray irradiation. J. Synchrotron Radiat. 14, 477–482.

Wood, S., Crerar, D.A., Borcsik, M.P., 1987. Solubility of the assemblage pyrite–pyrrhotite–magnetite–sphalerite–galena–gold–stibnite–bismuthinite–argentite–molybdenite in H$_2$O–NaCl–CO$_2$ solutions from 200 to 350 °C. Econ. Geol. 82, 1864–1887.

Zabinsky, S.I., Rehr, J.J., Ankudinov, A., Albers, R.S., Eller, M.J., 1995. Multiple scattering calculations of X-ray absorption spectra. Phys. Rev. B 52, 2995–3009.

Zotov, A.V., Baranova, N.N., 1989. Thermodynamic properties of the aurochloride solute complex AuCl$_2^-$ at temperatures of 350–500 °C and pressures of 500–1500 bars. Sci. Geol. Bull. 42, 335–342.

Zotov, N., Keppler, H., 2002. Silica speciation in aqueous fluids at high pressures and temperatures. Chem. Geol. 184, 71–82.

Zotov, A.V., Baranova, N.N., Dar,'yna, T.G., Bannykh, L.N., Kolotov, V.P., 1985. The stability of AuOH$^0_{sol}$ in water at 300–500 °C and 500–1500 atm. Geochem. Int. 22 (5), 156–161.

AUTEUR : Elena BAZARKINA

TITRE : Transferts du cadmium et du zinc par phase fluide et vapeur dans les processus hydrothermaux et volcaniques: étude expérimentale, modélisation physico-chimique et applications géologiques

DIRECTEURS DE THESE : Gleb POKROVSKI, Alexander ZOTOV

LIEU ET DATE DE SOUTENANCE : LMTG, Toulouse, 15 décembre 2009

RESUME :

Cette étude a pour but de quantifier le rôle de la phase fluide et vapeur dans le comportement de Zn et de Cd dans les processus hydrothermaux/volcaniques, en combinant mesures expérimentales en laboratoire (solubilité, potentiométrie, coefficients de partage) et spectroscopie d'absorption de rayons X in situ (XAS) avec modélisations physico-chimiques et analyses de gaz volcaniques naturels. Nos résultats mettent en évidence la formation de complexes chlorurés en phase fluide et vapeur de stoechiométrie $CdCl_m(H_2O)_n^{2-m}$ ayant des géométries octaédrique ou tétraédrique selon T et m_{Cl}. Les paramètres thermodynamiques générés pour ces complexes démontrent qu'ils sont les espèces majeures responsables du transport de Cd par les fluides naturels. Ces complexes chlorurés de Cd sont beaucoup plus stables que leurs analogues de Zn et jouent un rôle clé dans le fractionnement des deux métaux. L'ensemble des données expérimentales, thermodynamiques et analytiques obtenu permet de proposer un nouveau traceur géochimique des processus hydrothermaux basé sur le rapport Cd/Zn.

MOTS-CLES : cadmium, zinc, fluide hydrothermal, complexes chlorurés, constantes de stabilité, propriétés thermodynamiques, spectroscopie XAS, solubilité, potentiométrie, rapport Cd/Zn

TITLE : Cadmium and zinc transport by hydrothermal and volcanic fluids and vapors: experimental study, physical-chemical modeling and geological applications

ABSTRACT :

The goal of this work is to quantify the role of the vapor and fluid phases in the behavior of Zn and Cd in hydrothermal/volcanic environments, using a combination of laboratory experiments in model systems (solubility, potentiometry, partitioning) and in situ X-ray absorption spectroscopy (XAS) with physical-chemical modeling and analyses of natural fluids. Our results show the formation of chloride complexes with stoichiometries $CdCl_m(H_2O)_n^{2-m}$ and octahedral or tetrahedral geometries depending on T and m_{Cl}. The thermodynamic parameters generated for these species show that they are the main aqueous species responsible for the transport of cadmium in hydrothermal and volcanic settings. Our data demonstrate that Cd chloride complexes are far more stable than their Zn analogs. The ensemble of experimental, analytical and thermodynamic data obtained in this work permits to propose a new geochemical tracer of the evolution and composition of hydrothermal fluids based on the Zn/Cd ratio.

KEY WORDS : cadmium, zinc, hydrothermal fluids, chloride complexes, stability constants, thermodynamic properties, X-ray absorption spectroscopy, solubility, potentiometry, Cd/Zn ratio

DISCIPLINE : Geochemistry

INTITULE ET ADRESSE DU LABORATOIRE :

Laboratoire des Mécanismes et Transferts en Géologie (LMTG), Université de Toulouse, CNRS, OMP, 14, Avenue Edouard Belin, 31400 Toulouse